Lattice Boltzmann Simulation of Fluid Flows with Special Emphasis on Nanofluid Flow through Porous Structures: Development and Applications

A thesis submitted in partial fulfillment of the requirements for the award of the degree of

Doctor of Philosophy

by

Dhrubajyoti Kashyap

November, 2019

Department of Mechanical Engineering

Indian Institute of Technology Guwahati

Guwahati, India-781039

Certificate

It is certified that the work contained in the thesis entitled "Lattice Boltzmann Simulation of Fluid Flows with special emphasis on Nanofluid Flow through Porous Structures: Development and Applications" by Dhrubajyoti Kashyap, has been carried out under my supervision and that this work has not been submitted elsewhere for a degree.

November, 2019

(Anoop K Dass)
Professor
Department of Mechanical Engineering
Indian Institute of Technology Guwahati

Dedicated to My Parents

Acknowledgement

First of all, I express my gratitude to the Almighty for giving me strength and courage in my journey of completion of this thesis.

I would like to offer my sincere gratitude to my thesis supervisor, Prof. Anoop K Dass, for his invaluable contribution in this thesis. Apart from academic, his valuable guidance and motivation to complete a challenging task is admirable. He gave me ample freedom to carry my work on my own while providing necessary suggestions from time to time.

I would like to offer my sincere thanks to the doctoral committee; the chairman, Prof. Manmohan Pandey, the committee member, Prof. Niranjan Sahoo and external member, Prof. Gautam Barua for timely reviewing my work and providing the necessary feedback/suggestions to improve my work. Their valuable suggestions were critical in shaping the present form of the thesis.

I wish to acknowledge the contribution of anonymous reviewers of my two published Journal papers for their valuable suggestions which certainly improve my research work further.

I thank IIT Guwahati for providing the institute fellowship to carry out my research work. Besides, I sincerely thank High-Performance Computing Environment (PARAM-ISHAN) of IIT Guwahati for providing the computational facility to carry out a significant amount of the computations in my research work.

I thank my friends; Dr. Raushan, Dr. Sandeep, Dr. Gyan, Dr. Biplob, Bishwa, Deepak, Dr. Ujjwal, Dr. Binita, Sandip Da, Dr. Vijay, Ashish, Vishnu, Pranab, Satrughan, Soni, Bibhuti and many more for making a pleasant stay at the hostel. Special thank goes to Mirzaul, Subhra and Dr. Asif for their unconditional help at a personal level.

I take this opportunity to convey my gratefulness to my parents and my elder brother for their unbounded love & blessings and bearing patience throughout the journey.

November, 2019 Dhrubajyoti Kashyap

Abstract

This thesis is concerned with the lattice-Boltzmann simulation of various fluid flow and heat transfer problems. The initial work of the thesis concentrates on developing Fortran codes based on single-phase, single-relaxation-time (SRT) and multiple-relaxation-time (MRT) lattice Boltzmann methods. The comparative study between MRT- and SRT-based LBM indicates that for most cases both models provide comparable solutions for laminar flow regimes. Nevertheless, MRT-LB model has an edge over SRT-LB model due to its better stability in solving complex flow problems. Therefore, MRT-LB model is used to analyse the effect of Prandtl number varying from very low (Pr = 0.025) to high (Pr = 151) on natural- and mixed convection in a square cavity with an inner solid block.

The prime objective of the present thesis, however, is to understand the heat transfer and flow behaviour of nanofluids, where nano-sized particles are suspended in a base fluid. Nanofluid provides superior transport properties and heat transfer characteristics compared with conventional fluids. Nanofluids hold good promise for various heat transfer applications such as engine and electronic cooling systems, nuclear reactor, heat exchangers, material processing, pharmaceutical processes and solar thermal collectors. In this regard, a new multiple-relaxation-time (MRT) based two-phase thermal lattice Boltzmann method is developed for a nanofluid flow which is the extension of a previously established single-relaxation-time (SRT) based two-phase lattice Boltzmann model. The two-phase model provides better insights into nanofluid flows than single-phase model as it treats the base fluid and nanoparticles separately while considering different slip velocity mechanisms. Both these models (SRT and MRT) are then employed to carry out investigations on thermal cavity flow problems with a single-particle based nanofluid as well as a new kind of nanofluid, namely, hybrid nanofluid.

The present thesis then extends both (SRT and MRT) two-phase nanofluid algorithms to the field of a nanofluid-saturated porous structure. The simultaneous use of porous media and nanofluids has been a topic of interest due to the demand in high and controlled heat transfer rates in small-size systems. The novel LBM models based on the

SRT and MRT approach incorporate Brinkman-Forchheimer-extended Darcy model for porous medium into the two-phase model for nanofluid by considering appropriate assumptions. Several validation tests are performed to establish the credibility of the developed codes which provide a close agreement between present LBM solutions with published results.

To realise the applicability of these developed models, multiple natural and mixed convection cavity flow problems of practical relevance are investigated for a wide range of dimensionless parameters, namely, Rayleigh number, Richardson number, Prandtl number and Darcy number. The volume fractions of nanoparticles are considered to vary up to 3% to avoid their agglomeration in the base fluid. The success of these attempts has been substantiated through the presentation of various results and their analysis. The comprehensive analysis of results demonstrates that nanofluid with a lower volume fraction of nanoparticles has been effective in improving the overall efficiency of the thermal systems due to the augmentation of the heat transfer rate. However, the rise in total entropy generation with an increase in volume fraction of nanoparticles offsets this improvement to a certain extent.

This work also considers the influence of different boundary conditions on the flow and thermal behaviour for most of the studied flow problems. A detailed analysis of those flow problems is then made on the basis of both first and second law of thermodynamics to identify the optimal configuration with high energy efficiency, at which maximum heat transfer rate and minimum entropy generation prevail.

Contents

List of Figures

List of Tables

Nomenclature

Al_2O_3	Alumina
B	Adjustable coefficient
Be	Bejan number
BR	Blockage ratio (d/L)
c	Lattice speed $(\Delta x/\Delta t)$
c_θ, c_e, c_v	Relaxation parameters in moment space for D2Q5 MRT model
C	Diagonal relaxation matrix in moment space of g
C_P	Specific heat capacity, J kg^{-1} K^{-1}
C_s	Speed of sound in lattice scale
Cu	Copper
d	Length of a square inner block in the cavity, m
D_T	Thermophoretic diffusion coefficient
Da	Darcy number
e	Kinetic energy
$\mathbf{e}_i$	Discrete lattice velocity
f_i	Density distribution function
$\mathbf{F}$	Body force due to the presence of porous medium
$\mathbf{F}_B$	Brownian force
$\mathbf{F}_D$	Drag force
$\mathbf{F}_H$	Gravity and buoyant force in nanofluid
$\mathbf{F}_T$	Thermophoresis force
g_i	Temperature distribution function
$\mathbf{g}$	Acceleration due to gravity, m s^{-2}
$\mathbf{G}$	Boussinesq approximated buoyant force
$\mathrm{G_i}$	Gaussian random number
Gr	Grashof number $(\mathbf{g}\beta\Delta T L^3/(\nu^2))$
k	Thermal conductivity, W m^{-1} K^{-1}

k_b	Boltzmann's constant = 1.38066×10^{23} J K^{-1}
K	Permeability, m^2
L	Length of the cavity, m
m	Moment function for density distribution function in vector form
M	Transformation matrix for density distribution
n	Moment function for temperature distribution function in vector form
N	Transformation matrix for temperature distribution
$\mathbf{N}^{\sigma}$	Total inter-particle interaction forces on σ^{th} component
Nu	Nusselt number
P	Total force acting on the system
Pr	Prandtl number (ν/α)
$r_e, r_\varepsilon, r_q, r_\nu$	Relaxation parameters in moment space for D2Q9 MRT model
r	Position vector of arbitrary lattice node, $[x, y]$
R	Diagonal relaxation matrix in moment space of f
Ra	Rayleigh number $(\mathbf{g}\beta\Delta T L^3/(\nu\alpha))$
Ra_m	Darcy-Rayleigh number $(Ra \times Da)$
Re	Reynolds number $(V_0^* L/\nu)$
Ri	Richardson number (Gr/Re^2)
S_i	Total force term in LBM
S_θ	Non-dimensional entropy generation due to heat transfer
S_ψ	Non-dimensional entropy generation due to fluid friction
t	Lattice time
T	Dimensional temperature, K
T	Transpose of a matrix
u	Dimensionless velocity vector, $[u, v]$
$\mathbf{u}_T$	Thermophoretic velocity
V_0^*	Lid velocity, m s^{-1}
V_{lb}	Characteristic velocity in the lattice unit
w_i	Weighting factor

Greek symbols

α	Thermal diffusivity, $m^2\ s^{-1}$
β	Volume expansion coefficient, K^{-1}
γ	Inclination angle
Δt	Lattice time step
Δx	Lattice spacing
$\in$	Square of kinetic energy
ε	Porosity of the medium
ζ	Heat capacity ratio in porous media
μ	Dynamic viscosity, $kg\ m^{-1}\ s^{-1}$
ν	Kinetic viscosity, $m^2\ s^{-1}$
θ	Dimensionless temperature
ρ	Density of the fluid, $kg\ m^{-3}$
σ	Two components of nanofluid
τ_v	Viscous relaxation time
τ_θ	Thermal relaxation time
φ	Volume fraction of Nanoparticle
χ	Irreversibility factor in entropy generation
ψ	Dimensionless Stream function
Ω	Collision matrix

Subscript* and *Superscript

-	Average value
b	Bottom wall
c	Cold
cup	Cup-mixing
f	Base fluid
h	Hot
i	Number of the distribution function
l	Left wall

m	Mean value
max	Maximum
min	Minimum
nf	Nanofluid phase
p	Nanoparticles
r	Right wall
ref	Reference value
s	Porous matrix
t	Top wall
tot	Total
eq	Equilibrium
$*$	Dimensional variable

Abbreviations

BC	Boundary condition
BE	Boltzmann equation
BGK	Bhatnagar-Gross-Krook
CFD	Computational fluid dynamics
DF	Distribution function
DDF	Double-distribution-function
D2Q5	Two-dimensional five-velocity model (for temperature DF in MRT)
D2Q9	Two-dimensional nine-velocity model
D3Q19	Three-dimensional nineteen-velocity model
FDM	Finite difference method
FVM	Finite volume method
LB	Lattice Boltzmann
LBE	Lattice Boltzmann equation
LBM	Lattice Boltzmann method
LGA	Lattice gas automata
MRT	Multiple relaxation time
PDF	Particle distribution function

REV	Representative elementary volume
RMSD	Root-mean square deviation
SRT	Single relaxation time
TLBM	Thermal lattice Boltzmann method

Chapter 1

Introduction

1.1 Lattice Boltzmann method

Computational fluid dynamics (CFD) has been a major area of research in fluid mechanics for the last few decades. The prime objective of CFD is to model numerous fluid flows of practical and theoretical importance by using different numerical techniques and algorithms. CFD is useful in understanding various real-life flow problems with ease and cost-effectiveness compared to experiments. The transport equations of fluid flow and heat transfer can be formulated on three modes of scales, namely macroscopic, microscopic and mesoscopic scales based on Knudsen number. At each level, there is a definite model to represent the fluid flow by satisfying the three conservation laws in physics, namely conservation of mass, momentum, and energy. The conventional CFD techniques, for instance, finite difference method (FDM), finite volume method (FVM) [Patankar, 1980; Versteeg and Malalasekera, 2007; Anderson et al., 2013], and finite element method (FEM) [Zienkiewicz, 2014] are based on a macroscopic scale where partial differential equations (PDEs) like Navier Stokes (N-S) equations are solved. The convective terms of these equations involve nonlinearity which adds complexity to the solution algorithm. The instability of the algorithms is a key concern for these numerical schemes. The microscopic scale-based Molecular dynamics (MD) [Frenkel and Smit, 2002] is governed by Hamilton's equation, where the time evolution of interacting particles in a system is predicted. However, this leads to massive data utilisation in solving a problem with detailed molecular/atomic-level information. Therefore, massive computational resources and data reduction are some of the main drawbacks in MD models. The mesoscopic scale connects the macro-scale and micro-scale through approximation to the Boltzmann equation of the kinetic theory of gases. The lattice Boltzmann method (LBM) [Wolf-Gladrow, 2000; Succi, 2001; Ansumali and Karlin, 2002; Guo and Shu, 2013; Krüger et al., 2016] is a numerical

technique based on the microscopic particle models and mesoscopic kinetic equations. The basic idea of LBM is to construct simplified kinetic models that can solve the time evolution of the particle distribution function by obeying the desired macroscopic equations as the main focus of LBM lies in the averaged macroscopic behaviour. The use of simplified models to predict macroscopic fluid flows is based on the fact that the macroscopic dynamics of a fluid system is the outcome of the collective behaviour of a large number of microscopic particles in the system. Besides, macroscopic dynamics are less sensitive towards the fundamental details of microscopic physics. LBM has been dramatically improved over the last two decades to address a wide variety of engineering problems. It has demonstrated its ability in many areas of fluid flows under different conditions especially in treating single phase, multiphase, and multicomponent fluid flows [Shan and Chen, 1993; Huang et al., 2015], convective heat transfer [Guo et al., 2002], flows through porous media [Pan et al., 2004; Succi, 2001], magnetohydrodynamic [Dellar, 2002] and many more complex flow problems [Aidun and Clausen, 2010]

The relevant features of LBM which motivate its use despite the existence of various classical numerical methods such as FEM, FDM, and FVM can be outlined as follows:

a. The convection terms in LBM is linear, which is in contrast to the nonlinear convection terms in N-S equations. Thus, LBM handles the convection part with ease.
b. The pressure of LBM is determined locally using the equation of state. However, conventional CFD techniques for incompressible flows solve the pressure Poisson equation to obtain pressure. Often, different numerical difficulties like extensive computational time are associated in solving this Poisson equation.
c. LBM uses a simplified discrete Boltzmann equation with a minimal set of microscopic velocities, which significantly simplifies the calculations. The implementation of boundary conditions (in terms of particle distribution functions) is somewhat more straightforward compared to N-S equations which can take integral or differential forms.

d. LBM is local in space and explicit in time which makes its algorithm very simple compared to N-S equations solvers, which typically use an iterative procedure to obtain a converged solution.
e. LBM provides complete scalability for massively parallel computing as the particle collisions are local in nature.
f. Being a mesoscopic model, LBM can deal with small-scale details and can efficiently handle single phase and multiphase flows in complex geometries and interfacial phenomena.

Despite all these advantages, LBM suffers some limitations. Though it is increasingly being used for computing incompressible flows of various levels of complexity, its application to compressible fluid flows is very limited. This is because many of the convenient relations used by LBM is derived by assuming a low value of the Mach number. In Appendix B, an attempt has been made to compute a relatively simple compressible flow.

1.2 Literature review

1.2.1 Evolution of LBM

LBM is originally developed as an alternative numerical technique over conventional CFD techniques for isothermal incompressible Navier-Stokes equations [Benzi et al., 1992; Hou et al., 1995]. The governing equation of the LBM can be obtained theoretically using two different approaches. LBM is developed initially from a microscopic model known as a lattice gas cellular automata (LGCA) [Wolf-Gladrow, 2000]. LGCA is a simplified, fictitious molecular dynamic model with discrete space, time and particle velocities. During each time step, fictitious particles are updated via two alternating phases, namely the streaming and collision, according to a set of discrete collision rules while conserving the mass, momentum and energy. The LGCA model was first introduced by Herdy, Pomeau and Pazzis [1973] by considering a square lattice with four velocities, labelled as the HPP model. Frisch, Hasslacher and Pomeau [1986] proposed a new lattice gas automata model based on a triangular lattice and six velocities, namely

the FHP model. They showed that the FHP model has sufficient lattice isotropy to perform fluid simulations in the limits of incompressible fluid dynamics. However, the LGCA methods possess some inherent shortcomings like statistical noise, inflexibility to adjust the viscosity, non-Galilean invariance and an unphysical velocity-dependent pressure.

Several lattice Boltzmann equation (LBE) models based on LGCA are proposed by researchers to overcome the shortcomings of LGCA. Among them, the LBE model developed by McNamara and Zanetti [1988] is most relevant. In their model, they successfully eliminated the statistical noise by using a single particle distribution function instead of the Boolean fields and used Fermi-Dirac distributions as equilibrium functions. Higuera and Jimènez [1989] improved the numerical efficiency of the previous LBE model by using linearised collision operator. However, this LGCA-based LB technique is found to be inefficient in some conditions, such as simulation of the thermo-hydrodynamic system, implementation on the arbitrary mesh. This is attributed to a lack of thorough understanding of this method with respect to the Boltzmann equation. Besides this, the theoretical framework of LBM has rested upon the Chapman-Enskog (C-E) expansion [Chapman and Cowling, 1970] analysis of the LGA models, which limited its application up to a certain degree. Therefore, it is crucial in attaining direct connection of LBE along with collision term with kinetic theory (Boltzmann equation).

The second approach of the derivation of the LB model is based on the mesoscopic kinetic equation, known as the Boltzmann equation [Chen et al., 1991; Qian et al., 1992]. Different simplified collision models are developed to enhance computational accuracy and efficiency while replacing the collision operator derived from the LGCA. In this context, a Bhatnagar-Gross-Krook (BGK) [Bhatnagar et al., 1954] collision model is applied, which replace the collision parameter with one parameter known as the Single-Relaxation Time parameter. Chen et al. [1991] first introduced the BGK method to solve the equations of magnetohydrodynamics. They [Chen et al., 1992] later proposed lattice BGK method to recover N-S equations by using particular Maxwell type distribution function which provides flexibility to the transport coefficients and enhance the computational efficiency. This is the first instance of a connection between BE and LBE. However, He and Luo

[1997] have derived LB models from the Boltzmann BGK equation, which is entirely independent of lattice-gas automata. In their derivation of LBE from BE, the discretisation of phase space is achieved by coupling the discretisation of momentum space with the configuration space to obtain lattice structure. Thus, the framework of LBE rests on the foundation of BE, and the rigorous results of BE can be extended to the LBE through their explicit connection. After its development from BE, LBM has rapidly evolved into a self-standing research subject in the field of computational fluid dynamics. A part of the next chapter deals with the development of LBM from BE.

1.2.2 Natural- and mixed convection in enclosures

1.2.2.1 Buoyancy-induced cavity flow

The term convection derives from the Latin word ‘convectare’, which means to carry or bring together. In heat transfer analysis, the concept of convection refers to the process of moving thermal energy from or to a solid via an adjacent fluid in motion, in the presence of a temperature gradient. The convection is categorised into forced and natural convection depending on the source of the fluid motion. Forced convection is generated by the movement of fluid due to some external factor, such as fan and pump. Natural or free convection occurs in fluid in the presence of a buoyancy force due to density difference resulted from temperature difference within the fluid. Moreover, the interaction of lid-driven forced convection and the buoyancy induced convection results in a complex and intriguing flow and heat transfer phenomenon in the cavity, which is labelled as mixed convection. Buoyancy-induced convection flow problems are fully described by the two dimensionless parameters: Grashof (or Rayleigh) number and Prandtl number. Grashof number ($\mathbf{g}\beta\Delta TL^3/(\nu^2)$) describes the relationship between buoyancy and viscous effects in the flow and thus depends on the geometry and boundary conditions of the problem configuration. Rayleigh number characterises the fluid's flow regime, whether the flow is laminar or turbulent. For magnitudes of Rayleigh number lower than a particular critical value, there is little fluid motion, and the conduction heat transfer prevails. Prandtl number

is the intrinsic thermo-physical property of a fluid which provides the ratio of the momentum diffusivity to the thermal diffusivity (ν/α). The diffusivity of momentum in a fluid is indicated by kinematic viscosity. Similarly, the thermal diffusivity is the measure of the rate of diffusion of heat throughout a material. Prandtl number is also an indication of the relative thickness of the velocity boundary layer to the thermal boundary layer. When $Pr \rightarrow 1$, the boundary layers coincide which indicates that both momentum and heat diffuses through the fluid at about the same rate. For $Pr > 1$, the momentum diffusivity dominates the flow, which gives rise to a thicker velocity boundary layer than the thermal boundary layer and thereby the convection is more prominent than conduction. For $Pr < 1$, the heat diffuses quicker than momentum, which results in a thicker thermal boundary layer, and the conduction heat transfer is more effective than convection. Richardson number is the additional parameter that characterises the mixed convection flow. It measures the relative strength of the natural convection and forced convection. The limiting cases $Ri \rightarrow 0$ and $Ri \rightarrow \infty$ lead to the forced and natural convection dominating flows respectively.

The classical buoyancy-induced convection problems in cavities, particularly square and rectangular cavities, are widely investigated in literature [Mallinson and de Vahl Davis, 1977; de Vahl Davis, 1983; Markatos and Pericleous, 1984; Ostrach, 1988; Prasad and Koseff, 1996; Yapici and Obut, 2015] as it exhibits different interesting thermo-fluid dynamic characteristics despite its simple geometry. Many experimental and numerical investigations on natural and mixed convections are made by considering various thermal and velocity boundary conditions at the cavity walls. These benchmark flow problems provide simplification to different practical applications such as ventilation in buildings, electronic component cooling, heat exchangers, lubrication technologies, nuclear reactor, food and materials processing, solar energy collector [Incropera and DeWitt, 2002; Cengel, 2003; Bairi et al., 2014]. In energy-related applications, the higher heat transfer rates can be achieved by proper design of enclosures where natural or mixed convection play an important role in transporting energy. Among the experimental works on mixed convection flow, the work done by Prasad and Koseff [1996] is significant in analysing mixed convection in a lid-driven cavity for varying Richardson numbers from 0.1 to 1000.

However, with the rapid advancement of computational technology and methodology, the numerical work has gained more significance over experimental work as they facilitate understandings of different complex heat transfer systems in time and a cost-effective manner. Extensive numerical investigations using conventional CFD techniques [de Vahl Davis, 1983; Iwatsu et al., 1993; Khanafer and Chamkha, 1999; Sharif, 2007] were carried out on natural- and mixed convection by considering different thermal and velocity boundary conditions at the cavity walls. Iwatsu et al. [1993] numerically studied mixed convection flow in a square cavity with adiabatic sidewalls heated by top moving wall using a finite difference technique. Oztop and Dagtekin [2004] have used finite volume method to simulate mixed convection in a differentially heated square cavity with moving sidewalls for fixed *Pr* at 0.7 and Grashof number (*Gr*) at 10^4 while varying Richardson numbers discretely from 0.01 to 100. Basak et al. [2009] have implemented a Galerkin finite element method to investigate the effect of uniform and non-uniform heating of the bottom wall on mixed convection lid-driven flows in a square cavity. Yapici and Obut [2015] numerically investigated benchmark two-dimensional natural and mixed convection heat transfer in a cavity while comparing their results with different published literature.

Different lattice Boltzmann methods have been proposed such as, the multi-speed [Alexander et al., 1993], the hybrid approach [Lallemand and Luo, 2003] and the double-distribution-function (DDF) approach [He et al., 1998] to simulate heat transfer. The multi-speed model uses only one set of the distribution function. Hence, more discrete velocities are added to the density distribution functions to obtain the macroscopic temperature. However, the multi-speed model lacks numerical stability and limited to low range of temperature difference. In the hybrid approach, the lattice Boltzmann equation is used to simulate the fluid flow, while solving the energy equation by conventional numerical techniques such as finite difference method. Therefore, this model compromises the inherent advantage associated with basic LBM. He et al. [1998] proposed the DDF model, which introduces a separate governing equation for internal energy distribution function (IEDF) to simulate the temperature field. This equation is obtained by discretisation of the continuous evolution equation for IEDF similar to the fundamental equation for LBM. The

basic equation of LBM, i.e. equation for density distribution function, is used to simulate the macroscopic density and velocity. The DDF model provides stability and accuracy comparable to the hybrid approach. However, the complicated gradient operator term in the temperature evolution equation compromises the simplicity of the LBM to some extent. Therefore, Peng et al. [2003] proposed a simplified thermal lattice Boltzmann model for incompressible thermal flow problem while neglecting the pressure compression work and viscous heat dissipation. Besides, this model drops the gradient term in the evolution equation without sacrificing the numerical accuracy. In literature, a large number of LBM studies [Dixit and Babu, 2006; Guo et al., 2010; Mohamad and Kuzmin, 2010] are found concerning DDF model to simulate natural- and mixed- convection flow in cavities due to its advantage over conventional numerical technique. Peng et al. [2003] proposed a simplified thermal lattice Boltzmann model to simulate thermal flow problem. Mohamad and Kuzmin [2010] made a comprehensive analysis of natural convection problem using LBM, which revealed that LBM has the ability to simulate buoyancy-induced convection problem with high efficiency. Dixit and Babu [2006] simulated natural convection for higher Rayleigh numbers up to Rayleigh number equal to 10^{10}.

Most of the works concerning DDF approach are based on SRT-LBM due to its extreme simplicity. However, to obtain better stability, DDF approach based on the multiple relaxation time lattice Boltzmann equation is introduced by several researchers. Among these, Mezrhab et al. [2010] proposed a novel DDF based MRT-LBM to simulate natural convection flow in a square cavity for Rayleigh number up to 10^8. Wang et al. [2013] used Mezrhab's double MRT model to make a systematic investigation of natural and Rayleigh-Bénard convection in a cavity with Prandtl numbers of 0.71 and 7.0. Guo et al. [2010] used MRT-LB model to simulate mixed flow in a two-dimensional lid-driven rectangular cavity for different aspect ratios, Rayleigh and Reynolds numbers. Subsequently, the flow configurations with different flow geometry, boundary conditions and fluid properties have gained importance among the computational fluid dynamics community to explore various aspects associated with natural- and mixed- convection phenomenon.

1.2.2.2 Convection at different Prandtl numbers in cavities

Prandtl number is a dimensionless parameter which characterises both Natural- and mixed convection flow problems. The magnitude of Prandtl number is ranging from 10^{-3} (liquid metals) to 10^{5} (functional oils) in conventional fluids. Liquid metals or alkali metals are perfect working fluids in heat exchangers and primary coolant for Liquid Metal Fast Nuclear Reactors (LMFR) due to its low viscosity, low density, and high thermal conductivity. The convective flow of low Prandtl number fluid in the enclosure has many industrial applications, such as melting and solidification of metals. Mohamad and Viskanta [1991] are one of the pioneers to investigate low-Prandtl-number fluids during natural convection in the cavity. They numerically predicted steady-state solutions with an oscillatory transient period at low *Pr* (*Pr* = 0.001, 0.005 and 0.01*)* prior to periodic oscillations at the critical Grashof numbers. Kosec and Sarler [2013] employed a local meshless method to simulate natural convection in the cavity for low Prandtl number. Their predictions for Nusselt number are consistent with the predictions of Mohamad and Viskanta [1991]. Bejan [1984] investigated the effect of *Pr* on the criterion for the transition from pure forced convection to pure natural convection during mixed convection flow over a vertical wall. He found that this criterion of transition, as indicated by *Ri*, is different from low *Pr* fluids (i.e. $Pr \ll 1$) to high *Pr* fluids (i.e. $Pr \gg 1$). Moallemi and Jang [1992] have numerically studied the effect of *Pr* on mixed convective flow in a bottom heated square driven cavity. They concluded that the buoyancy effect is more prominent at higher values of *Pr*. Waheed [2009] investigated two flow configurations during mixed convection in a lid-driven cavity for a range of *Ri* from 0.01 to 100, *Pr* from 0.001 to 10, and aspect ratio from 1 to 4 at a fixed *Re* = 100. Cheng [2011] have carried out systematic numerical simulations of mixed convection in a 2D lid-driven square cavity with cold top moving-wall and insulated vertical walls to characterise the heat transfer behaviour for a wide range of Reynolds ($10 \leq Re \leq 2200$), Grashof ($100 \leq Gr \leq 4.84\times10^{6}$), Prandtl ($0.01 \leq Pr \leq 50$), and Richardson ($0.01 \leq Ri \leq 100$) numbers. Karimipour et al. [2013] performed LBM simulation on the mixed convection in an inclined cavity with the heated top wall moving for *Pr* of 0.07, 0.7 and 7 and reported an increase in heat transfer rate with *Pr* and inclination

angle. Li et al. [2016] used MRT-LBM to simulate natural convection for very low *Pr* in the range of 0.001 to 0.01 and found oscillatory solutions at lower Prandtl number. Recently, Bawazeer et al. [2019] investigated the same problem for a wide range of *Pr* (0.01-0.5) and *Ra* (10^4-10^8) using modified MRT-LB model.

1.2.2.3 Convection in cavities with inserted objects

The insertion of an object in a cavity-like configuration causes a prominent effect on the thermo-hydrodynamic behaviour of the fluid flow and heat transfer phenomena during natural and mixed convection [Ho et al., 1994; Islam et al., 2012; Khanafer and Aithal, 2013]. Besides, this inserted object can be used as a passive element to control heat transfer. Extensive studies concerning objects with different geometries, locations, physical and thermal conditions are documented by researchers which has practical relevance in applications like cooling of hot ingots, metal casting, electronic component cooling, heat exchanger, crystal growth, solar and nuclear reactors, etc. Ho et al. [1994] made an experimental and numerical investigation of natural convection in an air-filled insulated circular enclosure inserted with two horizontal, differentially heated cylinders. They observed that the overall fluid flow and heat transfer characteristics are strongly influenced by the diameters and gap width of the cylinders for varying Rayleigh numbers from 10^4 to 10^7. Khanafer and Aithal [2013] found that the average Nusselt number is a function of the cylinder radius at all studied *Ri* during mixed convection in a circular cylinder inserted lid-driven cavity. Islam et al. [2012] made a mixed convection investigation in a lid-driven cavity by inserting an isothermally heated rectangular block and square block respectively. Gangawane [2016] numerically investigated mixed convection in a lid-driven cavity with heated triangular block for a range of *Re*, *Pr* and *Gr* to recognise the critical Reynolds number.

1.2.3 Convective flow through porous media

In the context of natural and mixed convective heat transfer phenomenon, the heat transfer through porous media has always been an attractive and widely investigated topic

of research. The heat transfer through porous structures has physical significance in different practical applications such as separation process, infiltration of molten metals, food storage and processing, crude oil extraction, gas drying and transport process, geothermal operation, insulation of a building, metallurgy, pebble-bed nuclear reactor design, underground disposal of nuclear or non-nuclear waste. The porous medium is defined as a material with the interconnected voids or pores. A porous material is distinguished by its porosity which is the ratio of the pore space to the total volume of the material. It is also signified by its permeability that measures the flow conductivity in the porous medium. The permeability term is normalised by using non-dimensional parameter known as Darcy number (Da) through a relation $K = DaL^2$. Kaviany [1995], Nield and Bejan [1999] and Ingham and Pop [2005] amply documented the fundamental theory and the growing volume of works on flow through a porous medium in their books. Earlier studies in flow in porous media deals with Darcy law [Nield and Bejan, 1999] which provides a linear relationship between the flow velocity and the pressure gradient across the porous medium. Later developments in porous media led to extended models for the Darcy law such as Forchheimer's and Brinkman's equations [Nithiarasu et al., 1997] where the Forchheimer's model deals with large flow velocities and Brinkman's model considers the boundary effects. However, these models have some limitations and to overcome that, Nithiarasu et al. [1997] proposed a generalised model, namely Brinkman–Forchheimer-extended Darcy model, which takes into account all non-Darcy effects. They presented a detailed parametric study for natural convection in a rectangular porous cavity with constant or variable porosity. In literature, a number of experimental and numerical works are found in this area. In the last few decades, a large body of works (mostly computational), investigated natural-convection flow through a porous medium in enclosed cavities with various configurations using analytical based numerical computations [Bhattia et al., 2018] and conventional numerical techniques such as finite difference [Varol et al., 2009; Sheremet and Pop, 2015], finite volume [Motlagh et al. 2016; Siavashi et al., 2018] and finite element method [Nithiarasu et al., 1997; Kaluri and Basak, 2011].

The modelling technique for flow through porous media can be adopted to study

flow through a bundle of internal objects. These bundle of internal bodies can be arranged in a specific manner to obtain desired thermal behaviour which is relevant in many applications such as heat exchanger, cooling hot ingots, solidification and nuclear power reactor. The rod bundle geometry is common in many heat exchangers and nuclear reactor fuel. This bundle of objects can be investigated by considering them as a porous structure with suitable porosity and permeability values conforming to the thermo-hydraulic characteristics of those complex geometries. In literature, several studies on convective heat transfer involving a bundle of internal bodies are found where several studies are made by approximating the bundle as a single porous body to reduce the complexity in problem formulation and computational time. Haldar et al. [2000] numerically investigated laminar free convection in open-ended vertical 7-rod bundles by modelling them as a Darcy porous media, and the results found to be in good agreement with experimental measurements. Suresh et al. [2005a; 2005b] made experimental and numerical investigations of natural convection in a blocked subassembly of a fast breeder reactor filled with liquid sodium. Krishna et al. [2010] used non-Darcy porous media to model heat-generating bundle of rods and obtain satisfactory results while comparing with the experimental results. They stated that the non-Darcy porous model provides better insight into flow and heat transfer behaviour inside fuel assemblies compared to the Darcy model.

In the literature on LBM, the investigation of flow behaviour in the porous medium is made via two approaches based on the pore scale and the representative elementary volume (REV) scale. At the pore scale [Succi et al., 1989; Succi, 2001], the basic lattice Boltzmann equation (LBE) can be employed to simulate fluid flows in pores. Hence, the local information of flow at the microscopic level can be directly obtained. However, the requirement of the rigorous geometric details of the pores makes this approach computationally inefficient for large flow domain. While, LBM at the REV scale [Freed, 1998; Guo and Zhao, 2005] is a simple and computationally efficient approach to deal with the porous flow to get the desired macroscopic flow behaviour. Guo and Zhao [2002] proposed a lattice Boltzmann (LB) model at REV scale to study fluid flow in porous media where they incorporate porosity term in the equilibrium distribution function (EDF). They

modified the forcing term of LBE by considering the linear and nonlinear drag forces of the porous media. Guo and Zhao [2005] have further extended their isothermal model to thermal LBE model based on SRT-based double-distribution-function (DDF) approach. This generalised lattice Boltzmann model [Guo and Zhao, 2005] incorporates Brinkman–Forchheimer-extended Darcy equation to simulate the flow through the porous medium at the REV scale. In this context, Liu et al. [2014] have developed a thermal MRT-LB model based on DDF approach to simulate convection flow through porous media. Seta et al. [2006] showed that the LBM at REV scale provides sufficient reliability and the numerical efficiency in investigating convective heat transfer in porous media. Vijaybabu et al. [2017] employed SRT-LBM to make detail analysis on the flow and heat transfer characteristics of a 2D porous square cylinder placed in an infinite stream under the influence of aiding buoyancy. Vijaybabu and Dhinakaran [2019] numerically simulated MHD natural convection in a water-based nanofluid saturated square enclosure with an inner permeable triangular cylinder at REV scale. In LB simulation, the REV approach has been established as a reliable numerical tool to simulate porous flow problems.

1.2.4 Nanofluid flow and heat transfer in enclosures

The high-performance cooling system is a vital need for many applications, and one way to obtain it is by adopting an efficient and effective convective heat transfer process where fluid serves the purpose of a heat carrier. Therefore, it is essential to have an energy-efficient, inexpensive heat transfer fluid which eventually leads to the development of nanofluid as labelled by Choi and Eastman [1995] where nano-sized particles are suspended in a base fluid. The suspension of nanoparticles is favourable than the suspension of micro or millimetre-sized particles as nanofluid provides more stability due to their high surface to volume ratio and minimal erosion and clogging effect on the system. The introduction of nanoparticles is expected to augment the heat transfer characteristics of the base fluids due to particle's higher thermal conductivity compared to the base fluid (conventional fluid such as water, and industrial oil). However, the enhancement of the heat transfer characteristics depends on the thermophysical properties of nanofluid as well as

the particle sizes, shapes, volume fractions and stabilities [Gupta et al., 2017]. Ijam and Saidur [2012] have used SiC-water and TiO_2-water nanofluids as coolants for electronic devices which suggests nanofluid as a potential heat transfer enhancement tool for different practical problems. Putra et al. [2003] used Al_2O_3- and CuO-water nanofluids to make an experimental investigation on natural convection in a horizontal cylinder with differentially heated ends. They observed a systematic and definite deterioration in heat transfer performance with an increase in the volume fraction of nanoparticles. However, recent experimental investigations [Nnanna, 2007; Ho et al., 2010] assert an increase in the heat transfer rate for a low concentration of nanoparticles. Ho et al. [2010] carried out an experimental investigation on free convection in a differentially heated alumina-water nanofluid filled enclosure with nanoparticles varied from 0.1% to 4%.

Hadad et al. [2012] have made a comprehensive review study concerning experimental, numerical and analytical published works on heat transfer enhancement in natural convection using different nanofluids. The review study of Mehdi Bahiraei [2004] demonstrates that different numerical approaches such as conventional single-phase model, thermal dispersion Model, two-phase model and LBM. are considered by researchers to understand the behaviour of nanofluid in a flow problem. Sidik and Razali [2014] have reviewed the works dedicated to the use of the LB technique in simulating convective heat transfer problems using nanofluid. It is found from these review studies that most of the previous works are done using homogenous single-phase model for nanofluid where both the fluid and nanoparticles have negligible velocity and temperature difference. The single-phase model is easy to implement and computationally efficient, but it yields results which are strongly dependent on thermo-physical property model (particularly for the thermal conductivity and viscosity). Therefore, it is crucial to consider the two-phase model to get a clear picture of nanofluid flow where the base fluid and nanoparticles are treated separately by considering different slip velocity mechanisms. Buongiorno [2006] stated that the absolute nanoparticle velocity could be viewed as the sum of the base-fluid velocity and relative velocity (slip velocity as termed by him). He considered seven slip mechanisms in his mathematical model for nanofluid flow, which are inertia, Brownian diffusion,

thermophoresis, diffusiophoresis, Magnus effect, fluid drainage and gravity settling. He emphasised the effect of Brownian diffusion and the thermophoresis in the absence of turbulent effects. The comprehensive review studies of Kakaç and Pramuanjaroenkij [2016], Sidik et al. [2016b] and Vanaki et al. [2016] on both single-phase and two-phase models for nanofluid suggest that two-phase model provides more credible results than single-phase while making the comparison with the available experimental results. Sheikholeslami et al. [2014] numerically investigated two-phase nanofluid flow in a semi-annulus enclosure by consider-ing the effects of thermophoresis and Brownian motion. Garoosi and his co-researchers [Garoosi et al., 2014; Garoosi et al., 2015] have adopted a two-phase mixture model for nanofluid to carry out several useful finite volume investigations on natural- and mixed- convection in nanofluid-filled enclosures. Esfandiary et al. [2016] and Motlagh and Soltanipour [2017] used a two-phase model to study the nanofluid convective heat transfer in a square cavity. Their study revealed that the enhancement of heat transfer rate is accompanied by the increase of volume fraction up to 4%. However, very few studies concerning two-phase nanofluid model are found in the literature as obtained from a recent review study of Izadi et al. [2019]. In the study of nanofluid, LBM may provide an edge over conventional numerical techniques due to its mesoscopic nature which makes it convenient in incorporating the interactions between the suspended nanoparticles and fluid particles. It has gained attention among various researchers along with the ones that concentrate on cavity flow problems with nanofluids [He et al., 2011; Chen et al., 2015] while considering single-phase LB model. The review study of Li et al. [2015] indicates that there is a dearth of nanofluid studies based on the two-phase LBM model. Xuan and Yao [2005] and Eslamian et al. [2015] have proposed two-phase lattice Boltzmann models to investigate the effect of different interaction forces between nanoparticles and the base fluid. Qi et al. [2017] used two-phase lattice Boltzmann method to study the effects of two kinds of base fluid (water and Ga) and three different nanoparticle radii (20 nm, 40 nm and 80 nm) on the natural convection in a rectangular enclosure filled with Al_2O_3-water and Al_2O_3-Ga nanofluid at different Rayleigh numbers from 10^3 to 10^5.

The comprehensive review articles of Bahiraei [2004], and Sidik and Razali [2014] reveal that most of the published works deal with nanofluids with single nanoparticles. The advantage of particular single-particle nanofluid over the other depends on the properties of the suspended nanoparticle. Nanofluids with single ceramic nanoparticles such as Al_2O_3 and Cuo have better stability and chemical inertness but lower thermal conductivity compared to the metallic nanoparticles such as Cu and Al. However, the thermal properties of nanofluid can be improved further by adopting a new class of nanofluids known as hybrid nanofluid which is synthesised by dispersing two different nanoparticles in the base fluid either in a mixture or composite form [Jana et al., 2007]. Ho et al. [2011] have carried out an investigation on fully developed laminar forced convection in a tube by using a water-based hybrid nanofluid with two different nanoparticles Al_2O_3 and microencapsulated phase change material (MEPCM) respectively. They have found that hybrid nanofluid provides considerable heat transfer enhancement compared to regular nanofluid. Suresh et al. [2011] have carried out experimental work on hybrid Al_2O_3-Cu/water nanofluid with 0.1% volume fraction, which is synthesised from chemically prepared Al_2O_3-CuO mixture by utilising the hydrogen reduction technique. Recently, Sarkar et al. [2015], Sidik et al. [2016a] and Babu et al. [2017] are the researchers who have made excellent reviews on hybrid nanofluids to understand their different synthesis techniques, thermo-physical properties, fluid flow and heat transfer characteristics along with their various heat transfer applications. Recently, Mahian et al. [2019a; 2019b] have made comprehensive review studies on nanofluid in two parts. In the first part [Mahian et al., 2019a], they have presented fundamental and theoretical physics of nanofluids, and numerical approaches based on single-phase and two-phase approaches to model nanofluid flow. In the second part [Mahian et al., 2019b], they have summarised the primary CFD approaches based on macroscale-based, mesoscale-based, and microscale-based techniques for solving the transport equations associated with the nanofluid flow. Besides, the second part dealt with recent 3D works on nanofluid flow in various regimes and configurations which reveal that most of the 3D studies are used to analyse the thermal systems such as solar collectors and microchannels.

1.2.5 Nanofluid flow and heat transfer in porous media

The simultaneous use of porous media and nanofluids has been a topic of interest for their better heat transfer rates in small-size systems. The use of a porous medium can be an efficient means of controlling heat transfer performance in enclosures. Between the operating fluid and the porous structure, there is a greater surface contact area that allows an efficient interaction between convective heat transfer within pores and heat conduction in a solid matrix. Recently, several works on the simultaneous use of porous media and nanofluids are found in the literature, which is very useful for the optimisation of various engineering devices. Mahdi et al. [2015] and Kasaeian et al. [2017] summarised the works concerning convective heat transfer flow problems such as natural, forced and mixed convection through a nanofluid-saturated porous medium in different geometries in their review article. Nield and Kuznetsov [2014] have extended their previous model for the nanofluid that incorporates the effects of Brownian motion and thermophoresis by employing more realistic boundary condition for the nanoparticle fraction. They have analytically investigated Horton-Rogers-Lapwood problem for a nanofluid using linear instability theory. Mittal et al. [2013] showed from their mixed convection in a porous cavity filled with nanofluid that the average Nusselt number increases with an increase of Darcy number for a constant volume fraction. Shenoy et al. [2015] have made a comprehensive review of heat transfer and fluid flow of nanofluid saturated porous media in their book. Mehryan et al. [2017] have studied the natural convection of Al_2O_3/water nanofluid and Cu-Al_2O_3/water hybrid nanofluid in a square cavity filled with two types of porous medium materials, namely glass balls and aluminium foam. Rajarathinam et al. [2017] and Astanina et al. [2018] have used the single-phase model for nanofluid to analyse mixed convection in a nanofluid saturated porous cavity with different flow configurations. Sheremet et al. [2015] have employed the thermal nonequilibrium model, and Tiwari and Das single-phase nanofluid model to study natural convection in a square porous cavity filled with a nanofluid. Sheremet and Pop [2015] simulated free convection in a nanofluid saturated triangular porous enclosure using Buongiorno's mathematical model for nanofluid [Buongiorno, 2006]. Sheremet et al. [2017] used this model to analyse steady

natural convection in a partially heated wavy porous cavity filled with a nanofluid by considering the effects of Brownian diffusion and thermophoresis. Mohsen Sheikholeslami [2017; 2018a; 2018b] have made an extensive investigation on the nanofluid-saturated porous structure in the presence of a magnetic field using a single-phase lattice Boltzmann model.

1.2.6 Analysis of entropy generation due to convection in enclosures

In recent times, the second law-thermodynamics based entropy generation investigations have gained importance among the heat transfer community as it provides better insights into heat transfer analysis compared to the first law of thermodynamics based investigations. It is well established that the efficiency and overall performance of the heat transfer system can be improved by minimising the entropy generation, i.e., reducing the loss of available work. In thermal systems, the entropy generation is mainly contributed by heat transfer and fluid friction irreversibilities. The entropy generation minimisation (EGM) and the entropy generation analysis (EGA) have been evolved as useful and popular thermodynamic optimisation tools for thermodynamic systems. The EGM technique is generally a deterministic approach which aims to find optimal design variables at which minimum entropy generation rate prevails. The EGA identifies and reduces the thermodynamic irreversibilities based on a heuristic approach. These methods are first familiarised by Bejan [37] for different fluid-thermal engineering processes. Sciacovelli et al. [2015] have made a critical review study on the use of entropy generation analysis as an optimisation tool for the design of different types of engineering systems. Oztop and Al-Salem [2012], Mahian et al. [2013] and Biswal and Basak [2017] wrote review articles depicting the use of entropy generation in different flow configurations by using clear fluid and nanofluid respectively. Magherbi et al. [2003] and Ilis et al. [2008] are the researchers who have studied the effect of entropy generation on a benchmark problem of natural convection which is a rectangular cavity with differentially heated vertical walls and insulated horizontal walls. Das et al. [2017] have made an extensive review work on natural convection in various non-square enclosures filled with conventional fluid or nanofluid or

porous media subjected to different thermal boundary conditions. Roy et al. [2015] made entropy and heat transfer analysis for the mixed convection in a square cavity for various moving horizontal or vertical wall(s) with two different fluids with Prandtl numbers at 0.026 and 7.2 respectively. Wei et al. [2017] utilised LBM to study the effects of Prandtl number (Pr = 6, 20, 100 and 10^6) on entropy generation during Rayleigh-Bénard convection. Mahapatra et al. [2013] investigated the entropy generation during natural convection in a differentially heated cavity containing adiabatic and isothermal solid blocks. Nayak et al. [2016] have analysed the entropy generation and heat transfer for mixed convection flow problems in a nanofluid filled inclined skewed enclosure. Alsabery et al. [2018] and Al-Rashed et al. [2018] have made respectively two-dimensional and three-dimensional investigation to analyse the effect of heat transfer and entropy generation on mixed convection in a nanofluid saturated square and a cubic cavity filled with an isothermal block. Chattopadhyay et al. [2016] and Roy et al. [2016] have carried out different investigations to analyse the effect of porous medium on entropy generation during mixed convection for different velocity and thermal boundary conditions. Taghizadeh and Asaditaheri [2018] have analysed heat transfer and entropy generation during laminar mixed convection in an inclined lid-driven cavity with a circular porous cylinder inside. Hussain et al. [2018] have used the finite element method to study the effect of the internal heat generation and chemical reaction on the double-diffusive mixed convection in an Al_2O_3-water nanofluid-saturated square porous cavity. Siavashi et al. [2018] have used finite volume technique to study the effect of Cu-water nanofluid and porous fins on entropy generation during natural convection by using two-phase mixture model for nanofluid and Darcy-Brinkman-Forchheimer model for the porous region. Ashorynejada and Hoseinpour [2017] have analysed entropy generation during natural convection in a porous cavity filled with different nanofluids by implementing single-phase LBM. Ghasemi and Siavashi [2017] also used single-phase LB model to investigate the effect of different linear temperature distributions of sidewalls on entropy generation during natural convection in a Cu-water nanofluid filled porous cavity using a single-phase model. They found an optimal Rayleigh number to maximise heat transfer for each Darcy number.

1.3 Motivations and research objectives

The literature survey reveals that most of the previous numerical works on natural- and mixed convection in the cavity with solid cylinders or blocks inside are made using conventional numerical techniques such as finite volume method, finite difference method etc. Besides, most of the previous numerical works on this type of flow conditions are carried out using fluids with Prandtl numbers of the order of unity. The numerical works that use the LBM, particularly MRT-LBM, are very limited. This provides a motivation to carry out a simulation for low to high Prandtl numbers using MRT-LBM.

The literature review shows that a number of studies are undertaken to analyse heat transfer rate during natural and mixed convection in fluid-saturated porous media. However, the studies concerning entropy generation analysis are limited. Besides, the LBM studies are scarce in this context.

The detailed literature review depicts that most of the numerical studies on convective heat transfer in a nanofluid-filled cavity have been made using a single-phase fluid model. The numerical studies (both conventional CFD and LBM) concerning the two-phase model for nanofluid are found to be limited, where only a few studies deal with two-phase LBM simulation. Moreover, the use of hybrid nanofluid has been recently practised by very few researchers in the investigation of thermal flow problems in enclosures.

A perusal of literature suggests that a minimal number of works are available to understand the combined effect of both porous medium and nanofluid on fluid flow and heat transfer behaviour in spite of having different real-world engineering applications. Besides, most of the numerical studies concerning nanofluid-saturated porous media are carried out using the single-phase model for nanofluid. In the context of LBM literature, no two-phase LBM study has been reported yet to analyse convection flow in nanofluid saturated porous enclosures as per the author's best knowledge.

It is observed from the literature survey that most of the studies of heat transfer and flow phenomenon in clear or porous enclosures with or without nanofluid are restricted to the first law of thermodynamics. However, it is crucial to adopt the second law-based-

investigations to analyse heat transfer systems from a thermodynamics point of view, which are characterised by entropy generation.

In view of the above context, the objectives of the present investigation have been formulated as follows:

1. To check the applicability of multiple relaxation time (MRT) thermal lattice Boltzmann model in complex flow systems such as flow with very low and high Prandtl numbers.
2. Employment of generalised SRT- and MRT- lattice Boltzmann model based on Brinkman–Forchheimer extended Darcy model in simulating flow through the porous medium at representative elementary volume (REV) scale.
3. To see the possibility of developing a two-phase LB model for nanofluid based on MRT- approach.
4. To see the possibility for further extension of two-phase LB models to simulate nanofluid flow through a porous medium.
5. To examine the applicability of LBM to hitherto unexplored heat transfer problems in different cavity flow configurations such as flow through a porous medium, nanofluid flow, and nanofluid-saturated porous medium.
6. Employment of entropy generation analysis for all studied problems to identify the optimal configuration with high energy efficiency at which maximum heat transfer rate and minimum entropy generation prevail.

1.4 Thesis outline

The thesis has been organised into eight chapters. Brief contents of the chapters are described below.

Chapter 2 describes the brief background of the lattice Boltzmann method, the implementation technique of both SRT and MRT model, and different boundary condition treatments. The isothermal and thermal benchmarks cavity flow problems are simulated by using an in-house LBM-Fortran code based on both SRT- and MRT- lattice Boltzmann models. The satisfactory agreement of present results with the previously published results

shows its competence and gives the confidence to extend our code further to investigate natural- and mixed convection flows with different flow configurations and medium in clear and porous enclosures.

Chapter 3 focuses on the applicability of multiple relaxation time (MRT) thermal lattice Boltzmann model in complex flow systems such as flow with very low and high Prandtl number fluid. The MRT-LB model is used to analyse the effects of three different Prandtl numbers (Pr = 0.025, 5.83 and 151) on natural- and two mixed convection in a square cavity containing a hot square solid block at its centre with two different blockage ratios ($\frac{d}{L}$) of 0.25 and 0.5.

Chapter 4 is concerned with the application of generalised SRT- and MRT- lattice Boltzmann model based on Brinkman–Forchheimer extended Darcy model [Guo and Zhao, 2005; Liu et al., 2014] in simulating flow through the porous medium at representative elementary volume (REV) scale. The present work analyses the entropy generation and heat transfer for two different porous flow configurations, which are not addressed yet as per the authors' best knowledge.

Chapter 5 deals with the exploitation of established single-relaxation-time based two-phase LB model [Xuan and Yao, 2005] and the development of a new multiple-relaxation-time based two-phase model for nanofluid flow. Then hybrid nanofluid is used to investigate three different cases of buoyancy-assisted mixed convection cavity flow based on velocity and thermal boundary conditions.

Chapter 6 introduces a novel two-phase SRT-LBM model to simulate nanofluid flow through a porous medium by incorporating the Brinkman–Forchheimer-extended Darcy model. The present model is employed to investigate natural convection in a Cu/water nanofluid-saturated square porous cavity for the flow configuration, as mentioned in Chapter 4.

Chapter 7 introduces a novel two-phase MRT-LBM for nanofluid, which is an extension of developed two-phase SRT-LBM. This model is used to analyse the entropy generation during steady mixed convection in a double-sided lid-driven inclined cavity

while placing a hot permeable square cylinder at the cavity centre by using Al_2O_3/water nanofluid.

Chapter 8 includes a summary of the significant findings of the present thesis and the possible extensions of current work for uncovering the unseen facts.

Chapter 2

Lattice Boltzmann Method in a Nutshell

2.1 Introduction

The LBM [McNamara and Zanetti, 1988] originated from lattice gas (LG) automata [Wolf-Gladrow, 2000], was initially developed for the simulation of isothermal and incompressible flows. However, in recent years, LBM has been rapidly evolving as an alternative promising numerical tool for CFD as it establishes links between micro and macro scales to improve the understanding of fluid behaviour. It uses discrete Boltzmann equation to model the fluid flow by tracking the evolution of the particle distribution functions (PDF) which is the only unknown quantity of the LBM. LBM principally focuses on determining the averaged macroscopic properties despite its roots to the particle nature. The macroscopic variables, such as density and velocity, are obtained by evaluating the hydrodynamic moments of the PDF. This method can be seen as a special finite difference scheme for the kinetic equation of the discrete PDF as it utilises discrete lattice and discrete time.

2.2 Development of LBM

The LBM can be traced back to Boolean fluid model 'Lattice Gas Cellular Automata' that implements particles streaming and colliding in a fully discrete dimension. By satisfying mass conservation (number of Boolean particles) and momentum conservation, LGCA can yield Navier-Stokes equations. However, the derivation of the LB model from continuum Boltzmann equation makes it as a self-standing research subject in connection with statistical physics or kinetic theory equation. The LBE approximates the continuous BE by discretising physical space with a set of uniformly spaced lattice nodes and velocity space by a discrete set of microscopic velocity vectors. The time- and space-

averaged microscopic movements of particles are modelled using distribution functions, which obey specific particle interaction rules to satisfy Navier-Stokes equations.

2.2.1 Boltzmann transport equation

The Boltzmann equation was formulated by Ludwig Boltzmann [Succi, 2001; Mohamad, 2011] to describe the statistical distribution of particles in a thermodynamic system far from equilibrium. It is one of the essential kinetic equation for non-equilibrium statistical mechanics. The BE uses a statistical description known as distribution function, $f(\mathbf{r}, \mathbf{e}, t)$ which is the probable number of particles in a unit volume of fluid positioned about $\mathbf{r}$ in the physical space element $d^3\mathbf{r} = d\mathbf{x}d\mathbf{y}d\mathbf{z}$ with velocity $\mathbf{e}$ in the velocity space element $d^3\mathbf{e} = d\mathbf{u}d\mathbf{v}d\mathbf{w}$ at time t, to describe the mechanics of fluid. Mathematically, it is expressed by the following relation

$$\int f(\mathbf{r}, \mathbf{e}, t)\, d^3\mathbf{r} d^3\mathbf{e} = N \tag{2.1}$$

where N is the total number of molecules in the container.

If an external force $\mathbf{F}$ (which is given by $m\mathbf{a}(\mathbf{r}, t)$, where m is mass, and $\mathbf{a}$ is the acceleration of a particle) is applied to a particle. The number of particles will remain the same while neglecting collision of particles, and it is presented as [Mohamad, 2011]:

$$f\left(\mathbf{r} + \mathbf{e}dt, \mathbf{e} + \left(\frac{\mathbf{F}}{m}\right)dt, t + dt\right)d\mathbf{r}d\mathbf{e} - f(\mathbf{r}, \mathbf{e}, t)d\mathbf{r}d\mathbf{e} = 0 \tag{2.2}$$

Taking account of the collision between particles, then the equation becomes,

$$f\left(\mathbf{r} + \mathbf{e}dt, \mathbf{e} + \left(\frac{\mathbf{F}}{m}\right)dt, t + dt\right)d\mathbf{r}d\mathbf{e} - f(\mathbf{r}, \mathbf{e}, t)d\mathbf{r}d\mathbf{e} = \Omega(f)d\mathbf{r}d\mathbf{e}dt \tag{2.3}$$

$\Omega(f)$ is the collision operator. Dividing the above equation by $d\mathbf{r}d\mathbf{e}dt$ and taking the limit of $dt \to 0$, the rate of change of number of particles, i.e. distribution function is given by

$$\frac{df}{dt} = \Omega(f) \tag{2.4}$$

The total rate of change of distribution function can be expressed as,

$$df = \frac{\partial f}{\partial \mathbf{r}} d\mathbf{r} + \frac{\partial f}{\partial \mathbf{e}} d\mathbf{e} + \frac{\partial f}{\partial t} dt \tag{2.5}$$

Therefore, the Boltzmann transport equation can be stated as

$$\frac{\partial f}{\partial t} + \mathbf{e} \cdot \frac{\partial f}{\partial \mathbf{r}} + \frac{\mathbf{F}}{m} \cdot \frac{\partial f}{\partial \mathbf{e}} = \Omega(f) \tag{2.6}$$

For a system unaided by an external force, the Boltzmann equation can be given as,

$$\frac{\partial f}{\partial t} + \mathbf{e} \cdot \frac{\partial f}{\partial \mathbf{r}} = \Omega(f) \tag{2.7}$$

Single-particle distribution function $f(\mathbf{r}, \mathbf{e}, t)$ depends on the scattering of a particle due to collision with another particle. Collision operator, $\Omega(f)$ requires position and speed of both particles at time t (i.e. requires two body distribution function $f^2(\mathbf{r}, \mathbf{e}, t)$) which indeed require $f^3(\mathbf{r}, \mathbf{e}, t)$ and so on up to N body distribution function $f^N(\mathbf{r}, \mathbf{e}, t)$. This results in Liouville equation [Succi, 2001] which exactly describe Newtonian behaviour of N-particles. This hierarchy of coupled N equations is known as the BBGKY hierarchy [Succi, 2001]. To simplify this complicated collision term, Boltzmann has taken several key assumptions based on dilute gas of point-like particles having an only localised binary collision, due to which $Q(f, f)$ depends only on $f^2(\mathbf{r}, \mathbf{e}, t)$ and by taking the assumption of molecular chaos (i.e. no correlation of particles entering short-lived collision), he replaced $f^2(\mathbf{r}, \mathbf{e}, t)$ by the product of $f_1(\mathbf{r}, \mathbf{e}, t)$ with velocity $\mathbf{e}_1$ and $f_2(\mathbf{r}, \mathbf{e}, t)$ with velocity $\mathbf{e}_2$. The simplified collision operator becomes as follow

$$Q(f, f) = \int dC \int \mathbf{e}_2 \sigma(C) |\mathbf{e}_1 - \mathbf{e}_2| \, (f_1' f_2' - f_1 f_2) \tag{2.8}$$

where, C is the scattering angle, f and f' are distribution function before and after a collision, $\sigma(C)$ is the differential collision cross section for the two-particle collision.

2.2.2 Linearisation of collision operator

This complicated collision integral, i.e. $Q(f, f)$is a big obstacle when dealing with the Boltzmann equation. For simplification, simpler operator $J(f)$ replaces $Q(f, f)$ because rigorous information of two-body interactions has little influence on the values of

many experimentally measured quantities. This simplified collision integral $J(f)$ has to satisfy two constraints [Wolf-Gladrow, 2000] given as below:

1. $J(f)$ has to conserve the five collision invariants ψ_k of $Q(f,f)$, i.e.

$$\int \psi_k J(f) d^3\mathbf{r} d^3\mathbf{e} = 0 \tag{2.9}$$

   where, (k = 0, 1, 2, 3, 4), ψ_1 = 1 for conservation of mass, $\psi_{1,2,3}$ = $\mathbf{e}$ for conservation of momentum and ψ_4 = $\mathbf{e}^2$ for conservation of energy.

2. The collision term should have the ability to approximate the distribution function close to equilibrium distribution function, i.e. Maxwellian distribution by H-theorem.

If there are no external forces and the distribution function is independent of $\mathbf{r}$ and time t (i.e., for $t \to \infty$ under an arbitrary initial condition), then the distribution function $f(\mathbf{e})$ approaches equilibrium distribution function $f^{eq}(\mathbf{e})$ which satisfies the Boltzmann Transport equation (Eq. 2.7), when the right-hand side of the BE is zero, i.e.

$$\int dC \int \mathbf{e}_2 \sigma(C) |\mathbf{e}_1 - \mathbf{e}_2| (f_1' f_2' - f_1 f_2) = 0 \tag{2.10}$$

and there is only one possibility for this to be true, which is given as,

$$f_1' f_2' - f_1 f_2 = 0 \tag{2.11}$$

Equilibrium distribution function $f^{eq}(\mathbf{e})$ which satisfies this above condition is called Maxwell Boltzmann Distribution Function [Mohamad, 2011] which is given as,

$$f^{eq} = \rho \left(\frac{m}{2\pi k_B T}\right)^{\frac{D}{2}} \exp\left(-\frac{m(\mathbf{e}-\mathbf{u})^2}{2k_B T}\right) \tag{2.12}$$

where m is mass of one molecule, T is the temperature of the gas, $\mathbf{u}$ is a macroscopic velocity, k_B is the Boltzmann constant and D is the dimension of the space.

If the external body force is neglected, both of the two constraints on collision integral are satisfied by the popular BGK model developed by Bhatnagar, Gross and Krook [Bhatnagar et al., 1954]. A simple approximation for collision term which is obtained by exponentially relaxes to local equilibrium with a time constant as given below:

$$J(f) = -\left(\frac{f - f^{eq}}{\tau}\right) \tag{2.13}$$

where τ is a single relaxation time and f^{eq} is a local Maxwellian function.

2.2.3 Derivation of lattice Boltzmann equation

In LBE, the discretisation of time and space derivatives of discrete Boltzmann equation are approximated using a first-order finite difference scheme. In this context, LBE can be seen as a particular form of finite-difference of the DBE. Depending on the aptness in selecting the set of discrete velocities, time step and lattice spacing, the convection term of the LBE turns out to be a shifting of the distribution function from one lattice node to its neighbouring node. Basically, there are three necessary steps to obtain the LBE from simplified BE.

1. First, a suitable local equilibrium function is to be determined, which plays an essential role in the LBM. It is the function which determines what kind of flow conditions are solved employing LBE. The equilibrium distribution function, f^{eq} in the BGK collision operator is mainly the low Mach number Taylor series expansion of Maxwellian function for low Mach number.

$$f^{eq} = \frac{\rho}{(2\pi RT)^{\frac{D}{2}}} \exp\left(-\frac{\mathbf{e}^2}{2RT}\right)\left\{1.0 + \frac{\mathbf{e}.\mathbf{u}}{RT} + \frac{(\mathbf{e}.\mathbf{u})^2}{2(RT)^2} - \frac{\mathbf{u}^2}{2RT}\right\} + O(u^3) \tag{2.14}$$

where R is the gas constant.

From the kinetic theory, the specific internal energy can be expressed as,

$$E = \frac{1}{2}\mathbf{e}^2 = \frac{3}{2}RT \tag{2.15}$$

Therefore, it is obtained that RT is equal to $\frac{\mathbf{e}^2}{3}$ which is the value of the lattice speed of sound C_s in LBM. The f^{eq} can be viewed as a multiplication of weighting function $\psi(\mathbf{e}) = \frac{1}{(2\pi RT)^{\frac{D}{2}}} \exp\left(-\frac{\mathbf{e}^2}{2RT}\right)$ with a polynomial in $\mathbf{e}$. The Gauss quadrature rule is applied to evaluate continuous integrals as sums of a discrete set of weight functions w_i corresponding to each discrete velocity $\mathbf{e}_i$. It is given by,

$$\int \psi(\mathbf{e})\mathbf{e}^n \, d\mathbf{e} = \sum_i w_i \, \mathbf{e}_i^{eq} \tag{2.16}$$

This leads to discrete equilibrium distribution function, which is calculated by prescribed macroscopic density and velocity as follows [He and Luo, 1997]

$$f_i^{eq} = \rho w_i \left\{ 1.0 + \frac{\mathbf{e}_i . \mathbf{u}}{C_s^2} + \frac{(\mathbf{e}_i . \mathbf{u})^2}{2{C_s}^4} - \frac{\mathbf{u}^2}{2C_s^2} \right\} \tag{2.17}$$

The weighting factor (w_i) for D2Q9 lattice structure is provided as [Guo and Shu, 2013]:

$$w_i = \begin{Bmatrix} \frac{4}{9} & i = 0 \\ \frac{1}{9} & i = 1,..,4 \\ \frac{1}{36} & i = 5,..,8 \end{Bmatrix} \tag{2.18}$$

For the D3Q19 lattice structure, it is given by [Krüger et al., 2016]:

$$w_i = \begin{Bmatrix} \frac{1}{3} & i = 0 \\ \frac{1}{18} & i = 1,..,6 \\ \frac{1}{36} & i = 7,..,18 \end{Bmatrix} \tag{2.19}$$

The discrete velocity $\mathbf{e}_i$ for D2Q9 lattice structure is specified as [Guo and Shu, 2013]:

$$\mathbf{e}_i = \begin{Bmatrix} (0,0) & i = 0 \\ c(\cos[(i-1)\pi/2], \sin[(i-1)\pi/2]) & i = 1,..,4 \\ \sqrt{2}c(\cos[(2i-9)\pi/4], \sin[(2i-9)\pi/4]) & i = 5,..,8 \end{Bmatrix} \tag{2.20}$$

The discrete velocity $\mathbf{e}_i$ for D3Q19 lattice structure is presented as [Krüger et al., 2016]:

$$\mathbf{e}_i = \begin{Bmatrix} (0,0,0) & i = 0 \\ c(\pm 1,0,0), c(0,\pm 1,0), c(0,0,\pm 1) & i = 1,..,6 \\ c(\pm 1,\pm 1,0), c(0,\pm 1,\pm 1), c(\pm 1,0,\pm 1) & i = 7,..,18 \end{Bmatrix} \tag{2.21}$$

2. The discretisation of velocity space **e** to obtain the necessary and minimum number of discrete velocities $\mathbf{e}_i$.

$$\frac{\partial f_i}{\partial t} + \mathbf{e}_i \cdot \frac{\partial f_i}{\partial \mathbf{r}} = \left(\frac{f_i^{eq} - f_i}{\tau} \right) \tag{2.22}$$

This equation is termed as discrete Boltzmann equation

3. The discretisation of time and space is done to obtain the lattice Boltzmann equation, which works as the governing equation for LBM. The LBE is given as [He and Luo, 1997]

$$f_i(\mathbf{r} + \mathbf{e}_i \Delta t, t + \Delta t) - f_i(\mathbf{r}, t) = \frac{\Delta t}{\tau} \left(f_i^{eq} - f_i \right) \tag{2.23}$$

2.3 Algorithm of LBM

The general LBM algorithm consists of two fundamental steps: streaming and collision, which are followed by subsequent steps. However, the algorithm starts with an initialisation step to set the initial values of the distribution functions using discrete equilibrium distribution function. The general LBM algorithm can be described with the following steps:

1. The collision step (Fig. 2.1(b)) implements the collision operator, which models the interactions between pseudo-particles (distribution functions) by conserving mass and momentum and bring them back to their equilibrium states. The process of collision is local concerning each lattice site.

$$f_i(\mathbf{r}, t + \Delta t) = f_i(\mathbf{r}, t) + \frac{\Delta t}{\tau} \left(f_i^{eq} - f_i \right) \tag{2.24}$$

2. The streaming step (Fig. 2.1(c)) models the shifting of distribution functions in the direction of motion from one node to the adjacent nodes.

$$f_i(\mathbf{r} + \mathbf{e}_i \Delta t, t + \Delta t) = f_i(\mathbf{r}, t + \Delta t) \tag{2.25}$$

3. Then the boundary step is implemented, which defines the unknown distribution functions at the boundary lattice nodes.

4. These three steps are completed in one time-step of the LBM simulation. Hence, this sequence is repeated in a loop until the final time is reached.

2.4 Lattice structure in LBM

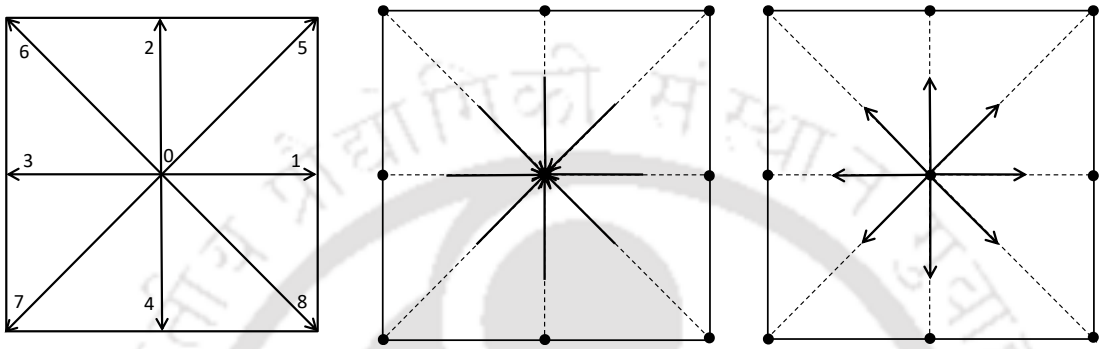

Fig. 2.1. (a) D2Q9 lattice model, (b) Collision process and (c) Streaming process in LBM

In LBM, all the particles are assumed to be residing at the fixed location called nodes of a lattice. These lattices are the regular arrangement of the particles in the domain and hence all particles should follow or move along these fixed paths thereby reducing the degree of freedom of the system. All particles should be streamed along these lattice links and collide at lattice sites. The lattice structure in LBM is symbolised by DmQn, where m is the number of dimension and n denotes the number of particle velocities, i.e., number of linkages of a node. Fig. 2.1(a) shows a lattice structure for two-dimensional flows namely D2Q9 lattice models with nine discrete velocities ($\mathbf{e}_i$) [Hou et al., 1995], and it is opted in this thesis work. In a D2Q9 model, each lattice node has eight neighbours as connected by eight links. The particle distribution functions (PDF) with their respective velocity $\mathbf{e}_i$ streams from one node to its neighbouring node in a streaming process along these links in unit time. For three-dimensional problems, cubic lattice structures commonly D3Q19 lattice model [Krüger et al., 2016] is used, as shown in Fig. 2.2. In this model, each node has eighteen neighbours as connected by eighteen links. These 9 speeds and 19 speeds provide sufficient isotropy to the 2D and 3D model respectively

and are sufficient for weakly compressible fluid applications. Besides, the use a rest particle in a discrete velocity set is to improve computational stability and reliability of the model.

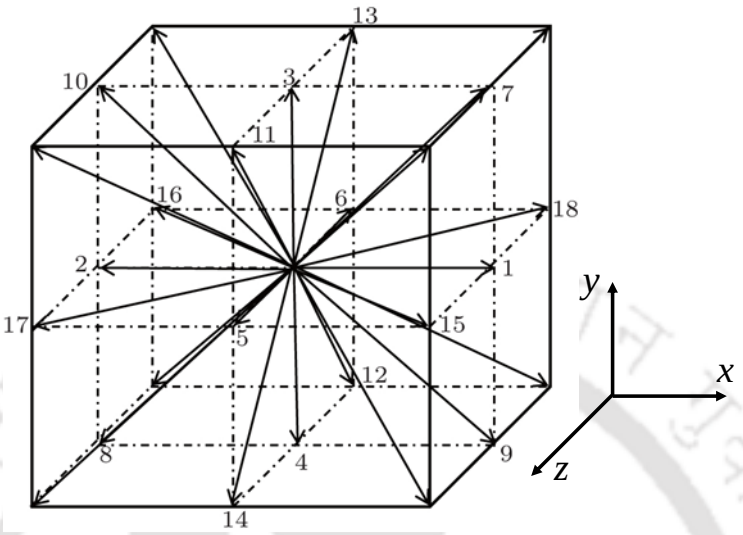

Fig. 2.2. D3Q19 lattice model

2.5 Methodology of basic LBM model

The Lattice Boltzmann algorithm (LBE) has two fundamental steps: streaming and collision. All LB models implement the streaming step in the same manner, which deals with shifting of the particle from one lattice node to the adjacent node. The collision step, which models the interactions between molecules, can be modified. Depending on linearised collision operator used in lattice Boltzmann equation, two approaches are mainly studied by researchers. The most popular and simple method is Bhatnagar-Gross-Krook (BGK) [Chen et al., 1991; Qian et al., 1992] collision model in which both bulk and shear viscosity are determined by single relaxation time (SRT) parameter. The SRT parameter is viscosity dependent which relaxes the different physical modes to their equilibria with the same rate, thereby leads to the deficiencies concerning its accuracy and stability. To overcome this limitation, a collision matrix with multiple relaxation times can be used, which allows choosing the bulk viscosity independently of the shear viscosity. d'Humi`eres [1992] introduced the multiple relaxation time (MRT) approach, which improves the numerical stability of LBM by relaxing the hydrodynamic and non-hydrodynamic moments

with different relaxation time. However, the proper implementation of the MRT method is 15% to 20% slower than the SRT method, as suggested by Lallemand and Luo [2000]. The methodology of both models for isothermal and thermal flows are provided in the following sections. In order to facilitate numerical calculation and analysis, the proper conversion from the physical unit to lattice unit has to be made (mentioned in details in Appendix A). For the simulation of lid-driven (temperature term is ignored) and mixed convection problem, the non-dimensional quantities are expressed as follows:

$$x = \frac{x^*}{L}; \qquad y = \frac{y^*}{L}; \qquad u = \frac{u^*}{V_0^*}; \qquad v = \frac{v^*}{V_0^*}; \qquad \theta = \frac{T - T_c}{T_h - T_c} \tag{2.26}$$

whereas, for the simulation of buoyancy induced convection, the macroscopic quantities are presented in their dimensionless form as:

$$x = \frac{x^*}{L}; \qquad y = \frac{y^*}{L}; \qquad u = \frac{u^* L}{\alpha_f}; \qquad v = \frac{v^* L}{\alpha_f}; \qquad \theta = \frac{T - T_c}{T_h - T_c} \tag{2.27}$$

where L and V_0^* are taken as the reference length and characteristic velocity of the fluid respectively. The symbols with '$*$' and without '$*$' indicate the variables in their dimensional and non-dimensional form respectively. θ stands for non-dimensional temperature and α_f is the thermal diffusivity of the fluid (or base fluid in case of nanofluid).

2.5.1 SRT-LBM model for isothermal flows

The governing equation for the lattice BGK model with a single relaxation time (SRT) is [Hou et al., 1995]

$$f_i(\mathbf{r} + \mathbf{e}_i \Delta t, t + \Delta t) = f_i(\mathbf{r}, t) + \frac{1}{\tau_\nu}\left(f_i^{eq}(\mathbf{r}, t) - f_i(\mathbf{r}, t)\right) \tag{2.28}$$

The suffix i ($0 \le i \le 8$ for D2Q9 model) refers to a PDF with velocity $\mathbf{e}_i$ at which DF streams from one node to its neighbouring node in a streaming process, $\mathbf{r} = [x, y]$ is the position vector of an arbitrary lattice node, and Δt is the lattice time step. The single relaxation time (τ_ν) determine the kinetic viscosity, $\nu = C_s^2 \Delta t(\tau_\nu - \frac{1}{2})$ and it relaxes

discrete density distribution function (f_i) towards its equilibrium distribution function (f_i^{eq}) in the collision process (given by the right-hand side of the equation).

2.5.2 MRT-LBM model for isothermal flows

The principle of MRT is to perform the collision process in the moment space rather than in the velocity space as the collision operator, $\Omega(f)$ is generally a full matrix. The MRT-LBM introduces different relaxation times that relax the respective moment of the distribution functions, thereby improving numerical stability and accuracy compared to SRT-LBM. The evolution equation for LBM-MRT model is given as [d'Humi`eres, 1992]:

$$f_i(\mathbf{r} + \mathbf{e}_i\Delta t, t + \Delta t) - f_i(\mathbf{r}, t) = -\mathrm{M}^{-1}\mathrm{R}\{\mathbf{m}(\mathbf{r}, t) - \mathbf{m}^{eq}(\mathbf{r}, t)\} \tag{2.29}$$

For D2Q9 model, the nine discretised distribution function corresponding to $\mathbf{e}_i$ and their nine moments in vector form are given as

$$\mathbf{f}(\mathbf{r}, t) = \{f_0(\mathbf{r}, t), f_1(\mathbf{r}, t), \dots\dots, f_8(\mathbf{r}, t)\}^{\mathrm{T}} \tag{2.30}$$

$$\begin{aligned}\mathbf{m}(\mathbf{r}, t) &= \{m_0(\mathbf{r}, t), m_1(\mathbf{r}, t), \dots\dots, m_8(\mathbf{r}, t)\}^{\mathrm{T}} \\ &= (\rho, e, \in, j_x, q_x, j_y, q_y, P_{xx}, P_{xy})^{\mathrm{T}}\end{aligned} \tag{2.31}$$

where ρ is the fluid density, e and $\in$ are related to the energy and its square, j_x and j_y are components of the momentum, q_x and q_y are the components of the energy flux, P_{xx} and P_{xy} correspond to the diagonal and off-diagonal components of the stress tensor. The superscript T denotes transpose operator.

The transformation matrix M is a 9×9 matrix that linearly transforms the density distribution functions (**f**) in velocity space to their velocity moments (**m**) in moment space and vice-versa follows:

$$\mathbf{m} = \mathrm{M}\mathbf{f}\,, \quad \mathbf{f} = \mathrm{M}^{-1}\mathbf{m} \tag{2.32}$$

The transformation matrix *M* is given by

$$\mathrm{M} = \begin{bmatrix} 1 & 1 & 1 & 1 & 1 & 1 & 1 & 1 & 1 \\ -4 & -1 & -1 & -1 & -1 & 2 & 2 & 2 & 2 \\ 4 & -2 & -2 & -2 & -2 & 1 & 1 & 1 & 1 \\ 0 & 1 & 0 & -1 & 0 & 1 & -1 & -1 & 1 \\ 0 & -2 & 0 & 2 & 0 & 1 & -1 & -1 & 1 \\ 0 & 0 & 1 & 0 & -1 & 1 & 1 & -1 & -1 \\ 0 & 0 & -2 & 0 & 2 & 1 & 1 & -1 & -1 \\ 0 & 1 & -1 & 1 & -1 & 0 & 0 & 0 & 0 \\ 0 & 0 & 0 & 0 & 0 & 1 & -1 & 1 & -1 \end{bmatrix} \tag{2.33}$$

The rows of M are distributed according to the order of tensor of the nine moments instead of the order of moment of the distribution functions. The first three rows correspond to three scalars ρ, e and $\in$ which are the 0^{th}, 2^{nd} and 4^{th} order moments of f_i respectively. The next four rows are related to four vectors j_x, q_x, j_y and q_y respectively where j_x and j_y are the first-order moments and q_x and q_y are the third-order ones. The last two rows are related to the second-order stress tensors, which are second-order moments. The equilibrium moments $\mathbf{m}^{eq}$ in vector form is given by [26]

$$\mathbf{m}^{eq} = \left\{\rho\left(1, -2 + 3\mathbf{u}^2, 1 - 3\mathbf{u}^2, u_x, -u_x, u_y, -u_y, u_x^2 - u_y^2, u_x u_y\right)\right\}^{\mathrm{T}} \tag{2.34}$$

In moment space the diagonal relaxation matrix R given as

$$\mathrm{R} = \mathrm{diag}(1, r_e, r_\in, 1, r_q, 1, r_q, r_v, r_v) \tag{2.35}$$

These relaxation parameters are chosen flexibly ($0 < r < 2$) while depending on the problem formulation. For the current isothermal flow simulation, they are set as r_e = $r_\in$ = 1.64 and r_q = 1.2. The parameter r_v is linked to kinetic viscosity ν as follows:

$$\frac{1}{r_v} = \frac{\nu}{C_s^2} + \frac{1}{2} \tag{2.36}$$

The MRT model reduces to the usual lattice BGK equation if all the relaxation parameters are set to single relaxation time (τ_v) where $\mathrm{R} = \frac{\mathrm{I}}{\tau_v}$ (I is the identity matrix).

In LBM, the macroscopic variables are obtained by taking moments of the distribution function. Fluid density ρ and velocity $\mathbf{u}$ are calculated by taking 0^{th} and 1^{st} moments of f_i respectively [Chen and Doolen, 1998].

$$\rho = \sum_{i=0}^{8} f_i \tag{2.37}$$

$$\rho \mathbf{u} = \sum_{i=0}^{8} f_i \, \mathbf{e}_i \tag{2.38}$$

2.5.3 SRT-LBM model for thermal flows

Peng et al.'s [2003] simplified DDF approach based on SRT-LBM is implemented to simulate heat transfer flow problems. The governing discretised lattice Boltzmann equations for density and temperature distribution function are given as

$$f_i(\mathbf{r} + \mathbf{e}_i \Delta t, t + \Delta t) = f_i(\mathbf{r}, t) + \frac{1}{\tau_v}\left(f_i^{eq}(\mathbf{r}, t) - f_i(\mathbf{r}, t)\right) + S_i \tag{2.39}$$

To incorporate the buoyancy force in this thermal lattice Boltzmann model, the force term (S) is added to the collision process. A number of LB forcing schemes are proposed in the literature to model external force term for different thermal problems. Among these, three popular forcing schemes are given as follows:

1. Luo's force model (conventional model) [Luo, 1993]

$$S_i = dtw_i \frac{\mathbf{e}_i . \mathbf{G}}{C_s^2} \tag{2.40}$$

2. Shan and Chen force model [Shan and Chen, 1994]

$$S_i = dtw_i \left\{\frac{\mathbf{e}_i - \mathbf{u}}{C_s^2} + \frac{\mathbf{e}_i(\mathbf{e}_i . \mathbf{u})}{C_s^4}\right\} . \mathbf{G} \tag{2.41}$$

3. Guo's force model [Guo et al., 2002c]

$$S_i = dtw_i \left\{1 - \frac{1}{2\tau_v}\right\}\left\{\frac{\mathbf{e}_i - \mathbf{u}}{C_s^2} + \frac{\mathbf{e}_i(\mathbf{e}_i . \mathbf{u})}{C_s^4}\right\} . \mathbf{G} \tag{2.42}$$

Among these three models, Guo's force model is found to be more appropriate one as it can correctly represent the Navier-Stokes equation on the macroscopic scale using Chapman-Enskog expansion.

G is defined as the external force per unit volume due to the presence of the buoyancy force. According to Boussinesq approximation, all the properties of fluid considered as constants except the density variation in the buoyancy force term. The buoyancy force per unit volume depends linearly on the temperature as follows [Cengel, 2003]

$$\mathbf{G} = \rho \mathbf{g} \beta (\theta - \theta_m) \tag{2.43}$$

where ρ is the density of the fluid at the mean temperature θ_m, **g** is the acceleration due to gravity, and β is the coefficient of thermal expansion.

For temperature distribution function the governing discretised lattice Boltzmann equation is given as [Peng et al., 2003]

$$g_i(\mathbf{r} + \mathbf{e}_i \Delta t, t + \Delta t) = g_i(\mathbf{r}, t) + \frac{1}{\tau_\theta}\Big(g_i^{eq}(\mathbf{r}, t) - g_i(\mathbf{r}, t)\Big) \tag{2.44}$$

The τ_v and τ_θ are single relaxation time (SRT) parameters that determine the kinetic viscosity, $v = C_s^2 \Delta t(\tau_v - \frac{1}{2})$ and thermal diffusivity, $\alpha = C_s^2 \Delta t(\tau_\theta - \frac{1}{2})$ respectively.

2.5.4 MRT-LBM model for thermal flows

The governing equation for LBM-MRT model for flow field with source term can be given as follows [Mezrhab et al., 2010]:

$$\begin{aligned} & f_i(\mathbf{r} + \mathbf{e}_i \Delta t, t + \Delta t) - f_i(\mathbf{r}, t) \\ & \quad = -\mathrm{M}^{-1}\mathrm{R}\{\mathbf{m}(\mathbf{r}, t) - \mathbf{m}^{eq}(\mathbf{r}, t)\} + \mathrm{M}^{-1}\left(\mathrm{I} - \frac{\mathrm{R}}{2}\right)\mathbf{S} \end{aligned} \tag{2.45}$$

In moment space the diagonal relaxation matrix R given as

$$\mathrm{R} = \mathrm{diag}(1, r_e, r_\in, 1, r_q, 1, r_q, r_v, r_v) \tag{2.46}$$

For all thermal flow simulation in this thesis work, the relaxation parameters are chosen as r_e = 1.64, 2 > $r_\epsilon \geq \frac{2}{1+Pr}$ and r_q = 1.2, where *Pr* is the Prandtl number. The total force term **S** is given by a column vector as follows [Wang et al., 2013]:

$$\mathbf{S} = \left\{\rho\left(0, 6\mathbf{u}.\mathbf{F}, -6\mathbf{u}.\mathbf{F}, F_x, -F_x, F_y, -F_y, 2(u_xF_x - u_yF_y), (u_xF_y + u_yF_x)\right)\right\}^{\mathrm{T}} \quad (2.47)$$

where,

$$F_x = 0; F_y = \mathbf{G} = \rho\mathbf{g}\beta(\theta - \theta_m) \quad (2.48)$$

The evolution equation for LBM-MRT model for temperature field is given as follows [Wang et al., 2013]

$$g_i(\mathbf{r} + \mathbf{e}_i\Delta t, t + \Delta t) - g_i(\mathbf{r}, t) = -\mathrm{N}^{-1}\mathrm{C}\{\mathbf{n}(\mathbf{r}, t) - \mathbf{n}^{eq}(\mathbf{r}, t)\} \quad (2.49)$$

For D2Q5 model, the suffix i refers to 5 discrete velocities $\mathbf{e}_i$ for D2Q5 lattice structure, the velocities are given as [Mezrhab et al., 2010]:

$$\mathbf{e}_i = \begin{cases} (0,0) & i = 0 \\ c(\cos[(i-1)\pi/2], \sin[(i-1)\pi/2]) & i = 1,..,4 \end{cases} \quad (2.50)$$

The diagonal relaxation matrix C is given by [Wang et al., 2013]

$$\mathrm{C} = \mathrm{diag}(1, c_\theta, c_\theta, c_e, c_v) \quad (2.51)$$

In the present simulation, the relaxation parameters are chosen as c_e = c_v = 1.8. The relaxation parameter c_θ in Eq. 2.51 is determined by the thermal diffusivity α as given below:

$$\frac{1}{c_\theta} = \frac{10\alpha}{(4+a)} + \frac{1}{2} \quad (2.52)$$

where the value of constant term a should be less than one to avoid numerical instability.

The transformation matrix N is a 5×5 matrix which linearly transforms the temperature distribution functions (**g**) to their moments (**n**) and vice-versa as follows:

$$\mathbf{n} = \mathrm{N}\mathbf{g}, \ \mathbf{g} = \mathrm{N}^{-1}\mathbf{n} \quad (2.53)$$

where N is given by

$$\mathrm{N} = \begin{bmatrix} 1 & 1 & 1 & 1 & 1 \\ 0 & 1 & 0 & -1 & 0 \\ 0 & 0 & 1 & 0 & -1 \\ -4 & 1 & 1 & 1 & 1 \\ 0 & 1 & -1 & 1 & -1 \end{bmatrix} \tag{2.54}$$

The equilibrium moments $\mathbf{n}^{eq}$ in vector form is given as [Mezrhab et al., 2010]:

$$\mathbf{n}^{eq} = (\theta, u\theta, v\theta, a\theta, 0)^{\mathrm{T}} \tag{2.55}$$

The characteristic velocity for mixed convection flow is taken as the lid velocity ($V_0^* = \sqrt{Ri\mathbf{g}\beta\Delta TL}$) whereas, the characteristic velocity of the natural convection flow is $\sqrt{\mathbf{g}\beta\Delta TL}$. The value of characteristic velocity in the lattice unit (V_{lb}) must be small in comparison to the lattice speed of sound C_s ($= 1/\sqrt{3}$) to satisfy incompressibility condition. In Thermal LBM, the velocity $\mathbf{u}$ is modified by taking into account the force effect as follows [Guo et al., 2002c]:

$$\rho\mathbf{u} = \sum_{i=0}^{8} f_i \, \mathbf{e}_i + \frac{\mathbf{G}}{2} \tag{2.56}$$

Temperature (θ) is the only conserved quantity which is calculated as 0^{th} moments of g_i [Peng et al., 2003] as given below:

$$\theta = \sum_{i=0}^{4} g_i \tag{2.57}$$

2.6 Initial and boundary condition treatments in LBM

Initial condition and boundary condition (BC) play a vital role in any flow problem to obtain the proper solution. Generally, macroscopic variables are directly implemented at these conditions in solving continuum flow problems using computational fluid dynamics techniques such as finite difference, finite volume method. However, in LBM, these physical conditions are needed to be expressed in terms of an only unknown parameter known as the discrete distribution function. Different approaches have been proposed by

researchers to obtain the distribution function from known macroscopic variables while maintaining the same physical meaning. To model initial condition in LBM, the equilibrium distribution function is most widely used [Hou et al. 1995] to initialise both density- and temperature- distribution function, which is represented as follows:

$$f_i(\mathbf{r},t) = f_i^{eq}(\mathbf{r},t);\ g_i(\mathbf{r},t) = g_i^{eq}(\mathbf{r},t) \tag{2.58}$$

A number of boundary schemes are available in LBM literature to specify the distribution functions at a boundary. These boundary conditions can be divided into two categories: link-wise and wet-node [Guo and Shu, 2013; Krüger et al. 2016].

The popular bounce-back (BB) model falls under link-wise schemes. This model simulates no-slip boundary condition on the stationary wall located midway on the link between lattice nodes (termed as a half-way bounce-back scheme). The enforcement of bounce back model on density distribution function is given as follows:

$$f_i(\mathbf{r}_b, \mathbf{e}_i, t) = f_i(\mathbf{r}_b, -\mathbf{e}_i, t) \tag{2.59}$$

where $\mathbf{r}_b$ is the position vector of the boundary node. In this approach, the distribution function is reversed back to its original location with the same sped after meeting a rigid boundary during its streaming.

Ladd et al. [1994] proposed a revised half-way bounce-back scheme to incorporate wall velocity into LBM framework as follows:

$$f_i(\mathbf{r}_b, \mathbf{e}_i, t) = f_i(\mathbf{r}_b, -\mathbf{e}_i, t) - 2\, w_i \rho_b \left\{\frac{\mathbf{e}_i . \mathbf{u}_w}{C_s^2}\right\} \tag{2.60}$$

where b and w denote the boundary node and wall node. It is evident that wall velocity $\mathbf{u}_w$ = 0 for a stationary boundary.

The boundary in wet-node boundary schemes is placed on a boundary node. The most common wet-node schemes are equilibrium scheme, non-equilibrium bounce-back method and non-equilibrium extrapolation method. In equilibrium scheme, the unknown distribution functions at the boundary are set equal to their equilibrium values as obtained from prescribed density and velocity at the boundary.

$$f_i(\mathbf{r}_b, t) = f_i^{eq}(\mathbf{r}_b, \rho_b, \mathbf{u}_w, t) \tag{2.61}$$

This BC provides satisfactory accuracy when relaxation time τ approaches 1.

Guo et al. [2002b] proposed a non-equilibrium extrapolation method (NEEM) on the basis of non-equilibrium distribution functions. The fundamental concept of this method is to a breakdown of the distribution functions (DF) into its equilibrium and non-equilibrium parts at the boundary node. The equilibrium DF is defined based on the stated macroscopic boundary conditions. Whereas, the non-equilibrium DF is approximated with a first-order extrapolation. It is expressed as follows:

$$f_i(\mathbf{r}_b, t) = f_i^{eq}\left(\mathbf{r}_b, \rho_f, \mathbf{u}_w, t\right) + \left(f_i\left(\mathbf{r}_f, t\right) - f_i^{eq}\left(\mathbf{r}_f, t\right)\right) \tag{2.62}$$

Where f, $\mathbf{r}_f$ and ρ_f represent the fluid node, position vector and density at the neighbouring fluid (inner) node respectively.

Zou and He [1997] proposed a non-equilibrium bounce-back method (NEBB), as the name suggests it is the bounce-back of the non-equilibrium distribution functions.

$$f_i^{neq}(\mathbf{r}_b, \mathbf{e}_i, t) = f_i^{neq}(\mathbf{r}_b, -\mathbf{e}_i, t) \tag{2.63a}$$

$$f_i(\mathbf{r}_b, \mathbf{e}_i, t) - f_i^{eq}(\mathbf{r}_b, \mathbf{e}_i, t) = f_i(\mathbf{r}_b, -\mathbf{e}_i, t) - f_i^{eq}(\mathbf{r}_b, -\mathbf{e}_i, t) \tag{2.63b}$$

In the thesis work, application of LB boundary schemes is limited to model BC at solid walls. However, different LB boundary schemes are proposed to treat curved boundary [Mei et al., 1999] and inflow/outflow conditions [Yu et al., 2003].

For thermal flow conditions, second-order accurate finite difference approximation (Neumann condition) on macroscopic temperature is implemented on thermally insulated walls, and Dirichlet condition is used for constant temperature walls [Peng et al., 2003]. To transform these temperature conditions to their distribution function (DF) counterpart, a second-order accurate non-equilibrium-extrapolation approach proposed by Guo et al. [2002a] is applied. In this approach, both equilibrium and non-equilibrium parts of DF are calculated from known temperatures at a boundary node and at a neighbouring fluid node.

$$g_i(\mathbf{r}_b, t) = g_i^{eq}(\mathbf{r}_b, \theta_w, \mathbf{u}_w, t) + \left(g_i\left(\mathbf{r}_f, t\right) - g_i^{eq}\left(\mathbf{r}_f, t\right)\right) \tag{2.64}$$

2.7 Post processing

2.7.1 Stream function

The stream function (ψ) is used to plot the streamlines which are tangential to the instantaneous velocity vector of the flow, thus displaying the fluid motion. The relationship between stream function and velocity components u and v for two-dimensional flows are given as:

$$u = \frac{\partial \psi}{\partial y}, \qquad v = -\frac{\partial \psi}{\partial x} \tag{2.65}$$

The positive and negative sign of ψ denotes the anticlockwise and clockwise circulation respectively.

2.7.2 Nusselt number

The overall heat transfer characteristics are best described by the non-dimensional parameter known as the Nusselt number (*Nu*). The average *Nu* for the whole domain ($\overline{Nu}$), along vertical left ($\overline{Nu_l}$) and right ($\overline{Nu_r}$) wall and along the horizontal bottom ($\overline{Nu_b}$) and top ($\overline{Nu_t}$) wall are respectively calculated as follows [Peng et al., 2003]:

$$\overline{Nu} = \frac{1}{L^2}\int_0^L \int_0^L Nu dx dy \tag{2.66a}$$

$$\overline{Nu_l}(\text{or } \overline{Nu_r}) = \frac{1}{L}\int_0^L Nu_x dy \tag{2.66b}$$

$$\overline{Nu_b}(\text{or } \overline{Nu_t}) = \frac{1}{L}\int_0^L Nu_y dx \tag{2.66c}$$

where $Nu = u\theta - \frac{k_{nf}}{k_f}\left(\frac{\partial \theta}{\partial x}\right)$, $Nu_x = -\frac{k_{nf}}{k_f}\left(\frac{\partial \theta}{\partial x}\right)$ and $Nu_y = -\frac{k_{nf}}{k_f}\left(\frac{\partial \theta}{\partial y}\right)$ are the local Nusselt number at all fluid nodes, at the vertical and horizontal surfaces respectively, and the integral is evaluated using Simpson's 1/3 rule. For flow without nanofluid, k_{nf} is set equal to k_f.

2.7.3 Entropy generation

For convective heat transfer system, the dimensionless local entropy generation for a two-dimensional heat and fluid flow is given by considering the local thermodynamic equilibrium of linear transport theory [Nield and Bejan, 1999]. The total local entropy generation within the fluid-saturated porous medium and at the solid boundaries is the sum of the entropy generation due to the heat transfer and fluid friction irreversibilities, as shown below:

$$S_{tot} = S_\theta + S_\psi \tag{2.67}$$

where S_θ and S_ψ are the dimensionless local entropy generation due to heat transfer and fluid friction irreversibilities respectively, which are presented mathematically as follows [Roy et al., 2016; Siavashi et al., 2018]:

$$S_\theta = \frac{k_{nf}}{k_f}\left[\left(\frac{\partial\theta}{\partial x}\right)^2 + \left(\frac{\partial\theta}{\partial y}\right)^2\right] \tag{2.68a}$$

$$S_\psi = \chi\frac{\mu_{nf}}{\mu_f}\left\{\frac{[u^2+v^2]}{Da} + \left[2\left(\frac{\partial u}{\partial x}\right)^2 + 2\left(\frac{\partial v}{\partial y}\right)^2 + \left(\frac{\partial v}{\partial x} + \frac{\partial u}{\partial y}\right)^2\right]\right\} \tag{2.68b}$$

To incorporate viscous dissipation in porous media, an additional term $\left(\frac{[u^2+v^2]}{Da}\right)$ is included in Eq. (2.68b). This viscous dissipation model proposed by Al-Hadhrami et al. [2003] is valid for low as well as high Darcy number. The irreversibility factor χ represents the ratio of the viscous entropy generation to thermal entropy generation which is presented as $\frac{\mu_f T_m (V_0^*)^2}{k_f (T_h - T_c)^2}$.

The total entropy generation due to heat transfer and viscous effect for the whole cavity are calculated by integrating their respective local entropy generation over the whole domain as follows:

$$\overline{S_\theta} = \int_0^L \int_0^L S_\theta \, dx dy \tag{2.69a}$$

$$\overline{S_\psi} = \int_0^L \int_0^L S_\psi dxdy \tag{2.69a}$$

The Bejan number, Be defined as the ratio between the entropy generation due to heat transfer and total entropy generation, is expressed [Roy et al., 2016] as:

$$Be = \frac{S_\theta}{S_{tot}} \tag{2.70}$$

It is known that the heat transfer irreversibility is dominant when Be approaches 1. When Be becomes much smaller than 0.5 the irreversibility due to the viscous effects dominates the system and if Be = 0.5 the entropy generation due to the viscous effects and heat transfer effects are equal.

2.7.4 Cup-mixing temperature

In convection flow, the thermal mixing in different configurations of the cavity is compared by calculating the average temperature known as cup-mixing temperature θ_{cup} across the cavity, which is the velocity weighted average temperature, as shown below [Basak et al., 2012]:

$$\theta_{cup} = \frac{\int_0^L \int_0^L \mathbf{u}\theta dxdy}{\int_0^L \int_0^L \mathbf{u} dxdy} \tag{2.71}$$

The higher values of θ_{cup} indicate a higher overall heating rate.

The degrees of temperature uniformity in different cavities are compared by computing root-mean-square-deviation (RMSD) based on cup-mixing temperature [Basak et al., 2012] and which is given as:

$$RMSD_{\theta_{cup}} = \sqrt{\frac{\sum_{j=1}^{N}\left(\theta_j - \theta_{cup}\right)^2}{N}} \tag{2.72}$$

N denotes the grid size (e.g., N is 151×151 for Ra = 10^3 in natural convection cavity problem). The lower values of RMSD indicate higher temperature uniformity in the cavity and vice-versa.

2.8 Benchmark cavity flow problems for code validation

Here, three different benchmark problems are simulated for isothermal and thermal flows to check the applicability of the FORTRAN-based LBM codes. The problem of the lid-driven cavity, and buoyancy-induced natural convection and mixed convection in the cavity are considered as the fundamental benchmark problems to test computational schemes for isothermal and thermal flows. The solutions for current simulations are assumed to be converged if their relative L1 - error norms are less than equal to 10^{-8}.

2.8.1 Lid-driven cavity flow in the square cavity and cubic cavity

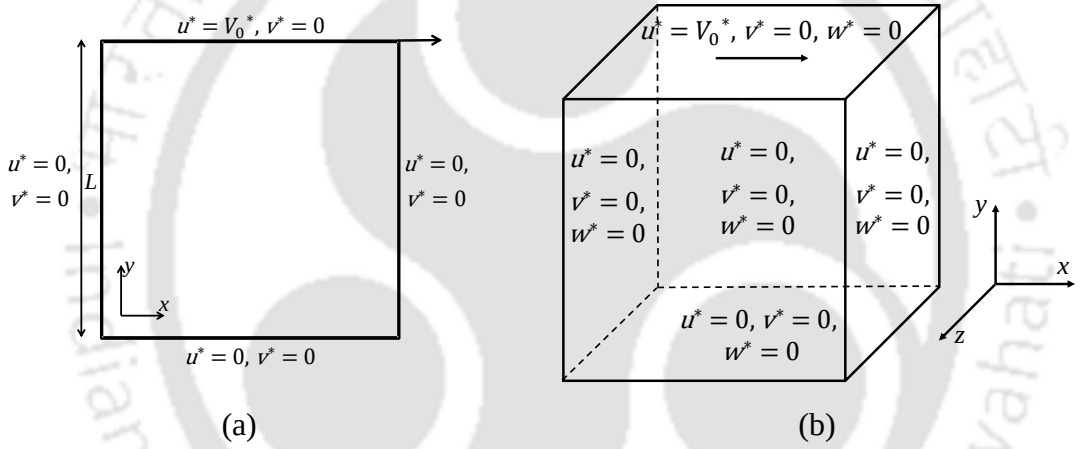

Fig. 2.3. Schematic diagram of the flow configuration with boundary conditions for (a) single lid-driven square cavity, (b) single lid-driven cubic cavity.

The flow configuration with boundary condition for the lid-driven square cavity flow is shown in Fig. 2.3(a). In this configuration, the upper horizontal lid moves towards the right with constant speed V_0^* while the other three walls are stationary. The flow is characterised by the Reynolds number, $Re = V_0^* L/\nu$, where L is the length of the cavity. The results are presented for three different Re = 100, 3200 and 7500 in a uniform grid size of 201×201.

To check the validity of both isothermal LB-SRT and LB-MRT models, the comparison of present results is made with the results of Ghia et al. [1982] in terms of the horizontal velocity u along the vertical centerline and the vertical velocity v along

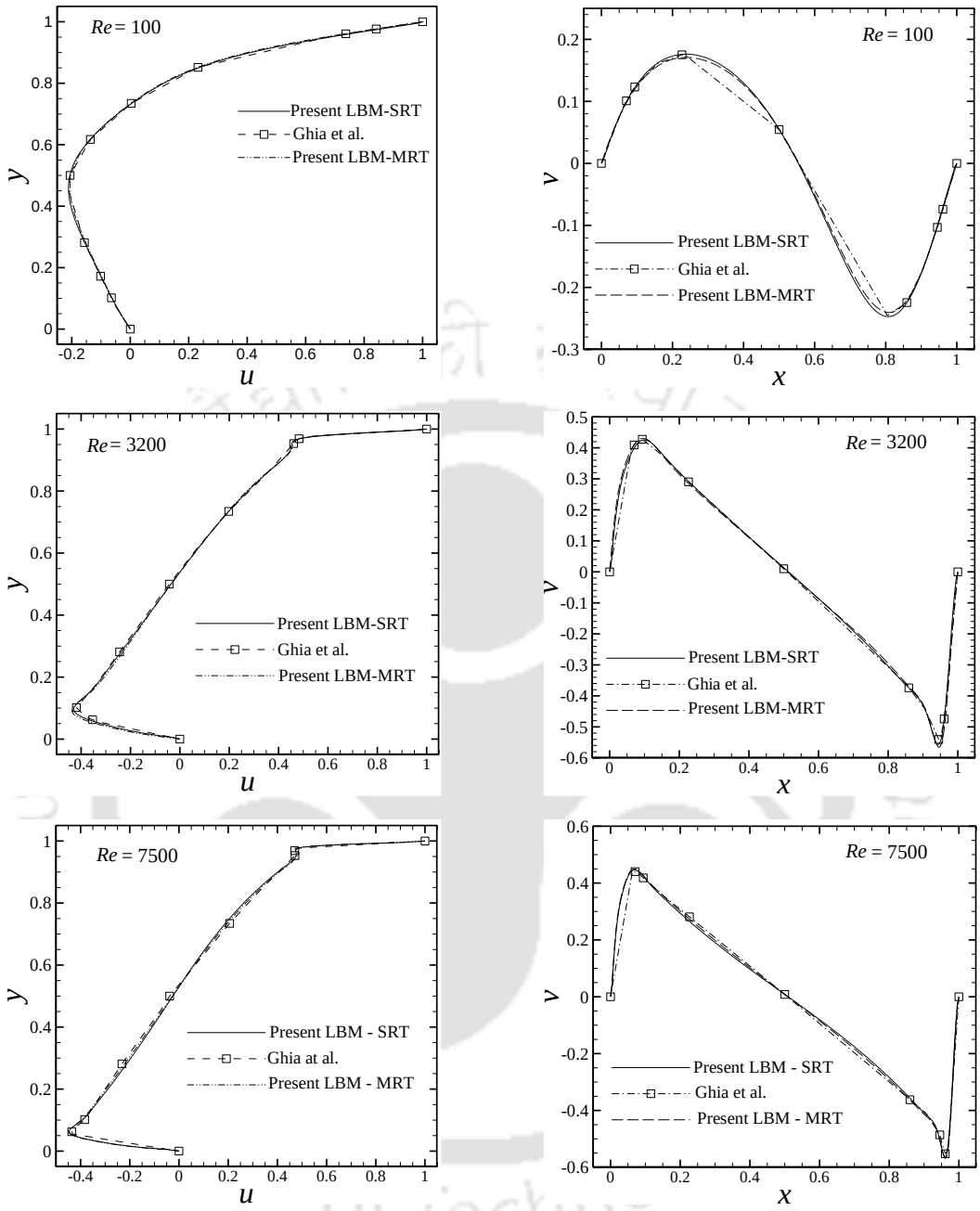

Fig. 2.4. Comparison of results in terms of dimensionless horizontal velocity u at y = 0.5 (left panel) and vertical velocity v at x = 0.5 (right panel) with Ghia et al. [1982] for Re = 100 (top panel), Re = 3200 (middle panel) and Re = 7500 (bottom panel).

horizontal centerline of the cavity (Fig. 2.4). The results show close agreement. However, with LB-MRT model, the converged solution is obtained with less time which signifies the fact that it is more stable compared to LB-SRT model. The LB-SRT and LB-MRT models are then used to perform three-dimensional computation of lid-driven problem in the cubic

cavity (Fig. 2.3(b)) for *Re* = 100, 400 and 1000 with a uniform grid size of 81×81×81. Fig 2.5 shows the comparison of LB-SRT and LB-MRT results with the published results of Ku et al. [1987] in terms of centreline u-velocity and v-velocity at mid-span (i.e., z = 0.5) of the cubic cavity and it displays a good agreement.

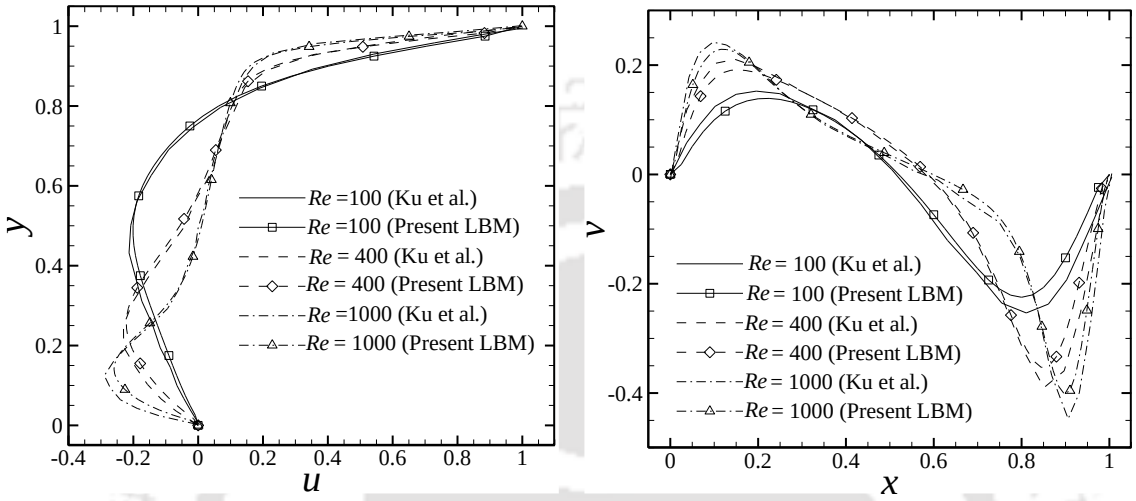

Fig. 2.5. Comparison of velocity profiles on vertical centerline (left) and horizontal centerline (right) of cubic cavity at *Re* = 100, 400 and 1000.

2.8.2 Natural convection in a square cavity

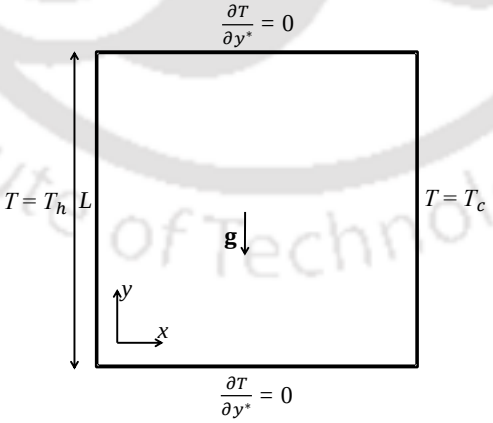

Fig. 2.6. Schematic diagram of the flow configuration with boundary conditions for natural convection in a square cavity.

Fig. 2.6 displays the flow configuration and boundary conditions for natural convection flow in an air-filled square cavity (*Pr* = 0.7). The flow configuration involves a

closed square cavity of unit length where the horizontal, as well as vertical walls of the cavity, are stationary. The horizontal walls are thermally insulated, and the left vertical wall is maintained at an isothermally hot and right vertical wall at isothermally cold temperature.

Table 2.1 Grid independence study

Variables	Grid sizes								
	Ra = 10^3			Ra = 10^4			Ra = 10^5		
	101× 101	151× 151	201× 201	151× 151	201× 201	251× 251	251× 251	301× 301	351× 351
v_{max}	3.601	3.636	3.653	19.298	19.388	19.441	67.545	67.714	67.843
$\overline{Nu_{\mathrm{lh}}}$	1.096	1.102	1.105	2.188	2.200	2.207	4.414	4.431	4.442
$\overline{S_\theta}$	1.078	1.090	1.096	2.164	2.183	2.194	4.385	4.407	4.423
$\overline{S_\psi}$	0.305	0.319	0.325	9.317	9.562	9.713	167.98	171.09	173.35

A grid sensitivity analysis is carried out to obtain grid-independent solutions for each of three different values of *Ra* during steady-state natural convection in an air filled square cavity. Table 2.1 gives the comparison of the grid sizes in terms of the dimensionless maximum vertical velocity (v_{max}) at the horizontal midline of the cavity, average Nu along the hot left wall of the cavity $\overline{Nu_{lh}}$, average total entropy generation due to heat transfer $\overline{S_\theta}$ and fluid friction $\overline{S_\psi}$ in the cavity for the configuration with a uniformly heated left wall. The grid sizes of 151×151 for *Ra* = 10^3, 201×201 for *Ra* = 10^4 and 301×301 for *Ra* = 10^5 are found to be suitable for all computations while taking note of the time-wise efficiency of the numerical simulations.

Table 2.2 Comparison of present work with de Vahl Davis [1983] and Magherbi et al. [2003].

Ra	$\overline{Nu}$		$\overline{S_{tot}}$		$\overline{Be}$	
	Present work	de Vahl Davis [1983]	Present work	Magherbi et al. [2003]	Present work	Magherbi et al. [2003]
10^3	1.107	1.118	1.430	1.470	0.778	0.765
10^4	2.201	2.238	11.795	12.488	0.190	0.181
10^5	4.424	4.509	175.780	194.647	0.0259	0.0232

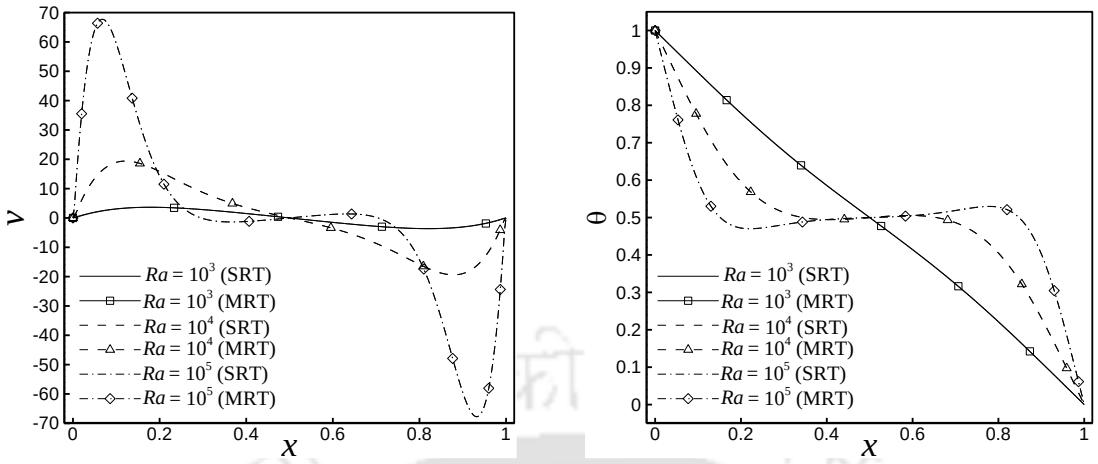

Fig. 2.7. Comparison of dimensionless vertical velocity v (left) and temperature θ (right) in the horizontal mid-plane of square cavity at different $Ra = 10^3$, 10^4 and 10^5.

Table 2.2 shows that the present code successfully reproduces the close approximation of published results of de Vahl Davis [1983] in terms of Nusselt number along the vertical hot wall and Magherbi et al.'s [21] results in terms of total entropy generation and Bejan number in the whole domain of the cavity with irreversibility factor fixed at 10^{-3}. Fig 2.7 depicts the comparison of LB-SRT and LB-MRT model for varying Ra from 10^3 to 10^5, and close agreement is observed.

Table 2.3 Comparison of present work with published results for higher Ra.

Ra	Method	y for u_{max}	u_{max}	x for v_{max}	v_{max}	$\overline{Nu}$
10^6	Present SRT	0.850	63.56	0.040	215.6	8.546
	Present MRT	0.851	63.852	0.0399	216.07	8.579
	de Vahl Davis [1983]	0.850	64.63	0.0379	219.36	8.799
10^7	Present SRT	0.880	142.41	0.024	669.56	15.62
	Present MRT	0.884	143.66	0.022	676.90	15.847
	Le Que´re´ [1991]	0.879	148.58	0.021	699.23	16.52
10^8	Present SRT	0.930	300.56	0.013	2089.48	27.935
	Present MRT	0.931	304.08	0.013	2109.22	28.342
	Le Que´re´ [1991]	0.928	321.87	0.012	2222.39	30.225

To check the robustness of the both SRT- and MRT-LBM calculations at higher Rayleigh number, the present study deals with the simulation of natural convection from

Ra = 10^6 to Ra = 10^8 as depicted in Table 2.3. Comparison of current results with the solutions available in the literature shows satisfactory agreement.

2.8.3 Mixed convection in a square cavity

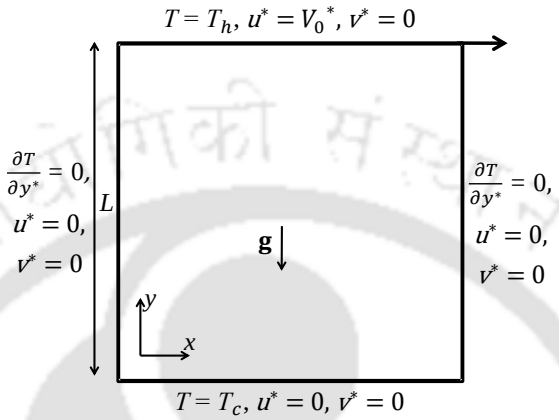

Fig. 2.8. Schematic diagram of the flow configuration with boundary conditions for single lid-driven mixed convection in cavity.

The present LBM code is validated for mixed convection flow problem in a clear square cavity with a horizontally moving hot top lid and adiabatic sidewalls, as shown in Fig. 2.8. The grid size of 301×301 is considered to carry out the simulations while considering time-wise efficiency.

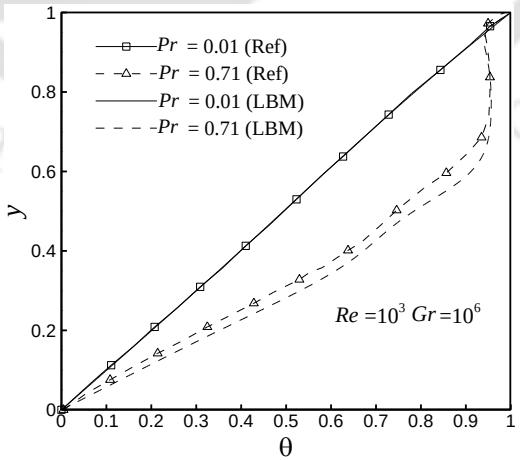

Fig. 2.9. Comparison of present results with Iwatsu et al. [1993] in terms of dimensionless temperature (θ) profile along the vertical mid-plane of square cavity for Pr = 0.01 and 0.71 at Re = 10^3 and Gr = 10^6.

Fig. 2.9 shows the variation of dimensionless temperature along the vertical mid-plane of the square cavity for $Re = 10^3$ and $Gr = 10^6$ at $Pr = 0.01$ and 0.71, which provides a good concordance of the present result with Iwatsu et al. [1993].

The results are then compared with the published works of Iwatsu et al. [1993] and Khanafer and Chamkha [1999] for fixed $Gr = 100$ and different Re of 100, 400 and 1000 respectively. The results are presented in Table 2.4 in terms of minimum dimensionless horizontal velocity (u_{min}) at vertical mid-plane, minimum and maximum dimensionless vertical velocity (v_{min} and v_{max}) at horizontal mid-plane and the average Nusselt number ($\overline{Nu_t}$) along the top wall. The comparison of results shows a good similitude.

Table 2.4 Comparison with Iwatsu et al. [1993] and Khanafer and Chamkha [1999].

Variables	$Re = 100$			$Re = 400$			$Re = 1000$		
	LBM	Ref. 1	Ref. 2	LBM	Ref. 1	Ref. 2	LBM	Ref. 1	Ref. 2
u_{min}	-0.2129	-0.2037	-0.2122	-0.3280	-0.3197	-0.3099	-0.3880	-0.3782	-
v_{min}	-0.2495	-0.2448	-0.2506	-0.4521	-0.4459	-0.4363	-0.5258	-0.5178	-
v_{max}	0.1764	0.1699	0.1765	0.3029	0.2955	0.2866	0.3767	0.3658	-
$\overline{Nu_t}$	2.02	1.94	2.01	4.029	3.84	3.91	6.454	6.33	6.33

*Ref. 1 (Iwatsu et al. [1993]); Ref. 2 (Khanafer and Chamkha [1999])

2.9 Summary

The present chapter provides the brief background of the lattice Boltzmann method, implementation technique of both SRT and MRT model, and different boundary condition treatments. This work deals with the simulations of different benchmark isothermal and thermal flow problems to validate the in-house LBM-Fortran codes based on both single-relaxation-time (SRT) and multiple-relaxation-time (MRT) lattice Boltzmann models. Elaborate comparisons of the present results with the published results obtained through conventional numerical techniques exhibit a close match. The comparison of SRT and MRT results indicate that both models provide comparable solutions while dealing with laminar flow regime specified by Rayleigh number of the order of 10^6. However, MRT-LB model offers better stability than SRT-LB model in solving flow with high Ra. Thus the

present LBM codes for computing isothermal and thermal flows stand validated. This suggests that the codes, with some additional features, when used to compute flows associated with newer physics, are likely to produce results that can be trusted with some certainty while making additional problem-specific validation tests.

Chapter 3

Effect of Prandtl Numbers on Convection in a Hot Block Inserted Square Cavity by MRT-LBM

3.1 Introduction

The natural- and mixed- convection problem in cavities are widely investigated in literature as they provide simplification to different practical applications such as processing of materials, air-conditioning, electronics cooling, heat exchangers, nuclear reactor insulation, food processing, solar energy collector etc. [Incropera and DeWitt, 2002; Cengel, 2003]. The insertion of an object in a cavity-like configuration has practical relevance in applications like cooling of hot ingots, metal casting, electronic component cooling, heat exchanger, crystal growth, solar and nuclear reactors, etc.

The literature survey reveals that a number of numerical works on natural- and mixed convection in the cavity with solid cylinders or blocks inside are made using conventional numerical techniques such as finite volume method and finite difference method. However, the studies concerning the LBM, particularly MRT-LBM, are minimal. Besides, most of these works are carried out using fluids with Prandtl numbers of the order of unity while taking into account the first law of thermodynamics based heat transfer analysis. The current flow problem considers three different *Pr* fluids of practical importance, namely, Sodium-potassium alloy (NaK) (*Pr* = 0.025), water (*Pr* = 5.83) and ethyl glycol (*Pr* = 151). As per the authors' best knowledge, no investigation is made to study the effect of different *Pr* fluids and blockage ratio (*BR*) on heat transfer and entropy generation for this type of flow condition.

3.2 Mathematical formulation of the problem

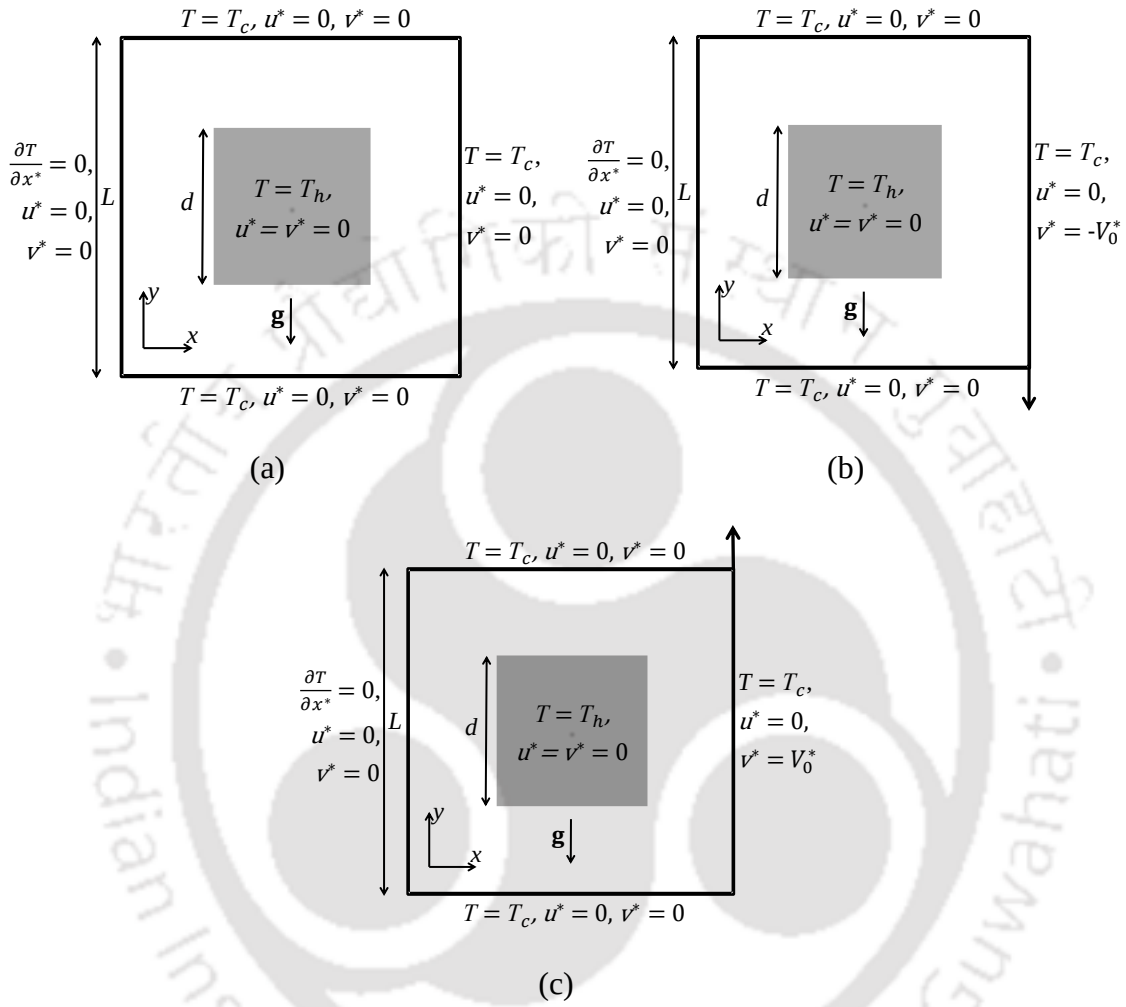

Fig. 3.1. Schematic diagram of the flow configuration for (a) natural convection (Case 1), (b) mixed convection with downward moving right wall (Case 2) and (c) mixed convection with upward moving right wall (Case 3).

The flow configuration and boundary conditions for the present study of convective heat transfer in a closed square cavity of unit length is shown in Figs. 3.1(a)-(c). In the schematic diagram of the present flow configuration for natural and mixed convection, the boundary conditions are presented in dimensional form. The left wall of the cavity is adiabatic while the other three walls are maintained at an isothermal cold temperature, as shown in Fig. 3.1. The isothermally heated square block induces natural convection. The case where all four cavity walls are stationary (Fig. 3.1(a)) is referred to as Case 1 in the

present work. Two different cases of single-sided lid-driven mixed convection are considered depending on the direction of the lid movement. The case where the cold right wall moves downward with a constant speed V_0^* (Fig. 3.1(b)) is referred to as Case 2 and the one where the cold right wall moves upward with a constant speed V_0^* (Fig. 3.1(c)) is referred to as Case 3**.**

Three different *Pr* fluids, namely, NaK (*Pr* = 0.025), water (*Pr* = 5.83) and ethyl glycol (*Pr* = 151) are considered in the present work. Their thermo-physical properties are mentioned in Table 3.1 [Incropera and DeWitt, 2002].

Table 3.1 Properties of NaK, water and ethyl glycol at *T* = 300 K.

Property (unit)	NaK (*Pr* = 0.025)	Water (*Pr* = 5.83)	Ethyl glycol (*Pr* = 151)
C_P (J kg^{-1} K^{-1})	955.0	4179.0	2415.0
ρ (kg m^{-3})	857.0	997.1	1114.4
k (W m^{-1} K^{-1})	22.29	0.613	0.252

For the convenience of numerical calculation and analysis, the non-dimensional forms of the variables are expressed as follows:

$$x = \frac{x^*}{L}; \qquad y = \frac{y^*}{L}; \qquad u = \frac{u^*}{V_0^*}; \qquad v = \frac{v^*}{V_0^*}; \qquad \theta = \frac{T - T_c}{T_h - T_c} \tag{3.1}$$

The three boundary conditions in non-dimensional form are given as follows:

$$u = 0; \quad v = 0; \quad \theta = 0 \quad \text{at } y = 0 \text{ and } 1$$

$$u = 0; \quad v = 0; \quad \frac{\partial \theta}{\partial y} = 0 \quad \text{at } x = 0 \tag{3.2}$$

$$u = 0; \quad v = 0 \text{ or } 1 \text{ or } -1; \quad \theta = 0 \quad \text{at } x = 1$$

The boundary condition at the block surface is set as

$$u = 0; \quad v = 0; \quad \theta = 1 \tag{3.3}$$

3.3 Grid independence study

Table 3.2 provides the grid-independence test for natural convection at $Gr = 10^4$ and $BR = 0.25$ for three different Pr. A grid-independence test for mixed convection (Case 3) is carried out by taking $Gr = 10^4$, $Ri = 1.0$ and $BR = 0.5$ at three different Pr, as shown in Table 3.3. The results obtained for four different grid sizes of 241×241, 321×321, 401×401 and 481×481 are compared based on the average Nusselt number over the surface of the block $\overline{Nu_h}$ and average total entropy generation throughout the cavity $\overline{S_{tot}}$. The extrapolated values of $\overline{Nu_h}$ and $\overline{S_{tot}}$ are also provided based on Richardson extrapolation method [Roache, 1997]. The maximum magnitudes of percentage error of $\overline{Nu_h}$ and $\overline{S_{tot}}$ between grid size of 401×401 and extrapolated values are found to be 4.4% and 3.1% for mixed convection at $Pr = 0.025$ and natural convection at $Pr = 151$ respectively. Whereas, for other cases, the magnitudes of the maximum percentage error lie well within 1.4%. So, for this current investigation, the grid size of 401×401 is found to be suitable for all computations while considering time-wise efficiency.

Table 3.2 Grid independence study for each of the three Pr for natural convection.

Pr (at BR = 0.25)	variables	Grid sizes				
		241×241	321×321	401×401	481×481	Extrapolated*
0.025	$\overline{Nu_h}$	4.221	4.253	4.275	4.291	4.314
	$\overline{S_{tot}}$	4.287	4.299	4.307	4.312	4.320
5.83	$\overline{Nu_h}$	6.455	6.539	6.593	6.610	6.661
	$\overline{S_{tot}}$	18.483	18.825	19.033	19.103	19.309
151	$\overline{Nu_h}$	13.68	13.893	14.029	14.084	14.218
	$\overline{S_{tot}}$	727.97	755.73	773.01	780.77	798.37

*Values calculated using Richardson extrapolation

To check time efficiency, the CPU time with grid size is compared by assuming the solutions for current simulations to be converged if their relative L_1 - error norms for dimensionless temperature is less than equal to 10^{-8}. A computer with Intel processor (Intel(R) Core(TM) i7-7700 CPU @ 3.60GH) and 16 GB memory (RAM) is utilised. For

the sake of brevity, the CPU times for different grid sizes are considered only for mixed convection (Case 3) at Pr = 5.83, Ri = 1.0 and BR = 0.5. It is found that the CPU time is about 20 minutes (nearly 0.115 million iterations) for grid size 241×241, about 36 minutes (nearly 0.148 million iterations) for grid size 321×321, about 79 minutes (nearly 0.181 million iterations) for grid size 401×401 and about 2 hours (nearly 0.213 million iterations) for grid size 481×481 to reach the steady state. Besides, the number of iterations or CPU time varies with Pr, Ra and Ri, and they are found to be more at higher Pr and Ra and lower Ri irrespective of grid size.

Table 3.3 Grid independence study for three Pr for mixed convection (Case 3).

Pr (at Ri = 1 and BR = 0.5)	variables	Grid sizes				
		241×241	321×321	401×401	481×481	Extrapolated*
0.025	$\overline{Nu_h}$	14.546	15.489	16.306	16.436	17.066
	$\overline{S_{tot}}$	8.514	8.570	8.612	8.625	8.662
5.83	$\overline{Nu_h}$	14.648	14.688	14.716	14.730	14.757
	$\overline{S_{tot}}$	14.754	14.806	14.837	14.851	14.883
151	$\overline{Nu_h}$	17.679	17.700	17.709	17.713	17.724
	$\overline{S_{tot}}$	22.942	23.205	23.399	23.455	23.626

*Values calculated using Richardson extrapolation

3.4 Code validation

Table 3.4 Comparison of present results with previously published works for low Prandtl number.

Ra (at Pr = 0.01)	$\overline{Nu}$				
	Present work	Ref. 1	Error magnitude (%) with Ref. 1	Ref. 2	Error magnitude (%) with Ref. 2
10^4	1.9238	-	-	1.9584	1.76
5×10^4	2.7824	2.8143	1.13	2.7991	0.59
10^5	3.1809	3.2344	1.65	-	-

*Ref. 1 (Mohamad and Viskanta [1991]); Ref. 2 (Kosec and Sarler [2013])

The current code is already validated with the published works of Iwatsu et al. [1993] and Khanafer and Chamkha [1999] for *Pr* of the order of unity and with Iwatsu et al. [1993] for *Pr* = 0.01 during mixed convection in a square cavity (mentioned in Chapter 2 in section 2.8.3). Further, the competency of current MRT-LBM code is checked with other published results of Mohamad and Viskanta [1991] and Kosec and Sarler [2013] during natural convection in a square cavity for low Prandtl number (*Pr* = 0.01). Table 3.4 presents the results in terms of the average Nusselt numbers along the hot wall of the cavity with their corresponding percentage error $\left(\left|\frac{\overline{Nu}_{ref}-\overline{Nu}_{present}}{\overline{Nu}_{ref}}\right| \times 100\%\right)$. The maximum magnitudes of percentage error of present results in comparison to the results of Mohamad and Viskanta [1991] and Kosec and Sarler [2013] are found to be 1.65% and 1.76% respectively.

Further, the code is validated with the published results of Islam et al. [2012] during mixed convection in a square cavity with an isothermally heated square block inside with a blockage ratio of 0.25 as depicted by Table 3.5. Moreover, the comparison of error magnitude between present MRT-LBM with SRT-LBM shows that MRT-LBM has higher accuracy than SRT-LBM. The minimum and maximum percentage error magnitude of average Nusselt numbers over the block surface $\left(\left|\frac{(\overline{Nu_h})_{ref}-(\overline{Nu_h})_{present}}{(\overline{Nu_h})_{ref}}\right| \times 100\%\right)$ for MRT-LBM are found to be 1.0% and 2.13% respectively compared to 1.2% and 2.34% for SRT-LBM. These deviations of present results from the published numerical results are acceptable due to the use of different numerical methodology with their associated errors and choice of convergence criteria for steady problems.

Table 3.5 Comparison of results in terms of $\overline{Nu_h}$ over the solid block at *BR* = 0.25.

Ri (at *Pr* = 0.71)	$\overline{Nu_h}$				
	Islam et al. [2012]	SRT-LBM	Error magnitude (%)	Present work (MRT-LBM)	Error magnitude (%)
0.1	5.6118	5.526	1.52	5.538	1.31
1.0	5.6935	5.560	2.34	5.572	2.13
10.0	7.9083	7.811	1.2	7.829	1.0

3.5 Results and discussions

Natural convection and two different cases of mixed convection based on velocity boundary conditions are considered in the present work. A comprehensive analysis is made to study the effect of Prandtl numbers (Pr = 0.025, 5.83 and 151) and Richardson numbers ($0.1 \leq Ri \leq 10$) on fluid flow and heat transfer for each case at fixed $Gr = 10^4$.

3.5.1 Natural convection

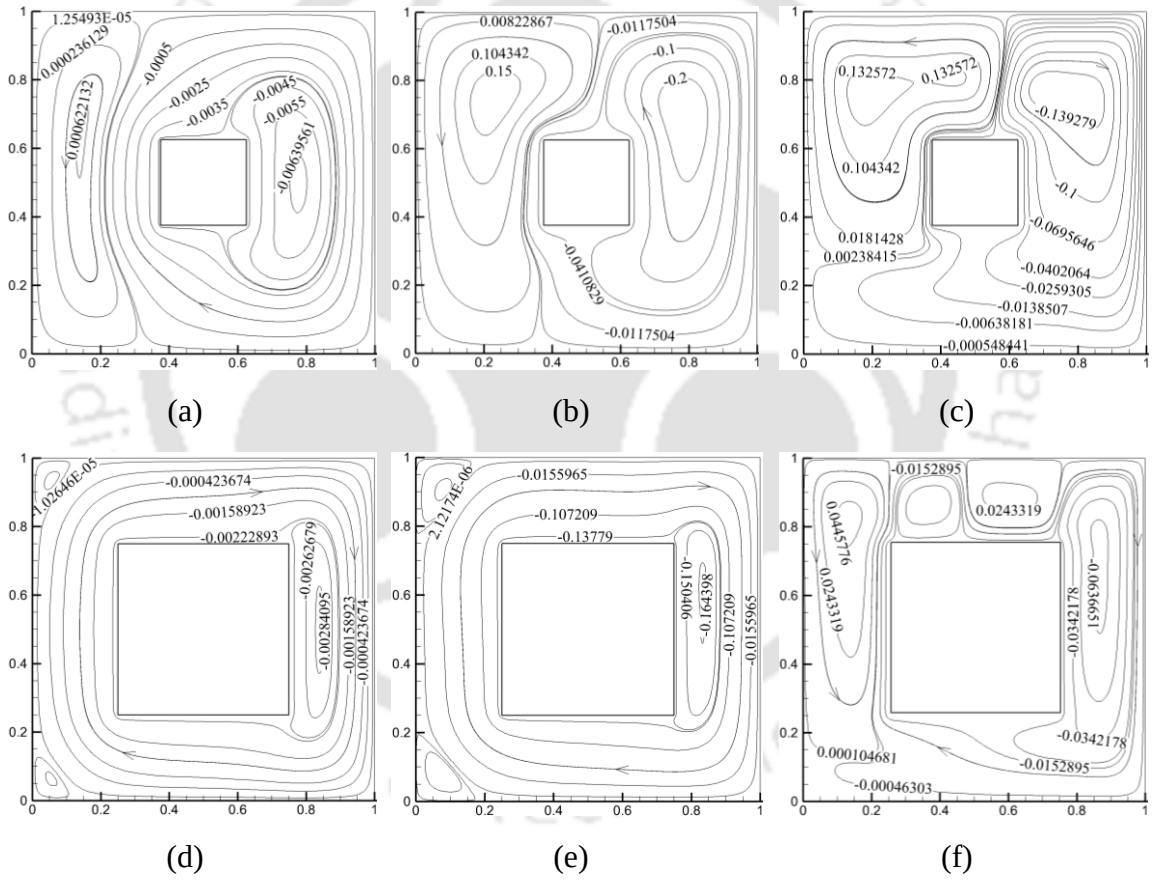

Fig. 3.2. Streamline Contours (ψ) for blockage ratio of 0.25 (a, b and c) and 0.5 (d, e and f) at Pr = 0.025 (left panel), Pr = 5.83 (middle panel) and Pr = 151 (right panel) for natural convection (Case 1) at fixed $Gr = 10^4$.

Figs. 3.2 and 3.3 show streamlines (ψ) and isotherms (θ) respectively for two blockage ratio of 0.25 and 0.5 at Pr = 0.025, 5.83 and 151 during natural convection at

fixed $Gr = 10^4$. Two primary vortices are observed astride the heated block for a blockage ratio of 0.25 regardless of the Prandtl number values. Figs. 3.2(a)-(c) show a clockwise primary vortex with major circulation at the right side and an anti-clockwise primary vortex with minor circulation at the left side of the heated block. This difference in flow strength is observed due to the presence of the cold right wall. The positive and negative values of ψ represent the anti-clockwise and clockwise circulation respectively. It is noticed that the convective flow increases with an increase in *Pr*, which leads to the displacement of the centres of primary vortices along the vertically upward direction. The right vortex grows in strength with increase in *Pr* and covers the bottom left region of the cavity at higher *Pr* = 151 due to the intensification of cooling effect from both the right and bottom wall. Figs. 3.2(d) and (e) depict that for blockage ratio of 0.5 at *Pr* = 0.025 and 5.83, a clockwise primary vortex is generated as the fluid heated up by the block is cooled down along the right vertical wall of the cavity. The flow behaves more like a channel flow than cavity flow due to restricted passage with an increase in blockage ratio. At *Pr* = 151, the ascending flow at the left side of block enhances and gets divided into three convective cells due to the presence of strong convection current. The maximum values of stream functions $|\psi_{max}|$ are obtained as 0.0065, 0.238 and 0.152 at *BR* = 0.25 for *Pr* = 0.025, 5.83 and 151 respectively. However, these values are found to be slightly lower at *BR* = 0.5 with 0.0028, 0.165 and 0.066 for *Pr* = 0.025, 5.83 and 151 respectively.

The isotherms plots in Fig. 3.3 depict that the temperature profiles are more clustered towards the surface of the heated block. This behaviour indicates that thin boundary layers are developed near the block. At higher *Pr*, the formation of boundary layers is observed near the cold top and right walls of the cavity due to the presence of strong buoyancy force. At lower *Pr* = 0.025, the heat transfer is mostly influenced by conduction, which is characterised by parallel isotherms between the block and isothermal walls of the cavity. At higher *Pr* = 5.83 and 151, a thermal plume is observed over the heated block due to enhancement of convection currents. The isotherms are more densely packed with an increase in blockage ratio, which results in a higher temperature gradient.

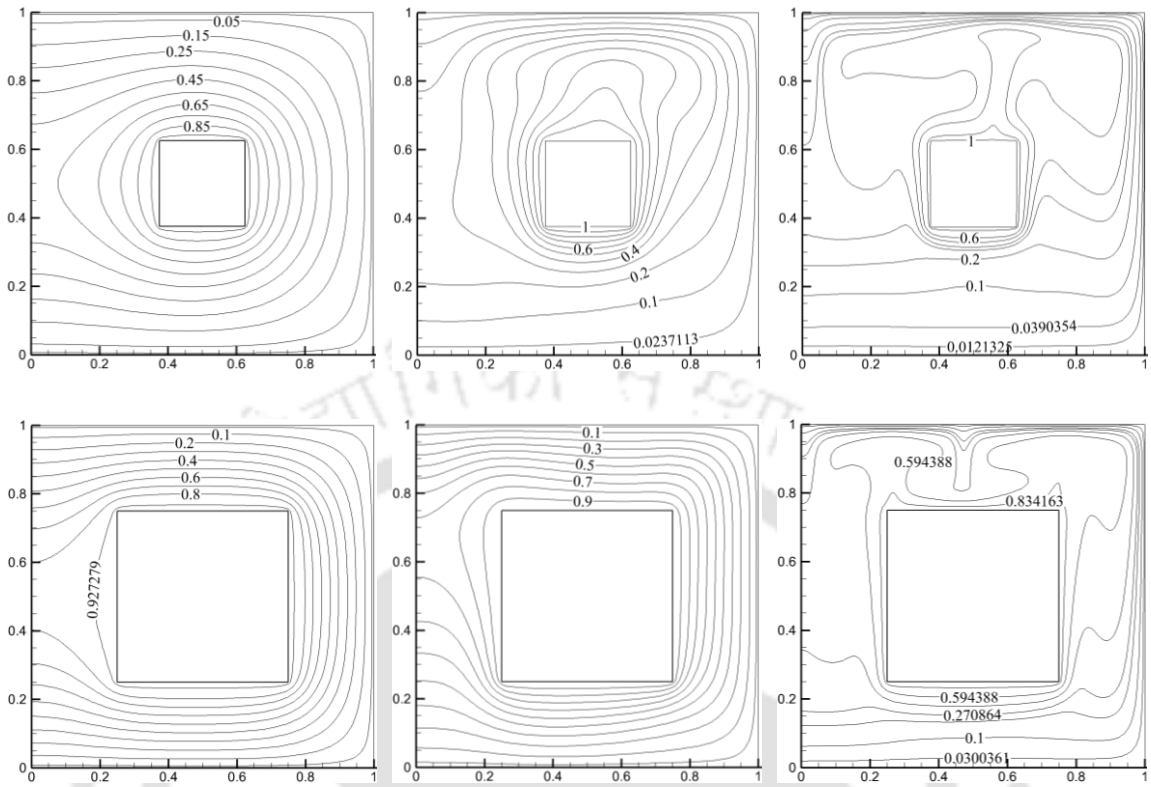

Fig. 3.3. Isotherms (θ) for blockage ratio of 0.25 (top panel) and 0.5 (bottom panel) at Pr = 0.025 (left panel), Pr = 5.83 (middle panel) and Pr = 151 (right panel) for natural convection (Case 1) at fixed $Gr = 10^4$.

Figs. 3.4(a)-(b) display the effect of Pr on the flow and thermal field in terms of non-dimensional vertical velocity v and temperature θ along the horizontal mid-plane of the cavity for two blockage ratios of 0.25 and 0.5. There is a reduction of the magnitude of the velocity with a decrease in Pr for both blockage ratios. For very low Pr = 0.025, the velocity approaches zero as the flow is dominated by the conduction mode of heat transfer, which is characterised by the smooth temperature profiles in Fig. 3.4(b). The magnitude of velocity is found to be maximum near the block and right cold wall due to the presence of strong buoyant force which increases the convective effect. The thinning of thermal boundary layers at these regions occur with an increase in Pr as indicated by steeper temperature gradients. The magnitude of velocity and temperature have a higher value at BR = 0.5 compared to BR = 0.25 due to the presence of higher temperature gradients resulting from the proximity of block surface to the cavity wall.

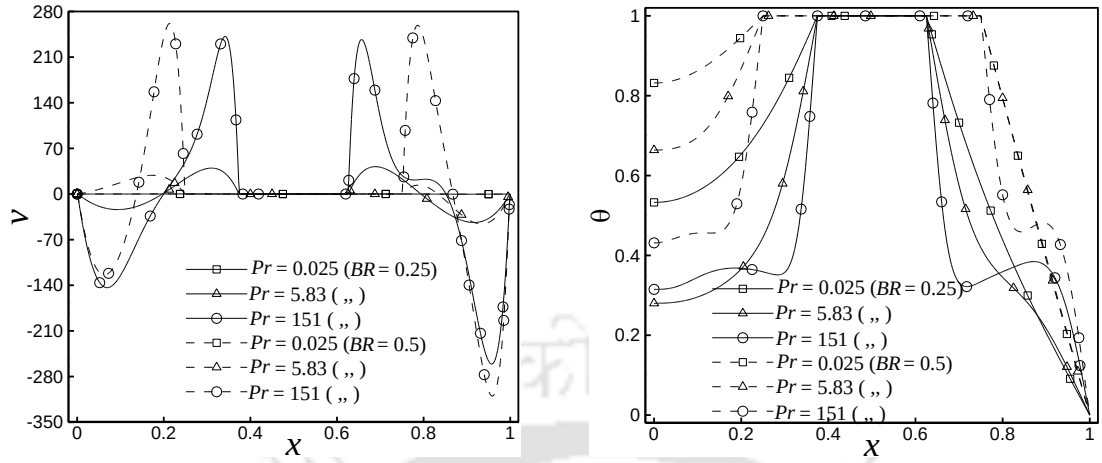

(a) (b)

Fig. 3.4. Comparison of dimensionless (a) vertical velocity *v* and (b) temperature θ in the horizontal mid-plane of the cavity for *Pr* = 0.025, 5.83 and 151 at blockage ratios of 0.25 and 0.5.

Figs. 3.5 and 3.6 depict the contours of local entropy generation due to heat transfer (S_θ) and fluid friction (S_ψ) respectively for *Pr* = 0.025, 5.83 and 151 during natural convection at blockage ratios of 0.25 and 0.5. It is observed that the local entropy generation due to heat transfer is mainly concentrated at the vicinity of the isothermal block, specifically at the four corners of the block. This is attributed to the high-temperature gradient at these regions resulting from the clustering of isotherms. The active zones of S_θ is also found at the middle of the top wall for higher *Pr* = 5.83 and 151 due to the development of thermal plume over the block. The intensities of both S_θ and S_ψ increase with Prandtl number due to the enhancement of buoyancy induced convection. The entropy generation due to fluid friction mostly occurs near the vertical sides of the square block and the vertical walls of the cavity due to the presence of high-velocity gradient caused by clustering of streamlines. At very low *Pr* = 0.025, the effect of S_ψ is found to be insignificant. It is evident from Figs. 3.5 and 3.6 that the magnitudes both S_θ and S_ψ increase with an increase in blockage ratio.

Table 3.6 presents the effect of heat transfer rates in terms of average Nusselt number over the block surface ($\overline{Nu_h}$) during natural convection. It is observed that $\overline{Nu_h}$

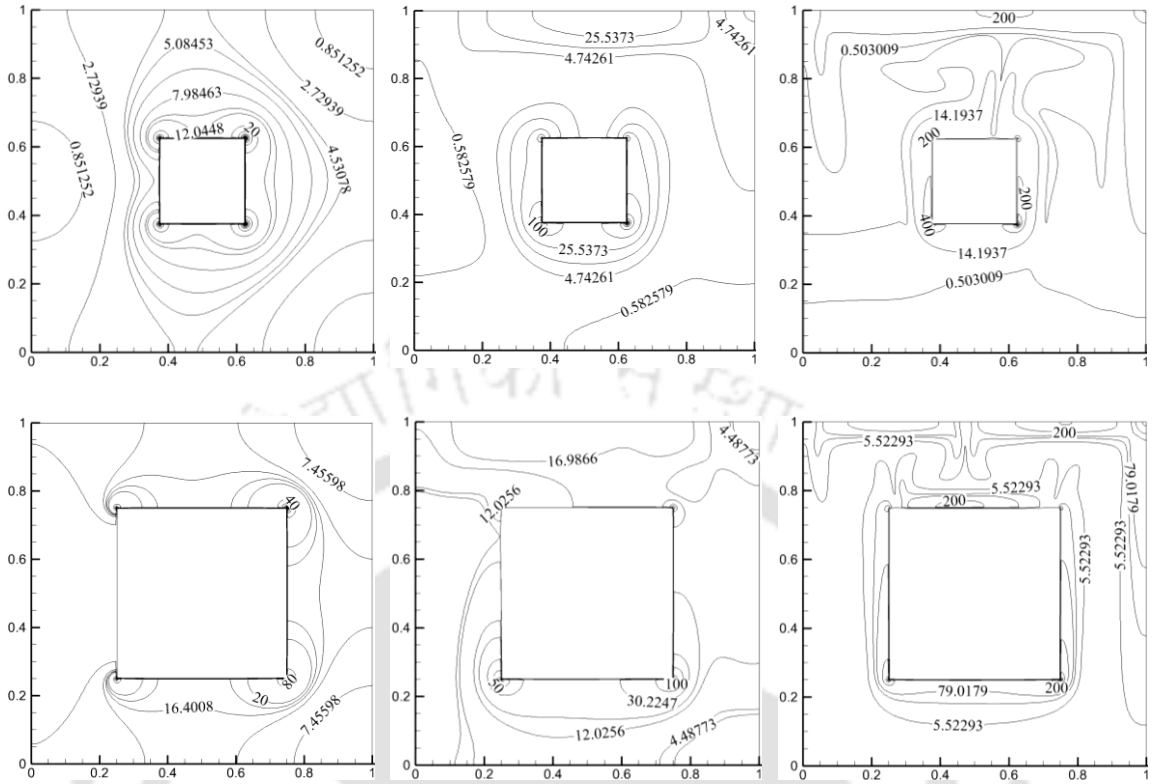

Fig. 3.5. Contours of local entropy generation due to heat transfer (S_θ) for blockage ratio of 0.25 (top panel) and 0.5 (bottom panel) at *Pr* = 0.025 (left panel), *Pr* = 5.83 (middle panel) and *Pr* = 151 (right panel) for natural convection (Case 1) at fixed $Gr = 10^4$.

increases with an increase in *Pr* and also with blockage ratio due to thinning of thermal boundary layers near the block. It is obtained from Table 3.6 that the variation of average entropy generation due to heat transfer ($\overline{S_\theta}$) over the whole cavity is comparable to the variation of average Nusselt number over the block surface ($\overline{Nu_h}$). This is attributed to the fact that both the quantities are functions of temperature gradients and S_θ is mostly concentrated near the block. Drastic augmentation of average total entropy generation due to viscous effect ($\overline{S_\psi}$) throughout the cavity is observed with increase in *Pr* due to increase in velocity gradient with buoyant force. However, it is interesting to observe that the value of $\overline{S_\psi}$ is lower for *BR* = 0.5 compared to *BR* = 0.25 at *Pr* = 0.025 and 5.83 due to the existence of lower velocity gradients. This is accredited to superior conduction effect at lower Rayleigh number ($Gr \times Pr$) which dominates the buoyancy induced convection. The

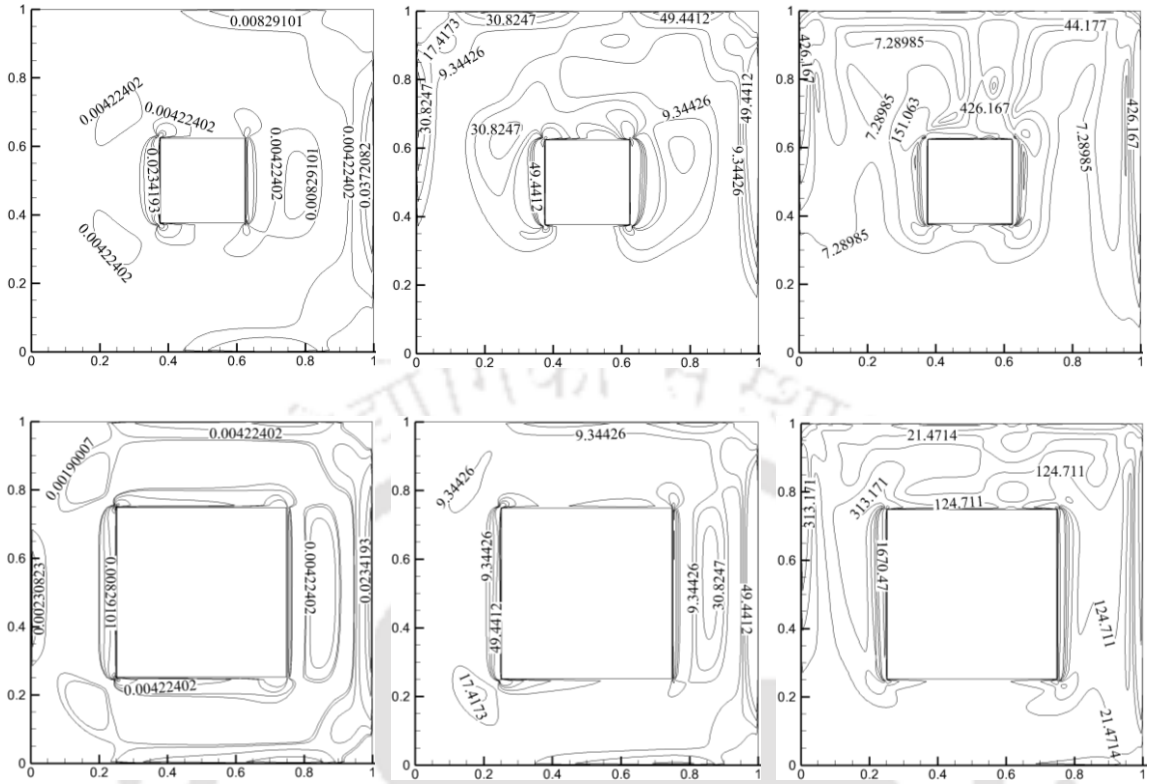

Fig. 3.6. Contours of local entropy generation due to viscous effect (S_ψ) for blockage ratio of 0.25 (top panel) and 0.5 (bottom panel) at Pr = 0.025 (left panel), Pr = 5.83 (middle panel) and Pr = 151 (right panel) for natural convection (Case 1).

entropy generation is mainly dominated by the heat transfer irreversibility at lower Pr = 0.025 as described by very high average Bejan number ($\overline{Be}$) over the whole cavity. However, $\overline{Be}$ decreases with an increase in Pr as the entropy generation due to viscous effect increases drastically.

Table 3.6 Results of natural convection in terms of $\overline{Nu_h}$, $\overline{S_\theta}$, $\overline{S_\psi}$ and $\overline{Be}$.

variables	Pr = 0.025		Pr = 5.83		Pr = 151	
	BR = 0.25	BR = 0.5	BR = 0.25	BR = 0.5	BR = 0.25	BR = 0.5
$\overline{Nu_h}$	4.275	8.518	6.593	9.109	14.029	22.354
$\overline{S_\theta}$	4.307	8.471	6.698	9.133	14.116	22.511
$\overline{S_\psi}$	0.0037	0.0021	12.335	8.586	75.88	103.50
$\overline{Be}$	0.9991	0.9997	0.3519	0.5154	0.1589	0.1786

3.5.2 Mixed convection

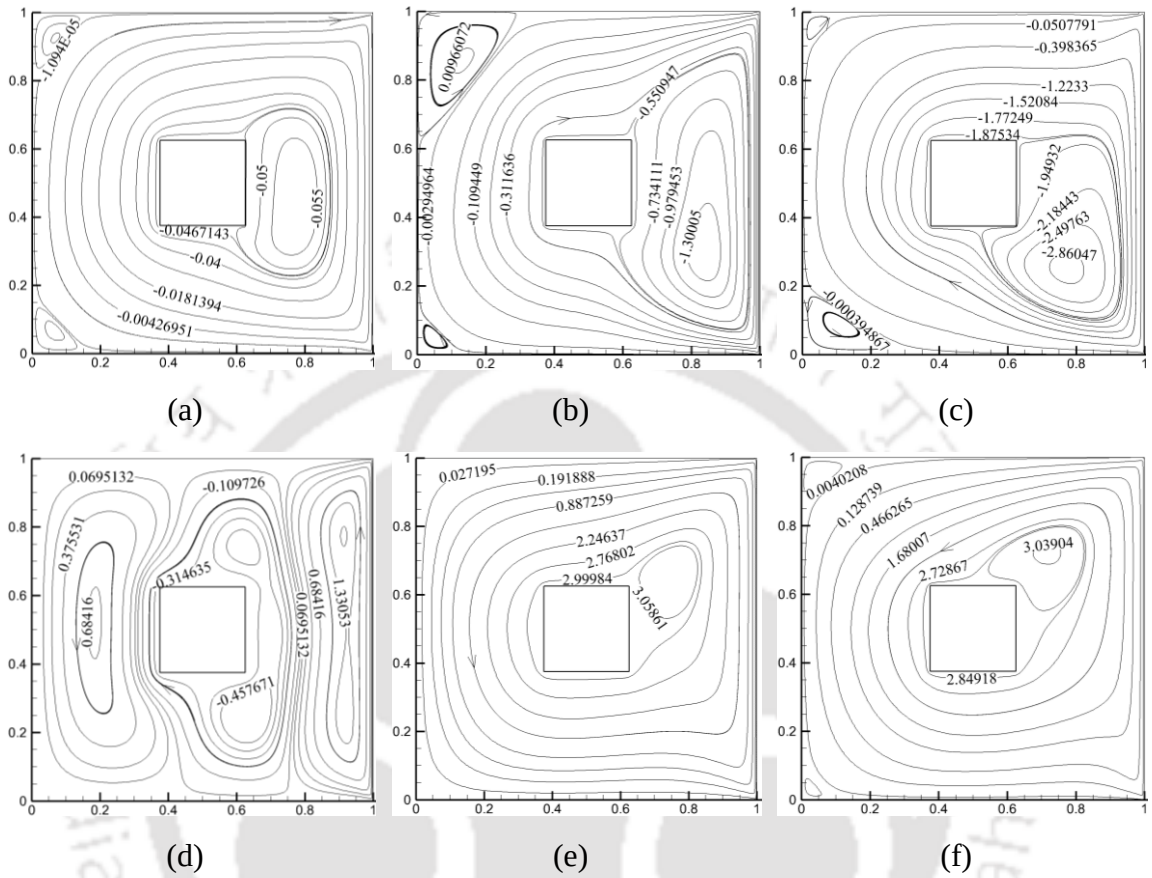

Fig. 3.7. Streamline contours (ψ) of Case 2 (a, b and c) and Case 3 (d, e and f) for Pr = 0.025 at Ri = 10 (left panel), Pr = 5.83 at Ri = 1 (middle panel) and Pr = 151 at Ri = 0.1 (right panel).

To show the effect of lid motion on the fluid and thermal behaviour, we simulate the two cases of mixed convection flow with Pr = 0.025 at Ri = 10, Pr = 5.83 at Ri = 1.0 and Pr = 151 at Ri = 0.1 respectively at just one blockage ratio of 0.25 for the sake of brevity (Figs. 3.7 and 3.8). A clockwise primary vortex is generated due to the downward movement of the cold right wall for Case 2 for all Pr. For Case 3 at Pr = 5.83 and 151, an anti-clockwise primary vortex is developed due to the upward movement of the cold right wall of the cavity. For these conditions, the centre of primary vortex lies in the right side of the blockage surface where the maximum value of stream function lies. However, for Case 3 at higher Ri = 10 for Pr = 0.025 (Fig. 3.7(d)), a clockwise vortex is formed around

the block, and two anti-clockwise vortices are formed near the vertical walls. This is attributed to the increase in the buoyancy induced convection with *Ri* around the vertical mid-plane of the cavity due to the heated block, which overcomes the effect of forced convection. It is evident from streamlines plots that for Case 2, the primary vortex becomes stronger with an increase in *Pr* irrespective of *Ri*. The magnitude of maximum stream function $|\psi_{max}|$ for Case 2 are found to be 0.06, 1.388 and 2.943 for *Pr* = 0.025 at *Ri* = 10, *Pr* = 5.83 at *Ri* = 1.0 and *Pr* = 151 at *Ri* = 0.1 respectively. The values of $|\psi_{max}|$ are found to be higher for Case 3 compared to Case 2 with values 1.532, 3.199 and 3.060 for *Pr* = 0.025 at *Ri* = 10, *Pr* = 5.83 at *Ri* = 1.0 and *Pr* = 151 at *Ri* = 0.1 respectively.

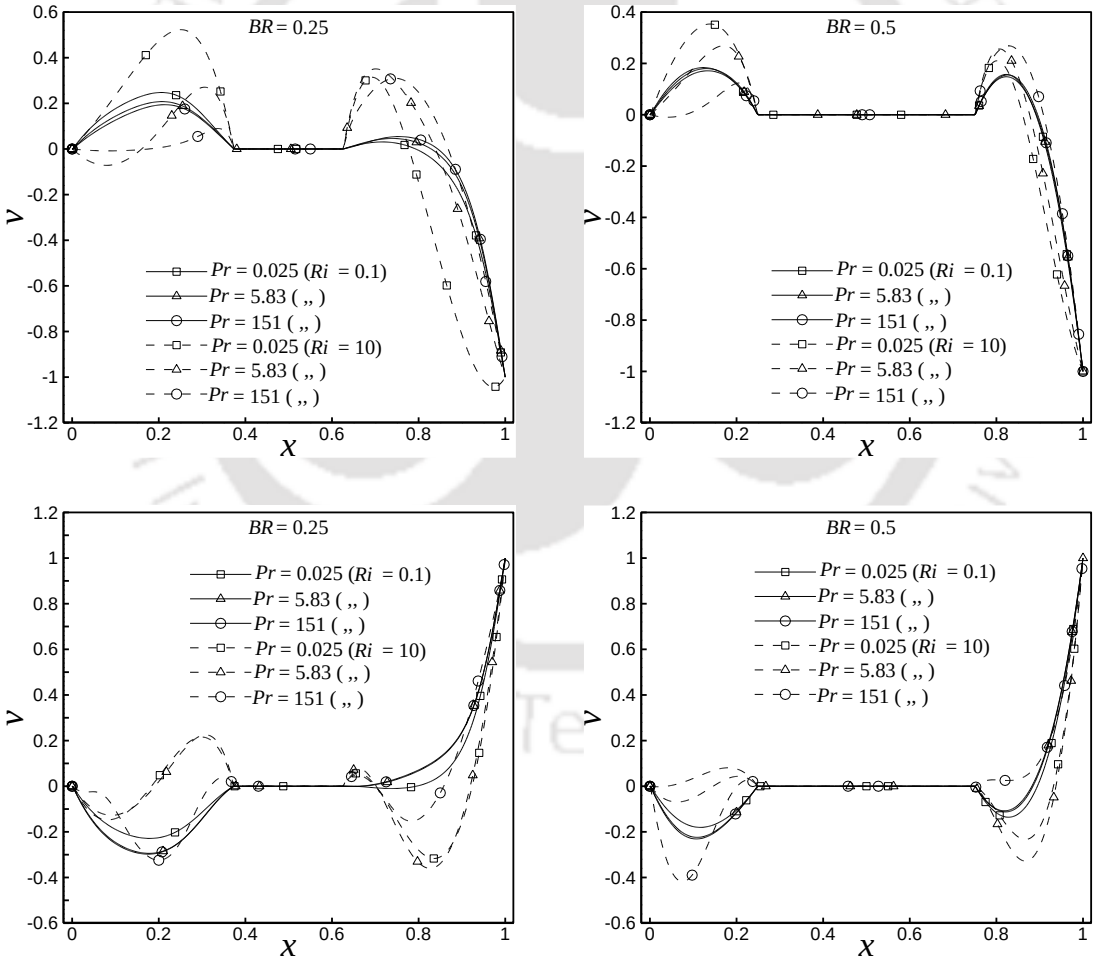

Fig. 3.8. Comparison of vertical velocity *v* for Case 2 (top panel) and Case 3 (bottom panel) at *Pr* = 0.025, 5.83 and 151 with *Ri* = 0.1 and 10 for *BR* = 0.25 and 0.5.

Fig. 3.8 depicts that at low *Ri* = 0.1, the change in velocity with *Pr* is minimal, and it is more evident for *BR* = 0.5. It is noticed that the overall magnitude of velocity increases with *Ri* due to clustering of streamlines resulting from enhanced convection effect. It is interesting to observe that at higher *Ri* = 10, the overall velocity decreases with an increase in *Pr*, which is in contrast to the case of natural convection. This is accredited to the dominating forced convection resulted from the movement of the lid.

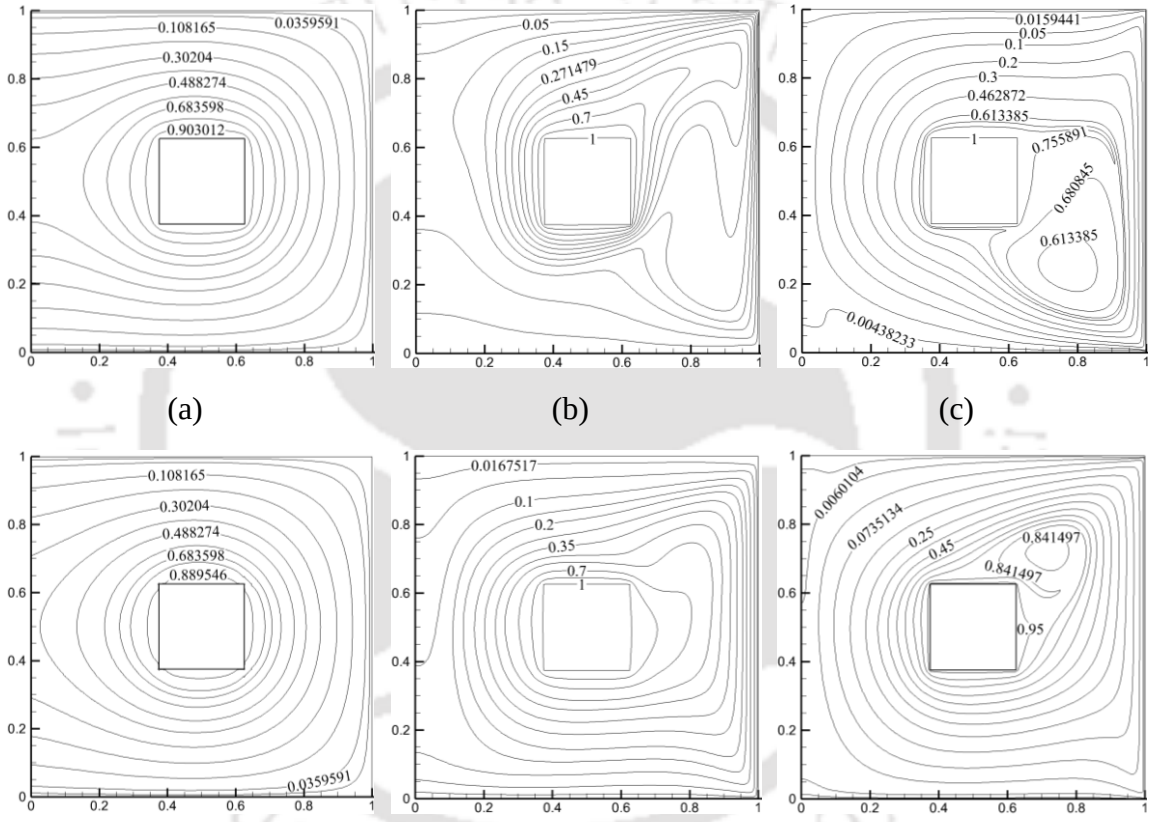

Fig. 3.9. Isotherms (θ) for Case 2 (a, b and c) and Case 3 (d, e and f) for *Pr* = 0.025 at *Ri* = 10 (left panel), *Pr* = 5.83 at *Ri* = 1 (middle panel) and *Pr* = 151 at *Ri* = 0.1 (right panel).

Fig. 3.9 show that the patterns of isotherm are in concordance with the streamline patterns at *Pr* = 5.83 and 151 for both cases of mixed convection. It is evident from Figs. 3.9(b) and (c) that the effect of thermal plume becomes weaker with decreases in *Ri* for Case 2 as forced convection due to downward moving wall dominates the natural convection. However, for Case 3 the thermal plume becomes more prominent at *Pr* = 151

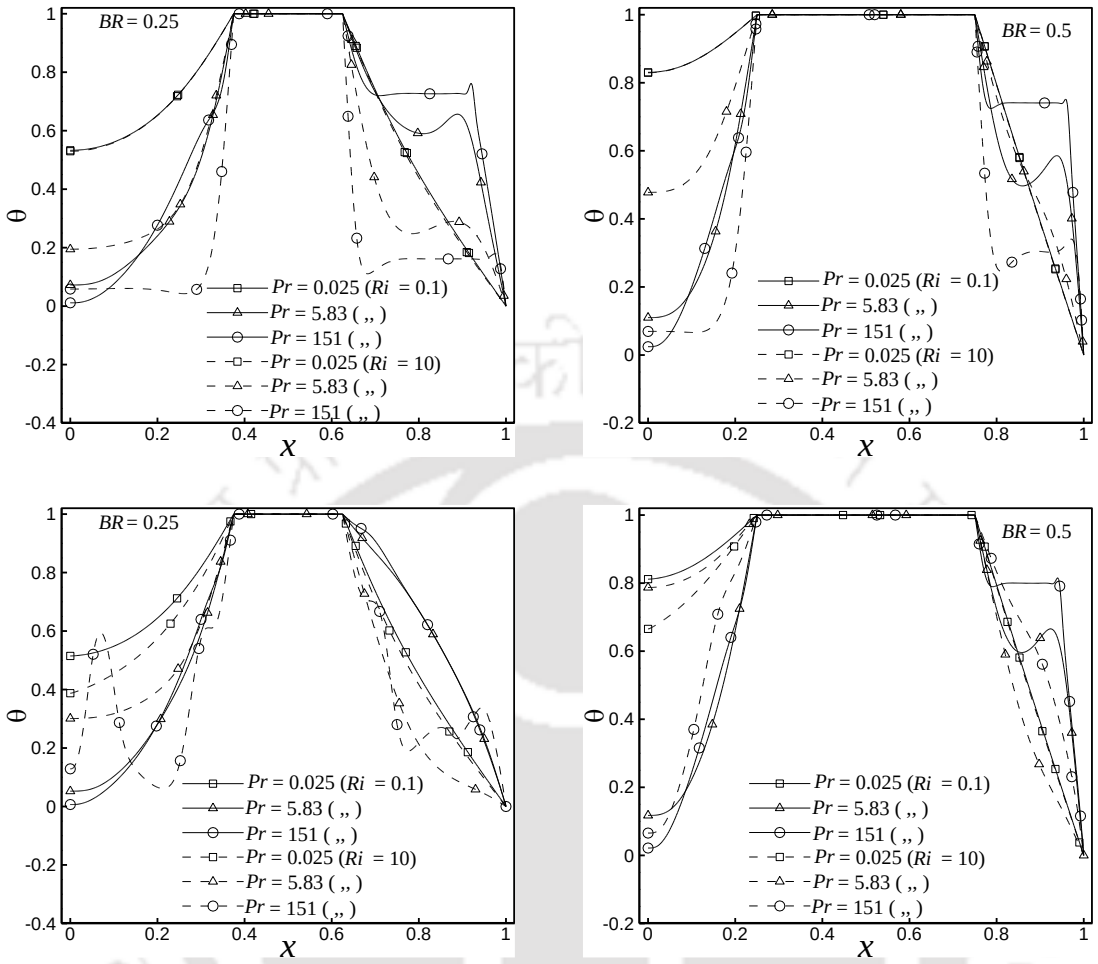

Fig. 3.10. Comparison of temperature θ for Case 2 (top panel) and Case 3 (bottom panel) at Pr = 0.025, 5.83 and 151 with Ri = 0.1 and 10 for BR = 0.25 and 0.5.

and Ri = 0.1 compared to Pr = 5.83 and Ri = 1, which is resulted from the upward movement of the right wall. There is no generation of the thermal plume at lower Pr as the conduction effect prevails even at higher Ri = 10. The isotherms pattern for mixed convection is comparable to natural convection at lower Pr = 0.025 due to the conduction dominated heat transfer which is characterised by a linear temperature profile, as shown in Fig. 3.10. At higher Pr = 5.83 and 151, the flow is mainly dominated by convection for Case 2 irrespective of studied values of Ri and BR. However, the conduction heat transfer prevails at lower Ri = 0.1 and BR = 0.25 for Case 3. The thermal boundary layer is found to be steeper with an increase in BR, and it is more relevant at higher Pr = 151. The thermal

boundary layer is more distinct near the block surface and the cold right lid for *Ri* = 1 and 10 respectively.

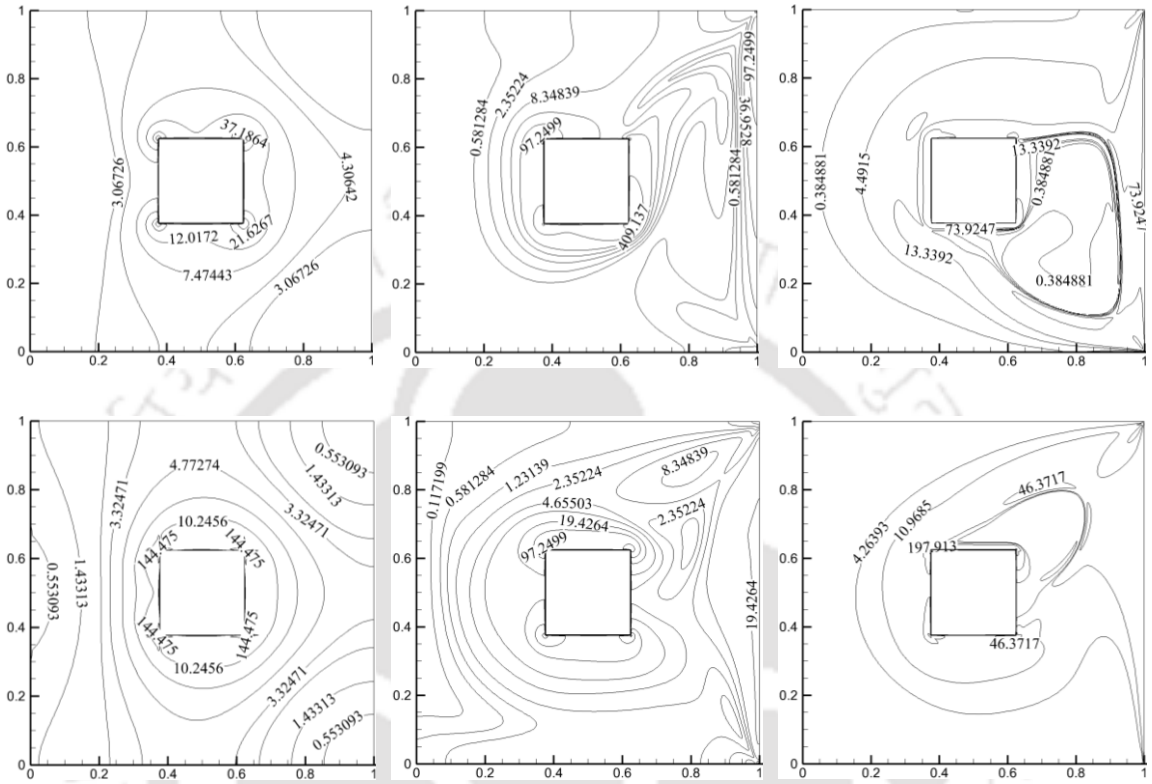

Fig. 3.11. Local entropy generation due to heat transfer (S_θ) for Case 2 (top panel) and Case 3 (bottom panel) for *Pr* = 0.025 at *Ri* = 10 (left panel), *Pr* = 5.83 at *Ri* = 1 (middle panel) and *Pr* = 151 at *Ri* = 0.1 (right panel).

Figs. 3.11 and 3.12 depict the effect of lid motion on the local entropy generation due to heat transfer (S_θ) and fluid friction (S_ψ) for *Pr* = 0.025 at *Ri* = 10, *Pr* = 5.83 at *Ri* = 1.0 and *Pr* = 151 at *Ri* = 0.1 for the two cases of mixed convection at blockage ratio of 0.25. It is observed that at lower *Pr* = 0.025 irrespective of *Ri*, the pattern of S_θ in mixed convection has some similarity with S_θ in natural convection which is more relevant to Case 2 as the conduction heat transfer dominates the flow phenomenon at lower *Pr*. The entropy generation due to heat transfer is mostly concentrated near the block surface at all *Pr* for both cases of mixed convection. However, the active zones of S_θ are found near the right cold lid at *Pr* = 5.83 and 151 which results in an overall increase in of S_θ due to the

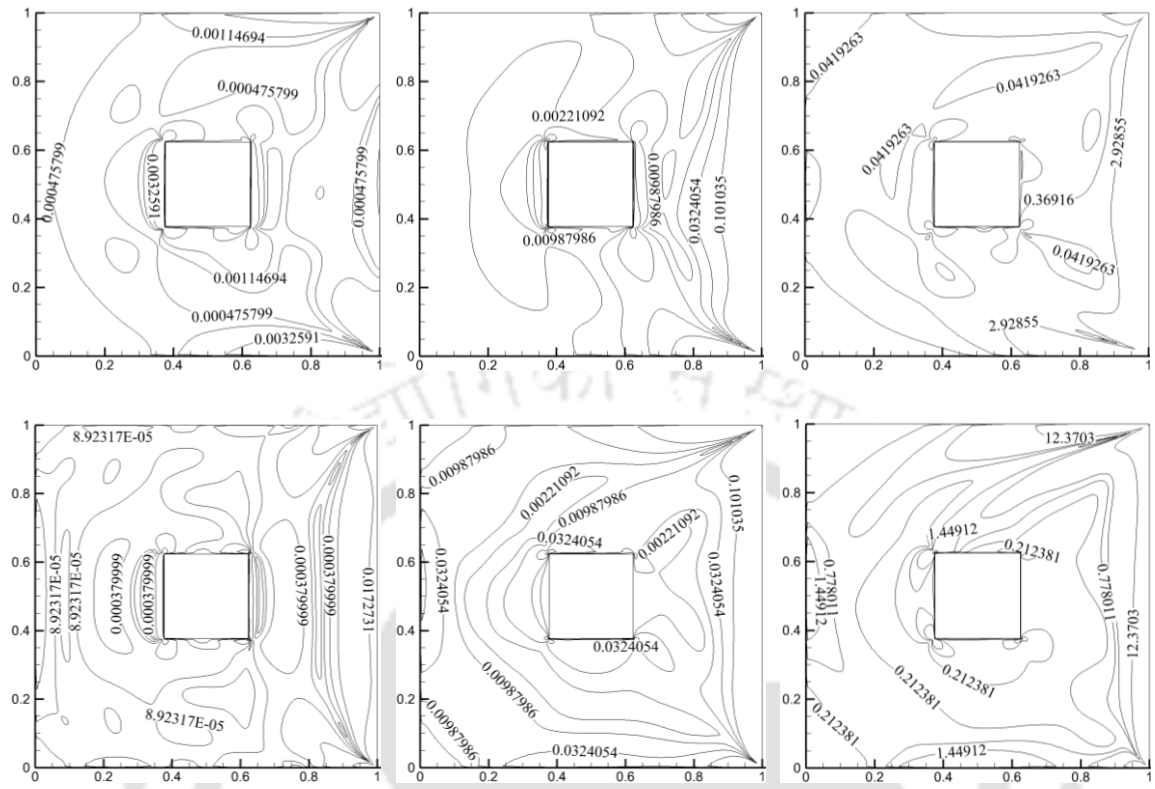

Fig. 3.12. Local entropy generation viscous effect (S_ψ) for Case 2 (top panel) and Case 3 (bottom panel) for Pr = 0.025 at Ri = 10 (left panel), Pr = 5.83 at Ri = 1 (middle panel) and Pr = 151 at Ri = 0.1 (right panel).

presence of strong convective force. The magnitude of maximum S_θ, $|S_{\theta,max}|$ for Case 2 are found to be 154.67, 1737.1 and 2102.4 for Pr = 0.025 at Ri = 10, Pr = 5.83 at Ri = 1.0 and Pr = 151 at Ri = 0.1 respectively. The value of $|S_{\theta,max}|$ = 2567.9 for Pr = 0.025 at Ri = 10 is drastically higher for Case 3 compared to Case 2. This is ascribed to the increase in the buoyancy induced convection with Ri around the mid-vertical plane of the cavity due to the heated block, which overcomes the effect of forced convection, as mentioned earlier. The values of $|S_{\theta,max}|$ are found to be 353.86 and 671.9 for Pr = 5.83 at Ri = 1.0 and Pr = 151 at Ri = 0.1 respectively. Fig. 3.12 reveal that the intensity of S_ψ increases with Prandtl number due to the enhancement of buoyancy induced convection irrespective of values of Ri. It is interesting to observe that the magnitudes of maximum S_ψ, $|S_{\psi,max}|$ are found to be similar for both cases of mixed convection with values 56.54, 3013.35 and 135056 for

Pr = 0.025 at *Ri* = 10, *Pr* = 5.83 at *Ri* = 1.0, and *Pr* = 151 at *Ri* = 0.1 respectively. This is attributed to the fact that the occurrence of S_ψ mostly being restricted to the vicinity of the heated block surface which is unaffected by the lid motion of cavity. At very low *Pr* = 0.025, the effect of S_ψ is found to be insignificant even at higher *Ri* = 10.

3.5.3 Heat transfer rates

Figs. 3.13(a)-(c) show the average Nusselt number over the block surface ($\overline{Nu_h}$) with an increase in *Ri* for three different *Pr* and two blockage ratios. The variation of $\overline{Nu_h}$ with *Ri* is found to be insignificant for Case 2 at *Pr* = 0.025. However, the drastic change of $\overline{Nu_h}$ with an increase in *Ri* is observed for Case 3 as the buoyancy induced convection augments with *Ri* around the heated block, as mentioned earlier. It is obtained for Case 2 that $\overline{Nu_h}$ increases with *Pr* values due to the presence of higher convective heat transfer resulting from higher momentum diffusivity at high *Pr*. For both cases, the value of $\overline{Nu_h}$ is found to be higher for *BR* = 0.5 compared to *BR* = 0.25 due to the presence of higher temperature gradients astride the block resulting from isotherm clustering except Case 3 for *Pr* = 151 at *Ri* = 10. At *Pr* = 5.83 with *BR* = 0.5, the values of $\overline{Nu_h}$ decrease with *Ri* as the forced convection decreases where fluid velocity has a strong influence on temperature gradient across the block. However, this dependency is compromised at lower blockage ratio, which results in irregular flow behaviour. The flow is mainly dominated by buoyancy induced convection at *Pr* = 151. It is observed at *Pr* = 151 that the lid motion aids the buoyancy force which results in continuous augmentation of $\overline{Nu_h}$ with *Ri* for Case 2 at *BR* = 0.5 and Case 3 at *BR* = 0.25. For Case 2 at *BR* = 0.25, the value of $\overline{Nu_h}$ decreases after *Ri* = 1 as the aiding effect of lid motion is not prominent. However, for Case 3 at *BR* = 0.5, the cause for reduction of $\overline{Nu_h}$ is ascribed to the opposing lid motion, which forces the cold fluid to move upward. It is interesting to observe that the use of lid motion has a positive effect on the heat transfer rate while comparing the results with the natural convection case in terms of $\overline{Nu_h}$. This is more prominent for Case 2 of mixed convection at higher *Pr* = 5.83 and 151.

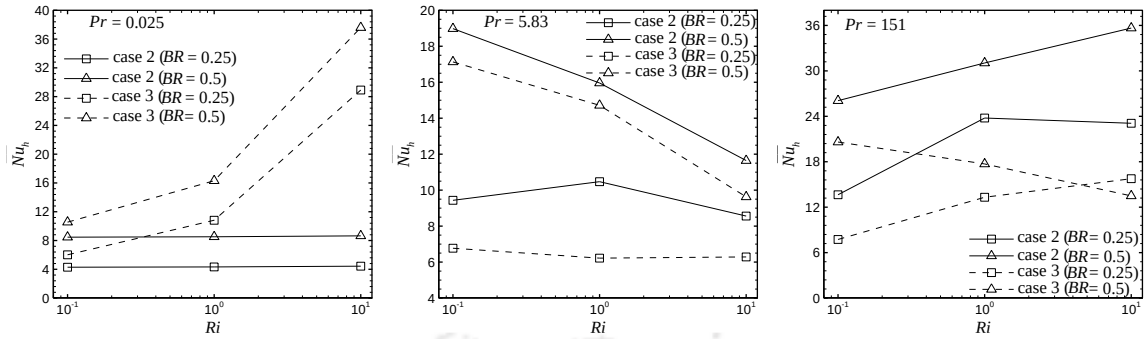

Fig. 3.13. Variations of $\overline{Nu_h}$ with *Ri* at *BR* = 0.25 and 0.5 for (a) *Pr* = 0.025, (b) *Pr* = 5.83 and (c) *Pr* = 151.0.

3.5.4 Entropy generation and Bejan numbers

It is interesting to find from Figs. 3.14(a)-(c) that the variation of average entropy generation due to heat transfer ($\overline{S_\theta}$) over the whole cavity with *Ri* follows the same pattern as $\overline{Nu_h}$ in Figs. 3.13(a)-(c) as both the quantities are functions of temperature gradients. Besides, the magnitudes of $\overline{S_\theta}$ is found to be comparable to the values of $\overline{Nu_h}$ with the exception of *Pr* = 0.025 for Case 3 which signifies that S_θ is mostly concentrated at the surface of the block. For Case 3 at *Pr* = 0.025, the values of $\overline{S_\theta}$ is less than $\overline{Nu_h}$ as S_θ is mostly confined to the four corners of the block due to conduction dominated heat flow. Figs. 3.14(d)-(f) depict that the average total entropy generation due to viscous effect ($\overline{S_\psi}$) throughout the cavity increases with the augmentation of *Pr* and *BR* as the fluid circulation becomes stronger due to enhanced convection. However, the augmentation of $\overline{S_\psi}$ with *Pr* is not significant in mixed convection compared to the case for natural convection. It is observed for both cases of mixed convection that $\overline{S_\psi}$ decreases with increase in *Ri* up to *Ri* = 1 due to the lid motion, which dampens the viscous effect. Further increment of *Ri* leads to a small change in $\overline{S_\psi}$ in Case 2. However, $\overline{S_\psi}$ increases after *Ri* = 1 for Case 3 at all studied values of *Pr* and *BR* except for *Pr* = 151 at *BR* = 0.25 as the friction increases due to opposing movement of lid and buoyancy force. Figs. 3.14(g)-(i) show that the heat transfer irreversibility mostly dominates the entropy generation at all *Pr* irrespective of *Ri*

values which is signified by high average Bejan number ($\overline{Be}$) over the whole cavity. $\overline{Be}$ marginally decreases with *Pr* up to *Pr* = 5.83 due to a slight increment of entropy generation due to friction. However, the value of $\overline{Be}$ is lower at *Pr* = 151 as S_ψ increases significantly along with S_θ sue to enhanced convection. The variation of $\overline{Be}$ with *Ri* has resemblance with a variation of $\overline{S_\theta}$ at *Pr* = 5.83 and 151.

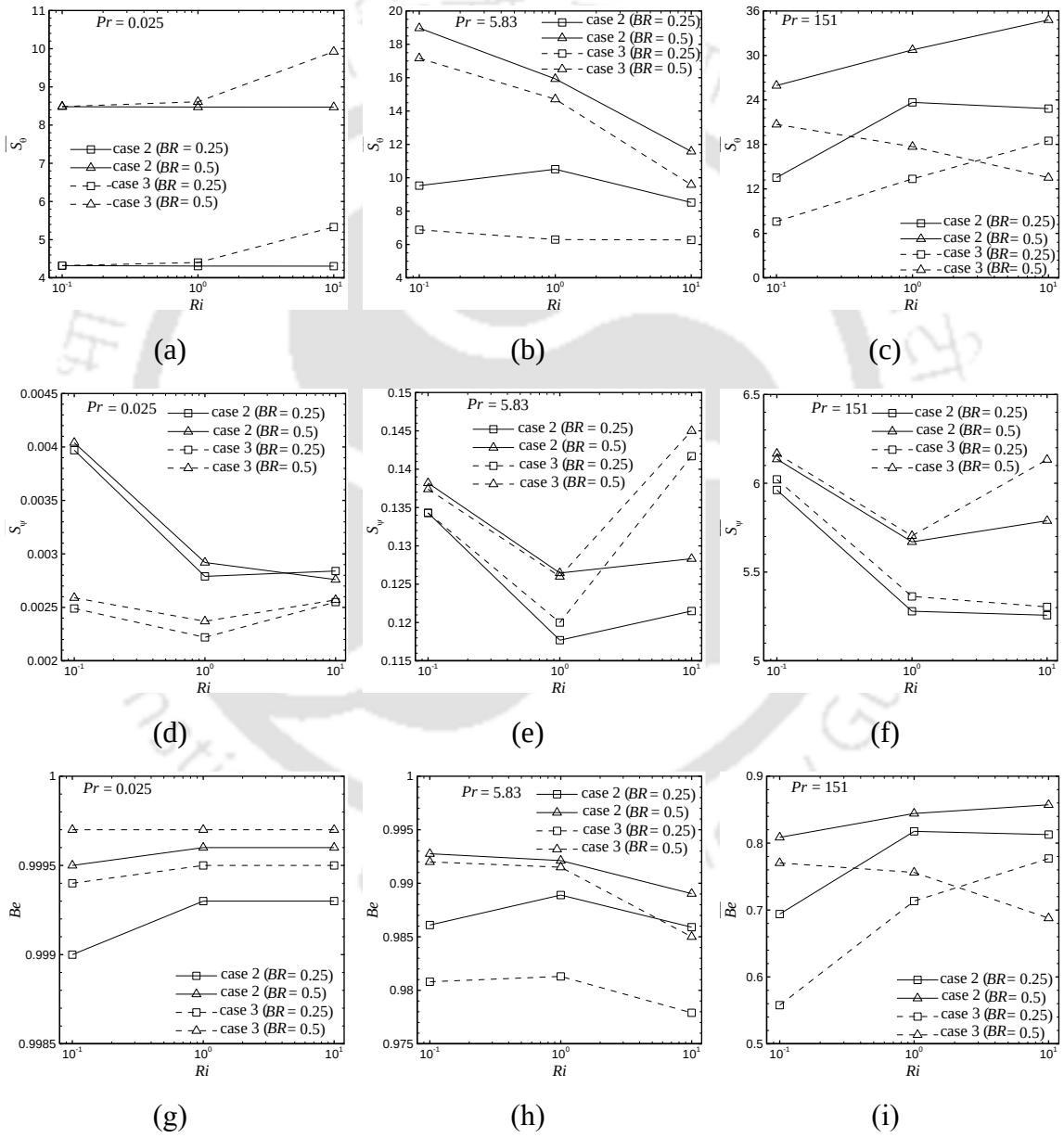

Fig. 3.14. Variations of $\overline{S_\theta}$ (a, b and c), $\overline{S_\psi}$ (d, e and f) and $\overline{Be}$ (g, h and i) with *Ri* for *Pr* = 0.025 (left panel), *Pr* = 5.83 (middle panel) and *Pr* = 151.0 (right panel).

3.6 Conclusions

The current work attempts to provide new insights on heat transfer rate and entropy generation for varying *Pr* from low (*Pr* = 0.025) to high values (*Pr* = 151) while placing a heated square block in a square cavity. Three different cases of boundary conditions are considered, which leads to natural and mixed convection in the cavity. A comprehensive analysis is carried out to understand the combined effects of these phenomena and the block size on the heat transfer rate and entropy generation. A multiple relaxation time based thermal lattice Boltzmann model is implemented to model the flow while carefully validating the present code with published results. Thus results for the current flow problems enjoy good credibility. The present mixed convection flow problem deals with three different Richardson numbers *Ri* = 0.1, 1 and 10 for a fixed Grashof number of *Gr* = 10^4. The results show that heat transfer rates in terms of average Nusselt number over the block surface ($\overline{Nu_h}$) increases with an increase in *Pr* for both natural and mixed convection as the convective heat transfer augments. The value of $\overline{Nu_h}$ is found to be higher at *BR* = 0.5 compared to *BR* = 0.25 for all three cases due to the occurrence of higher temperature gradients astride the block resulting from isotherm clustering except in Case 3 (upward moving right wall) for *Pr* = 151 at *Ri* = 10. The average entropy generation due to heat transfer ($\overline{S_\theta}$) follows the same pattern as $\overline{Nu_h}$ due to the very high concentration of S_θ near the block. The drastic augmentation of average total entropy generation due to viscous effect ($\overline{S_\psi}$) with an increase in *Pr* is more pertinent to natural convection than mixed convection. This eventually raises the total entropy generation throughout the cavity for natural convection. The mixed convection with a downward moving right wall Case 2 (downward moving right wall) provides a better heat transfer performance in comparison to the other two cases due to presence higher heat transfer rate and moderate total entropy generation.

Chapter 4

Flow through Porous Medium using SRT-LBM and MRT-LBM

4.1 Introduction

Natural and mixed convection in porous media has attracted much attention in heat transfer community as it has many engineering applications such as infiltration of molten metals, gas drying and transport process, crude oil extraction, geothermal operation, separation process, thermal reservoir, insulation of the building, pebble-bed nuclear reactor design, etc. The thermal boundary conditions such as uniform and non-uniform heating or cooling play a vital role in the overall process of convective heat transfer. The works related to natural convection in a cavity with non-uniform temperature variations at the walls have gained importance among the research community in recent years as it is observed in various practical applications like microwave heating of food materials, air conditioning in the room, cooling of electronic equipment, solar collector, etc.

Besides, the modelling technique for flow through porous media can be adopted to study flow through a bundle of internal objects. These bundle of internal bodies can be arranged in a specific manner to obtain desired thermal behaviour which is relevant in many applications such as heat exchanger, cooling hot ingots, solidification and nuclear power reactor etc. This phenomenon can be investigated by considering these internal objects as a porous structure with suitable porosity and permeability values conforming to the thermo-hydraulic characteristics of these complex geometries.

A perusal of literature suggests that several studies are undertaken to analyse heat transfer rate during natural and mixed convection in fluid-saturated porous media. However, studies concerning entropy generation analysis are limited. In this context, LBM studies are scarce. Therefore, the present work exploits thermal lattice Boltzmann method (TLBM) to analyse the entropy generation and heat transfer for two different porous flow

configurations, which are not addressed yet as per the authors' best knowledge. The objective of the first problem is to utilise SRT-TLBM to analyse the effect of four different thermal boundary conditions on entropy generation and heat transfer in a water-saturated porous cavity. The second problem deals with MRT-TLBM to investigate the influence of a hot permeable inner square block on entropy generation during mixed-convection in a water-filled inclined cavity.

4.2 Mathematical formulation of porous flow

The macroscopic governing equations for fluid flow and heat transfer through a porous medium are formulated by making assumptions that the local thermal equilibrium exists between both fluid phase and solid phase of the porous media. Both phases have constant properties except the density in the buoyancy force term, which is satisfied by the Boussinesq approximation. The governing equations for mass, momentum and energy are given below [Nithiarasu et al., 1997]

$$\nabla . \mathbf{u} = 0 \tag{4.1a}$$

$$\frac{\partial \mathbf{u}}{\partial t} + (\mathbf{u}.\nabla)\left(\frac{\mathbf{u}}{\varepsilon}\right) = -\frac{1}{\rho_f}\nabla(\varepsilon p) + \nu_e \nabla^2 \mathbf{u} + \mathbf{F} + \varepsilon \mathbf{G} \tag{4.1b}$$

$$\zeta \frac{\partial \theta}{\partial t} + \mathbf{u}.\nabla\theta = \nabla.(\alpha_e \nabla\theta) \tag{4.1c}$$

where **u**, p, and θ represent the volume-averaged fluid velocity vector, pressure and temperature respectively. The variables t, ν_e and α_e stand for a time, effective kinetic viscosity and thermal diffusivity respectively. The coefficient ζ $(= \varepsilon + (1-\varepsilon)\rho_s C_{ps}/\rho_f C_{pf})$ gives the heat capacity ratio between solid and fluid phases, where C_P is the specific heat at constant pressure. The porosity (ε) of the porous medium is defined as the ratio of void space to the total volume of the medium. For the current problem, thermal diffusivity of the solid matrix and fluid is considered to be identical, i.e., $\alpha_e = \alpha_f = \alpha_s$ and ζ is set equal to one. The body force **F** [Nithiarasu et al., 1997] due to the effect of the porous medium is given as follows:

$$\mathbf{F} = -\frac{\varepsilon\nu}{K}\mathbf{u} - \frac{\varepsilon F_\varepsilon}{\sqrt{K}}|\mathbf{u}|\mathbf{u} \tag{4.2}$$

The Darcy-Forchheimer relation is utilised in the current study to model momentum loss of flow through a porous medium due to inertia (linear Darcy term) and viscous effects (nonlinear Forchheimer term) as denoted by the first and second terms of the force equation (Eq. 4.2). The Forchheimer coefficient F_ε strongly depends on the geometry of the permeable membrane. Based on the Ergun's correlation [Ergun, 1952] for flow through packed columns, the geometric function (F_ε) of the porous medium is given by:

$$F_\varepsilon = \frac{1.75}{\sqrt{150\varepsilon^3}} \tag{4.3}$$

The porous medium is mainly characterised by its porosity ε and permeability K. Both are related to each other through the following relation [Ergun, 1952]:

$$K = \frac{\varepsilon^3 d_s^2}{150(1-\varepsilon)^2} \tag{4.4}$$

The above relation suggests different combinations of porosity and permeability based on the average particle diameter d_s of spherical beads and d_s is taken as 1 cm for 1 m characteristic length L of the flow domain. The permeability term is normalised by using non-dimensional parameter known as Darcy number (Da) through a relation $K = DaL^2$. The external force term $\mathbf{G}$ takes into account the gravity force only and is denoted as:

$$\mathbf{G} = \rho\mathbf{g}\beta(\theta - \theta_m) \tag{4.5}$$

where ρ is the fluid density at the reference temperature θ_m.

4.2.1 Methodology of SRT-LBM for convection heat transfer in porous media

The first problem of current work adopts Guo and Zhao's [2005] generalised thermal lattice Boltzmann model to simulate the flow through the porous medium at the representative elementary volume (REV) scale. This model modifies the equilibrium distribution function (EDF) and the force term by including the porosity term. The force

term takes into account the linear and nonlinear drag forces of the porous media based on Brinkman–Forchheimer extended Darcy model. To model the heat transfer phenomenon, SRT-based double-distribution-function (DDF) approach [Guo and Zhao, 2005] is adopted with slight modifications to incorporate the effect of the porous medium. The evolution equation of density-distribution function for generalised LBM is given as [Peng et al., 2003]:

$$f_i(\mathbf{r}+\mathbf{e}_i\Delta t, t+\Delta t) = f_i(\mathbf{r},t) + \frac{1}{\tau_v}\left(f_i^{eq}(\mathbf{r},t) - f_i(\mathbf{r},t)\right) + S_i \tag{4.6}$$

The equilibrium distribution function f_i^{eq} is modified to incorporate porosity of the porous medium as follows:

$$f_i^{eq} = \rho w_i \left\{1.0 + \frac{\mathbf{e}_i.\mathbf{u}}{C_s^2} + \frac{(\mathbf{e}_i.\mathbf{u})^2}{2\varepsilon {C_s}^4} - \frac{\mathbf{u}^2}{2\varepsilon C_s^2}\right\} \tag{4.7}$$

The force term (S_i) is calculated using Guo et al.'s force model as below [Guo et al., 2002c]:

$$S_i = w_i\left\{1 - \frac{1}{2\tau_v}\right\}\left\{\frac{\mathbf{e}_i - \mathbf{u}}{C_s^2} + \frac{\mathbf{e}_i(\mathbf{e}_i.\mathbf{u})}{\varepsilon C_s^4}\right\}.(\mathbf{F} + \varepsilon\mathbf{G}) \tag{4.8}$$

For temperature distribution function the governing discretised lattice Boltzmann equation is given as:

$$g_i(\mathbf{r}+\mathbf{e}_i\Delta t, t+\Delta t) = g_i(\mathbf{r},t) + \frac{1}{\tau_\theta}\left(\, g_i^{eq}(\mathbf{r},t) - g_i(\mathbf{r},t)\right) \tag{4.9}$$

The equilibrium distribution function g_i^{eq} is given as:

$$g_i^{eq} = w_i\theta\left\{1.0 + \frac{\mathbf{e}_i.\mathbf{u}}{2C_s^2}\right\} \tag{4.10}$$

4.2.2 Methodology of MRT- LBM for convection heat transfer in porous media

The second problem of current work uses Liu et al.'s [2014] MRT-based thermal lattice Boltzmann model to simulate the flow through the porous medium at the representative elementary volume (REV) scale. The key point of the present method is to

choose the appropriate equilibrium moment and discrete force term in the moment space. Thus, this model introduces porosity into the equilibrium moments and force terms in the moment space. Two lattice structures D2Q9 and D2Q5 are used to calculate density distribution function (f_i) and temperature distribution function (g_i) respectively. The evolution equation for MRT-LBM model for flow field with source term can be given as follows [Liu et al., 2014]

$$f_i(\mathbf{r}+\mathbf{e}_i\Delta t, t+\Delta t) - f_i(\mathbf{r},t) = -\mathrm{M}^{-1}\mathrm{R}\{\mathbf{m}(\mathbf{r},t)-\mathbf{m}^{eq}(\mathbf{r},t)\} + \mathrm{M}^{-1}\left(\mathrm{I}-\frac{\mathrm{R}}{2}\right)\mathbf{S} \tag{4.11}$$

The equilibrium moments $\mathbf{m}^{eq}$ in vector form is given by,

$$\mathbf{m}^{eq} = \left\{\rho\left(1,-2+\frac{3\mathbf{u}^2}{\varepsilon},1-\frac{3\mathbf{u}^2}{\varepsilon},u_x,-u_x,u_y,-u_y,\frac{u_x^2-u_y^2}{\varepsilon},\frac{u_xu_y}{\varepsilon}\right)\right\}^{\mathrm{T}} \tag{4.12}$$

The total force term **S** is given by a column vector as follows:

$$\mathbf{S} = \left\{\rho\left(0,\frac{6\mathbf{u}.\mathbf{F}}{\varepsilon},-\frac{6\mathbf{u}.\mathbf{F}}{\varepsilon},F_x,-F_x,F_y,-F_y,\frac{2(u_xF_x-u_yF_y)}{\varepsilon},\frac{(u_xF_y+u_yF_x)}{\varepsilon}\right)\right\}^{\mathrm{T}} \tag{4.13}$$

where

$$F_x = \mathbf{F};\ F_y = \mathbf{F}+\varepsilon\mathbf{G} \tag{4.14}$$

In moment space, the diagonal relaxation matrix R is given as [Wang et al., 2013]

$$\mathrm{R} = \mathrm{diag}(1, r_e, r_\in, 1, r_q, 1, r_q, r_v, r_v) \tag{4.15}$$

The MRT-LB equation governs the temperature distribution function is given as [Liu et al., 2014]:

$$g_i(\mathbf{r}+\mathbf{e}_i\Delta t, t+\Delta t) - g_i(\mathbf{r},t) = -\mathrm{N}^{-1}\mathrm{C}\{\mathbf{n}(\mathbf{r},t)-\mathbf{n}^{eq}(\mathbf{r},t)\} \tag{4.16}$$

The diagonal relaxation matrix C is given by,

$$\mathrm{C} = \mathrm{diag}(1, c_\theta, c_\theta, c_e, c_v) \tag{4.17}$$

The equilibrium moments $\mathbf{n}^{eq}$ in vector form is given as [Wang et al., 2013]:

$$\mathbf{n}^{eq} = (\theta, \frac{u\theta}{\zeta}, \frac{v\theta}{\zeta}, a\theta, 0)^{\mathrm{T}} \tag{4.18}$$

The coefficient ζ gives the heat capacity ratio between solid porous media and fluid and this value is taken as 1 for simplicity in the present problem.

4.2.3 Determination of macroscopic variables

Fluid density ρ and velocity $\mathbf{u}$ are calculated by taking 0th and 1st moments of f_i respectively. However, for flow through a porous medium, the volume-averaged velocity $\mathbf{u}$ is modified by taking into account the force effect as follows [Guo and Zhao, 2005]:

$$\rho = \sum_{i=0}^{8} f_i \tag{4.19}$$

$$\rho\mathbf{u} = \sum_{i=0}^{8} f_i \, \mathbf{e}_i + \frac{\varepsilon \mathbf{F}}{2} \tag{4.20}$$

The equation (4.20) is a nonlinear one as the force term $\mathbf{F}$ contains velocity $\mathbf{u}$. However, the implicitness of velocity can be eliminated by making use of its quadratic form as:

$$\mathbf{u} = \frac{\mathbf{v}}{c_0 + \sqrt{c_0^2 + c_1 |\mathbf{v}|}} \tag{4.21}$$

where the auxiliary velocity $\mathbf{v}$ and two other parameters c_0 and c_1 are given as [Guo and Zhao, 2005]:

$$\rho\mathbf{v} = \sum_{i=0}^{8} f_i \, \mathbf{e}_i + \frac{\varepsilon \mathbf{G}}{2}; \quad c_0 = \frac{1}{2}\left(1 + \varepsilon \frac{\vartheta}{2K}\right); \quad c_1 = \varepsilon \frac{F_\varepsilon}{2\sqrt{K}} \tag{4.22}$$

It is noted that as $\varepsilon = 1$, the generalised lattice Boltzmann equation (GLBE) reduces to the standard LBE for flows in the absence of porous media. Besides, for $F_\varepsilon = 0$ in the GLBE, a simplified LBE for the Brinkman-extended Darcy model can be obtained.

The temperature (θ) is calculated as 0th moments of g_i [Guo and Zhao, 2005] which are given for SRT- and MRT- LBM respectively as:

$$\zeta\theta = \sum_{i=0}^{8} g_i \, ; \; \zeta\theta = \sum_{i=0}^{4} g_i \tag{4.23}$$

4.3 Formulation of the first problem: Natural convection in a porous cavity

The physical system considered for current problem consists of a closed fluid-saturated porous square cavity with side L. Four different configurations of heating condition are considered at the left vertical wall by applying uniform, sinusoidal and linear temperature distributions respectively. For all four cases, the right vertical wall is uniformly cooled while keeping the top and bottom walls thermally insulated, as shown in Fig. 4.1. At all four walls, a no-slip impermeable velocity boundary condition is used. In the schematic diagram of the present flow configuration (Fig. 4.1), the boundary conditions for four different cases are presented in a dimensional form.

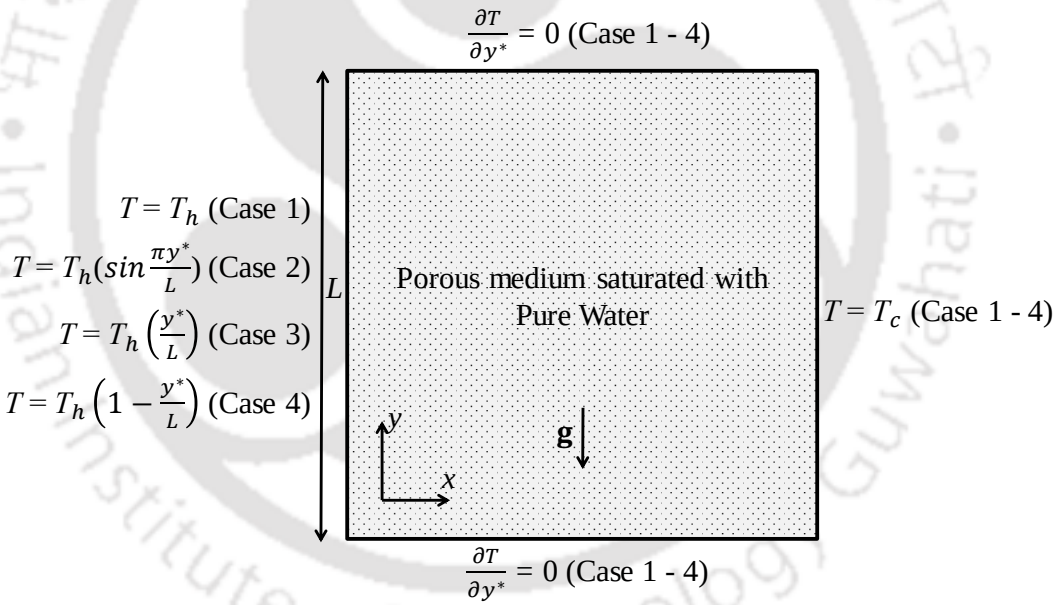

Fig. 4.1. Schematic diagram of the flow configuration with boundary conditions.

For the convenience of numerical calculation and analysis, the variables are expressed in the non-dimensional form as follows:

$$x = \frac{x^*}{L}; \qquad y = \frac{y^*}{L}; \qquad u = \frac{u^* L}{\alpha_f}; \qquad v = \frac{v^* L}{\alpha_f}; \qquad \theta = \frac{T - T_c}{T_h - T_c} \tag{4.24}$$

The boundary conditions in the non-dimensional form are given as follows:

$$u = 0, \quad v = 0, \quad \frac{\partial \theta}{\partial y} = 0 \qquad \text{at } y = 0, 1$$

$$u = 0, \quad v = 0, \quad \theta = 1 \text{ or } (\sin \pi y) \text{ or } (y) \text{ or } (1 - y) \qquad \text{at } x = 0 \tag{4.25}$$

$$u = 0, \quad v = 0, \quad \theta = 0 \qquad \text{at } x = 1$$

4.3.1 Grid independence study

A grid sensitivity analysis is carried out to obtain grid-independent solutions for each of three different values of *Ra* during steady-state natural convection in a water-filled square cavity. Table 4.1 gives the comparison of the grid sizes in terms of the dimensionless maximum vertical velocity (v_{max}) at the horizontal midline of the cavity, average Nu along the hot left wall of the cavity $\overline{Nu_{lh}}$, average total entropy generation due to heat transfer $\overline{S_\theta}$ and fluid friction $\overline{S_\psi}$ throughout the cavity for the configuration with a uniformly heated left wall. A grid size of 151×151 for $Ra = 10^3$, 201×201 for $Ra = 10^4$ and 301×301 for $Ra = 10^5$ are found to be suitable for all computations while taking note of the time-wise efficiency of the numerical simulations.

Table 4.1 Grid independence study

Variables	Grid sizes								
	$Ra = 10^3$			$Ra = 10^4$			$Ra = 10^5$		
	101 × 101	151 × 151	201 × 201	151 × 151	201 × 201	251 × 251	251 × 251	301 × 301	351 × 351
v_{max}	3.613	3.646	3.663	19.47	19.55	19.60	72.285	72.495	72.647
$\overline{Nu_{lh}}$	1.094	1.103	1.108	2.211	2.229	2.238	4.585	4.608	4.623
$\overline{S_\theta}$	1.083	1.096	1.103	2.196	2.218	2.230	4.568	4.595	4.614
$\overline{S_\psi}$	0.030	0.032	0.033	0.969	0.996	1.012	18.301	18.633	18.875

4.3.2 Code validation

The natural-convection in a differentially heated square porous cavity is investigated to check the validity of code in simulating porous thermal flow while

comparing the results with published works of Nithiarasu et al. [1997] and Nguyen et al. [2015]. Table 4.2 depicts a good concordance between the results in terms of the average Nusselt number ($\overline{Nu}$) along the hot wall of the cavity for different *Ra* and *Da* at *Pr* fixed at 1.0, which gives the confidence to carry out the present problem using the current LBM code.

Table 4.2 Comparison of present results for $\overline{Nu}$ with published results.

Ra	*Da*	$\overline{Nu}$								
		ε = 0.4			ε = 0.6			ε = 0.9		
		LBM	Ref. 1	Ref. 2	LBM	Ref. 1	Ref. 2	LBM	Ref. 1	Ref. 2
10^3	10^{-2}	0.998	1.01	1.005	1.003	1.015	1.010	1.008	1.023	1.015
10^4	10^{-2}	1.341	1.408	1.404	1.468	1.530	1.533	1.605	1.64	1.667
10^5	10^{-4}	1.056	1.067	1.062	1.059	1.071	1.065	1.061	1.072	1.066
10^6	10^{-4}	2.546	2.55	2.702	2.650	2.725	2.764	2.731	2.740	2.817

*Ref. 1 (Nithiarasu et al. [1997]); Ref. 2 (Nguyen et al. [2015])

4.3.3 Results and discussion

The effects of four different thermal boundary conditions on fluid flow and thermal behaviour during natural convection in a closed square porous cavity filled with pure water are discussed. The numerical simulations are carried for a range of Rayleigh number *Ra* discretely varying from 10^3 to 10^5 and Darcy number *Da* from 10^{-6} to 10^{-1} while keeping fixed porosity at 0.5. For current simulations, the value of irreversibility factor χ in entropy generation is fixed at 10^{-2} which was considered by earlier researchers for flow through a porous medium during natural convection [Baytas, 2000; Basak et al., 2012]. The detailed comparative studies are made among them to find out the efficient heating strategy. The numbers of plots are presented to show the effect of *Da* and *Ra* on the average Nu along the left hot wall ($\overline{Nu}_{lh}$) and for the whole domain ($\overline{Nu}$) of the cavity, average total entropy generation due to heat transfer irreversibility ($\overline{S_\theta}$) and fluid friction irreversibility ($\overline{S_\psi}$), average Bejan number ($\overline{Be}$), thermal mixing (θ_{cup}) and degrees of temperature uniformity ($RMSD_{\theta_{cup}}$).

4.3.3.1 Streamlines, isotherms and contours of entropy generation

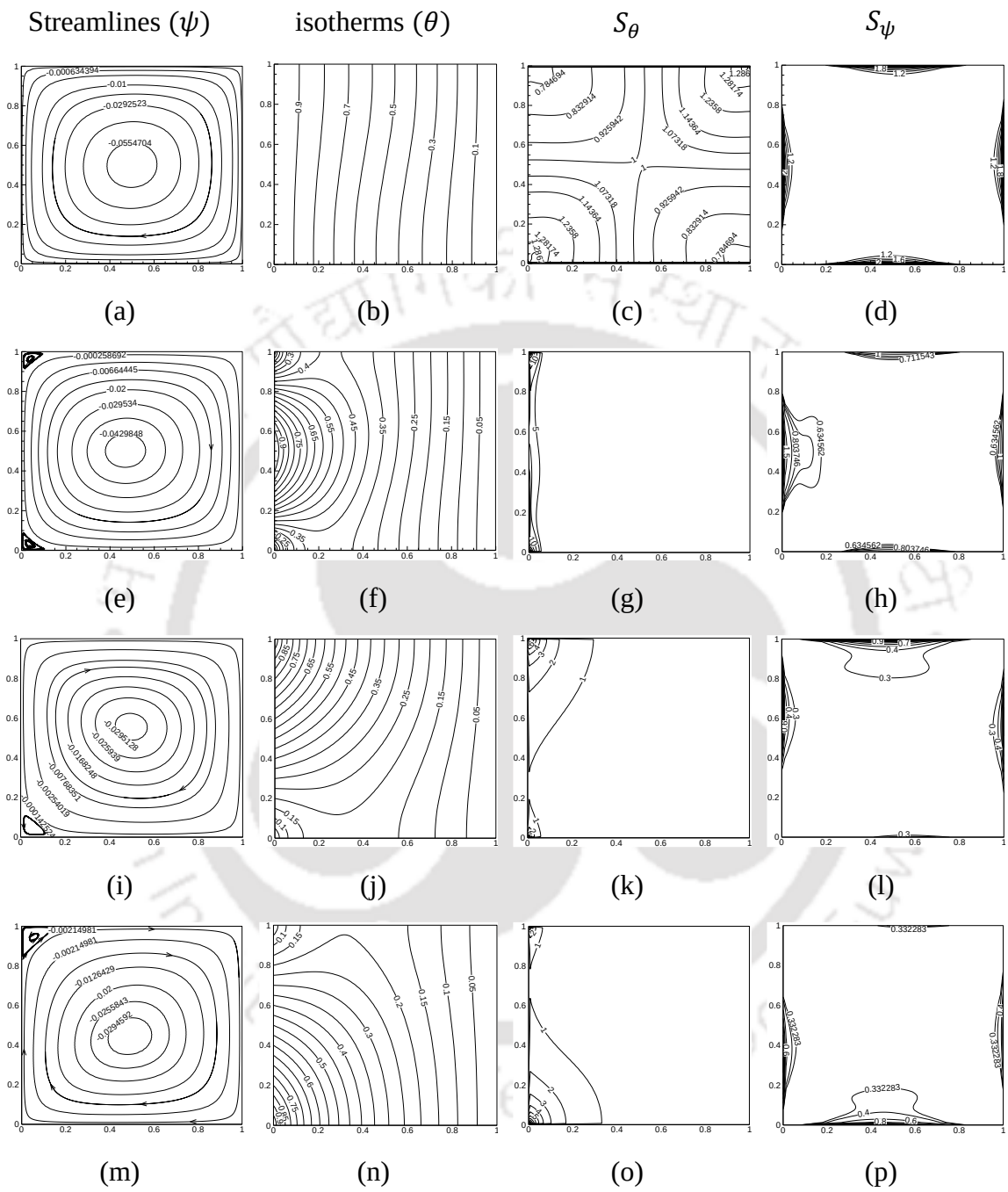

Fig. 4.2. Streamlines (ψ), isotherms (θ), local entropy generation due to heat transfer (S_θ) and due to viscous effect (S_ψ) for (a, b, c, d) uniform, (e, f, g, h) sinusoidal, (i, j, k, l) bottom to top linear and (m, n, o, p) top to bottom linear heating respectively at Ra = 10^3 with Da = 10^{-2}.

The results obtained are for the natural convection in a differentially heated porous cavity where four different heating configurations are applied at the vertical walls of the cavity by adopting the isothermal, sinusoidal, bottom to top linear and top to bottom linear temperature distributions respectively. Figs. 4.2-4.4 show the results in terms of contours of dimensionless stream function, isotherm, local entropy generation due to heat transfer and fluid friction for four different thermal boundary conditions. For the lower Darcy-Rayleigh number Ra_m = 10, computations are carried out for $Ra = 10^3$ with $Da = 10^{-2}$ and $Ra = 10^5$ with $Da = 10^{-4}$. For the higher value of $Ra_m = 10^3$, computations are carried out for $Ra = 10^5$ with $Da = 10^{-2}$. The streamline contours show that a clockwise rotating primary vortex is formed for each configuration of boundary conditions as the fluid heated up by the left wall is cooled down along the right wall of the cavity. However, there are secondary vortices at the top-left and bottom-left corners for sinusoidal heating, the bottom-left corner for the bottom to top linear heating and the top-left corner for the top to bottom linear heating of the left wall due to the non-uniformity in temperature variation as seen from Figs. 4.2(e), (i) and (m) respectively. At a low value of $Ra = 10^3$, irrespective of Da the fluid flow is induced by weak buoyant forces as characterised by a small magnitude of stream function. The maximum value of stream function $|\psi_{max}|$ exists at the centre of each of the primary vortices where their values are 0.06, 0.045 and 0.030, 0.031 for the isothermal, sinusoidal, bottom to top linear and top to bottom linear heating respectively. Figs. 4.2(b), (f), (j) and (n) show that the flow is mainly dominated by conduction which is characterised by the vertically parallel isotherms spanning the entire cavity. It is found in sinusoidal and linear heating that the heating rate near the wall is comparatively lower than uniform heating, thus inducing weak buoyant force which results in lower thermal gradient throughout the domain. From Fig. 4.2(c) it is noticed that for uniform heating, the significant value of S_θ is extended up to the mid-portion of the cavity from the left bottom and the top right corners of the cavity where the maximum value of S_θ ($|S_{\theta,max}|$ = 1.291) lies. In the case of sinusoidal heating, S_θ along the left wall with the maximum value equal to 59.25 near the bottom left and top left corners of the cavity due to the presence of significant thermal gradients at these positions. For bottom to top linear and top to bottom

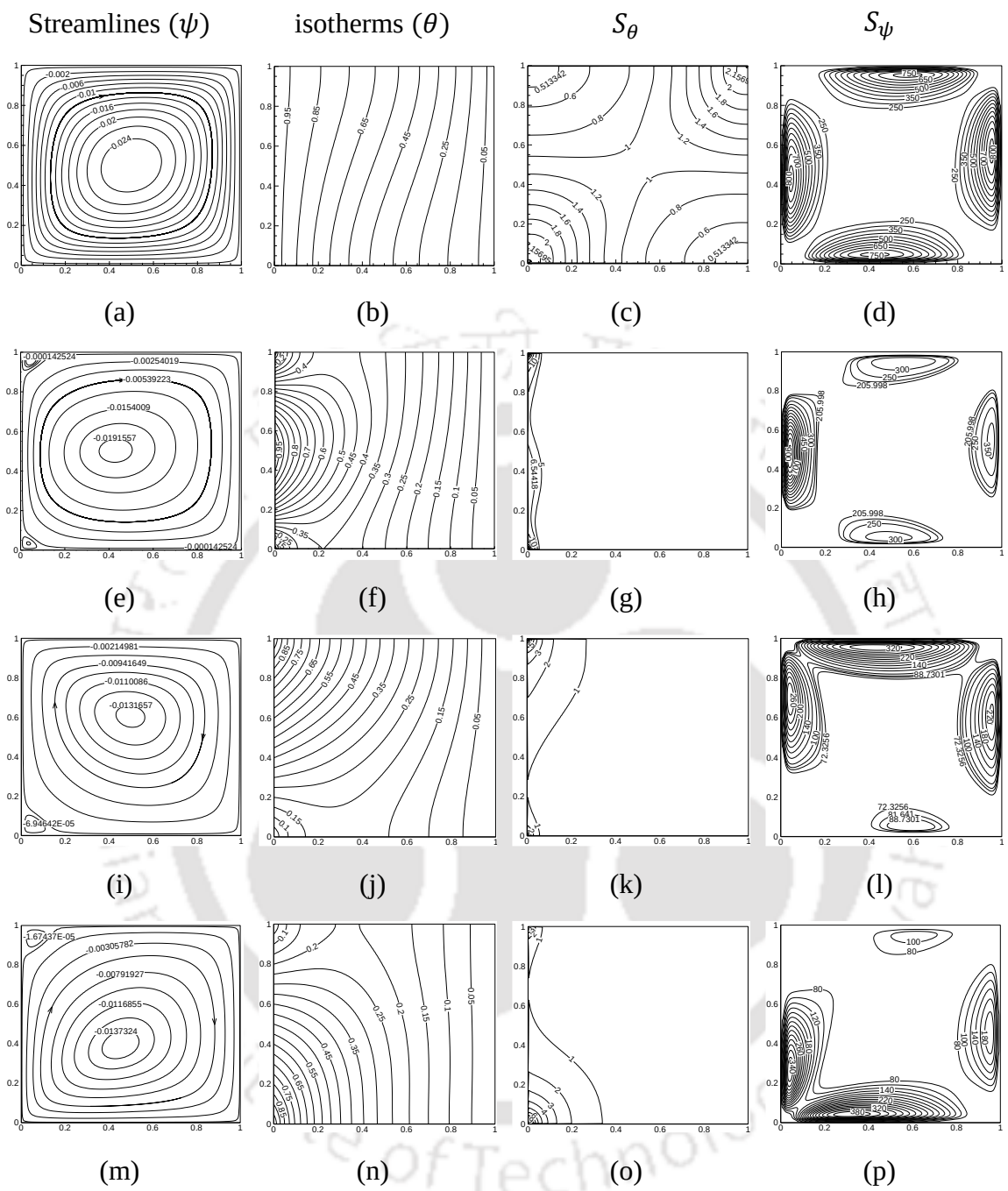

Fig. 4.3. Streamlines (ψ), isotherms (θ), local entropy generation due to heat transfer (S_θ) and due to viscous effect (S_ψ) for (a, b, c, d) uniform, (e, f, g, h) sinusoidal, (i, j, k, l) bottom to top linear and (m, n, o, p) top to bottom linear heating respectively at Ra = 10^5 with Da = 10^{-4}.

linear heating, $|S_{\theta,max}|$ with values 13.824, 14.628 respectively are found at that corner of the left wall where maximum wall temperature lies for each case. However, the entropy

generation due to fluid friction is significantly lower at low *Ra* due to weak convection in the cavity. For all four cases, S_ψ is concentrated at the vertical walls of the cavity where the maximum magnitudes $|S_{\psi,max}|$ are found to be 3.937, 5.57, 1.812 and 1.958 for uniform, sinusoidal and bottom to top linear and top to bottom linear heating respectively. The active zones of S_ψ are also found at the top and bottom walls for uniform and sinusoidal heating whereas for the bottom to top linear heating and top to bottom linear heating they exist at the top wall and bottom wall respectively.

For a low value of *Da*, i.e. at10^{-4}, the conduction dominated flow and heat transfer phenomenon prevails even for higher *Ra* at 10^5 as circular streamlines in the core of cavity, and vertical isotherms spanning the entire cavity are observed, which are similar to the case for low *Ra*. Figs. 4.3(a), (e), (i), and (m) reveal that the values of ψ within the cavity are found to be lower at low *Da* values irrespective of *Ra* which implies diminishing flow rate as the loosely interconnected voids restrict the fluid flow in the porous medium. However, the value of ψ is higher near the vertical walls compared to the case for low *Ra* (Fig. 4.2) as the increasing buoyancy induced motion with *Ra* is confined to the walls due to lower *Da*. The maximum values of ψ found at the centre of the primary vortices are 0.026, 0.020, 0.013 and 0.014 for uniform, sinusoidal, bottom to top linear and top to bottom linear heating respectively. The value of S_ψ increases with *Ra* due to increasing velocity gradient with the buoyant force, which is found to be concentrated at the vertical walls of the cavity. The values of $|S_{\psi,max}|$ are 821.78, 918.89 and 337.424, 399.15 for uniform, sinusoidal, bottom to top linear and top to bottom linear heating respectively. It is noticed from Figs. 4.3(c), (g), (k) and (o) that the contours of S_θ are found to be similar to the low *Ra* case (Fig. 4.2) for all four cases. However, their magnitudes increase where $|S_{\theta,max}|$ are 2.668, 85.76, 17.268 and 21.91 respectively for four cases.

The magnitudes of the stream function increases, implying higher velocity, as *Ra* increases to 10^5 with high *Da* value due to the enhancement of buoyancy-induced circulatory motion inside the cavity as seen from Figs. 4.4(a), (e), (i) and (m). The $|\psi_{max}|$ with values 0.274, 0.25, 0.174 and 0.263 for uniform, sinusoidal, bottom to top linear and top to bottom linear heating respectively are found at the centre of primary vortices for each

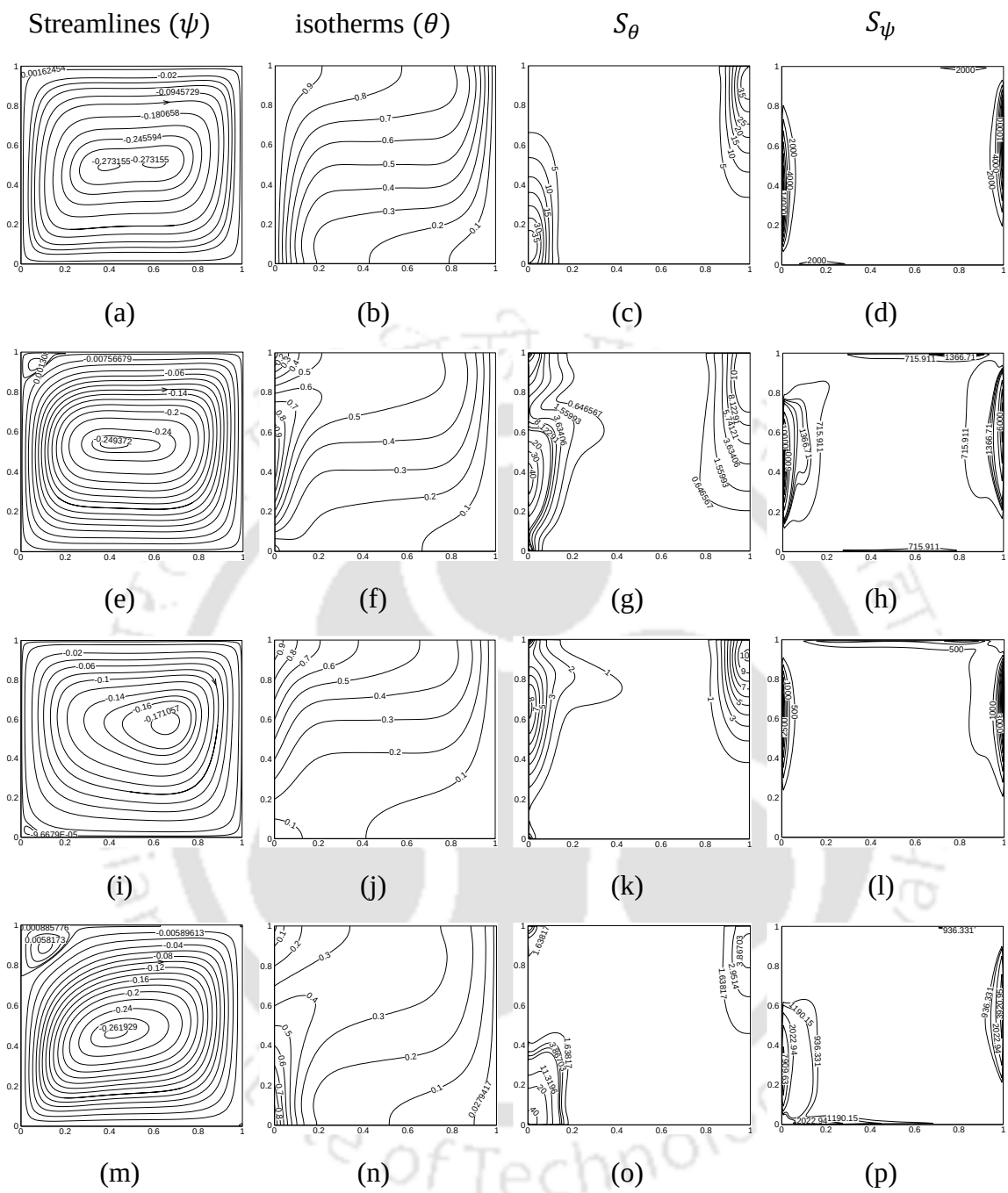

Fig. 4.4. Streamlines (ψ), isotherms (θ), local entropy generation due to heat transfer (S_θ) and due to viscous effect (S_ψ) for (a, b, c, d) uniform, (e, f, g, h) sinusoidal, (i, j, k, l) bottom to top linear and (m, n, o, p) top to bottom linear heating respectively at Ra = 10^5 with Da = 10^{-2}.

of the cases. For sinusoidal and bottom to top linear heating, the secondary vortex at the bottom left corner diminishes in size with an increase in *Ra* due to the reduction of the

thermal gradient at this zone. However, the secondary vortex at the top left corner for both sinusoidal and top to bottom linear heating increases in size as more fluid heated up is cooled down by the low-temperature zone at the top left corner of the cavity due to their temperature distribution. It is noticed from Figs. 4.4(b), (f), (j) and (n) that the distinct thermal boundary layers are developed near both the vertical walls of the cavity which is more significant for the case of uniform heating. The thinning of the thermal boundary layer occurs with the increase in *Ra* and *Da* due to the presence of higher temperature gradients. It is seen from Figs. 4.4(c)-(d), (g)-(h), (k)-(l) and (o)-(p) that the entropy generation increases due to both heat transfer and fluid friction with the increase in *Ra* and *Da* values for isothermal, sinusoidal and top to bottom linear heating respectively. However, for the bottom to top linear heating, the maximum value of S_θ ($|S_{\theta,max}|$ = 16.223) is low compared to the case for low *Da* due to enhanced thermal mixing at higher *Da*. For both uniform and top to bottom linear heating, S_θ is found to be concentrated at the lower portion of the left wall and the upper portion of the right wall with maximum values of S_θ = 42.72 and 85.118 respectively near the bottom left corner of the cavity. Sinusoidal heating has high S_θ compared to other cases with its maximum value equal to 97.756 near the bottom left portion. The significant value of S_θ is also noticed near the upper portion of the right vertical wall due to the enhancement of thermal energy transport at high *Ra* and *Da*. The value of S_ψ is changing drastically with *Ra* for all four cases due to the increase in velocity gradient mostly at the side walls which act as strong concentrators of S_ψ with the maximum magnitudes of 15037.4, 13712.7, 5447.9 and 10976.4 for uniform, sinusoidal, bottom to top linear and top to bottom linear heating respectively near the central position of the side wall.

It is observed from the above analysis that entropy generation due to both thermal and fluid irreversibilities is obtained at the walls of the cavity with their maximum concentration at the vertical walls for the benchmark problem, i.e., the case of uniform heating. Therefore, an attempt has been made to minimise the effect of $\overline{S_\theta}$ and $\overline{S_\psi}$ at the vertical walls in the cavity by adopting three different heating configurations at the left vertical wall. However, sinusoidal and top to bottom linear heating of left wall have much

higher $\overline{S_\theta}$ and $\overline{S_\psi}$ at their respective active zones in the cavity compared to the bottom to top linear heating. Further, the detailed analysis in terms of average Nusselt number, average entropy generation, average Bejan Number, the thermal mixing and the temperature uniformity in the cavity is made to have a clear picture of optimal boundary condition.

4.3.3.2 Average heat transfer rate and entropy generation

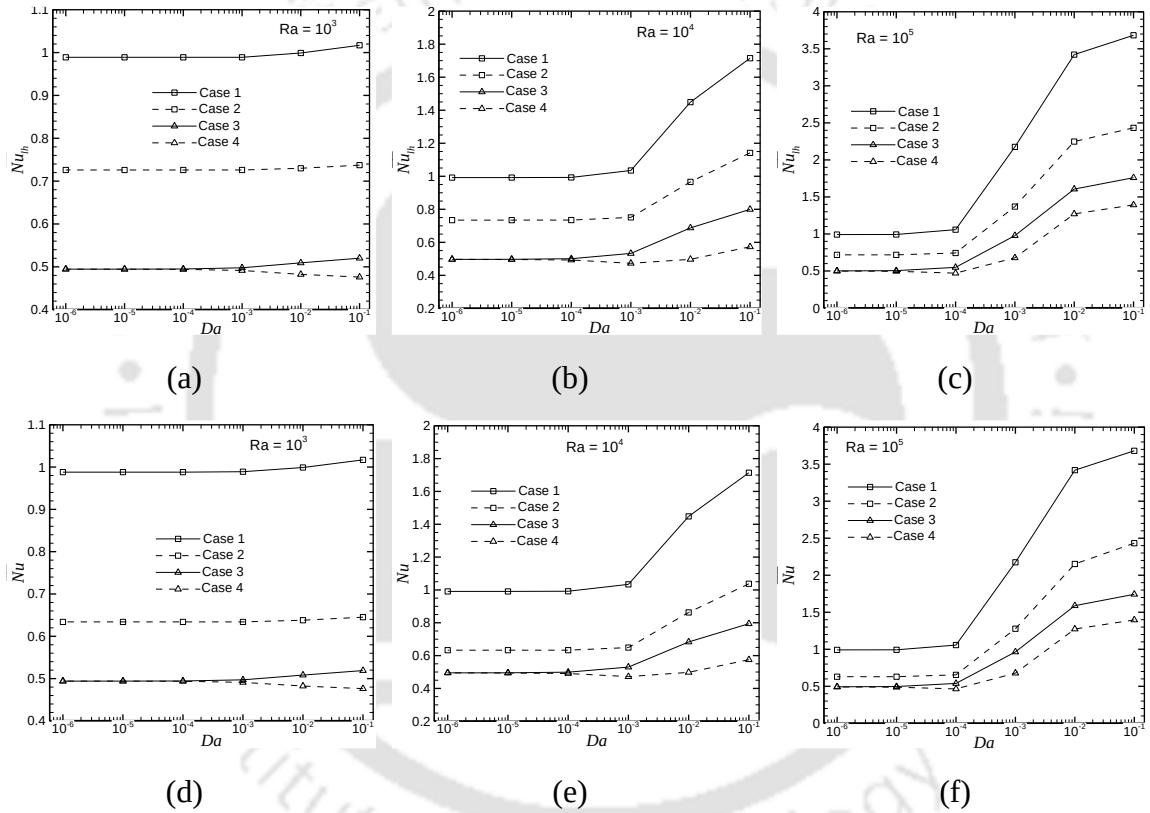

Fig. 4.5. Variations of (a, b and c) $\overline{Nu_{lh}}$ and (d, e and f) $\overline{Nu}$ with *Da* for four different boundary conditions at three different *Ra*'s of 10^3, 10^4 and 10^5 respectively.

Fig. 4.5 gives the effect of porous medium on the heat transfer in terms of average Nusselt number along the hot wall ($\overline{Nu_{lh}}$) and over the whole domain ($\overline{Nu}$) of the cavity for all four cases of boundary conditions with *Da* varying from 10^{-6} to 10^{-1} at three different *Ra*'s of 10^3, 10^4 and 10^5 respectively. The variation of $\overline{Nu}$ with *Da* is found to be insignificant at *Ra* = 10^3. However, $\overline{Nu}$ slightly decreases with the increase in *Da* at *Ra* = 10^3 for the top to bottom linear heating where the flow is mainly dominated by conduction

mode of heat transfer. It is observed from Figs. 4.5(b)-(c) and (e)-(f) that the $\overline{Nu}$ increases with *Da* at *Ra* = 10^4 and 10^5 as the effect of convective heat transfer get augmented due to increase in buoyant force near the hot and cold vertical walls of the cavity. The maximum and minimum $\overline{Nu}$ are attained for the case of uniform heating and top to bottom linear heating, respectively.

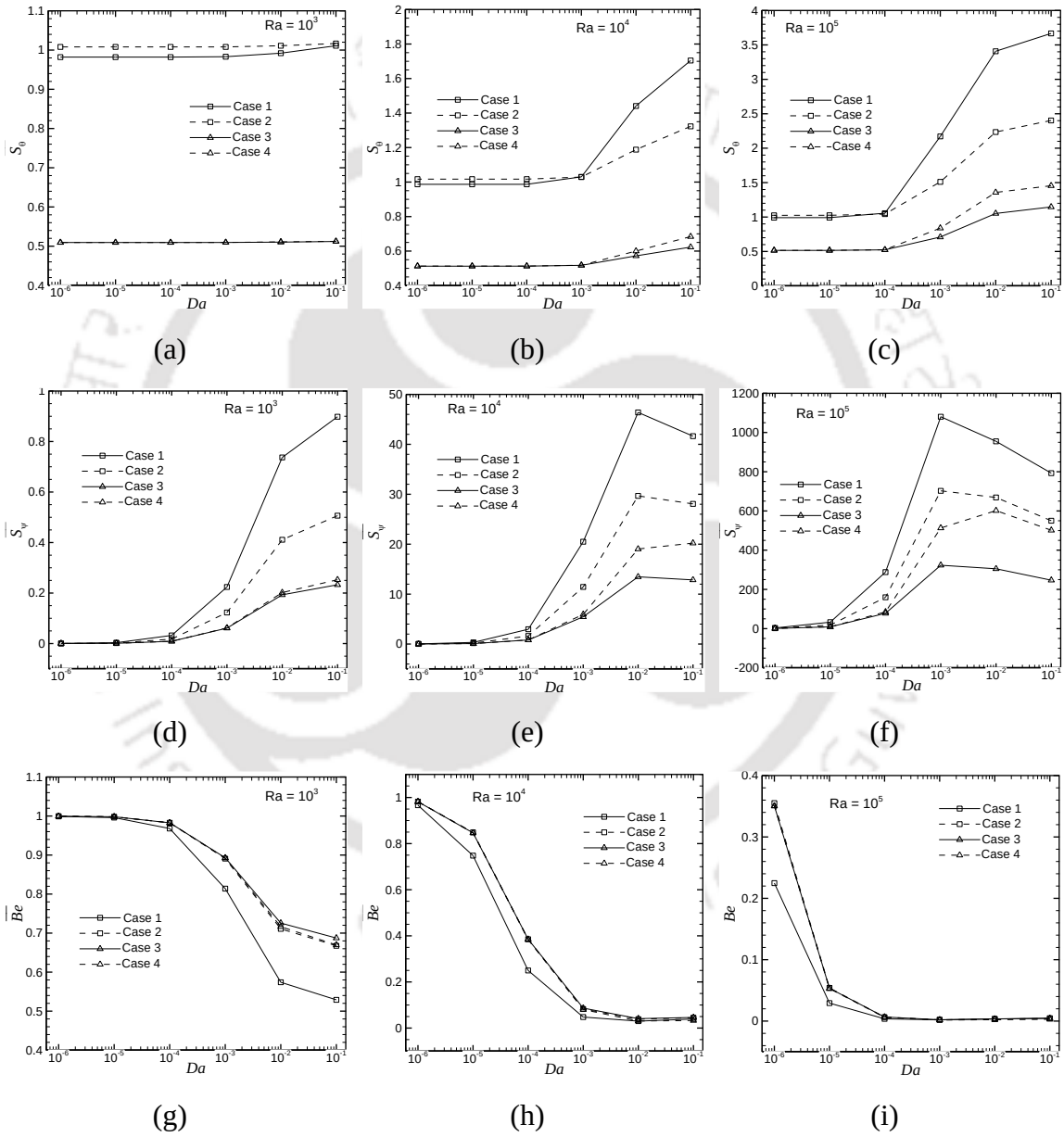

Fig. 4.6. Variations of (a, b and c) $\overline{S_\theta}$, (d, e and f) $\overline{S_\psi}$ and (g, h and i) $\overline{Be}$ with *Da* for four different boundary conditions at three different *Ra*'s of 10^3, 10^4 and 10^5 respectively.

The augmentation of the average entropy generation due to heat transfer ($\overline{S_\theta}$) throughout the cavity with an increase in *Da* in Figs. 4.6(a)-(c) resembles the variation of the average Nusselt number in Fig. 4.5; thus, the same arguments prevail for both cases as both quantities are the function of temperature gradients. The average entropy generation due to viscous effect ($\overline{S_\psi}$) throughout the cavity increases with increase in *Da* value for *Ra* = 10^3 for all the boundary conditions. However, it is interesting to see that $\overline{S_\psi}$ first increases and then decreases with increase in *Da* for all cases at *Ra* = 10^4 and 10^5 due to the presence of strong buoyant force at higher *Da* which overpowers the adverse effects of drag force on fluid velocity. At all studied values of *Ra* and *Da*, $\overline{S_\theta}$ and $\overline{S_\psi}$ are found to be maximum for uniform heating and minimum for the case of the bottom to top linear heating. It is seen that at low *Da* values for *Ra* = 10^3 and 10^4, the effect of S_ψ is trivial and the entropy generation is mainly contributed by heat transfer irreversibility which is characterised by high average Bejan number ($\overline{Be}$) over the whole cavity as shown in Figs. 4.6(g)-(h). The lower value of $\overline{Be}$ at higher *Ra* and *Da* indicate that the effect of frictional irreversibility is more prominent compared to heat transfer irreversibility. However, $\overline{Be}$ decreases with increase in *Da* at all studied values of *Ra* due to increasing velocity gradient with buoyant force.

4.3.3.3 Calculation of $\overline{Nu}/\overline{S_{tot}}$, θ_{cup} and $RMSD_{\theta_{cup}}$

The ratio between the $\overline{Nu}$ and the $\overline{S_{tot}}$ is calculated to make a comparison among the boundary conditions in terms of energy efficiency and their variation with *Da* are plotted in Figs. 4.7(a)-(c) for *Ra* = 10^3, 10^4 and 10^5 respectively. $\overline{Nu}/\overline{S_{tot}}$ is found to be higher for both linear heating compared to other two cases for lower values of Darcy-Rayleigh number, Ra_m = 10 and 10^2 at *Ra* = 10^3 and 10^4 and lower values of *Da* = 10^{-5} and 10^{-6} at *Ra* = 10^5 as the heat transfer is controlled by conduction. However, the uniform heating has a higher value of $\overline{Nu}/\overline{S_{tot}}$ at higher Ra_m = 10^3 and 10^4 for *Ra* = 10^4 and 10^5 and at low Ra_m = 10 and 10^2 for higher *Ra* = 10^5 where flow field is dominated by convection. Figs. 4.7(d)-(f) depicts that variation of θ_{cup} is almost constant with *Da* for all

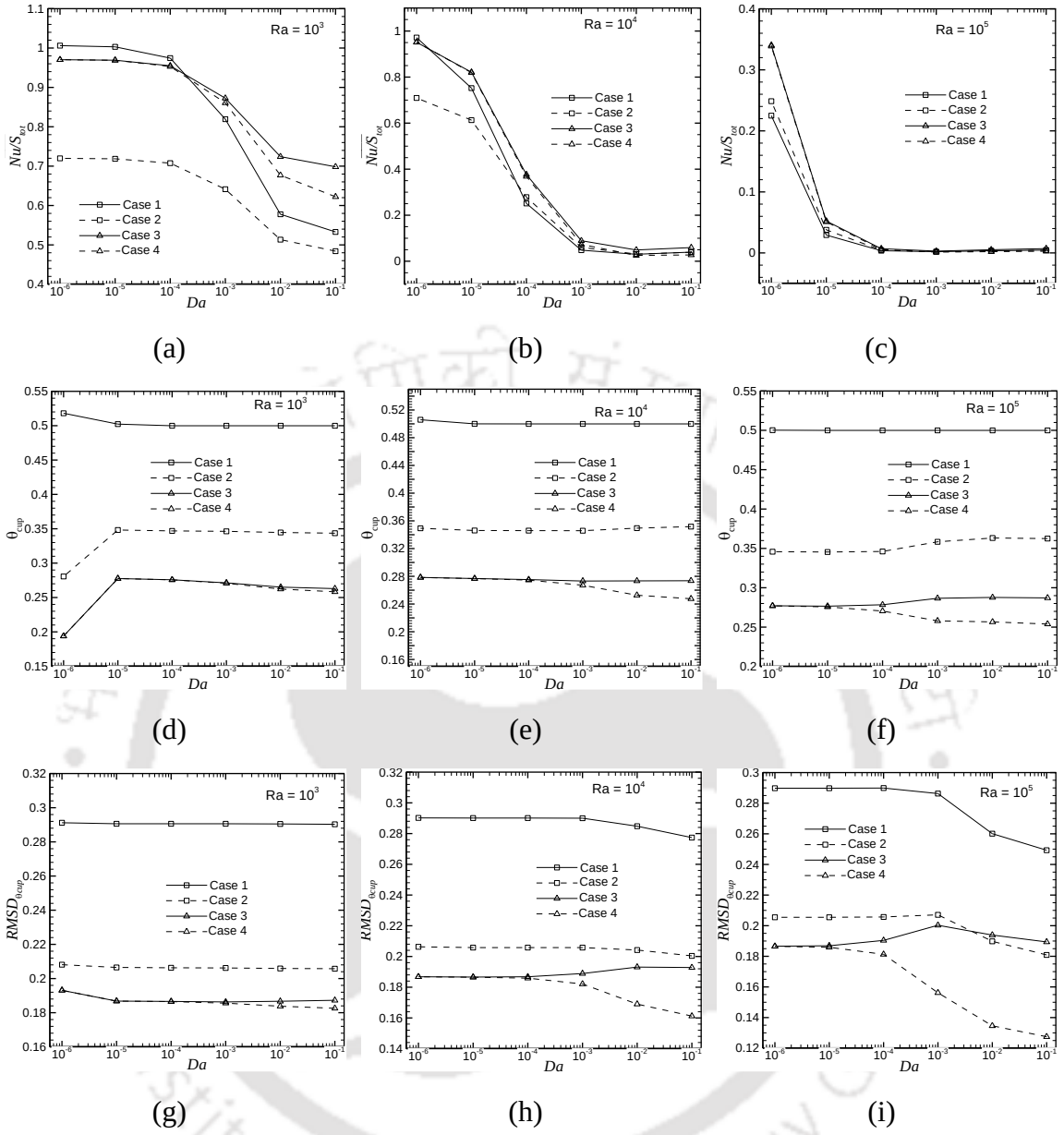

Fig. 4.7. Variations of (a, b and c) $\overline{Nu}/\overline{S_{tot}}$, (d, e and f) θ_{cup} and (g, h and i) $RMSD_{\theta_{cup}}$ with *Da* for four different boundary conditions at three different *Ra*'s of 10^3, 10^4 and 10^5 respectively.

cases with slight enhancement at higher *Ra* and *Da* for the bottom to top linear heating, thus improving the thermal mixing. Figs. 4.7(g)-(i) indicates that the $RMSD_{\theta_{cup}}$ decreases with increase in *Da*, i.e., the temperature uniformity in the cavity increases for both cases of uniform and top to bottom linear heating.

4.3.4 Conclusions

The detailed analysis of the effect of four different thermal boundary conditions on natural convection in a fluid-saturated square porous cavity is made by considering the entropy generation, heat transfer and degree of temperature uniformity. The current investigation deals with a number of non-dimensional parameters like *Ra* varying from 10^3-10^5, *Da* from 10^{-1}-10^{-6} at ε = 0.5. For an optimal boundary condition in terms of energy efficiency, the higher heat transfer rate and the thermal mixing in the cavity are desired, but this leads to undesirable higher entropy generation and lower temperature uniformity over the whole domain of the cavity, as observed for the case of uniform heating. Sinusoidal heating is not suitable due to its poor energy efficiency compared to other cases as it has low $\overline{Nu_N}/\overline{S_{tot,N}}$ and moderate thermal mixing and temperature uniformity. At *Ra* = 10^3, both the cases of linear heating have comparable energy efficiency due to their negligible variation of calculated parameters. However, between the two cases of linear heating, bottom to top linear heating has higher heat transfer rate, temperature uniformity and thermal mixing and lower entropy generation at higher *Ra* = 10^4 and 10^5. It is noticed that at very low values of *Da* = 10^{-5} and 10^{-6} for all *Ra*'s, $\overline{Nu}/\overline{S_{tot}}$ is found to be higher for all four configurations where the heat transfer mechanism is mainly controlled by conduction as flow rate diminishes. Therefore, it is understood that the values of *Ra* and *Da* play a vital role in determining the optimum condition of $\overline{Nu}$, $\overline{S_{tot}}$, θ_{cup} and $RMSD_{\theta_{cup}}$. Thus, a compromise has to be made between higher heat transfer rate, lower total entropy generation, superior thermal mixing and greater temperature uniformity to make an optimum choice for this flow condition. Accordingly, it can be concluded that the uniform heating is found to be more suitable for higher *Ra* = 10^5, and higher Ra_m = 10^3 at *Ra* = 10^4 whereas, bottom to top linear heating can be an effective and alternative heating condition for lower *Ra* = 10^3 and 10^4 at low Darcy-Rayleigh number, Ra_m = 10 and 10^2. In Chapter 6, further investigations are carried out for nanofluid-filled porous cavity by considering both uniform and bottom to top linear heating condition at the left wall of the cavity at their respective optimum Ra_m values.

4.4 Formulation of the second problem: Mixed convection in the inclined cavity with an inner heated porous block

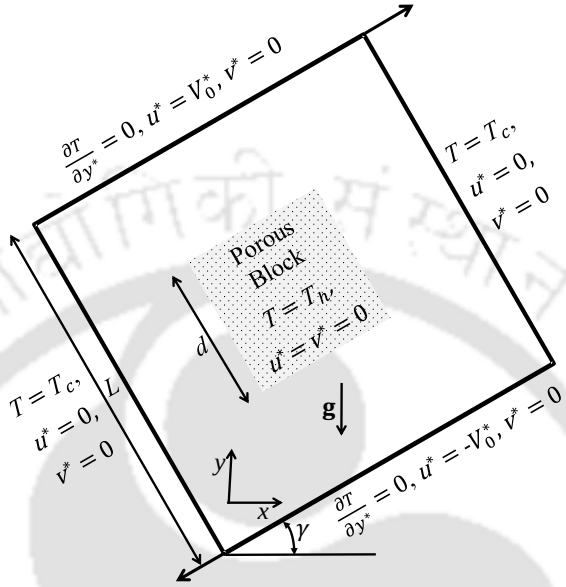

Fig. 4.8. Schematic diagram of the flow configuration with boundary conditions.

Fig. 4.8 shows the model configuration and boundary conditions for the present mixed convection flow problem in a square inclined cavity of length L which contains a permeable square block at the cavity centre having fixed size (d) equal to $0.25L$. Four different inclination angles γ = 0°, 30°, 60° and 90° of the cavity are considered. In the present flow configuration, the insulated top wall and the bottom wall of the cavity move towards the right and left respectively with a constant speed V_0^*. The vertical walls of the cavity are kept at the isothermally cold and square block is at isothermally hot condition. The gravitational acceleration acts in the negative y-direction, as shown in Fig. 4.8. In the present simulation, the heated porous block is assumed to be made of spherical beads. The porosity and permeability of the porous structure depend on the number and size of these beads, void between them and their connectivity. However, changes of these parameters lead to the variation of diameter (d_s) of spherical bead, which eventually changes the topography of the entire porous medium. Therefore, the diameter (d_s) of the bead is kept constant at $0.01d$ to retain uniformity.

For the convenience of numerical calculation and analysis, the non-dimensional forms of the variables are expressed as follows:

$$x = \frac{x^*}{L}; \qquad y = \frac{y^*}{L}; \qquad u = \frac{u^*}{V_0^*}; \qquad v = \frac{v^*}{V_0^*}; \qquad \theta = \frac{T - T_c}{T_h - T_c} \tag{4.26}$$

The boundary conditions in non-dimensional form for the square cavity is given as follows:

$$\begin{aligned} &u = 0; && v = 0; && \theta = 0 && \text{at } x = 0 \text{ and } 1 \\ &u = 0; && v = -1; && \frac{\partial \theta}{\partial y} = 0 && \text{at } y = 0 \\ &u = 0; && v = 1; && \frac{\partial \theta}{\partial y} = 0 && \text{at } y = 1 \end{aligned} \tag{4.27}$$

The boundary condition in non-dimensional form for the inner permeable square block is given as:

$$u = 0; \qquad v = 0; \qquad \theta = 1 \tag{4.28}$$

4.4.1 Grid independence study

Table 4.3 Grid independence study

Darcy number	variables	Grid sizes			
		241×241	321×321	401×401	481×481
10^{-2}	$\overline{Nu}$	11.8745	12.9734	13.722	13.9737
	$\overline{S_{tot}}$	14.7673	15.299	15.6465	15.730
10^{-3}	$\overline{Nu}$	8.8320	9.3138	9.6276	9.7485
	$\overline{S_{tot}}$	9.908	10.1825	10.359	10.4125
10^{-4}	$\overline{Nu}$	6.5244	6.6898	6.7955	6.809
	$\overline{S_{tot}}$	6.933	7.044	7.1152	7.123

Table 4.3 provides the grid-independence test for mixed convection at $Gr = 10^4$, $Ri = 1.0$ and $BR = 0.25$ for three different Darcy numbers Da. The results obtained for four different grid sizes of 241×241, 321×321, 401×401 and 481×481 are compared based on the average Nusselt number over the surface of the block $\overline{Nu_h}$ and average total entropy

generation throughout the cavity $\overline{S_{tot}}$. From this investigation, the grid size of 401×401 is found to be suitable for all computations while considering time-wise efficiency.

4.4.2 Code validation

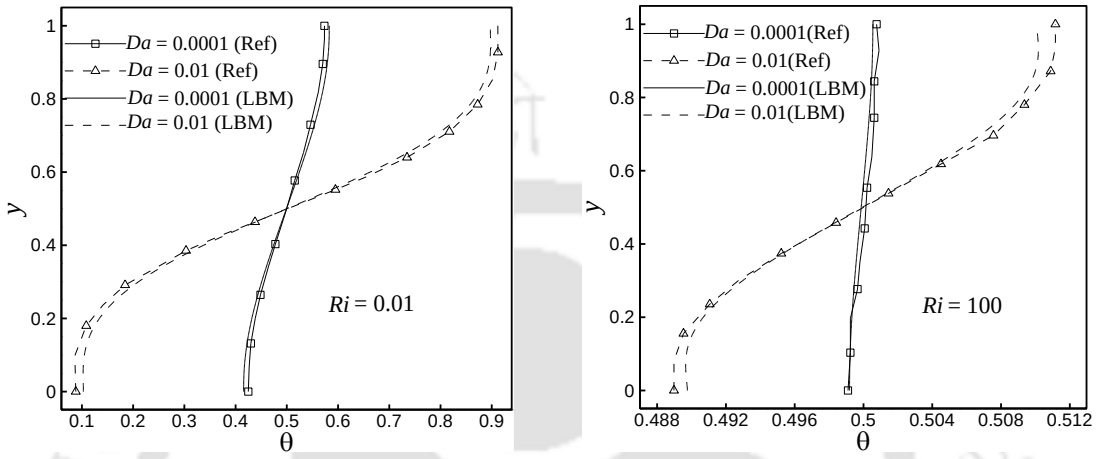

Fig. 4.9. Comparison of present results and Vishnuvardhanarao and Das [2009] in terms of dimensionless temperature (θ) profile along the vertical mid-plane of square cavity for Ri = 0.01 and 100 at Da = 10^{-4} and 10^{-2}.

Table 4.4 Comparison of present results for $\overline{Nu}$ with Vishnuvardhanarao and Das [2009].

Ri	$\overline{Nu}$					
	$Gr = 10^4$		$Gr = 10^3$		$Gr = 10^2$	
	Present work	Published work	Present work	Published work	Present work	Published work
0.01	15.671	16.294	7.372	8.828	2.964	3.051
0.1	7.592	8.8525	2.844	3.215	1.272	1.308
1.0	3.471	3.86	1.357	1.386	1.027	1.062
10.0	2.008	2.076	1.066	1.092	0.999	1.022
100.0	1.599	1.64	1.017	1.035	0.996	1.008

To check the ability of present code in simulating thermal flow problems concerning porous structure, the current results are compared with the published works of Vishnuvardhanarao and Das [2009] for mixed-convection in a two-sided lid-driven differentially heated square porous cavity. Fig. 4.9 shows the comparison of results in terms

of dimensionless temperature profile along the vertical mid-plane of square cavity for *Ri* = 0.01 and 100 at *Da* = 10^{-4} and 10^{-2}, which provides a close agreement. Further, Table 4.4 depicts a good concordance between the results in terms of the average Nusselt number along the hot wall of the cavity for different *Ri* and *Gr* at fixed *Da* = 10^{-2} and *Pr* = 0.71.

4.4.3 Results and discussion

A detailed comprehensive analysis of present mixed convection problem is made for discretely varying Richardson numbers (*Ri*) from 0.1 to 10 at fixed Grashof number *Gr* = 10^4 and porous block height (*d*) = 0.25*L*. The flow is simulated for four different Darcy numbers (*Da*) equal to 10^{-6}, 10^{-4}, 10^{-3} and 10^{-2} with their respective values of porosity equal to 0.611, 0.930, 0.975 and 0.992. Four different inclination angles γ = 0°, 30°, 60° and 90° of the cavity are considered. A number of plots are presented to show the effect of inclination angle, *Da* and *Ra* on the average *Nu* over the porous block surface ($\overline{Nu_h}$), average total entropy generation due to heat transfer irreversibility ($\overline{S_\theta}$) and fluid friction irreversibility ($\overline{S_\psi}$). The numerical results obtained for the two cases are discussed in the following sections.

4.4.3.1 Streamlines, isotherms and contours of entropy generation

Fig. 4.10 shows the effect of Richardson number *Ri* discretely varying from 0.1 to 10 on the fluid and thermal behaviour for fixed *Da* = 10^{-2} while considering just one inclination angle γ = 0° for the sake of brevity. The results are presented in terms of contours of dimensionless stream function, isotherm, local entropy generation due to heat transfer and fluid friction. At lower *Ri* = 0.1, a clockwise rotating primary vortex covered the whole cavity which is generated due to the direction of top and bottom adiabatic walls movement. However, at higher *Ri*, an anti-clockwise rotating secondary vortex is formed at the left side of the cavity due to higher buoyancy induced convection which overcomes the effect of forced convection. The size of this secondary vortex increases with increase in *Ri*. The centre of secondary vortex shifts towards the vertical mid-plane of the cavity

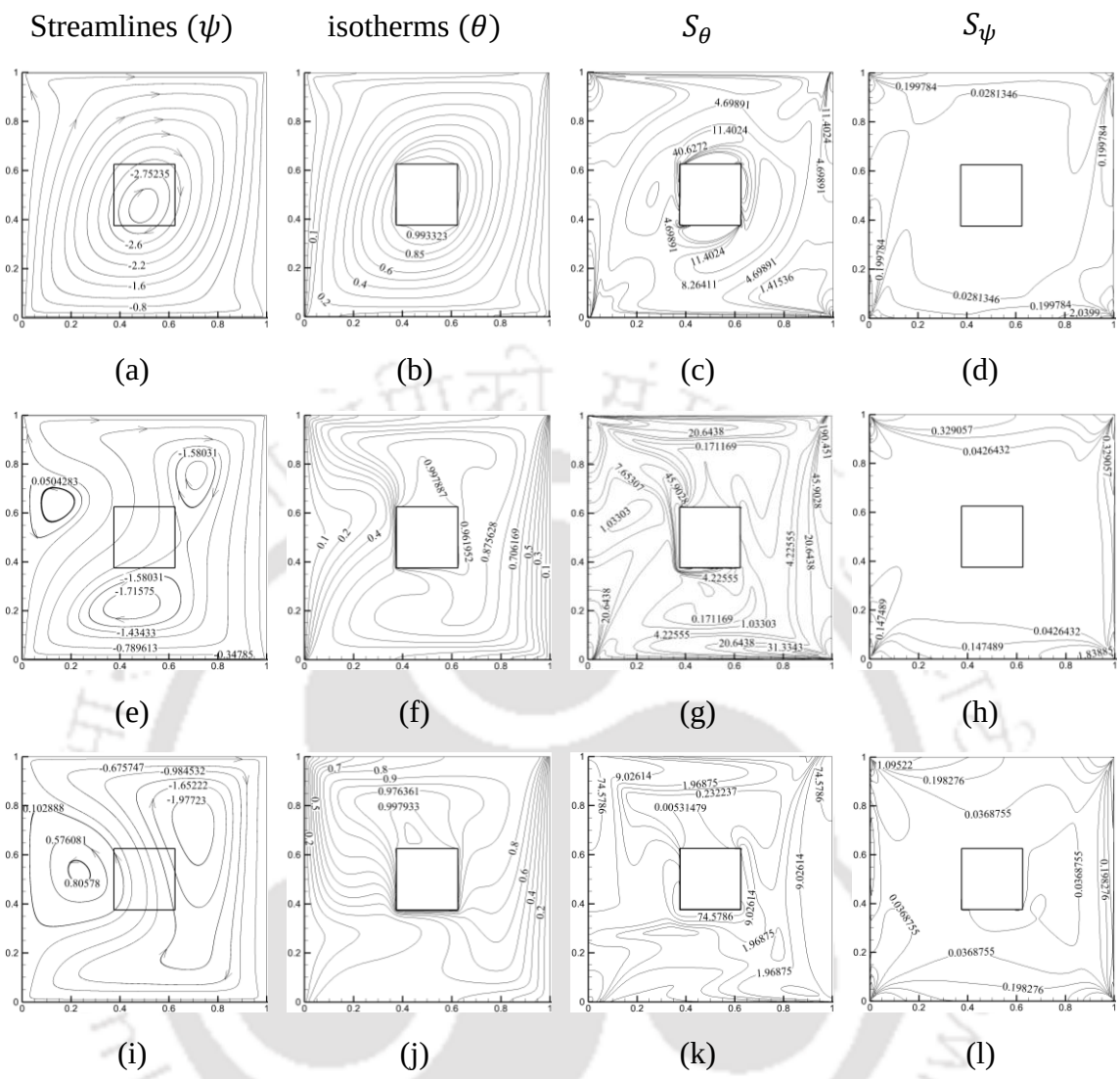

Fig. 4.10. Streamlines (ψ), isotherms (θ), local entropy generation due to heat transfer (S_θ) and due to viscous effect (S_ψ) at *Ri* = 0.1 (a, b, c, d), *Ri* = 1 (e, f, g, h) and *Ri* = 10 (i, j, k, l) for $Da = 10^{-2}$.

with the maximum value of stream function equal to 0.867 lies for *Ri* = 10. Accordingly, the primary vortex changes its shape and size. It is evident from streamline plots that the primary vortex is stronger at lower *Ri* = 0.1 with a maximum stream function value $|\psi_{max}|$ is equal to 2.821. The $|\psi_{max}|$ is found to be equal to 1.815 at *Ri* = 1, this lower value is attributed to the formation of two opposite circulating vortices. However, $|\psi_{max}|$ increases with further increase in *Ri* due to the augmentation of convection current with a value of 2.21 for *Ri* = 10. The patterns of isotherm are in concordance with the streamline patterns

at *Ri* = 0.1 and 1. The thermal plumes are observed at *Ri* = 1 and 10 (Fig. 4.10(f) and (j)) which is more prominent at *Ri* = 10. This is attributed to penetration of hot fluid into the low temperature zone above the heated block due to convected motion generated by buoyancy force. There is no generation of the thermal plume at lower *Ri* as the heat transfer is dominated by forced convection. The clustering of isotherms is found near the block surface and the vertical walls for *Ri* = 1 and 10, and it is more significant at higher *Ri* due to stronger buoyancy induced convection current.

Figs. 4.10(c), (g) and (k) depict that the contour of S_θ are in concordance with isotherms as S_θ is a function of temperature. The entropy generation due to heat transfer is mostly concentrated around the permeable block surface and at the four corners of the cavity. There is an overall increase in S_θ with *Ri* due to the augmentation of strong buoyancy induced convection. The magnitude of maximum S_θ, $|S_{\theta,max}|$ are found to be 1228.3, 2819.0 and 4084.2 for *Ri* = 0.1, 1 and 10 respectively. However, the intensity of the entropy generation due to fluid friction S_ψ decreases with increase in *Ri* as stronger convection velocity prevails. Mostly, S_ψ is restricted to the vicinity of the corners of the cavity where the maximum magnitude $|S_{\psi,max}|$ lies. $|S_{\psi,max}|$ are obtained as 2385.7, 1806.5 and 1558.0 for *Ri* = 0.1, 1 and 10 respectively.

Fig. 4.11 depicts the effect of Darcy number discretely varying from 10^{-6} to 10^{-3} on the fluid and thermal behaviour for fixed *Ri* = 10 and inclination angle $\gamma = 0°$. A clockwise rotating primary vortex and an anti-clockwise rotating secondary vortex are formed at all Darcy numbers for higher *Ri* due to higher buoyancy induced convection as mentioned earlier. It is observed from Fig. 4.11(a) that very small amount of fluid is flowing through the porous block and thus it behaves more like a solid block. The streamlines, approaching the block, get deflected and adhere to the surface of porous block. The flow rate increases with increase in *Da* due to higher permeability of the medium and thus allows more amount of fluid to enter the porous block. At higher *Da* = 10^{-3}, the fluid is flowing freely through the porous block as seen by very less or no deflection in streamline contours in Fig. 4.11(i). This is attributed to high permeability which augments the fluid velocity. Figs. 4.11(b), (f) and (j) depict that the strength of thermal plume increases with increase in *Da* due to the

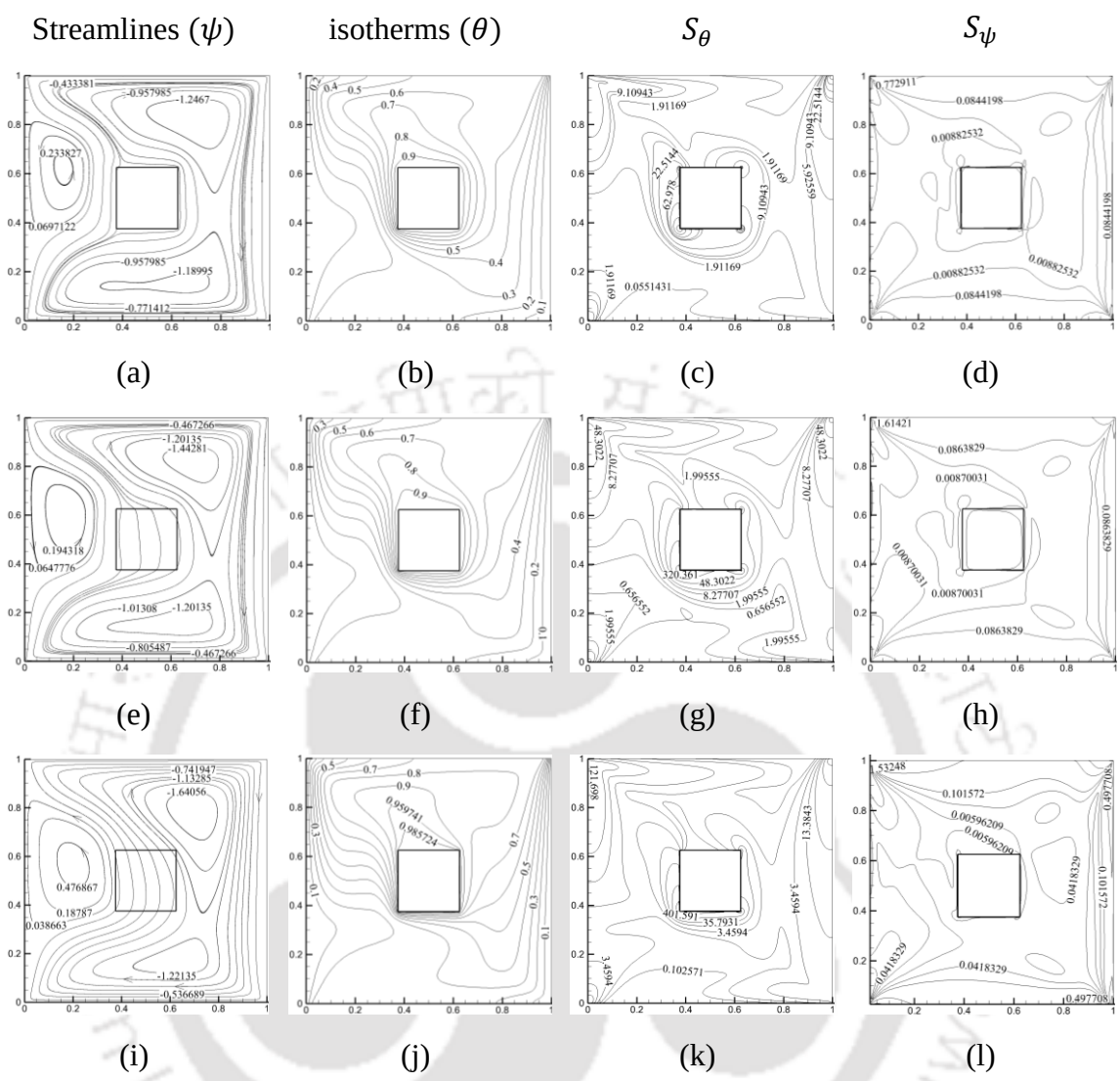

Fig. 4.11. Streamlines (ψ), isotherms (θ), local entropy generation due to heat transfer (S_θ) and due to viscous effect (S_ψ) at $Da = 10^{-6}$ (a, b, c, d), $Da = 10^{-4}$ (e, f, g, h) and $Da = 10^{-3}$ (i, j, k, l) for $Ri = 10$ and $BR = 0.25$.

augmentation of buoyancy induced convection current with intense flow velocity. This eventually results in thinning of the thermal boundary layer near the block surface and the vertical walls. It is interesting to observe that the thermal plume slightly deviates from the vertical axis of the heated block and inclines towards left of the axis due to stagnation of cold fluid near the top left region of the cavity.

It is observed from Figs. 4.11(c), (g) and (k) that the concentration of entropy generation due to heat transfer S_θ is maximum at the left bottom corner of the porous block and at the top corners of the cavity. The enhancement of buoyancy force with Darcy number

results in an overall increase of S_θ. The magnitude of maximum S_θ, $|S_{\theta,max}|$ are found to be 1151.9, 1651.9 and 3328.6 for Da = 10^{-6}, 10^{-4} and 10^{-3} respectively. It is interesting to observe that the overall entropy generation due to fluid friction augments with an increase in Da. This is attributed to the flowing of more fluid through the porous block, which contributed to an additional velocity gradient. The maximum values of S_ψ, $|S_{\psi,max}|$ locate at the corners of the cavity and their magnitudes are 957.4, 1460.2 and 1531.2 for Darcy numbers equal to 10^{-6}, 10^{-4} and 10^{-3} respectively.

4.4.3.2 Variation of velocity and temperature with *Ri*, *Da* and *φ*

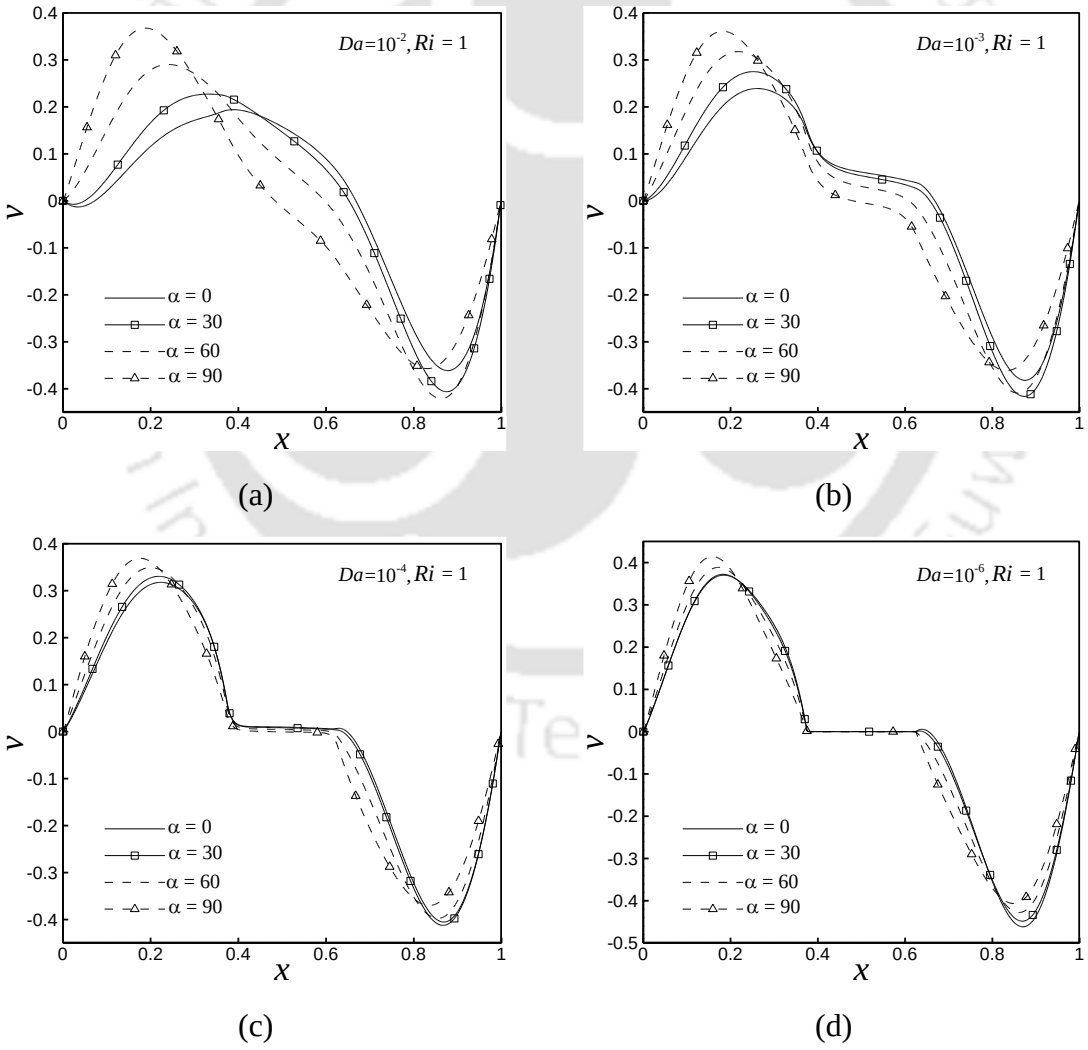

Fig. 4.12. Comparison of dimensionless vertical velocity v in the horizontal mid-plane of the cavity at Ri = 1 for Da equal to (a) 10^{-2}, (b) 10^{-3}, (c) 10^{-4} and (d) 10^{-6} respectively.

Figs. 4.12(a)-(d) and 4.13(a)-(c) provide the comparison of the results in terms of dimensionless vertical velocity v in the horizontal midline of the cavity for different inclinations at the range of Da and Ri. Figs. 4.12(a)-(d) depict that the flow rate diminishes and velocity approaches zero when Da reaches a very low value of about 10^{-6} for all four inclination angles. It indicates that at very low Da the fluid flow is restricted by the porous block and thus it acts as a solid block which is in accordance with the stream function contour. The maximum magnitude of velocity (upward) increases with inclination angle at the left side of the cavity due to the formation of the larger anti-clockwise secondary vortex and this flow behaviour is more prominent at high Da = 10^{-2}. However, the velocity at downward direction occurs at the right side of the cavity due to formation clockwise primary vortex and these maximum values are comparable for all inclination angles.

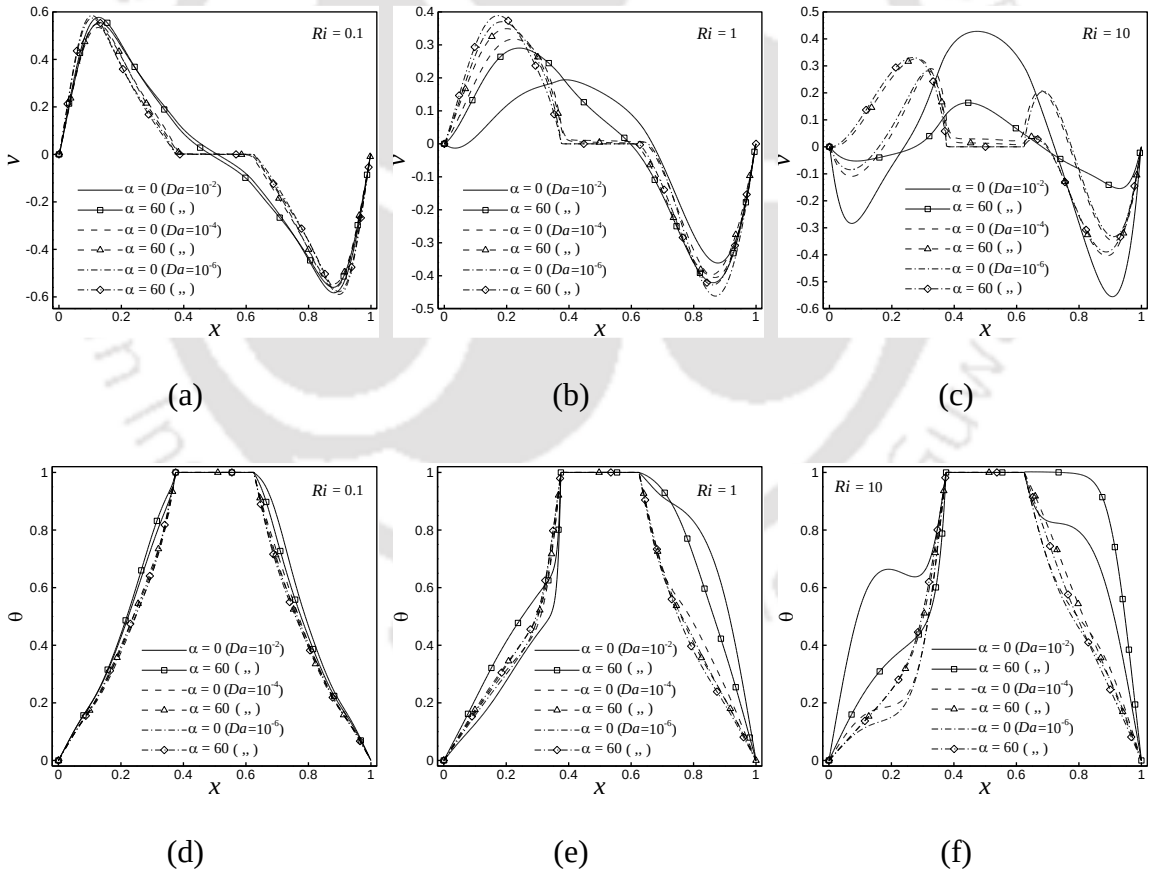

Fig. 4.13. Comparison of dimensionless vertical velocity v (a, b and c) and temperature θ (d, e and f) in the horizontal mid-plane of the cavity for Ri's of 0.1, 1 and 10 respectively at Da = 10^{-2}, 10^{-4} and 10^{-6}.

Figs. 4.13(a)-(c) show that at fixed Darcy number, the flow velocity increases inside the porous block with an increase in Richardson number. This is attributed to the existence of stronger buoyancy induced convection at higher *Ri* which forces more fluid to flow through the porous block. However, this velocity inside the porous block decreases with a rising inclination angle of the cavity. Figs. 4.13(d)-(f) show the variation of dimensionless temperature θ in the horizontal midline of the cavity with inclination angles at different Darcy and Richardson numbers. It is observed that at lower *Ri* = 0.1, the flow is mainly dominated by the conduction mode of heat transfer as characterised by the linear temperature profiles. This indicates that for this particular type of flow configuration, the lid-driven shear force is not strong enough to induce forced convection in the cavity. However, with an increase in *Ri*, the free convective effect due to buoyancy-driven flow increases which disturbs the linearity of the temperature profile. This effect is more prominent at higher Darcy number. The presence steeper temperature gradients near the vertical walls of the cavity, more prominently at the right wall, results in the development of thermal boundary layers at those regions.

4.4.3.3 Heat transfer rates

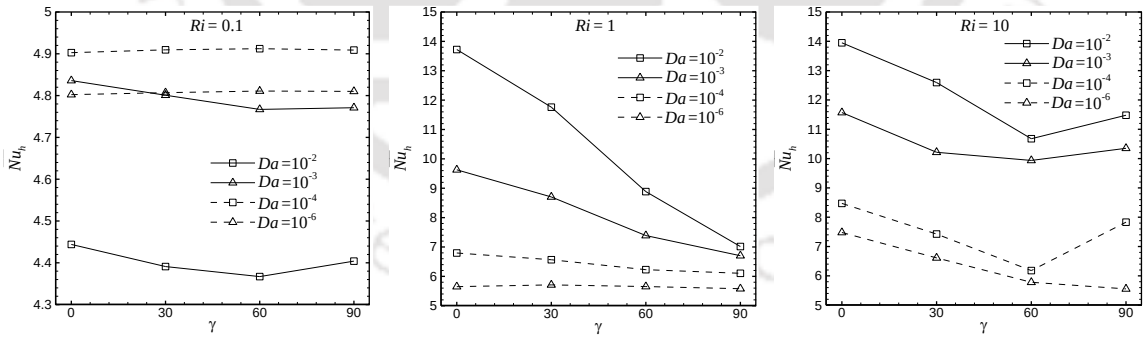

Fig. 4.14. Variations of $\overline{Nu_h}$ with inclination angle (γ) at (a) *Ri* = 0.1, (b) *Ri* = 1.0 and (c) *Ri* = 10.0 for different Darcy numbers.

Fig. 4.14 gives the effect of inclination angles γ on the heat transfer in terms of average Nusselt number over the surface of the hot porous block ($\overline{Nu_h}$) for a range of *Da* varying discretely from 10^{-6} to 10^{-2} at three different *Ri*'s of 0.1, 1 and 10 respectively. The

variation of $\overline{Nu_h}$ with γ is less significant at lower *Ri* = 0.1 in comparison to higher *Ri*. This is attributed to the dominance of conduction mode of heat transfer which is also characterised by the lower value of $\overline{Nu_h}$. The irregular behaviour of $\overline{Nu_h}$ at *Ri* = 0.1 with the change in *Da* indicates that the effect of the square porous block is less significant on fluid flow as the flow is mostly dominated by the lid-driven induced forced convection. It is interesting to observe (Fig. 4.14(b)) that the value of $\overline{Nu_h}$ is significantly higher at *Ri* = 1 for all *Da* in comparison to *Ri* = 0.1 as the effect of convective heat transfer get augmented due to increase in buoyant force near the porous block. However, the enhancement $\overline{Nu_h}$ with further increase in *Ri* becomes negligible for *Da* = 10^{-2}. The drastic reduction of $\overline{Nu_h}$ with the increase in γ occurs for *Da* = 10^{-3} and 10^{-2} at *Ri* = 1 as the shear-driven force opposes the buoyancy-driven force. However, change in $\overline{Nu_h}$ with γ is observed to be trivial at lower *Da* where the buoyancy effect is less prominent in controlling the flow behaviour. At higher *Ri* = 10, $\overline{Nu_h}$ decreases with increase in γ up to 60° due to the reduction of buoyancy induced convection. However, $\overline{Nu_h}$ augments with further increase in γ up to 90° due to enhancing effect of buoyancy force as it acts in the vertical direction for *Da* = 10^{-4}, 10^{-3} and 10^{-2}. At lower *Da* = 10^{-6}, $\overline{Nu_h}$ reduces continuously up to 90° due to the existence of a lower buoyant force.

4.4.3.4 Entropy generation (S_θ and S_ψ) and Bejan number (Be)

The variation of average entropy generation due to heat transfer ($\overline{S_\theta}$) throughout the cavity with an increase in inclination angles γ (Figs. 4.15(a)-(c)) resembles the variation of the average Nusselt number over the block surface $\overline{Nu_h}$ (Fig. 4.14). Therefore, the same arguments prevail for both quantities which are the function of temperature gradients. Besides, the values of $\overline{S_\theta}$ over the whole cavity is slightly higher than $\overline{Nu_h}$ over the block surface which indicates that S_θ is mostly concentrated at the surface of the porous block. However, the reduction of $\overline{S_\theta}$ with a decrease in *Da* and γ is observed for all *Ri*s which is in contrast to $\overline{Nu_h}$ at *Ri* = 0.1. This is attributed to the dominating force convection resulted

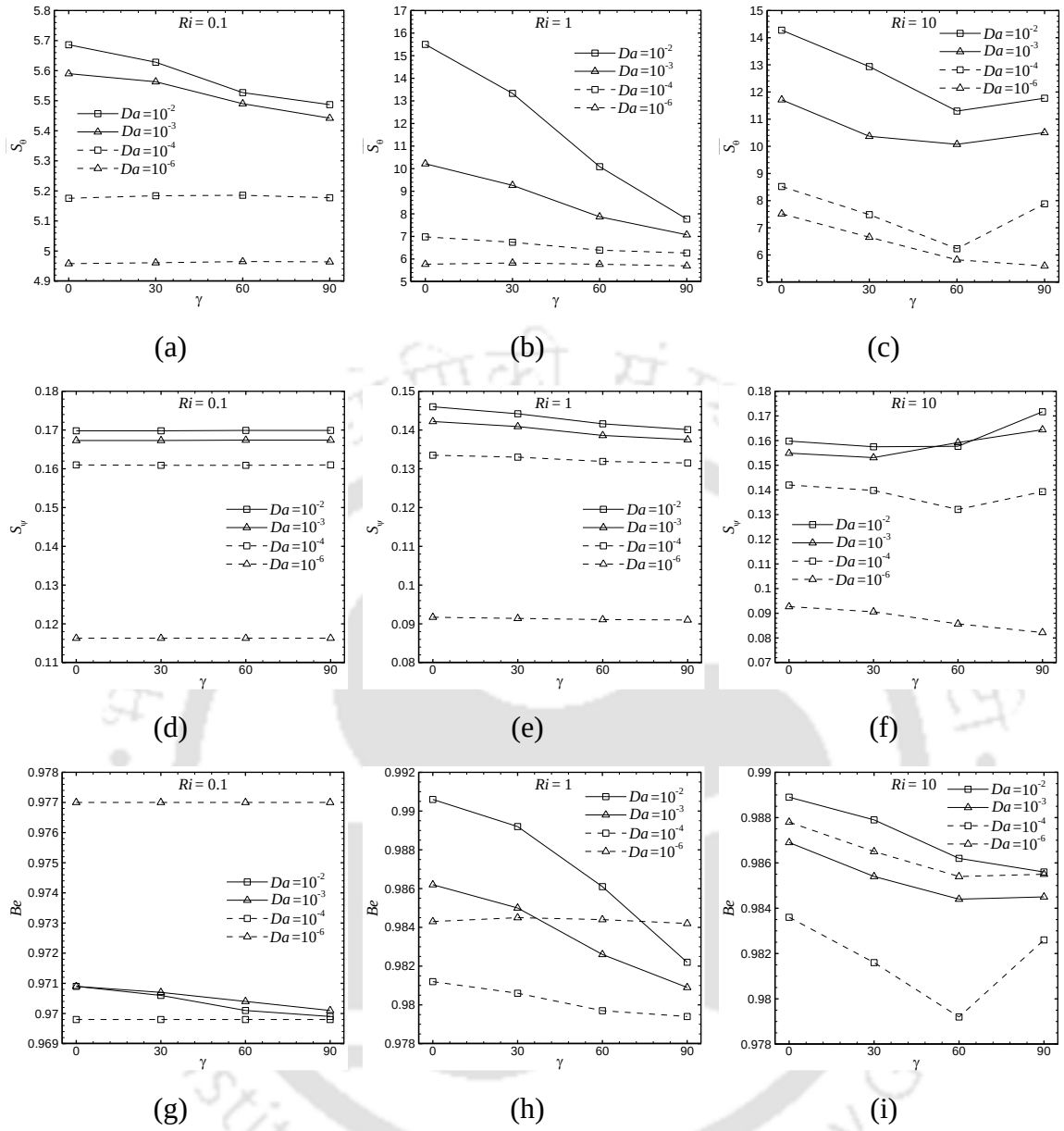

Fig. 4.15. Variations of $\overline{S_\theta}$ (a, b and c), $\overline{S_\psi}$ (d, e and f) and $\overline{Be}$ (g, h and i) with inclination angle (γ) for Ri = 0.1 (left panel), Ri = 1.0 (middle panel) and Ri = 10.0 (right panel) respectively at Da = 10^{-2}, 10^{-3}, 10^{-4} and 10^{-6}.

from movement of horizontal walls, thus, the concentration of S_θ is found to be higher near these walls at Ri = 0.1. Fig. 4.15(d) depicts that the change of average entropy generation due to viscous effect ($\overline{S_\psi}$) throughout the cavity with γ is negligible at Ri = 0.1 for all Darcy numbers. A similar observation is obtained for Ri = 1 except for higher Da = 10^{-3} and 10^{-2} where the reduction of $\overline{S_\psi}$ occurs with an increase in γ. However, at higher Ri = 10, $\overline{S_\psi}$ first

decreases and then increases with increase in γ for all *Da* except at *Da* = 10^{-6} where it decreases continuously up to 90°. It is seen from Figs. 4.15(g)-(i) that at all *Da* and *Ri* values, the effect of S_ψ is trivial and the entropy generation is mainly contributed by heat transfer irreversibility S_θ which is characterised by high average Bejan number ($\overline{Be}$) over the whole cavity. The value of $\overline{Be}$ reduces with increase in γ for *Da* = 10^{-4}, 10^{-3} and 10^{-2} at *Ri* = 1 due to reduction of $\overline{S_\theta}$. For *Da* = 10^{-3} and 10^{-2} at *Ri* = 10, the continuous reduction of $\overline{Be}$ up to 90° is observed despite the rise in $\overline{S_\theta}$ after 60°. This is attributed to the fact that the enhancement of frictional irreversibility is more prominent compared to heat transfer irreversibility.

4.4.3.5 Ratio of average Nusselt number to total entropy generation

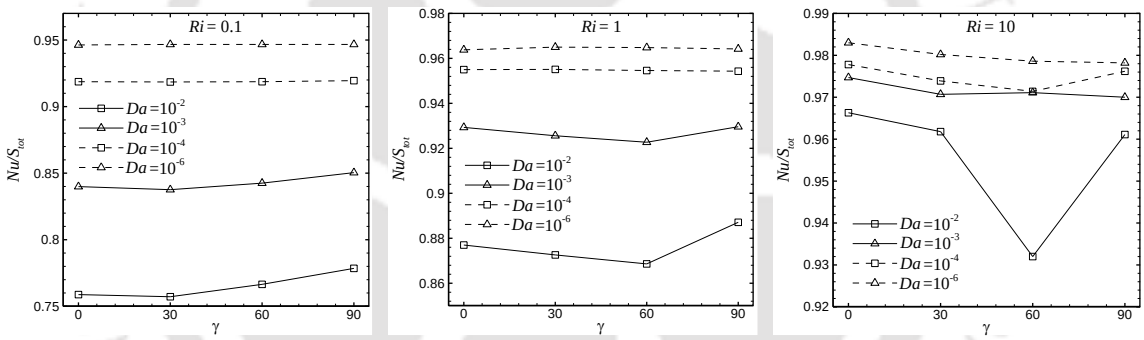

Fig. 4.16. Variations of $\overline{Nu_h}/\overline{S_{tot}}$ with inclination angle (γ) at *Ri* = 0.1 (left panel), *Ri* = 1.0 (middle panel) and *Ri* = 10.0 (right panel) respectively.

Figs. 4.16 depict the ratio of $\overline{Nu_h}$ and $\overline{S_{tot}}$ to make a comparison among the inclination angles from the viewpoint of both 1st and 2nd laws of thermodynamics. It is observed that at lower *Ri* = 0.1, $\overline{Nu_h}/\overline{S_{tot}}$ is found to be higher at larger inclination angles for higher *Da* = 10^{-3} and 10^{-2} as the flow is dominated by forced convection. The variation of $\overline{Nu_h}/\overline{S_{tot}}$ is negligible for lower *Da* = 10^{-4} and 10^{-6} at *Ri* = 0.1 and 1. At *Da* = 10^{-2}, $\overline{Nu_h}/\overline{S_{tot}}$ first decreases up to γ = 60° and then increases with increase in γ for *Ri* = 1 and 10. It is observed that the values of $\overline{Nu_h}/\overline{S_{tot}}$ for inclination angles, γ = 0° and 90° are comparable to each other and higher compared to the rest.

4.4.3.6 Conclusions

The effect of inclination angle and inner permeable square block on flow and thermal behaviour has been studied during laminar two-sided mixed convection in a square cavity. The results show that Darcy number and Richardson number have a profound influence on heat transfer rate and entropy generation. Moreover, the results indicate that the inclination angle of the cavity can be seen as a control parameter for fluid flow and heat transfer. The existence of conduction mode of heat transfer at lower Ri = 0.1 results in less significant variation of $\overline{Nu_h}$ with inclination angle γ compared to higher Ri. Besides, at lower Ri, the effect of a square porous block is less significant on fluid flow and heat transfer as the flow phenomenon is mostly dominated by the lid-driven induced forced convection. However, with an increase in Ri, the porous block has a higher influence on fluid flow as indicated by the enhancement of the heat transfer rate. At Ri = 1, both buoyancy and shear-driven forces play an important role where they oppose each other and this results in a drastic reduction of $\overline{Nu_h}$ with increase in γ for Da = 10^{-3} and 10^{-2}. The entropy generation is mainly controlled by heat transfer irreversibility S_θ, whereas the effect of fluid friction irreversibility S_ψ is not significant as characterised by high average Bejan number ($\overline{Be}$) over the whole cavity. The results reveal that the values of $\overline{Nu_h}/\overline{S_{tot}}$ for inclination angles γ = 0° and 90° are comparable to each other and are higher compared to the other two inclination angles.

Chapter 5

Two-Phase SRT-LBM and MRT-LBM for Nanofluid Flow in a Cavity

5.1 Introduction

Nanofluid has gained importance among the heat transfer communities as it enhances the efficiency of the heat transfer system compared with conventional fluids such as water, and industrial oil. Different numerical approaches such as conventional single-phase model, thermal dispersion model, two-phase model and LBM. are considered by researchers to understand the behaviour of nanofluid in a nanofluid-filled cavity flow problem. However, most of the numerical studies have been made using a single-phase fluid model to analyse the effect of different boundary conditions on the heat transfer rate. Besides, the numerical works concerning the two-phase model for nanofluid are very limited, which motivates us to carry out the present work. The current nanofluid study can be distinguished into three objectives. First objective deals with the exploitation of established single-relaxation-time based two-phase LB model [Xuan and Yao, 2005] and the development of a new multiple-relaxation-time based two-phase model for nanofluid flow. Careful validation of current two-phase LB model with the published works is made. The second objective is to make a comparative analysis between recently developed hybrid nanofluids and regular nanofluids while simulating natural convection in a differentially heated square cavity. In this work, two hybrid Al_2O_3-Cu/water nanofluids with 9:1 and 7:3 mixture ratio of Al_2O_3 and Cu nanoparticles are considered respectively along with two different single-particle nanofluids Al_2O_3/water and Cu/water. The third objective is to use Al_2O_3-Cu/water nanofluid with 9:1 mixture ratio to investigate further by considering three different cases of buoyancy-assisted mixed convection cavity flow based on velocity and thermal boundary conditions. To the best of author's knowledge, the two-phase model for nanofluid was not considered before for this kind of flow conditions.

5.2 Numerical methodology for nanofluid flow

5.2.1 Determination of properties of a nanofluid

The thermophysical properties of the base fluid and copper- and alumina-nanoparticles are given in Table 5.1 [Incropera and DeWitt, 2002].

Table 5.1 Properties of water, copper and alumina at T = 300 K.

Property (unit)	Water	Cu	Al_2O_3
C_P (J kg^{-1} K^{-1})	4179	385	765
ρ (kg m^{-3})	997.1	8933	3970
k (W m^{-1} K^{-1})	0.613	401	36
β (K^{-1})	27.6×10^{-5}	1.67×10^{-5}	0.85×10^{-5}
d_p(m)	3.85×10^{-10}	2.5×10^{-8}	2.5×10^{-8}

The hybrid Al_2O_3-Cu nanoparticles is a mixture of Al_2O_3 and Cu nanoparticles in the ratio of 9:1 and 7:3 and their total volume fraction in water is considered up to 3%. The effective density of the hybrid water-based nanofluid is determined based on mixture theory formula for different $\varphi = \varphi_{Al_2O_3} + \varphi_{Cu}$ is given as [Sarkar et al., 2015]:

$$\rho_{nf} = (1-\varphi)\rho_f + \varphi_{Al_2O_3}\rho_{Al_2O_3} + \varphi_{Cu}\rho_{Cu} \tag{5.1}$$

The volumetric heat capacity at constant pressure and coefficient of thermal expansion of the nanofluid are respectively written as follows [Sarkar et al., 2015]:

$$(\rho C_P)_{nf} = (1-\varphi)(\rho C_P)_f + \varphi_{Al_2O_3}(\rho C_P)_{Al_2O_3} + \varphi_{Cu}(\rho C_P)_{Cu} \tag{5.2}$$

$$\beta_{nf} = \frac{(1-\varphi)(\rho\beta)_f + \varphi_{Al_2O_3}(\rho\beta)_{Al_2O_3} + \varphi_{Cu}(\rho\beta)_{Cu}}{\rho_{nf}} \tag{5.3}$$

Two empirical correlations as proposed by Corcione [2011] are adopted in current work for predicting the effective thermal conductivity and dynamic viscosity of nanofluid. These empirical correlations show a 1.86% standard deviation of error while comparing with a large number of experimental data available in the literature and are given as follows:

$$\mu_{nf} = \frac{\mu_f}{\left(1.0 - 34.87\left(\frac{d_p}{d_f}\right)^{-0.3} \varphi^{1.03}\right)} \tag{5.4}$$

$$k_{nf} = k_f\left(1.0 + 4.4{Re_p}^{0.4} Pr^{0.66}\left(\frac{T}{T_f}\right)^{10}\left(\frac{\varphi_{Al_2O_3}k_{Al_2O_3} + \varphi_{Cu}k_{Cu}}{\varphi k_f}\right)^{0.03} \varphi^{0.66}\right) \tag{5.5}$$

where the average nanofluid temperature T is taken as 300 K while fixing the temperature difference ΔT (= $T_h - T_c$) between the hot and cold walls at 10 K, T_f is the freezing point of water and d_p is the diameter of a nanoparticle. The nanoparticle Reynolds number Re_p is given as follows:

$$Re_p = \frac{(2\rho_f k_b T)}{(\pi {\mu_f}^2 d_p)} \tag{5.6}$$

The thermal diffusivity is obtained by:

$$\alpha_{nf} = \frac{k_{nf}}{(\rho C_P)_{nf}} \tag{5.7}$$

5.2.2 Forces acting on the two-phase nanofluid system

To interpret the dynamics of the suspended nanoparticles, the colloidal theory can be adopted while considering nanofluid as one type of colloidal suspension. Several interaction forces such as the drag, Brownian and thermophoresis forces between suspended nanoparticles and base fluid along with the external forces such as the buoyancy and gravitational forces are acted on the nanofluid system [Xuan and Yao, 2005] which are given in detail below:

The gravity and buoyancy force acted on the nanofluid system is:

$$\mathbf{F}_{\mathrm{H}} = -\frac{\pi d_p^3 \mathbf{g}\Delta\rho}{6} \tag{5.8}$$

where $\Delta\rho$ is the mass density difference between the suspended nanoparticle and the base fluid.

The Drag force acts in the direction opposite to the motion of a particle in a fluid. Hence, it is proportional to the velocity difference Δu between the nanoparticle and the base fluid known as the slip velocity in the nanofluid system. The drag force is calculated while satisfying the Stokes law assumptions as follows:

$$\mathbf{F}_{\mathrm{D}} = -6\pi d_p \mu_f \Delta \mathbf{u} \tag{5.9}$$

where μ_f refers to the viscosity of the fluid.

The continuous collision of suspended nanoparticles with the base fluid molecules results in the random motion of particles known as Brownian motion. The force causes Brownian motion known as Brownian force is determined as a Gaussian white noise process [Eslamian et al., 2015]:

$$\mathbf{F}_{\mathrm{B}} = \mathrm{G_i}\sqrt{\frac{6\pi d_p \mu_f k_B \theta}{\Delta t}} \tag{5.10}$$

where $\mathrm{G_i}$ is referred to as zero-mean Gaussian random number with unit variance and k_B is the Boltzmann constant.

The thermophoretic force is applied to suspended nanoparticles in the opposite direction of temperature gradient due to the migration of particles from the zone of higher temperature to lower temperature. The thermophoretic force based on the Stokes equation is expressed as [Eslamian et al., 2015]:

$$\mathbf{F}_{\mathrm{T}} = 3\pi d_p \mu_f \mathbf{U}_{\mathrm{T}} \tag{5.11}$$

The thermophoretic velocity $\mathbf{U}_{\mathrm{T}}$ can be termed as nanoparticle migration velocity, which is presented as:

$$\mathbf{U}_{\mathrm{T}} = -D_{\mathrm{T}} \Delta\theta \tag{5.12}$$

The thermophoretic diffusion coefficient D_{T} in a liquid is calculated based on hydrodynamics theory as below:

$$D_{\mathrm{T}} = 2A \frac{k_f}{2k_f + k_p} \frac{\mu_f}{\rho_f \theta} \tag{5.13}$$

The A is a coefficient which is the function of physical properties and temperature of the base fluid.

The total forces per unit volume acting on a nanoparticle and base fluid in the lattice Boltzmann method are given as follows [Xuan and Yao, 2005]:

$$\mathbf{N}^p = \frac{n}{V}\left(\mathbf{F}_\mathrm{H} + \mathbf{F}_\mathrm{D} + \mathbf{F}_\mathrm{B} + \mathbf{F}_\mathrm{T}\right) \tag{5.14}$$

$$\mathbf{N}^f = -\frac{n}{V}\left(\mathbf{F}_\mathrm{D} + \mathbf{F}_\mathrm{B}\right) \tag{5.15}$$

where n is the number of particles in the given lattice with lattice volume V.

5.2.3 SRT based two-phase thermal lattice Boltzmann method

In the current work, the nanofluid is considered as a non-homogeneous two-phase (or two-component) fluid which considers a significant slip velocity between nanoparticles and the base fluid. The fluid flow is two dimensional, laminar, incompressible, and Newtonian. The thermo-physical properties are kept constant for both fluid and nanoparticles except the density in the buoyancy force term, which is satisfied by the Boussinesq approximation. Therefore, to simulate nanofluid flow using LBM, the two-component based DDF approach is implemented, where each component is treated with separate density distribution functions and temperature distribution functions as follows [Xuan and Yao, 2005]:

$$f_i^{\sigma}(\mathbf{r} + \mathbf{e}_i\Delta t, t + \Delta t) = f_i^{\sigma}(\mathbf{r}, t) + \frac{1}{\tau_v{}^{\sigma}}\left(f_i^{\sigma eq}(\mathbf{r}, t) - f_i^{\sigma}(\mathbf{r}, t)\right) + P_i^{\sigma} \tag{5.16}$$

where $\sigma = f$ and p represent the two components of nanofluid, respectively the base fluid and suspended nanoparticles. The distribution function f_i^{σ} for each component are relaxed towards their equilibrium distribution function $f_i^{\sigma eq}$ by using respective single relaxation parameters $\tau_v{}^{\sigma}$ as given below [Xuan and Yao, 2005]:

$$f_i^{\sigma eq} = \rho^{\sigma} w_i \left\{1.0 + \frac{\mathbf{e}_i.\mathbf{u}^{\sigma}}{C_s^2} + \frac{(\mathbf{e}_i.\mathbf{u}^{\sigma})^2}{2C_s{}^4} - \frac{\mathbf{u}^{\sigma 2}}{2C_s^2}\right\} \tag{5.17}$$

In LBM, the total force ($P_i{}^{\sigma}$) in the nanofluid flow system is calculated as below:

$$P_i{}^{\sigma} = dt\left\{1 - \frac{1}{2\tau_v{}^{\sigma}}\right\}\left\{\frac{\mathbf{e}_i - \mathbf{u}^{\sigma}}{C_s^2} + \frac{\mathbf{e}_i(\mathbf{e}_i.\mathbf{u}^{\sigma})}{C_s^4}\right\}.\{w_i\mathbf{G} + B_i\mathbf{N}^{\sigma}\} \tag{5.18}$$

where $\mathbf{N}^{\sigma}$ refers to the total inter-particle interaction forces acted on σ^{th} component of the nanofluid per unit lattice volume and B_i is the adjustable coefficient as given below [Eslamian et al., 2015]:

$$B_i = \begin{Bmatrix} 0 & i = 0 \\ \frac{1}{9} & i = 1,..,4 \\ \frac{1}{36} & i = 5,..,8 \end{Bmatrix} \tag{5.19}$$

The external force term $\mathbf{G}$ is the buoyancy force experienced by the base fluid as the summation of buoyancy and gravity force acted on nanoparticles is considered separately in equation 5.8. Therefore, $\mathbf{G}$ is calculated based on the base fluid properties, and it is given as:

$$\mathbf{G} = \rho_f \mathbf{g}\beta_f(\theta - \theta_m) \tag{5.20}$$

where ρ_f is the base fluid density at the reference temperature θ_m and β_f is the coefficient of thermal expansion of the base fluid.

The macroscopic kinetic viscosity ν^{σ} is related to lattice parameter $\tau_v{}^{\sigma}$ as:

$$\nu^{\sigma} = C_s^2\left(\tau_v{}^{\sigma} - \frac{1}{2}\right) \tag{5.21}$$

The governing two-phase discretised lattice Boltzmann equation for temperature distribution function is [Xuan and Yao, 2005]:

$$g_i{}^{\sigma}(\mathbf{r} + \mathbf{e}_i\Delta t, t + \Delta t) = g_i{}^{\sigma}(\mathbf{r}, t) + \frac{1}{\tau_\theta{}^{\sigma}}\left(g_i^{\sigma eq}(\mathbf{r}, t) - g_i{}^{\sigma}(\mathbf{r}, t)\right) \tag{5.22}$$

The equilibrium distribution function $g_i^{\sigma eq}$ for each component is presented as [Xuan and Yao, 2005]:

$$g_i^{\sigma eq} = w_i\theta^{\sigma}\left\{1.0 + \frac{\mathbf{e}_i.\mathbf{u}^{\sigma}}{2C_s^2}\right\} \tag{5.23}$$

The macroscopic thermal diffusivity for each component α^{σ} is related to the single relaxation time ${\tau_\theta}^{\sigma}$ as:

$$\alpha^{\sigma} = C_s^2\left({\tau_\theta}^{\sigma} - \frac{1}{2}\right) \tag{5.24}$$

5.2.4 MRT based two-phase thermal lattice Boltzmann method

To simulate nanofluid flow and heat transfer, the MRT based two-phase LB model is formulated in this work. The governing equation for this model to determine density distribution functions is given as follows:

$$\begin{aligned}&\mathbf{f}^{\sigma}(\mathbf{r}+\mathbf{e}_i\Delta t, t+\Delta t) - \mathbf{f}^{\sigma}(\mathbf{r},t)\\ &\quad = -\mathrm{M}^{-1}\mathrm{R}^{\sigma}\{\mathbf{m}^{\sigma}(\mathbf{r},t) - \mathbf{m}^{\sigma,eq}(\mathbf{r},t)\} + \mathrm{M}^{-1}\left(\mathrm{I}-\frac{\mathrm{R}^{\sigma}}{2}\right)\mathbf{S}^{\sigma}\end{aligned} \tag{5.25}$$

Where σ refers to two components of nanofluid, $\sigma = f$ for base fluid and $\sigma = p$ for suspended nanoparticles. The distribution functions ($\mathbf{f}^{\sigma}$) and its moments ($\mathbf{m}^{\sigma}$) are represented in vector form as follows:

$$\mathbf{f}^{\sigma}(\mathbf{r},t) = \{f_0^{\sigma}(\mathbf{r},t), f_1^{\sigma}(\mathbf{r},t), \dots\dots, f_8^{\sigma}(\mathbf{r},t)\}^{\mathrm{T}} \tag{5.26}$$

$$\mathbf{m}^{\sigma}(\mathbf{r},t) = \{m_0^{\sigma}(\mathbf{r},t), m_1^{\sigma}(\mathbf{r},t), \dots\dots, m_8^{\sigma}(\mathbf{r},t)\}^{\mathrm{T}} \tag{5.27}$$

The transformation matrix $\mathbf{M}$ linearly transforms the distribution functions ($\mathbf{f}^{\sigma}$) for both components to their velocity moments ($\mathbf{m}^{\sigma}$) and vice-versa as expressed below:

$$\mathbf{m}^{\sigma} = \mathbf{M}\mathbf{f}^{\sigma}, \ \mathbf{f}^{\sigma} = \mathbf{M}^{-1}\mathbf{m}^{\sigma} \tag{5.28}$$

The equilibrium moments $\mathbf{m}^{\sigma,eq}$ in vector form is given by,

$$\mathbf{m}^{\sigma,eq} = \left\{\rho^{\sigma}\left(1, -2+3\mathbf{u}^{\sigma 2}, 1-3\mathbf{u}^{\sigma 2}, u_x^{\sigma}, -u_x^{\sigma}, u_y^{\sigma}, -u_y^{\sigma}, u_x^{\sigma 2} - u_y^{\sigma 2}, u_x^{\sigma}u_y^{\sigma}\right)\right\}^{\mathrm{T}} \tag{5.29}$$

The total force term ($\mathbf{S}^{\sigma}$) are presented by column vector as follows:

$$\begin{aligned}\mathbf{S}^{\sigma} = \Big\{\rho^{\sigma}\big(0, 6\mathbf{u}^{\sigma}.\mathbf{P}^{\sigma}, -6\mathbf{u}^{\sigma}.\mathbf{P}^{\sigma}, P_x^{\sigma}, -P_x^{\sigma}, P_y^{\sigma}, -P_y^{\sigma}, 2(u_x^{\sigma}P_x^{\sigma} - u_y^{\sigma}P_y^{\sigma}), (u_x^{\sigma}P_y^{\sigma}\\ + u_y^{\sigma}P_x^{\sigma})\big)\Big\}^{\mathrm{T}}\end{aligned} \tag{5.30}$$

where

$$P_x^f = \mathbf{N}^f;\ P_y^f = \mathbf{G} + \mathbf{N}^f \tag{5.31}$$

$$P_x^p = P_y^p = \mathbf{N}^p \tag{5.32}$$

In moment space the diagonal relaxation matrix R^σ is given as:

$$\mathrm{R}^\sigma = \mathrm{diag}(1, r_e^\sigma, r_\in^\sigma, 1, r_q^\sigma, 1, r_q^\sigma, r_v^\sigma, r_v^\sigma) \tag{5.33}$$

The parameter r_v^σ is linked to ν^σ as:

$$\frac{1}{r_v^\sigma} = \frac{\nu^\sigma}{C_s^2} + \frac{1}{2} \tag{5.34}$$

The governing two-component MRT-LB equation for temperature field is formulated as:

$$g_i{}^\sigma(\mathbf{r} + \mathbf{e}_i\Delta t, t + \Delta t) - g_i{}^\sigma(\mathbf{r}, t) = -\mathbf{N}^{-1}\mathrm{C}^\sigma\{\mathbf{n}^\sigma(\mathbf{r}, t) - \mathbf{n}^{\sigma,eq}(\mathbf{r}, t)\} \tag{5.35}$$

For D2Q5 model, the suffix i refers to 5 discrete velocities. C^σ is the diagonal relaxation matrix for thermal D2Q5 model is given by,

$$\mathrm{C}^\sigma = \mathrm{diag}(1, c_\theta^\sigma, c_\theta^\sigma, c_e^\sigma, c_v^\sigma) \tag{5.36}$$

The relaxation parameter c_θ^σ in Eqn. (5.36) is determined by the α^σ as given below:

$$\frac{1}{c_\theta^\sigma} = \frac{10\alpha^\sigma}{(4 + a)} + \frac{1}{2} \tag{5.37}$$

The transformation matrix **N** is a 5×5 matrix which linearly transforms the **g** to **n** and vice-versa as follows

$$\mathbf{n} = \mathbf{N}\mathbf{g},\ \mathbf{g} = \mathbf{N}^{-1}\mathbf{n} \tag{5.38}$$

The equilibrium moments $\mathbf{n}^{\sigma,eq}$ is given by,

$$\mathbf{n}^{\sigma,eq} = \left(\theta^\sigma, u_x^\sigma.\theta^\sigma, u_y^\sigma.\theta^\sigma, a\theta^\sigma, 0\right)^{\mathrm{T}} \tag{5.39}$$

5.2.5 Calculations of macroscopic variables

In LBM, the macroscopic variables are obtained by taking moments of the distribution function. The fluid density ρ^σ and velocity $\mathbf{u}^\sigma$ for both components are calculated by taking 0th and 1st moments of $f_i{}^\sigma$ respectively. However, for the simulation

nanofluid flow, the velocity $\mathbf{u}^{\sigma}$ is modified by considering the inter-particle forces acting on the nanofluid system as follows:

$$\rho^{\sigma} = \sum_{i=0}^{8} f_i{}^{\sigma} \tag{5.40}$$

$$\rho^{f}\mathbf{u}^{f} = \sum_{i=0}^{8} f_i{}^{f}\,\mathbf{e}_i + \frac{(\mathbf{G}+\mathbf{N}^{f})}{2} \tag{5.41}$$

$$\rho^{p}\mathbf{u}^{p} = \sum_{i=0}^{8} f_i{}^{p}\,\mathbf{e}_i + \frac{\mathbf{N}^{p}}{2} \tag{5.42}$$

In TLBM, temperature for each component (θ^{σ}) is calculated as 0^{th} moments of $g_i{}^{\sigma}$ as given below:

$$\theta^{\sigma} = \sum_{i=0}^{8} g_i{}^{\sigma} \tag{5.43}$$

The overall velocity and temperature of nanofluid are calculated based on the mixture theory formula [Xuan and Yao, 2005] as follows:

$$\rho_{nf}\mathbf{u}_{nf} = (1-\varphi)\rho^{f}\mathbf{u}^{f} + \varphi\rho^{p}\mathbf{u}^{p} \tag{5.44}$$

$$\theta_{nf} = (1-\varphi)\theta^{f} + \varphi\theta^{p} \tag{5.45}$$

5.3 Grid independence study

To simulate natural convection in the cavity, a grid sizes of 151×151 for $Ra = 10^3$, 201×201 for $Ra = 10^4$ and 301×301 for $Ra = 10^5$ are used for all computations (as obtained from grid independence test shown in chapter 4 in section 4.3.1 for natural convection in a water-filled cavity) while maintaining volume fraction of nanoparticles (φ) equal to zero.

Fig. 5.1 shows a grid-independence test for each of the three different cavity configurations of mixed convection flows in a nanofluid-filled square cavity for $Ri = 1.0$ at $Gr = 10^4$ with $\varphi = 0.02$. The results obtained for five different grid sizes of 151×151, 201×201, 251×251, 301×301 and 351×351 are compared by using average Nusselt

number along the hot wall of the cavity $\overline{Nu}$ and average total entropy generation throughout the cavity $\overline{S_{tot}}$. It is observed that the grid size of 301×301 is suitable for all computations to retain the time-wise efficiency of the numerical simulations.

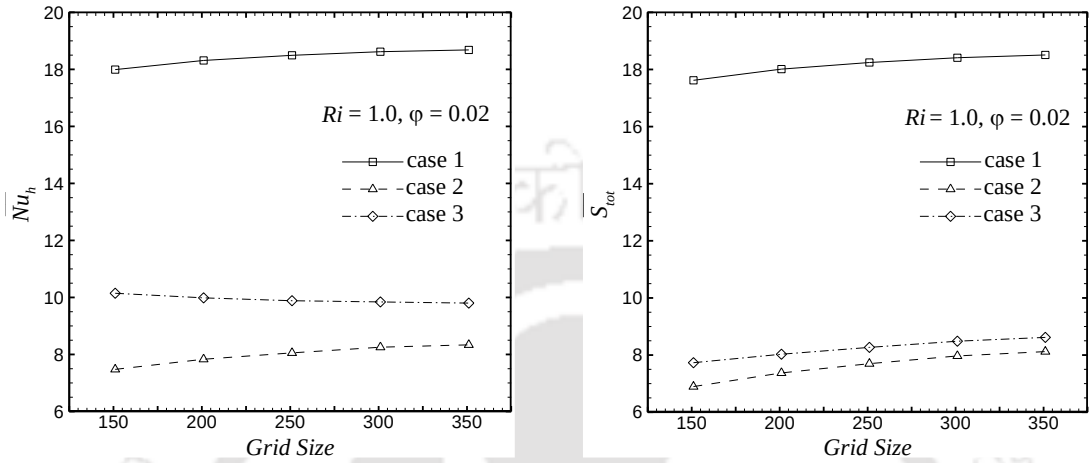

(a) (b)

Fig. 5.1. Variation of (a) $\overline{Nu_h}$ and (b) $\overline{S_{tot}}$ with grid size for each of the three different cases.

5.4 Code validation

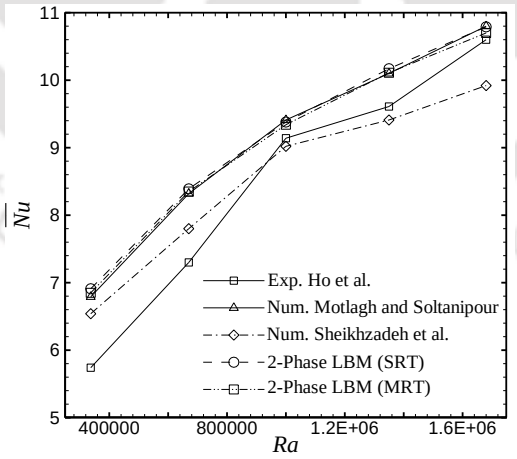

Fig. 5.2. Comparison of the present results for the average Nusselt number $\overline{Nu}$ with the experimental- and numerical results.

The results of present SRT- and MRT- based two-phase LBM codes are validated with Ho et al.'s experimental work [2010] and Buongiorno's nanofluid model-based

numerical works of Sheikhzadeh et al. [2013] and Motlagh and Soltanipour [2017] while simulating natural convection in a square cavity filled with Al_2O_3-nanofluid for different *Ra* at φ = 3%. Fig. 5.2 shows a very close agreement of results in terms of average Nu with Motlagh and Soltanipour [2017] and reasonable agreement with Sheikhzadeh et al. [2013] and Ho et al. [2010]. However, a deviation of numerical results from Ho et al.'s experimental work is observed at $Ra \leq 10^6$, as for the numerical model it is difficult to take into consideration of all possible hydro-thermal behaviours of nanofluids although these published works of conventional numerical techniques and current LBM model take into account different slip mechanisms of nanofluid.

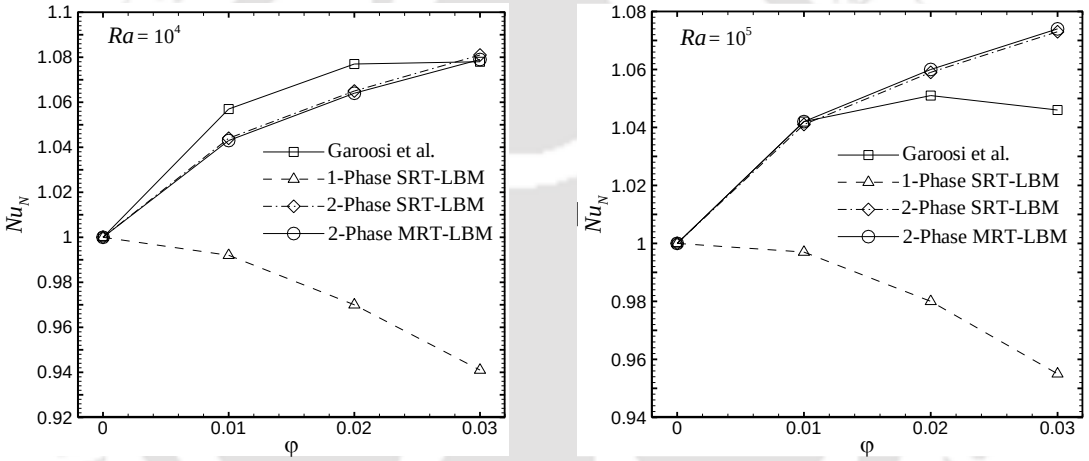

Fig. 5.3. Comparison of the normalised Nusselt number $\overline{Nu}_N$ for current single- and two-phase LBM with Garoosi et al. [2014].

Furthermore, to check the ability of the code for the simulation of nanofluid heat transfer, an attempt is made to compare both SRT- and MRT- based two-phase LBM and standard SRT-based single-phase LBM model with the published work of Garoosi et al. [2014] in terms of normalised Nusselt number $\overline{Nu}_N = \overline{Nu}_\varphi / \overline{Nu}_{\varphi=0}$ for two different particle diameters at *Ra* = 10^4 and 10^5, as shown in Fig. 5.3. The results reveal that the single-component LB model fails to mimic the nanofluid flow behaviour during natural convection for all calculated *Ra*'s. However, both two-phase LBM models have successfully obtained the desired accuracy. Besides, the results obtained by SRT- and

MRT- based two-phase LBM are comparable to each other, which allows carrying out the present computations using either one of two-phase LBM code.

The competency of both two-phase LBM codes is checked further to simulate a mixed convection nanofluid flow in a two-sided lid-driven cavity. The results are validated with the published work of Garoosi et al. [2014]. Fig. 5.4 depicts the results in terms of normalised Nusselt number $\overline{Nu}_N$ for two different Ri = 0.1 and 10 at $Gr = 10^4$ with volume fraction of Al_2O_3 nanoparticles φ ranging from 0% to 3% with diameter (d_p) = 25 nm. It is found that the results for single-phase LB model deviate from two-phase LBM, which provides close resemblance to the published results. Therefore, based on these validations, it can be concluded that both two-phase LBM models provide solutions with higher accuracy.

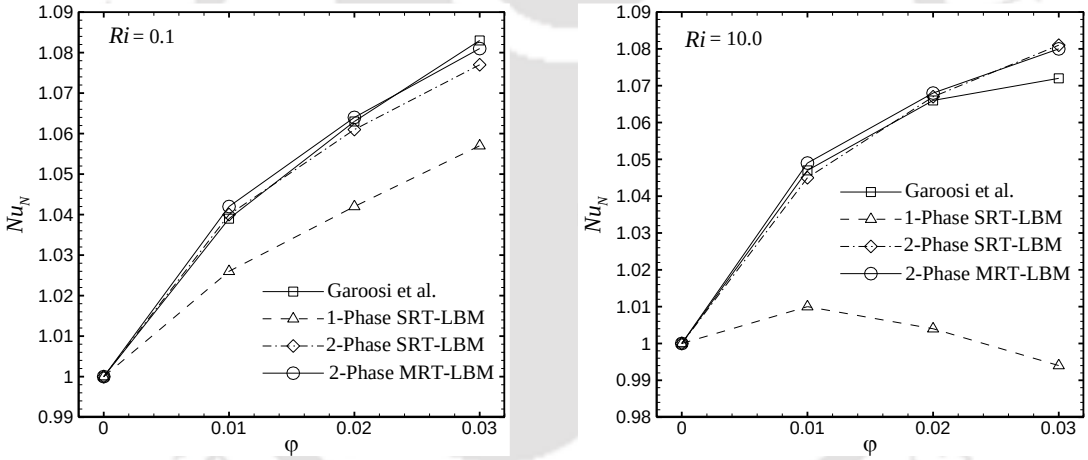

Fig. 5.4. Comparison of the normalised Nusselt number $\overline{Nu}_N$ for current single- and two-phase LBM with Garoosi et al. [2014].

5.5 Formulation of the first problem: Comparative study of hybrid nanofluid with regular nanofluid during natural convection in a cavity

The benchmark problem of natural convection flow in a square cavity filled with nanofluid is considered for current flow configuration where the vertical walls are

differentially heated, and the horizontal walls are thermal insulated. The non-dimensional form of the boundary conditions is given as follows:

$$\begin{aligned} &u = 0; \quad v = 0; \quad \frac{\partial \theta}{\partial y} = 0 \quad \text{at } y = 0 \text{ and } 1 \\ &u = 0; \quad v = 0; \quad \theta = 1 \quad \text{at } x = 0 \\ &u = 0; \quad v = 0; \quad \theta = 0 \quad \text{at } x = 1 \end{aligned} \tag{5.46}$$

5.5.1 Results and discussion

The detailed comparative studies between hybrid Al_2O_3-Cu/water nanofluids and regular Al_2O_3/water nanofluids during natural convection in a cavity problem are made on the basis of average Nu along the left hot wall ($\overline{Nu}_{lh}$), average total entropy generation due to heat transfer irreversibility ($\overline{S_\theta}$) and fluid friction irreversibility ($\overline{S_\psi}$) and performance coefficient parameter ($\overline{Nu_N}/\overline{S_{tot,N}}$). Four different water-based nanofluids are considered, which are two hybrid Al_2O_3-Cu/water nanofluids with 9:1 and 7:3 mixture ratio of Al_2O_3 and Cu nanoparticles respectively and two separate single-particle nanofluid Al_2O_3/water and Cu/water respectively. The simulations are carried out for Rayleigh numbers Ra = 10^3, 10^4 and 10^5 while considering the volume fraction of nanoparticles up to 3%.

5.5.1.1 Heat transfer rates: Nusselt numbers

Figs. 5.5(a), (c) and (e) show that the heat transfer rate is maximum with Cu/water nanofluid due to its higher thermal conductivity and minimum with Al_2O_3/water nanofluid at Ra = 10^3, 10^4 and 10^5. The heat transfer rate is presented in terms of the average Nusselt number along the hot wall ($\overline{Nu_h}$) of the cavity. Higher percentage augmentation of $\overline{Nu_h}$ with φ is found at Ra = 10^3 for all four nanofluids as the conductive effect is more prominent than convective effect. However, this percentage deteriorates with increase in φ, which is more evident for Al_2O_3/water nanofluid. This is attributed to the more

substantial retardation effect of viscosity of nanofluid compared to the aiding effect of thermal conductivity.

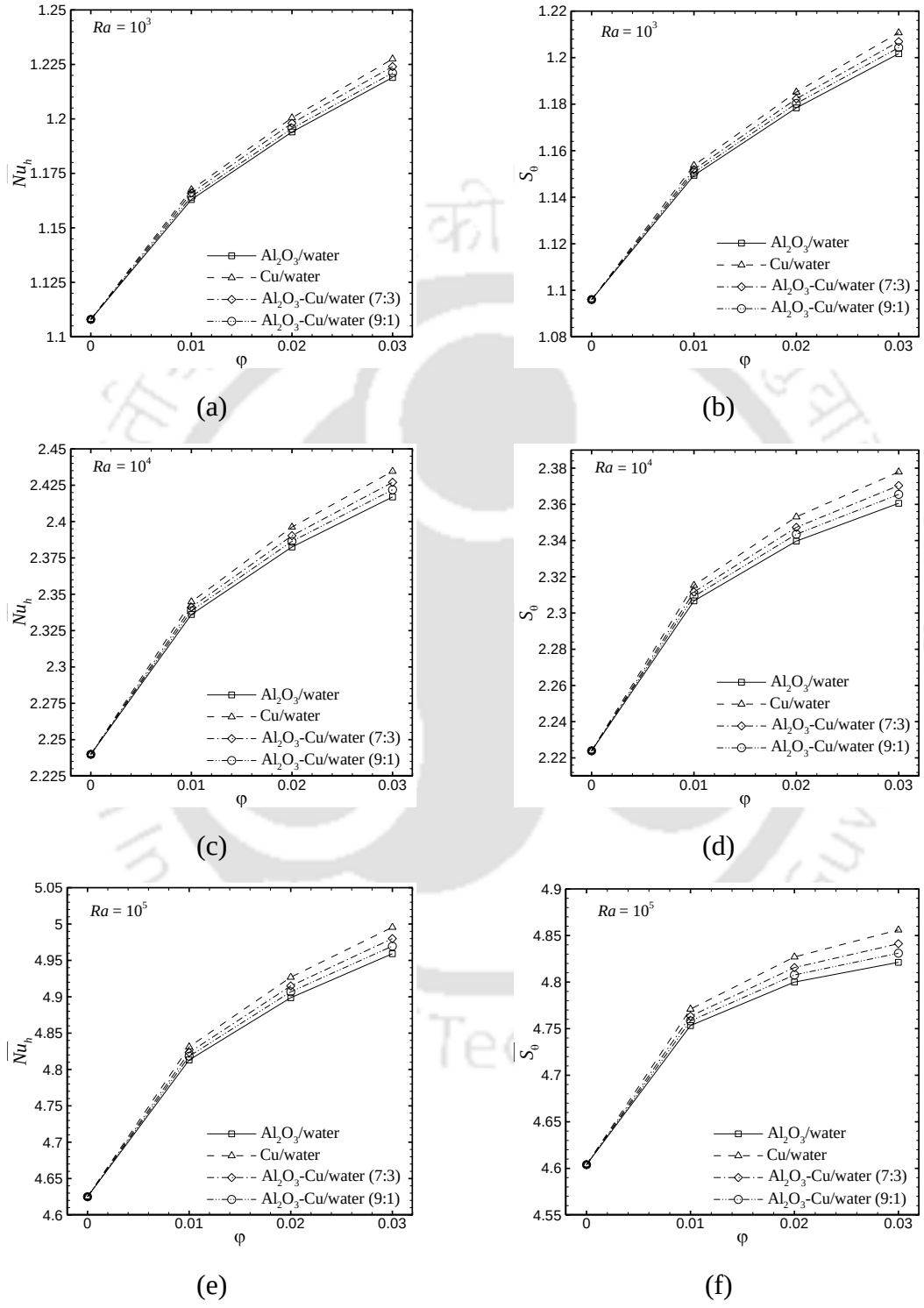

Fig. 5.5. Variations of $\overline{Nu_h}$ (a, c and e) and $\overline{S_\theta}$ (b, d and f) with φ of all four nanofluids for $Ra = 10^3$ (top panel), $Ra = 10^4$ (middle panel) and $Ra = 10^5$ (bottom panel).

5.5.1.2 Entropy generation

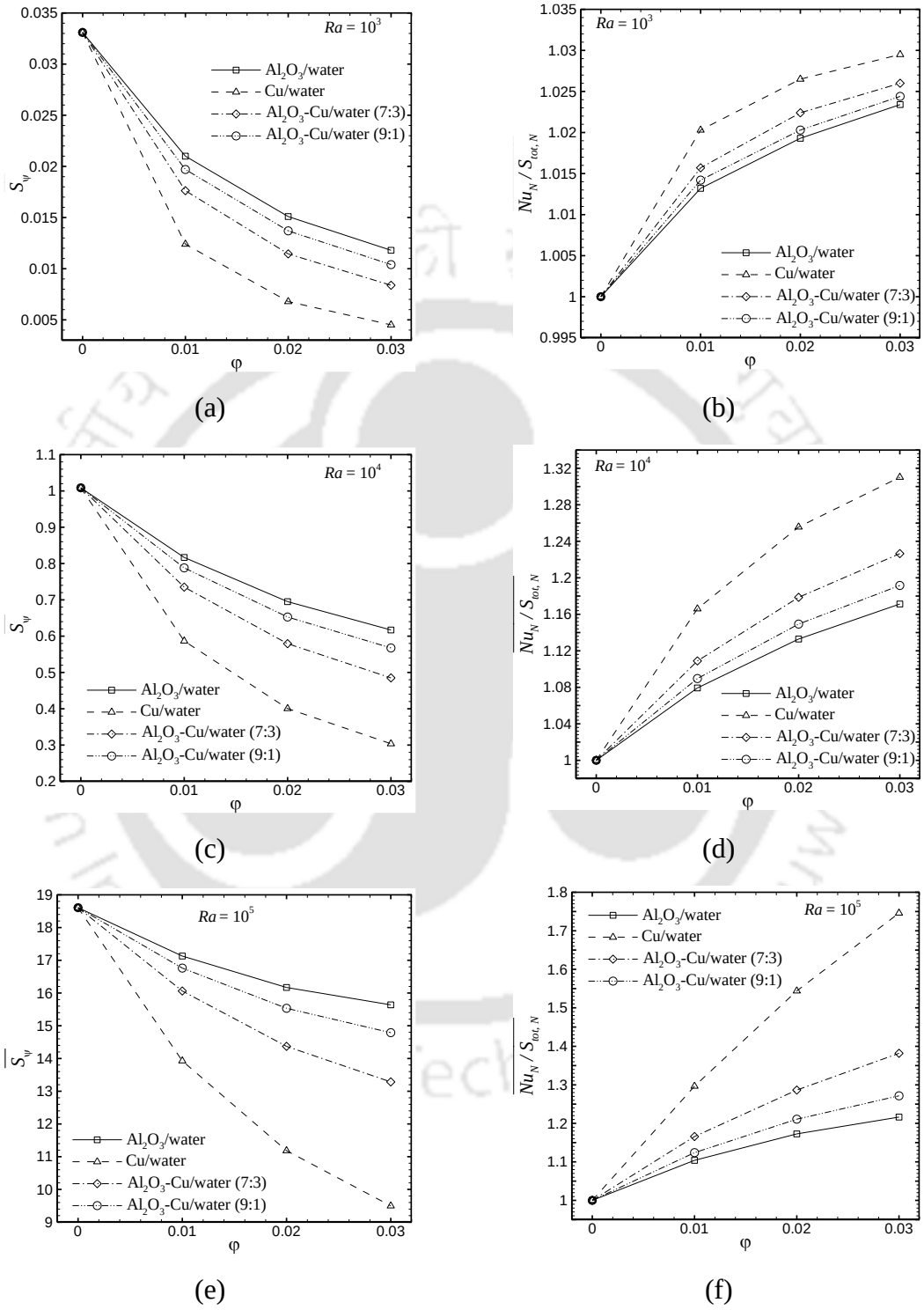

Fig. 5.6. Variations of $\overline{S_\psi}$ (a, c and e) and $\overline{Nu_N}/\overline{S_{tot,N}}$ (b, d and f) with φ of all four nanofluids for $Ra = 10^3$ (top panel), $Ra = 10^4$ (middle panel) and $Ra = 10^5$ (bottom panel).

Figs. 5.5(b), (d) and (f) depict that the average entropy generation due to heat transfer ($\overline{S_\theta}$) throughout the cavity follows the same pattern as the average Nusselt number along the hot wall of the cavity with φ as both are the function of temperature gradients. It is observed from Figs. 5.6(a), (c) and (e) that the average total entropy generation due to viscous effect ($\overline{S_\psi}$) continuously decreases with increase in φ for Cu/water nanofluid as fluid velocity decreases due to retardation of convective effect.

5.5.1.3 Performance analysis

In order to evaluate the effect of volume fractions of nanoparticles in terms of energy efficiency, the performance coefficient parameter is considered which is the ratio between the normalised average Nusselt number ($\overline{Nu_N} = \overline{Nu}/\overline{Nu_{\varphi=0}}$) and the normalised average total entropy generation due to both heat transfer and fluid friction irreversibilities ($\overline{S_{tot,N}} = \overline{S_{tot}}/\overline{S_{tot,\varphi=0}}$). It is observed from Figs. 5.6(b), (d) and (f) that $\overline{Nu_N}/\overline{S_{tot,N}}$ increases with φ for all *Ra*s. The percentage enhancement of performance coefficient parameter with φ is found to be higher at *Ra* = 10^5 due to the reduction of $\overline{S_\psi}$. The maximum and minimum magnitudes of performance coefficient parameter are obtained for Cu/water nanofluid and Al_2O_3/water nanofluid respectively. Therefore, from the viewpoints of both 1st and 2nd law of thermodynamics, it is evident that Cu/water nanofluid provides better energy efficiency compared to other three nanofluids in a natural convection cavity flow system.

5.5.1.4 Conclusions

In the current work, a comparative study is made between hybrid nanofluids and regular nanofluids during natural convection in a differentially heated cavity on the basis of energy efficiency. Two hybrid Al_2O_3-Cu/water nanofluids with 9:1 and 7:3 mixture ratio of Al_2O_3 and Cu nanoparticles and two different single-particle nanofluids, namely, Al_2O_3/water and Cu/water are considered. A two-component thermal lattice Boltzmann model for nanofluid is adopted, which provides a solution with better accuracy than the single-component LB

model. The results are obtained for Ra = 10^3 and 10^5 while keeping volume fraction $\varphi \leq$ 3%. It is obtained from the results that Cu/water nanofluid has a higher heat transfer rate due to its higher thermal conductivity compared to other nanofluids. Besides, Cu/water nanofluid has lower entropy generation due to viscous effect, thus making it the most energy-efficient in terms of performance coefficient for natural convection cavity flow system. However, it possesses lower stability and chemical inertness. Therefore considering this, the Al_2O_3-Cu/water hybrid nanofluid can serve as an alternative fluid as it provides favourable conditions in terms of efficiency as well as stability due to its synergistic effect resulting from two different single-particle nanofluids.

5.6 Formulation of the second problem: Mixed convection in a hybrid Al_2O_3-Cu/Water nanofluid saturated cavity

Figs. 5.7(a)-(c) show the schematic diagrams for the current mixed convection problem in a closed square cavity of unit length. Three different configurations of boundary conditions based on moving walls and differentially heated walls are presented in the dimensional form.

Case 1: The hot left wall moves upward, and the cold right wall moves downward with a constant speed V_0^* while maintaining the stationary horizontal walls thermally insulated (Fig. 5.7(a)).

Case 2: The thermally insulated top wall moves towards the right and the bottom wall towards left with a constant speed V_0^*. The vertical walls are stationary while maintaining the left wall at a higher temperature than the right wall (Fig. 5.7(b)).

Case 3: The thermally insulated vertical walls move upward with a constant speed V_0^*. The horizontal walls stationary while maintaining the bottom wall at a higher temperature than the top wall (Fig. 5.7(c)).

All three flow configurations considered in the current problem are the cases of aiding mechanism of mixed convection flow where shear-driven flow due to the direction

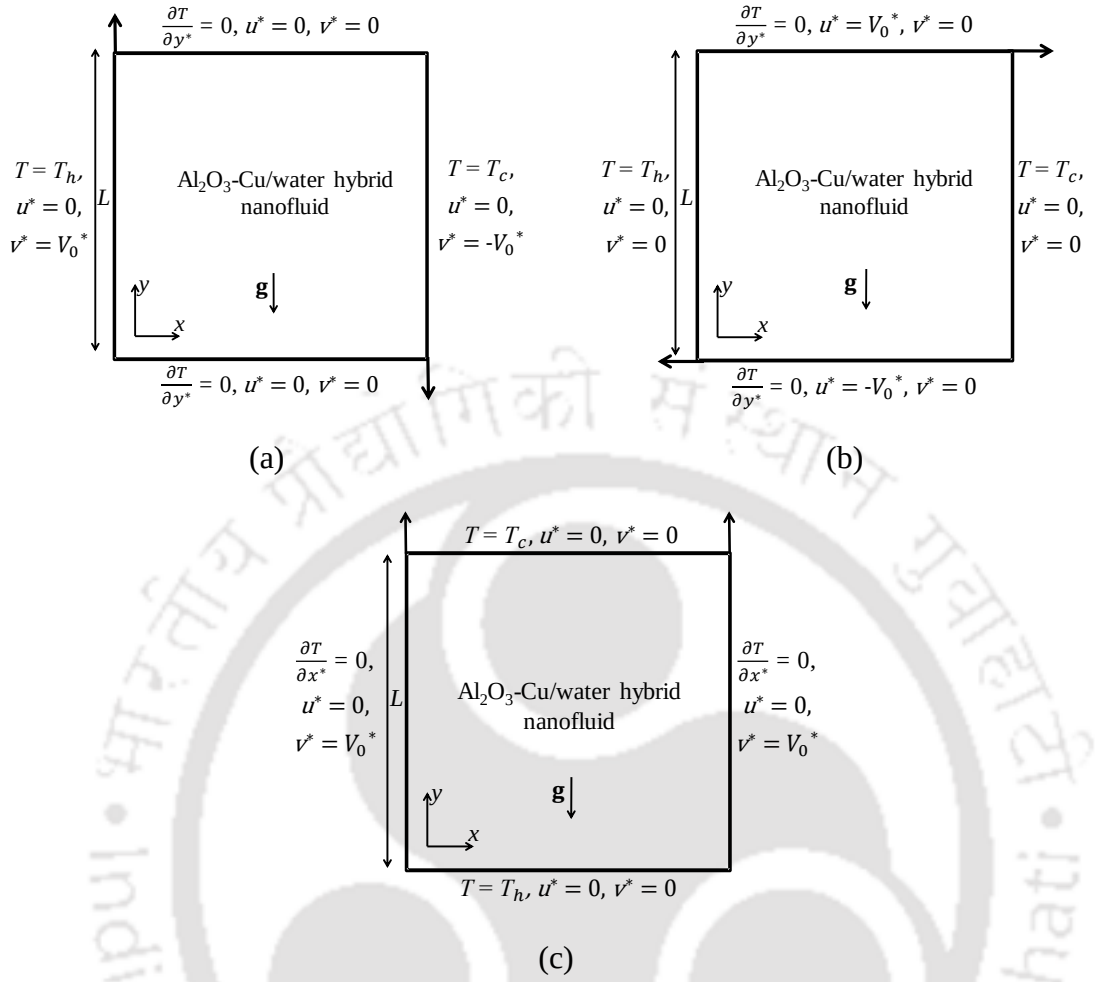

Fig. 5.7. Schematic diagram of the flow configuration with boundary conditions for (a) Case 1, (b) case 2 and (c) case 3.

of moving walls assists the buoyancy-driven flow due to differentially heated walls of the cavity. The non-dimensional variables of the current flow problem can be expressed as:

$$x = \frac{x^*}{L};\qquad y = \frac{y^*}{L};\qquad u = \frac{u^*}{V_0^*};\qquad v = \frac{v^*}{V_0^*};\qquad \theta = \frac{T-T_c}{T_h-T_c} \tag{5.47}$$

The non-dimensional form of the three boundary conditions are presented as follows:

Case 1:

$$\begin{aligned} &u = 0; && v = 0; && \frac{\partial \theta}{\partial y} = 0 && \text{at } y = 0 \text{ and } 1 \\ &u = 0; && v = 1; && \theta = 1 && \text{at } x = 0 \\ &u = 0; && v = -1; && \theta = 0 && \text{at } x = 1 \end{aligned} \tag{5.48a}$$

Case 2:

$$\begin{aligned} u &= -1; & v &= 0; & \frac{\partial \theta}{\partial y} &= 0 & \text{at } y &= 0 \\ u &= 1; & v &= 0; & \frac{\partial \theta}{\partial y} &= 0 & \text{at } y &= 1 \\ u &= 0; & v &= 0; & \theta &= 1 & \text{at } x &= 0 \\ u &= 0; & v &= 0; & \theta &= 0 & \text{at } x &= 1 \end{aligned} \tag{5.48b}$$

Case 3:

$$\begin{aligned} u &= 0; & v &= 0; & \theta &= 1 & \text{at } y &= 0 \\ u &= 0; & v &= 0; & \theta &= 0 & \text{at } y &= 1 \\ u &= 0; & v &= 1; & \frac{\partial \theta}{\partial x} &= 0 & \text{at } x &= 0 \text{ and } 1 \end{aligned} \tag{5.48c}$$

5.6.1 Results and discussion

A detailed comparative study of three different boundary conditions is made to get an idea of the optimal condition in terms of entropy generation and heat transfer characteristics. A number of simulations are carried out for each case to investigate the effect of Richardson number Ri ($0.1 \leq Ri \leq 10$) and volume fraction of hybrid nanoparticle φ ($\leq 3\%$) on fluid flow and heat transfer behaviour. The results are presented in detail in the following sections in terms of stream functions, isotherms, Nusselt number, entropy generation, thermal mixing, and temperature uniformity.

5.6.1.1 Effect of boundary conditions on stream function contours

Figs. 5.8-5.11 present the results for three different cases of aiding mechanism of mixed convection in a water-saturated cavity in terms of contours of dimensionless stream function, isotherm, and local entropy generation due to heat transfer and fluid friction respectively. The results are obtained for varying Ri from 0.1 to 10 with $Gr = 10^4$ and $Pr = 6.2$ respectively. It is observed from the streamlines plot for Case 1 and Case 2 (Figs. 5.8(a) and (d)) that a single clockwise-rotating primary vortex is formed due to heating up of fluid

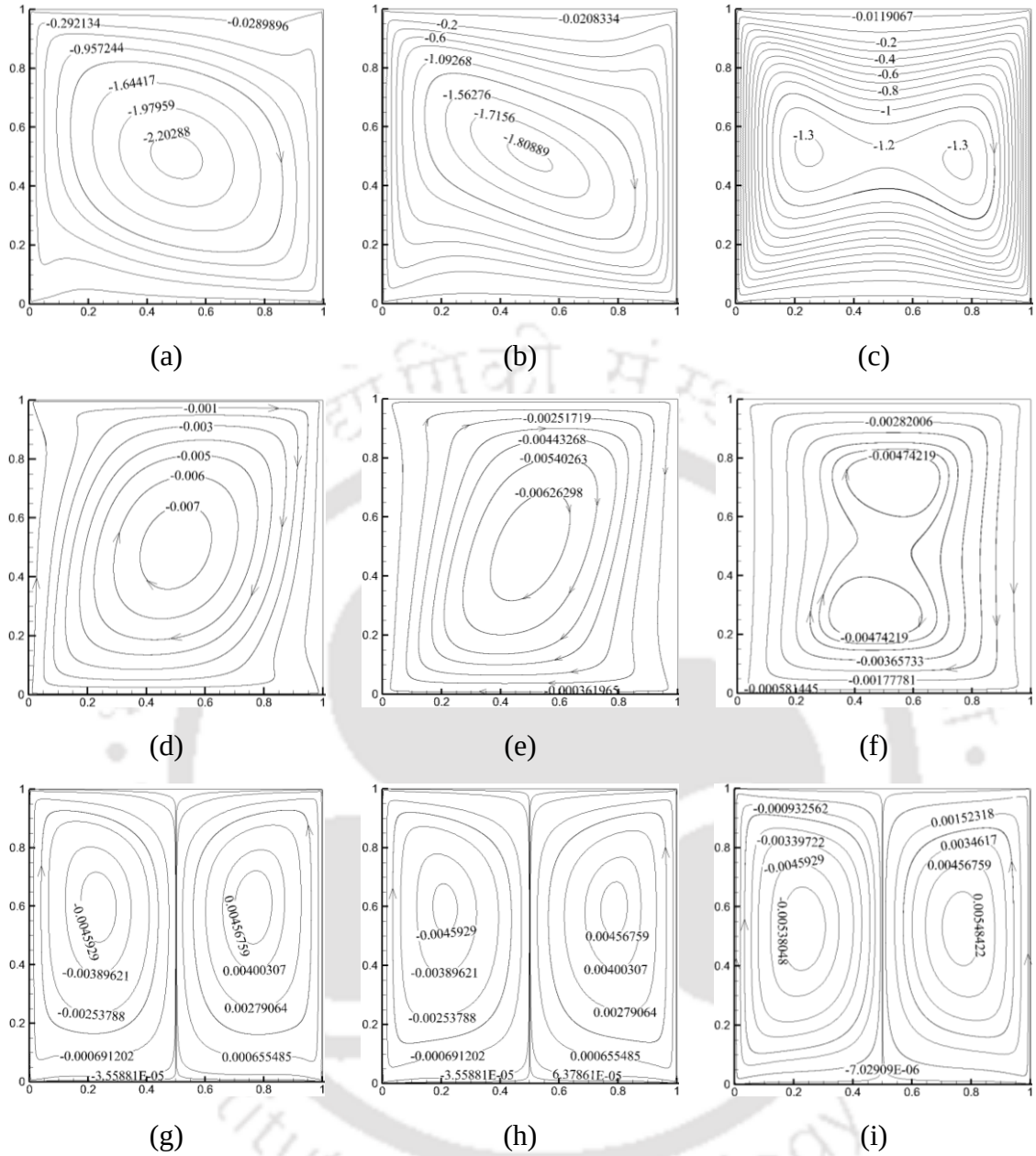

Fig. 5.8. Streamlines (ψ) for Case 1 (a, b, c), Case 2 (d, e, f) and Case 3 (g. h, i) at *Ri* = 0.1 (left panel), *Ri* = 1.0 (middle panel) and *Ri* = 10.0 (right panel).

by the left wall and cooling down by the right wall of the cavity. Two symmetric counter-rotating primary vortices are formed for Case 3 (Fig. 5.8(g)) where fluid heated by the hot bottom wall is moved up by the vertical moving walls and cooled down by the cold top wall. This symmetric solution about the vertical midline of the cavity for Case 3 is found at all studied parameters due to the presence of symmetrical geometry and boundary conditions. At the low value of *Ri* = 0.1, the forced convection dominated fluid flow is

observed due to lid motions and this is quite obvious from the definition of Richardson number. The stream function has a maximum value at the centre of primary vortex for each case where Case 1 has a higher value of $|\psi_{max}|$ = 2.258 compared to Case 2 ($|\psi_{max}|$ = 0.0076) and Case 3 ($|\psi_{max}|$ = 0.0049). This signifies that the buoyancy-driven free convection is aided more strongly by forced convection for Case 1 due to the directions of moving lids. The fluid horizontal velocity for Case 3 is stagnated at the vertical midline of the cavity. The strength and shape of the primary vortices are affected considerably with the variation of *Ri* values as observed from stream-function contours.

Figs. 5.8(b) and (e) show that for Case 1 and Case 2 at *Ri* = 1.0, the primary vortex tends to become more elliptic in the core zone of the cavity as the free convection effect increases with *Ri*. It is observed for Case 1 that the primary vortex cells are elongated towards the bottom left corner and top right corner of cavity whereas for Case 2 they are elongated towards the corners at the top left and bottom right of the cavity. However, the effect of *Ri* on primary vortices for Case 3 (Fig. 5.8(h)) is not that much significant compared to other two cases due to the occurrence of two equal-sized counter-rotating vortices. The magnitude of maximum stream function $|\psi_{max}|$ is found to be decreasing with *Ri* with values of 1.823, 0.0069 and 0.0047 for Case 1, Case 2 and Case 3 respectively.

Figs. 5.8(c) and (f) show that for Case 1 and Case 2 the primary vortex in the core region breaks up into two equal-sized co-rotating vortices indicating that the convection effect due to free convection is found to dominate forced convection at this higher *Ri* = 10.0. However, no apparent changes in flow pattern are observed with increase in *Ri* for Case 3 due to its symmetrical geometry and boundary conditions, as mentioned earlier. The maximum magnitude of stream function decreases for Case 1 and Case 2 with values equal to 1.584 and 0.005 respectively, whereas $|\psi_{max}|$ increases for Case 3 with magnitude equal to 0.0058.

5.6.1.2 Effect of boundary conditions on isotherms

Figs. 5.9(a), (d) and (g) depict the development of distinct thermal boundary layers near the vertical walls for Case 1 and 2 and near the bottom wall of the cavity for Case 3

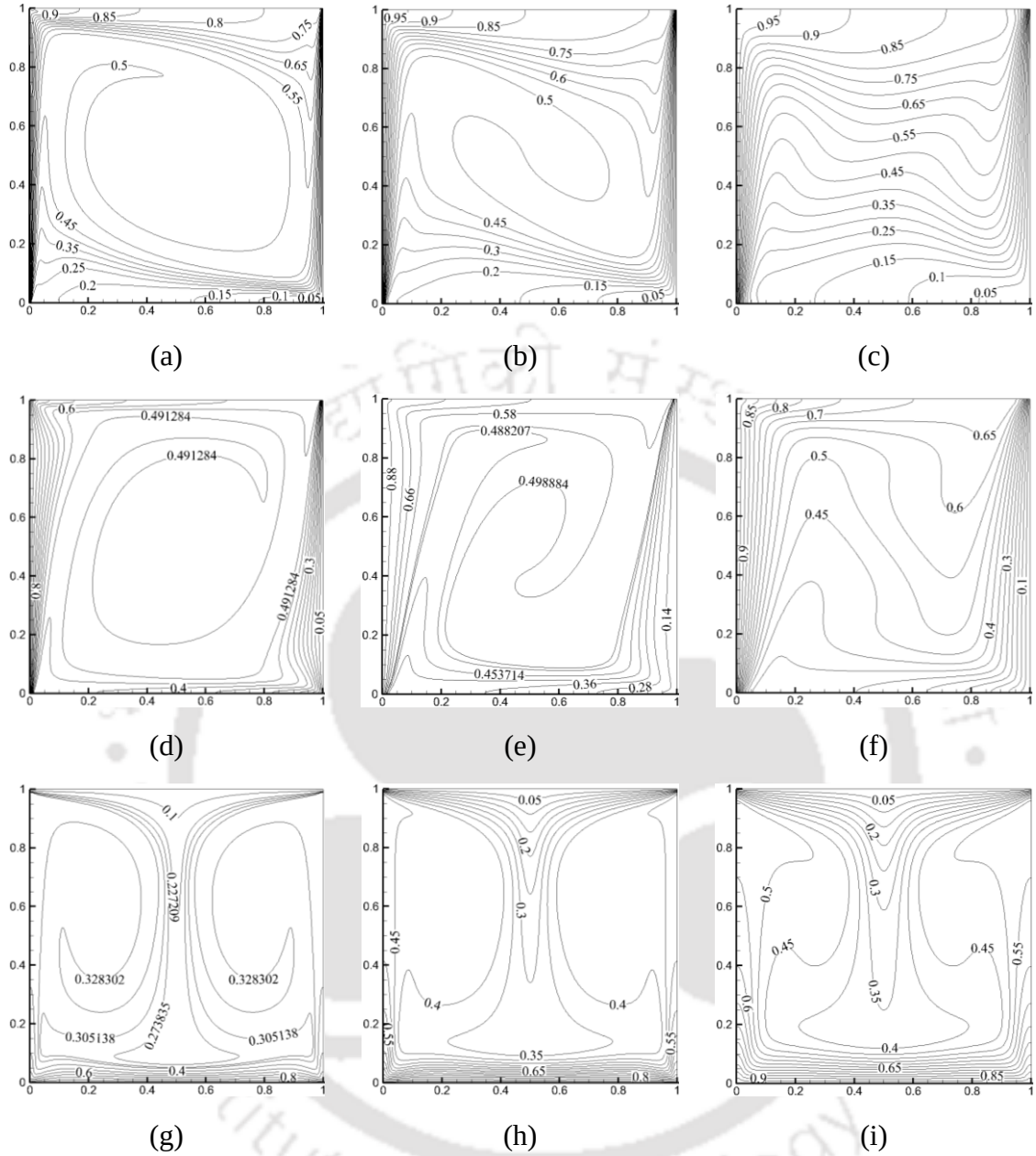

Fig. 5.9. Isotherms (θ) for Case 1 (a, b, c), Case 2 (d, e, f) and Case 3 (g. h, i) at *Ri* = 0.1 (left panel), *Ri* = 1.0 (middle panel) and *Ri* = 10.0 (right panel).

due to strong convection dominated flow at *Ri* = 0.1. The reverse stratification of isotherms is observed in the core zone of the cavity for Case 3 (Fig. 5.9(g) where the free convection is dominant in configuring the flow and thermal field. From the isotherms in Figs. 9(b), (e) and (h), it is found that the thermal boundary layer thickness increases with *Ri* which indicates that intensity of overall convection effect decreases and that eventually results in the reduction of thermal gradients and thermal entropy generation. Figs. 5.9(c) and (f) that

the isotherms at the core zone of the cavity become stratified due to the increasing influence of free convection effect on the flow field, which resembles the natural convection in a differentially heated cavity. Fig. 5.9(i) depicts that the reverse stratification for Case 3 increases with *Ri*. The thickening of the thermal boundary layer continues with increasing *Ri* owing to the existence of lower temperature gradients at the differentially heated boundaries of the cavity.

5.6.1.3 Effect of boundary conditions on entropy generation contours

It is found from Figs. 5.10(a), (d) and (g) that the entropy generation due to heat transfer irreversibility is mostly concentrated near the differentially heated walls of the cavity for all three cases, i.e., near the vertical walls for Case 1 and Case 2 and near the horizontal bottom wall and the corners of the top wall for Case 3 as higher thermal gradients exist at these positions. The effect of S_θ on fluid flow is more significant for Case 1 with the maximum value of S_θ ($|S_{\theta,\max}|$ = 36127.9) than Case 2 ($|S_{\theta,\max}|$ = 3497.44) and Case 3 ($|S_{\theta,\max}|$ = 1515.83). However, the viscous entropy generation is considerably lower compared to thermal entropy generation as forced convection dominates free convection (Figs. 5.11(a), (d) and (g)). For all three cases, the active zones of S_ψ are located at the four corners of the cavity with the maximum magnitudes $|S_{\psi,\max}|$ of 1790.57, 1546.3 and 1546.3 for Case 1, Case 2 and Case 3 respectively. However, the strength of S_θ and S_ψ become low at the core zone of the cavity where very low thermal and velocity gradients occur.

The maximum values S_θ at *Ri* = 1.0 are found to be 9376.5, 2271.45 and 872.25 for Case 1, Case 2 and Case 3 respectively, which are lower than the values at *Ri* = 0.1 (Figs. 5.10(b), (e) and (h)). It seems that S_θ decreases more significantly with an increase in *Ri* for Case 1 compared to the other two cases. The value of S_ψ decreases with increase in *Ri* as the velocity gradient decreases with reducing convection effect. The values of $|S_{\psi,\max}|$ are 1790.57, 1150.35 and 1150.33 for Case 1, Case 2 and Case 3 respectively (Figs. 5.11(b), (e) and (h)).

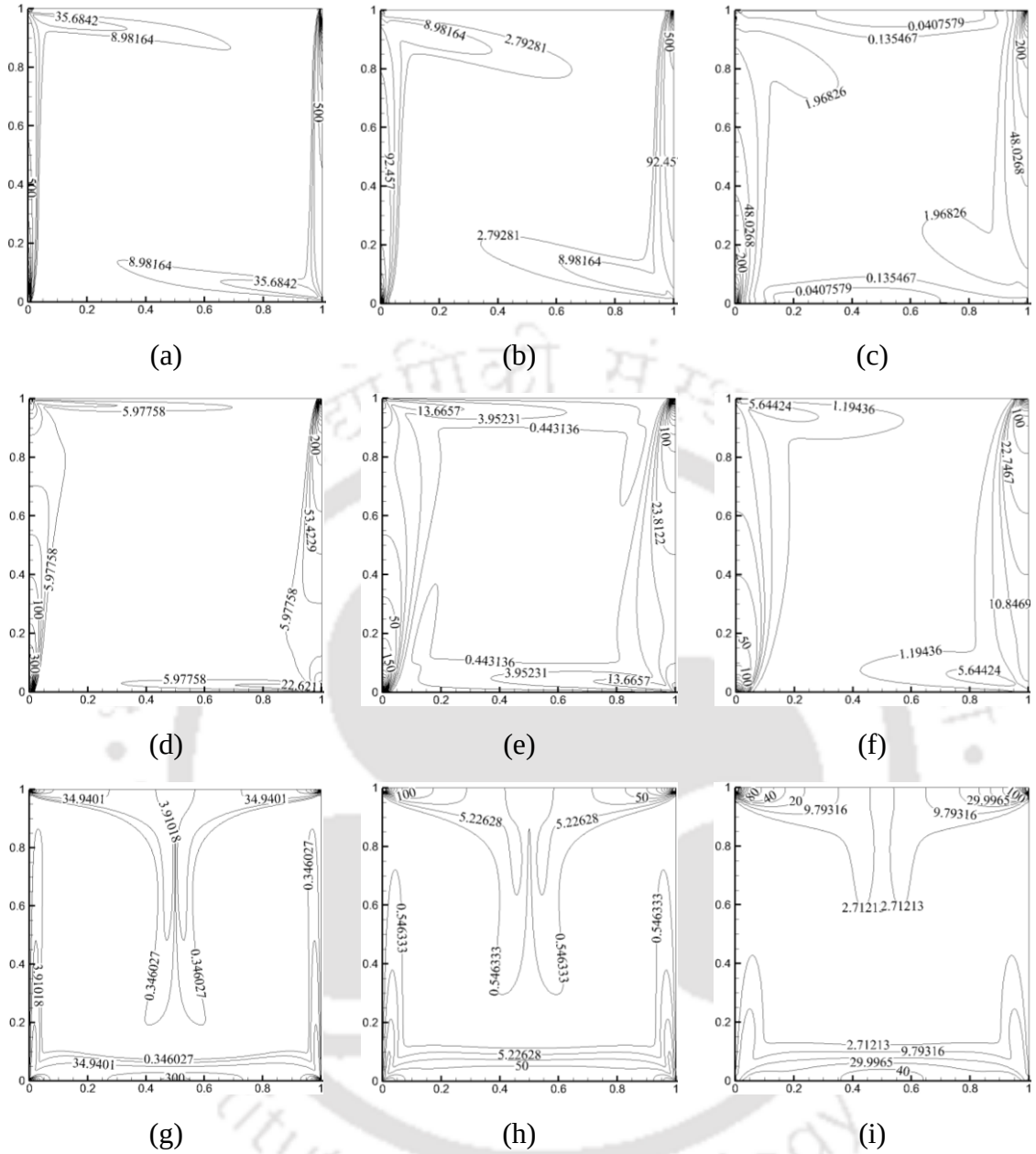

Fig. 5.10. Local entropy generation due to heat transfer (S_θ) for Case 1 (a, b, c), Case 2 (d, e, f) and Case 3 (g. h, i) at *Ri* = 0.1 (left panel), *Ri* = 1.0 (middle panel) and *Ri* = 10.0 (right panel) respectively.

Figs. 5.10(c), (f) and (i) depict that the entropy generation due to heat transfer further decreases with increase in *Ri*. The maximum values S_θ are found to be 1404.21, 709.39 and 370.93 for Case 1, Case 2 and Case 3 respectively. It seems that S_θ decreases more considerably with an increase in *Ri* for Case 1 and Case 2 compared to Case 3 as the reduction of overall convection effect due to forced convection is more significant for these

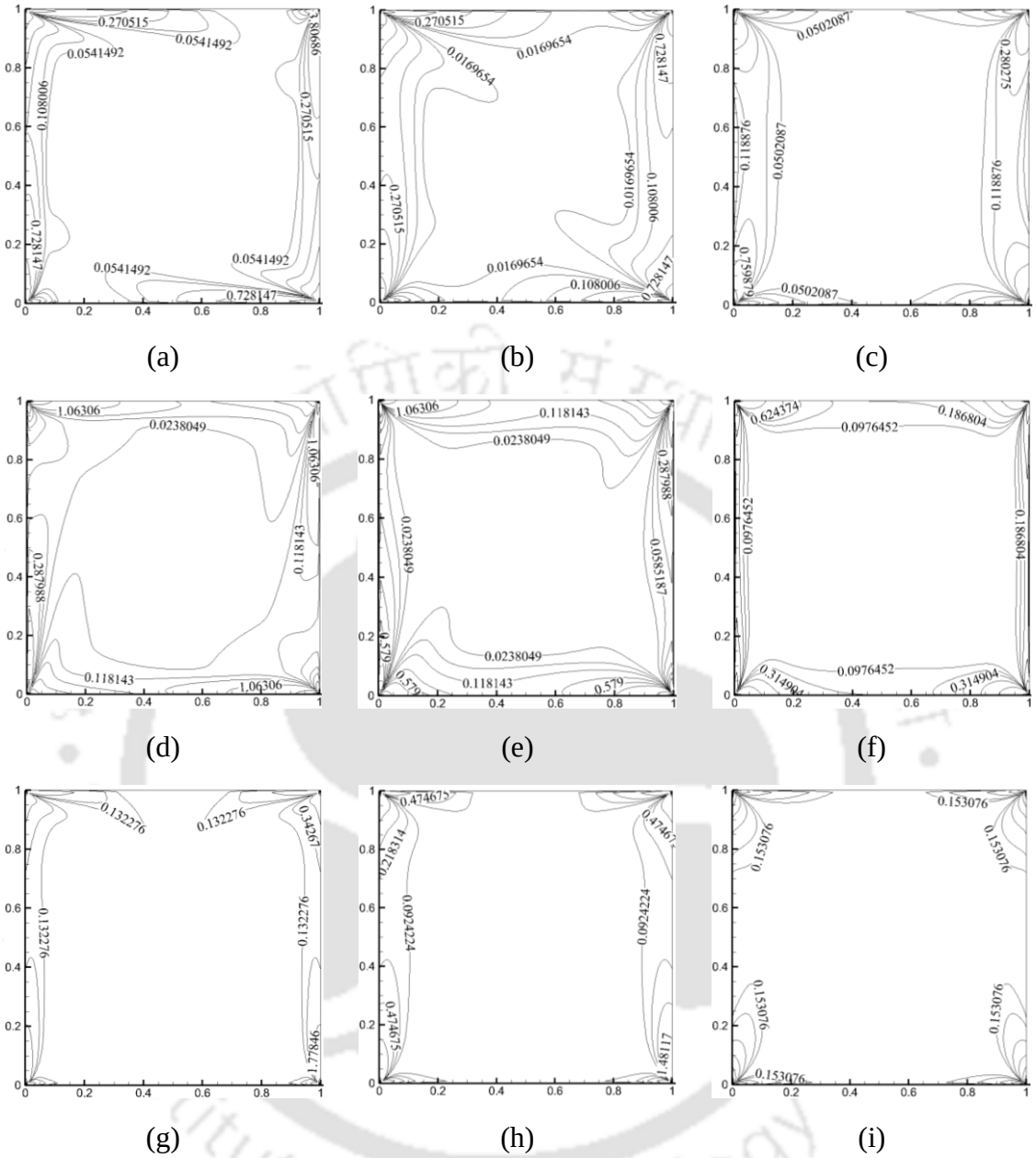

Fig. 5.11. Local entropy generation due to viscous effect (S_ψ) for Case 1 (a, b, c), Case 2 (d, e, f) and Case 3 (g. h, i) at *Ri* = 0.1 (left panel), *Ri* = 1.0 (middle panel) and *Ri* = 10.0 (right panel).

two cases. For Case 3 (Fig. 5.10(i)), the influence of free convection is found to be dominating forced convection due to the orientation of the velocity boundary condition. It is interesting to find for Case 1 (Figs. 5.11(a)-(c)) that the maximum magnitude of $|S_{\psi,\max}|$ which is found at the boundaries of cavity remains same for all calculated *Ri*s as the forced convection due to lid motions dominate free convection at these zones in comparison to the

other two cases. The values of $|S_{\psi,\max}|$ for Case 2 and Case 3 slightly reduces to 953.07 and 952.9 respectively (Figs. 5.11(f) and (i)) as overall velocity gradient decreases due to the reduction of forced convection effect.

The above investigation suggests that entropy generations due to both heat transfer and fluid friction irreversibilities are mainly concentrated at the differentially heated walls of the cavity owing to the existence of higher velocity and temperature gradients. To carry out further investigations using nanofluid, a hybrid Al_2O_3-Cu/water nanofluid with 9:1 mixture ratio of Al_2O_3 and Cu nanoparticles is used to study its energy efficiency while maintaining nanoparticle volume fraction up to 3% to retain stable suspension and uniform dispersion. In the following sections, the effect of *Ri* and φ are studied in detail.

5.6.1.4 Variation of velocity and temperature with *Ri* and φ

Fig. 5.12 depict the effect of *Ri* and φ on the fluid flow and thermal behaviour in terms of the distribution of non-dimensional vertical velocity v and temperature θ along the mid-plane of the cavity. The results are obtained for *Ri* = 0.1, 1.0 and 10.0 while keeping φ at 0% and 3%. It is noticed that the average flow velocity decreases with the increase in *Ri* values for all three cases, which is in accordance with the stream function contour. The addition of nanoparticles decreases the thickness of the velocity boundary layer for Case 1 and Case 3 along the moving walls as indicated by the steeper velocity gradient. For Case 2, an increase in φ induces thicker velocity boundary layer along the stationary walls as indicated by the gentler velocity gradient. This phenomenon is attributed to the augmentation in viscosity with φ, which results in the reduction of average velocity throughout the cavity. The variation of velocity with φ is more pronounced for Case 2 and Case 3 in comparison to Case 1 as the effect of nanofluid is not apparent for Case 1 due to strong forced convection which overpowers the retardation effect of viscosity. It is recognised that the thickness of thermal boundary layer decreases and thus the convective effect increases with a decrease in *Ri* for all three cases which is indicated by steeper temperature gradient near the differentially heated walls of the cavity. There is no significant change in temperature gradient observed with the addition of nanoparticles for

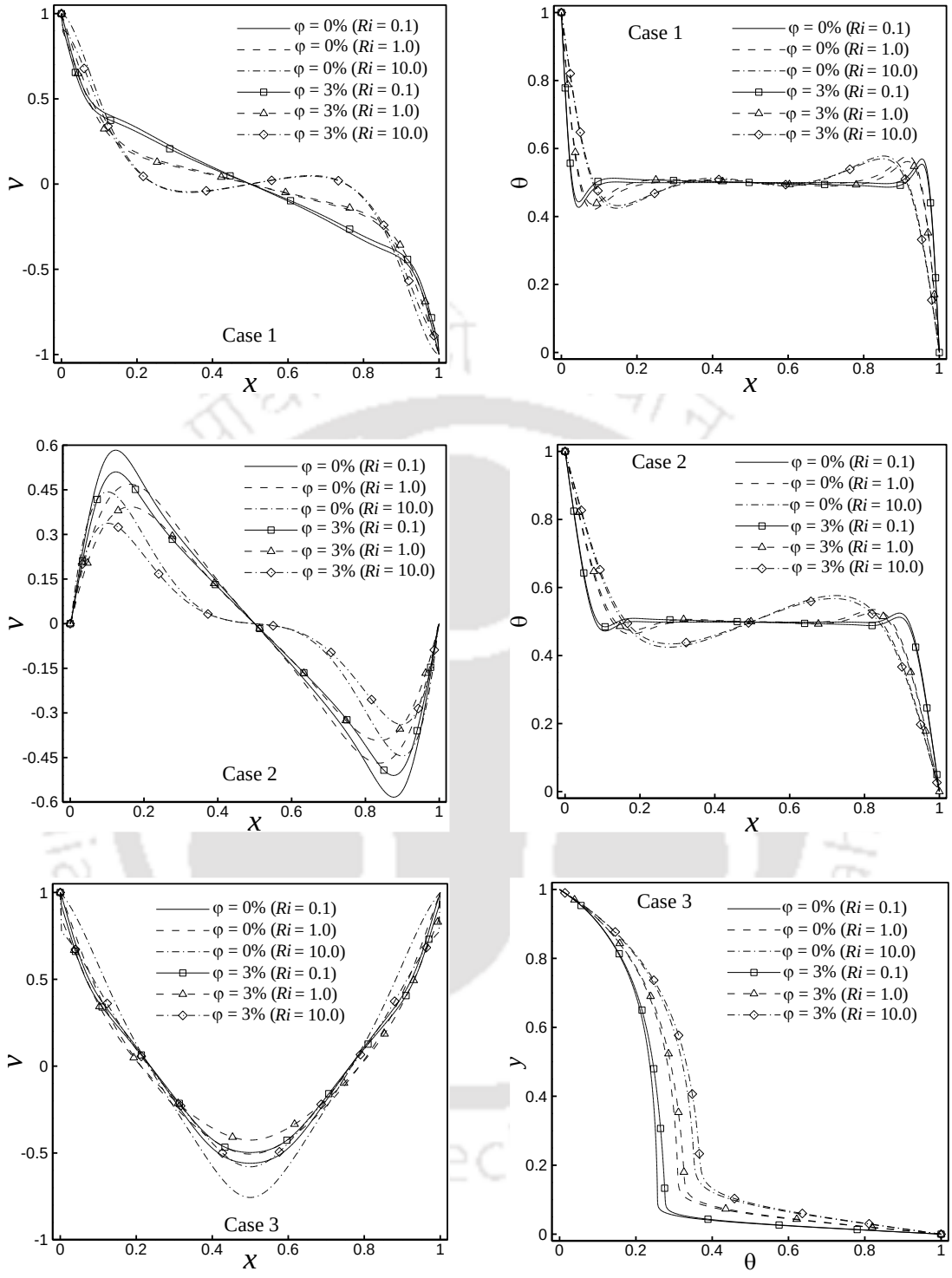

Fig. 5.12. Comparison of v (left panel) and θ (right panel) for three cases at Ri's of 0.1, 1 and 10 respectively with φ = 0% and 3%.

all three cases. However, the average temperature throughout the cavity decreases due to the reduction of the buoyancy effect in the core zone with an increase in φ.

5.6.1.5 Heat transfer rates

Figs. 5.13(a), (c) and (e) show the reduction of average Nusselt number along the hot wall ($\overline{Nu_h}$) of the cavity with an increase in *Ri* due to the reduction of overall convection effect for all three cases as mentioned earlier. The optimum heat transfer rate is observed for Case 1 due to the strong aiding effect of the shear-driven flow on buoyancy-driven flow whereas for Case 2 the value of Nu is minimum as the aiding effect is not significant due to the directions of lids movement. It is observed that at higher *Ri* values, $\overline{Nu}$ is found to be comparable for Case 2 and Case 3 due to the occurrence of free convection dominated heat transfer phenomenon. The average Nu along the hot wall ($\overline{Nu_h}$) of the cavity increases with φ for all three cases as the addition of nanoparticles enhances the thermal conductivity of the fluid. Figs. 5.13(b), (d) and (f) exhibit the percentage enhancement of heat transfer rate as indicated by normalised average Nusselt number ($\overline{Nu_N}$) which is the ratio of average Nu of nanofluid to that of the base fluid. It is observed that the maximum $\overline{Nu_N}$ decreases with increases in *Ri* for Case 2 due to the augmented retardation effect of viscosity and drag force with the increase in free convection. However, it is interesting to find that maximum $\overline{Nu_N}$ increases with *Ri* for Case 3 despite an increase in the reverse stratification with φ. This anomalous behaviour is attributed to the increase in the particulate buoyancy force due to variation nanoparticle density in the presence of Brownian motion and thermophoresis. Therefore, it is realised that the Brownian motion and thermophoresis play an essential role in the nanofluid flow and heat transfer where they enhance the heat transfer rate by making the nanofluid less viscous due to consideration of slip velocity between the nanoparticles and base fluid. For all three cases, the maximum percentage augmentation of heat transfer is found at φ = 0.03 for all *Ri*s. However, the percentage augmentation of heat transfer rate gradually deteriorates with increase in φ as seen by the reducing inclination angle of $\overline{Nu_N}$ profile with φ due to the enhancement of viscosity. Therefore, it can be concluded that the heat transfer rate increases up to a certain volume fraction termed as an optimum nanoparticle volume fraction (φ_{opt}) due to two opposing effects .i.e., retardation effect of viscosity and drag force and the aiding effect of thermal conductivity of nanoparticle, Brownian force and thermophoretic force.

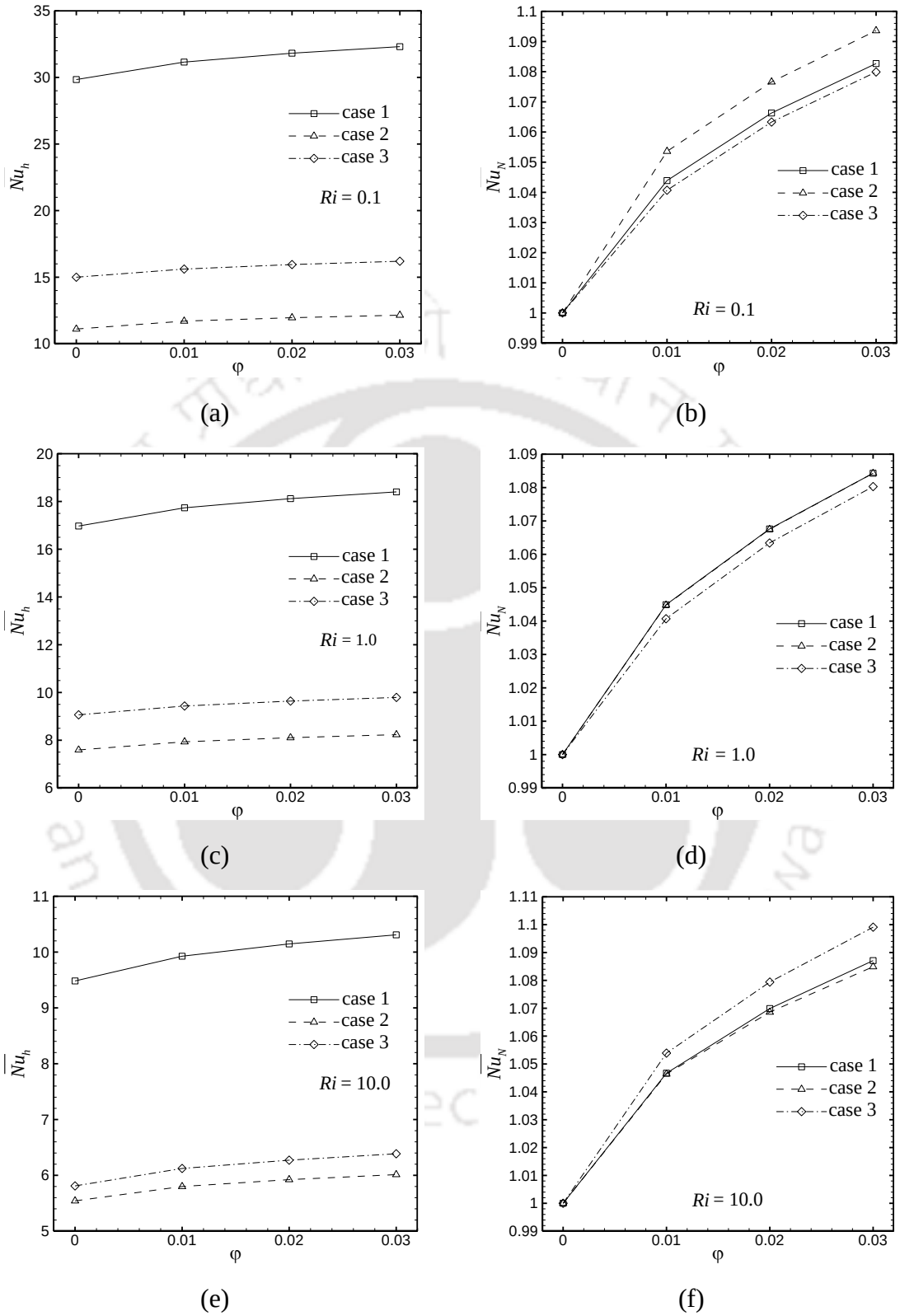

Fig. 5.13. Variations of $\overline{Nu_h}$ (left panel) and $\overline{Nu_N}$ (right panel) with φ for three cases at *Ri* = 0.1 (a and b), *Ri* = 1.0 (c and d) and *Ri* = 10.0 (e and f) respectively.

5.6.1.6 Entropy generation and Bejan numbers

It is interesting to find from Figs. 5.14(a)-(c) that the variation of average entropy generation due to heat transfer ($\overline{S_\theta}$) over the whole cavity with φ resembles the profile for the average Nusselt number along the hot wall (Figs. 5.13(a)-(c)) as both the quantities are functions of temperature gradients with the concentration of S_θ near differentially heated walls of the cavity. It is noticed that the average magnitudes of $\overline{S_\theta}$ is found almost similar to $\overline{Nu_h}$ for Case 1 and Case 2 whereas for Case 3, $|\overline{S_\theta}|$ is lower than $|\overline{Nu_h}|$ and with an increase in *Ri* it approaches the values of $\overline{S_\theta}$ for Case 2. This phenomenon is attributed to the presence of thermal stratification in Case 3, which causes the reduction of thermal gradients at the core zone of the square cavity. The magnitudes of average total entropy generation due to viscous effect ($\overline{S_\psi}$) throughout the cavity at different values of *Ri* are found to be lower for Case 1 compared to the other two cases as seen from Figs. 5.14(d)-(f). A drastic augmentation of $\overline{S_\psi}$ with φ is observed as the addition of nanoparticles increases viscosity. The variation of $\overline{S_\psi}$ with φ is found to be comparable for Case 2 and Case 3 where the maximum percentage augmentation of $\overline{S_\psi}$ increases with *Ri* as the addition of nanoparticles makes the nanofluid more viscous during free convection in comparison to forced convection. However, the maximum percentage augmentation of $\overline{S_\psi}$ for Case 1 decreases with increase in *Ri* due to the presence of higher velocity gradient resulting from strong forced convection as mentioned earlier.

It is observed from Figs. 5.14(g)-(i) that the entropy generation is dominated by the heat transfer irreversibility for all flow conditions at all *Ri* values as described by high average Bejan number ($\overline{Be}$) over the whole cavity while considering the effect of Richardson number with or without nanofluid. However, $\overline{Be}$ slightly decreases with *Ri* as the entropy generation due to heat transfer decreases. For all *Ri*s, Case 1 has a higher $\overline{Be}$ than the other two cases owing to the higher temperature gradient in the flow field. It is found that $\overline{Be}$ decreases with φ at all values of *Ri* for all three cases, and this reduction is more prominent at higher *Ri* = 10 due to the enhancement of entropy generation due to fluid friction with φ.

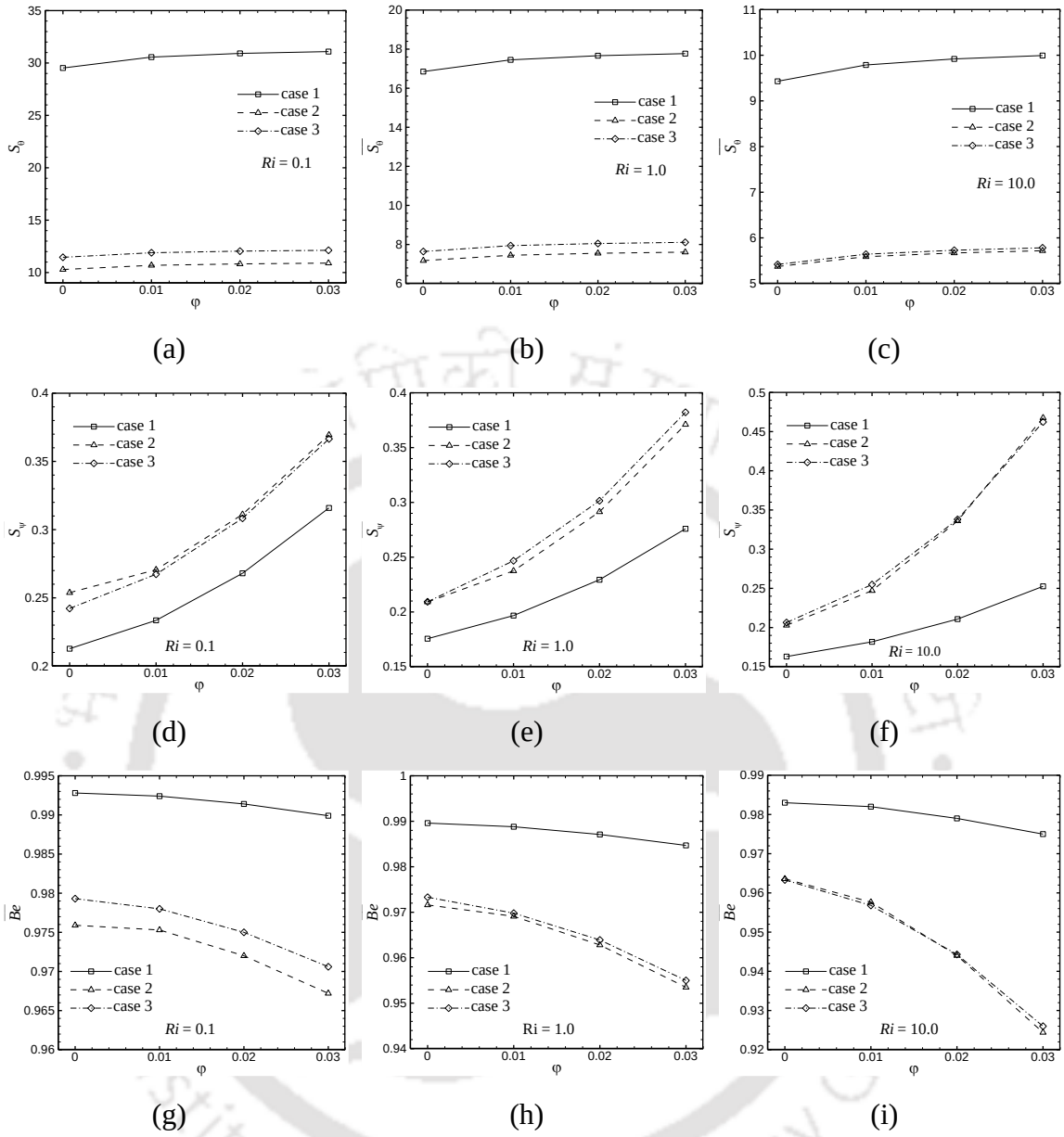

Fig. 5.14. Variations of $\overline{S_\theta}$ (a, b and c), $\overline{S_\psi}$ (d, e and f) and $\overline{Be}$ (g, h and i) with φ for three cases at *Ri* = 0.1 (left panel), *Ri* = 1.0 (middle panel) and *Ri* = 10.0 (right panel).

5.6.1.7 Performance analysis

A performance coefficient parameter is considered to evaluate the effects of Richardson numbers and volume fractions of nanoparticles in terms of energy efficiency. Figs. 5.15(a)-(c) reveal that $\overline{Nu_N}/\overline{S_{tot,N}}$ decreases with increase in *Ri*, which is apparent from the plots for $\overline{Nu}$ and $\overline{S_\theta}$. This signifies that for all three boundary conditions, forced convection

dominated flow condition at lower Ri = 0.1 provides much desirable energy efficiency compared to free convection dominated condition at higher Ri = 10.0. It is interesting to find that Case 1 has the lowest performance coefficient parameter as the values of desirable heat transfer rate and undesirable total entropy generation almost identical. Case 3 has relatively higher $\overline{Nu_N}/\overline{S_{tot,N}}$ compared to the other two cases making it more energy efficient by taking into consideration of entropy generation. Although marginal, continuous enhancement of $\overline{Nu_N}/\overline{S_{tot,N}}$ is observed with φ at Ri = 0.1 for all three cases. For Case 1, this enhancement is more prominent compared to the other two cases. Further, for Case 1, $\overline{Nu_N}/\overline{S_{tot,N}}$ increases with φ for all Ris as the maximum percentage augmentation of $\overline{S_\psi}$ decreases with increase in Ri and φ. For the other two cases, $\overline{Nu_N}/\overline{S_{tot,N}}$ decreases with φ after φ > 2% and φ > 1% for Ri = 1 and 10 respectively. This signifies that the effectiveness of nanofluid in terms of energy efficiency is found to be trivial for Case 2 and Case 3 due to enhanced retardation effect of entropy generation which dampens the positive effect of augmented heat transfer rate with φ. As stated earlier, the analysis of the 1st law of thermodynamics provides an optimal volume fraction based on the heat transfer rate. However, it is necessary to consider the viewpoints of both 1st and 2nd law of thermodynamics as it suggests another optimal volume fraction in terms of performance coefficient parameter at which the heat transfer rate of the system is more prominent compared to the total entropy generation.

Figs. 5.15(d)-(f) show that Case 1 and Case 2 have higher and identical overall thermal mixing in the whole cavity as indicated by the higher value of θ_{cup} than Case 3 for all studied Ris. However, the variation of θ_{cup} is found to be negligible with φ as the convective mode of heat transfer prevails for all conditions except for Case 3 at Ri = 10 where the slight enhancement of θ_{cup} is observed with φ. Case 1 and Case 3 provide lower and higher temperature uniformity in the cavity respectively as indicated by $RMSD_{\theta_{cup}}$(as shown in Fig. 5.15(g)-(i)). However, Case 2 provides moderate temperature uniformity along with higher thermal mixing, which makes it a desired condition to attain suitable temperature distribution. Figs. 5.15(g)-(i) display that a slight enhancement of temperature

uniformity with φ is observed for Case 1 due to the reduction of $RMSD_{\theta_{cup}}$ whereas the reduction of $RMSD_{\theta_{cup}}$ with φ is insignificant for Case 2 and Case 3.

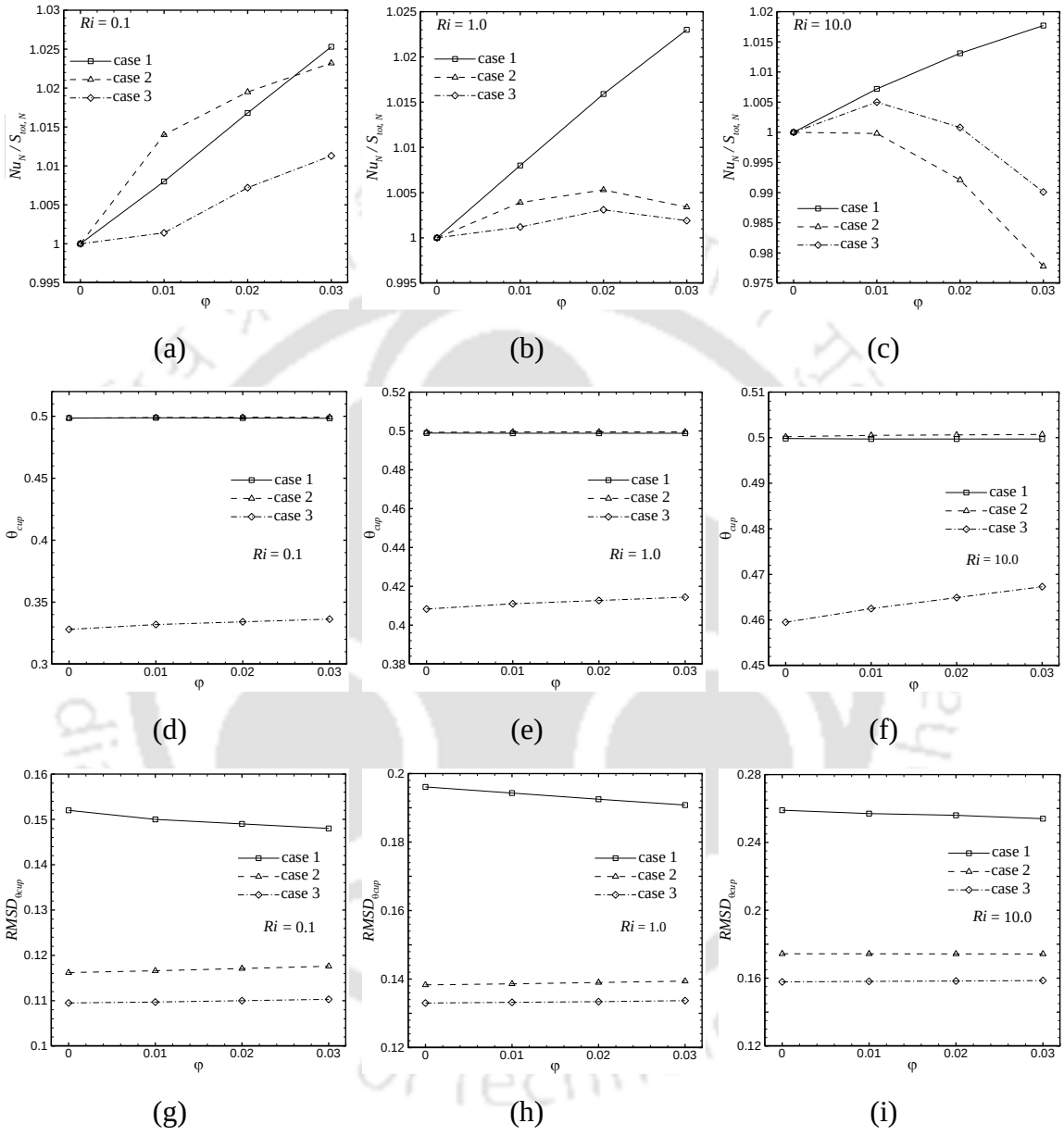

Fig. 5.15. Variations of $\overline{Nu_N}/\overline{S_{tot,N}}$ (a, b and c), θ_{cup} (d, e and f) and $RMSD_{\theta_{cup}}$ (g, h and i) with φ for three cases at Ri = 0.1 (left panel), Ri = 1.0 (middle panel) and Ri = 10.0 (right panel) respectively.

5.6.1.8 Conclusions

This work attempts to study three different cases of boundary conditions depending on the choice of moving walls and differentially heated walls of the cavity. The selected boundary conditions provide the aiding mechanism of mixed convection flow as the shear-driven flow due to the direction of moving walls assists the buoyancy-driven flow owing to differentially heated walls of the cavity. A detailed analysis has been made by considering the effect of boundary conditions and different values of *Ri* on the heat transfer rate, entropy generation due to heat transfer and fluid friction irreversibilities, thermal mixing, and temperature uniformity during mixed convection in the closed square cavity. A two-component DDF-based thermal lattice Boltzmann model for nanofluid is implemented by making careful validation with the published results. The current investigation deals with three different Richardson numbers *Ri* = 0.1, 1 and 10 while maintaining a fixed Grashof number $Gr = 10^4$. The volume fraction of nanoparticles (φ) of hybrid Al_2O_3-Cu/water with 9:1 mixture ratio of Al_2O_3 and Cu nanoparticles is kept less than equal to 3%. The major outcomes of present work can be summarised as follows:

1. The convective mode of heat transfer prevails at all flow conditions where forced convection dominates at lower *Ri* and free convection at higher *Ri*. The higher heat transfer rate is observed at lower *Ri* due to the strong aiding effect of shear force on the buoyancy force. The entropy generation in the system is mainly controlled by heat transfer irreversibility.
2. Case 1 gives lower performance coefficient parameter $\overline{Nu_N}/\overline{S_{tot,N}}$ due to its higher total entropy generation over the whole cavity, although it provides a higher heat transfer rate compared to the other two cases. Case 3 offers higher performance coefficient parameter due to the presence of lower heat transfer irreversibility. The slight improvement of performance coefficient parameter for Case 2 over Case 1 is attributed to its lowest entropy generation along with the heat transfer rate. The reduction of $\overline{Nu_N}/\overline{S_{tot,N}}$ with an increase in *Ri* for all three boundary conditions signifies that forced convection-dominated flow condition provides much desirable energy efficiency compared to free convection.

3. The addition of nanoparticle has a positive effect on the heat transfer rate but gives rise to higher entropy generation. Therefore, the current investigation suggests two different optimal volume fractions where one is based on the maximum heat transfer rate and the other one is based on performance coefficient parameter while considering the viewpoints of both first and second laws of thermodynamics. The optimum values of $\overline{Nu}$, $\overline{S_{tot}}$, θ_{cup} and $RMSD_{\theta_{cup}}$ in a given system have a strong dependency on Richardson numbers while showing a weak dependence on volume fractions of nanoparticles.
4. The two-phase LB model provides a more accurate prediction of the nanofluid behaviour compared to the single-phase LB model due to the consideration of different slip mechanisms. Brownian motion and thermophoresis effect contribute to the enhancement of the heat transfer rate by making the nanofluid less viscous while the drag force provides an attenuation effect on heat transfer.

Chapter 6

Two-Phase SRT-LBM Simulation of Natural Convection in a Cu-Water Nanofluid-Filled Porous Cavity

6.1 Introduction

The simultaneous use of porous media and nanofluids has been a topic of interest for their better heat transfer rates in small size systems. The use of a porous medium can be an efficient means of controlling heat transfer performance in enclosures. The bigger surface contact area exists between the working fluid and porous structure which provides an effective interaction between convective heat transfer inside pores and heat conduction in a solid matrix. Recently, an increasing number of works on the simultaneous use of porous media and nanofluids are found in the literature, which is very useful for the optimisation of various engineering devices. A perusal of literature suggests that several studies have been undertaken to analyse the effect of different thermal boundary conditions on entropy generation during natural convection in fluid-saturated porous media. However, very few numerical studies are found concerning nanofluid-saturated porous media, where most of the studies are made using a single-phase model for nanofluid. This work adopts the SRT-based two-phase thermal lattice Boltzmann model for nanofluid and extends it to flow in a porous medium by considering the Brinkman–Forchheimer-extended Darcy model. The code is first successfully validated by obtaining the close agreement of present results with the previously established works. The current work deals with the previous problem concerning natural convection in a square porous cavity (mentioned in Chapter 4 in section 4.3) by using Cu-water nanofluid as a heat transfer fluid.

6.2 Numerical methodology for nanofluid-saturated porous flow using SRT-LBM

To simulate nanofluid flow through a porous medium, nanoparticles are assumed to be suspended in the base fluid in a uniform manner using either surfactant or surface charge technology to avoid their agglomeration and deposition in the porous matrix [Nield and Kuznetsov, 2014]. The local thermal equilibrium exists between the nanofluid and porous medium by assuming their high interaction. The porous medium is considered to be homogeneous, isotropic and fully saturated with fluid and have identical thermal properties with fluid. Besides, both phases have constant thermophysical properties except the density in the buoyancy force term, which is satisfied by the Boussinesq approximation. In the simulation of two-component flow using LBM, each component is treated with two separate distribution functions as follows [Xuan and Yao, 2005]:

$$f_i^{\sigma}(\mathbf{r}+\mathbf{e}_i\Delta t, t+\Delta t) = f_i^{\sigma}(\mathbf{r},t) + \frac{1}{\tau_v{}^{\sigma}}\left(f_i^{\sigma eq}(\mathbf{r},t) - f_i^{\sigma}(\mathbf{r},t)\right) + P_i^{\sigma} \tag{6.1}$$

where σ refers to two components of nanofluid, $\sigma = f$ for base fluid and $\sigma = p$ for suspended nanoparticles. The equilibrium distribution function $f_i^{\sigma eq}$ and the total force term ($P_i{}^{\sigma}$) are modified by including the porosity term are given as:

$$f_i^{\sigma eq} = \rho^{\sigma} w_i \left\{1.0 + \frac{\mathbf{e}_i.\mathbf{u}^{\sigma}}{C_s^2} + \frac{(\mathbf{e}_i.\mathbf{u}^{\sigma})^2}{2\varepsilon C_s{}^4} - \frac{\mathbf{u}^{\sigma 2}}{2\varepsilon C_s^2}\right\} \tag{6.2}$$

$$P_i{}^{f} = \left\{1 - \frac{1}{2\tau_v{}^{f}}\right\}\left\{\frac{\mathbf{e}_i - \mathbf{u}^{f}}{C_s^2} + \frac{\mathbf{e}_i(\mathbf{e}_i.\mathbf{u}^{f})}{\varepsilon C_s^4}\right\}.\{w_i\mathbf{F} + B_i\mathbf{N}^{f}\} \tag{6.3}$$

$$P_i{}^{p} = \left\{1 - \frac{1}{2\tau_v{}^{p}}\right\}\left\{\frac{\mathbf{e}_i - \mathbf{u}^{p}}{C_s^2} + \frac{\mathbf{e}_i(\mathbf{e}_i.\mathbf{u}^{p})}{\varepsilon C_s^4}\right\}.\{B_i\mathbf{N}^{p}\} \tag{6.4}$$

$\mathbf{N}^{\sigma}$ represents the total inter-particle interaction forces on σ^{th} component of the nanofluid per unit lattice volume, which is mentioned in details in chapter 5 in section 5.2.2.

The body force **F** takes into account the linear and nonlinear drag forces of the porous media based on Brinkman–Forchheimer extended Darcy model along with the external force term while considering the physical properties of the base fluid as follows:

$$\mathbf{F} = -\frac{\varepsilon \nu^f}{K}\mathbf{u}^{\mathbf{f}} - \frac{\varepsilon F_\varepsilon}{\sqrt{K}}\left|\mathbf{u}^{\mathbf{f}}\right|\mathbf{u}^{\mathbf{f}} + \varepsilon \mathbf{G} \tag{6.5}$$

The Darcy-Forchheimer relation used in this work to model the momentum loss of flow through a porous medium are discussed in chapter 4.

For temperature distribution function, the governing two-component discretised lattice Boltzmann equation is similar to the nanofluid model [Xuan and Yao, 2005] by considering the fact that local thermal equilibrium exists between the nanofluid and porous medium due to assumption of their high interaction. The equation is represented as:

$$g_i{}^{\sigma}(\mathbf{r} + \mathbf{e}_i\Delta t, t + \Delta t) = g_i{}^{\sigma}(\mathbf{r}, t) + \frac{1}{\tau_\theta{}^{\sigma}}\left(g_i^{\sigma eq}(\mathbf{r}, t) - g_i{}^{\sigma}(\mathbf{r}, t)\right) \tag{6.6}$$

The single relaxation parameter for each component $\tau_\theta{}^{\sigma}$ relaxes $g_i{}^{\sigma}$ towards their equilibrium distribution function $g_i^{\sigma eq}$ which is written as:

$$g_i^{\sigma eq} = w_i\theta^{\sigma}\left\{1.0 + \frac{\mathbf{e}_i.\,\mathbf{u}^{\sigma}}{2C_s^2}\right\} \tag{6.7}$$

6.2.1 Calculations of macroscopic variables

The density ρ^{σ} and velocity $\mathbf{u}^{\sigma}$ for flow through a nanofluid saturated porous medium are presented as follows:

$$\rho^{\sigma} = \sum_{i=0}^{8} f_i{}^{\sigma} \tag{6.8}$$

$$\rho^f\mathbf{u}^f = \sum_{i=0}^{8} f_i{}^f\,\mathbf{e}_i + \frac{\varepsilon(\mathbf{F} + \mathbf{N}^f)}{2} \tag{6.9}$$

$$\rho^p \mathbf{u}^p = \sum_{i=0}^{8} f_i{}^p \, \mathbf{e}_i + \frac{\varepsilon \mathbf{N}^p}{2} \tag{6.10}$$

It is worthy of mentioning here that the force term for porous medium deals with the properties of the base fluid. This is the crucial part of this new model which is backed by the assumption that the nanoparticles are uniformly suspended in the base fluid, as mentioned earlier. This assumption is quite popularly used by the researchers [Nield and Kuznetsov, 2014] while investigating nanofluid saturated porous medium using other conventional numerical technique. Besides, it is reasonable to assume this approximation as the volume fractions of nanoparticles is very low ($\varphi \leq 3\%$). The equation (6.9) is a nonlinear one as the force term $\mathbf{F}$ contains velocity $\mathbf{u}^f$. However, the implicitness of velocity can be eliminated by making use of its quadratic form, as discussed earlier in chapter 4 in section 4.2.3.

$$\mathbf{u}^f = \frac{\mathbf{v}^f}{c_0 + \sqrt{c_0^2 + c_1 |\mathbf{v}^f|}} \tag{6.11}$$

The auxiliary velocity $\mathbf{v}^f$ is modified to incorporate the inter-particle forces in the nanofluid system, which is given as follows:

$$\rho^f \mathbf{v}^f = \sum_{i=0}^{8} f_i{}^f \, \mathbf{e}_i + \frac{\varepsilon(\mathbf{G} + \mathbf{N}^f)}{2} \tag{6.12}$$

The other parameters c_0 and c_1 are already introduced in chapter 4.

The temperature for each component (θ^σ) is determined similar to nanofluid flow while incorporating the coefficient ζ that gives the heat capacity ratio, as mentioned earlier in Chapter 4.

$$\zeta \theta^\sigma = \sum_{i=0}^{8} g_i{}^\sigma \tag{6.13}$$

6.3 Problem formulation

The current work is the extension of the previous study concerning natural convection in a square porous cavity, as included in Chapter 4. The present work considers the uniform and bottom to top linear heating condition at the left wall of the cavity at their respective optimum Ra_m values (mentioned in Chapter 4). The schematic diagram of the present flow configuration with the boundary conditions is shown in Fig. 6.1.

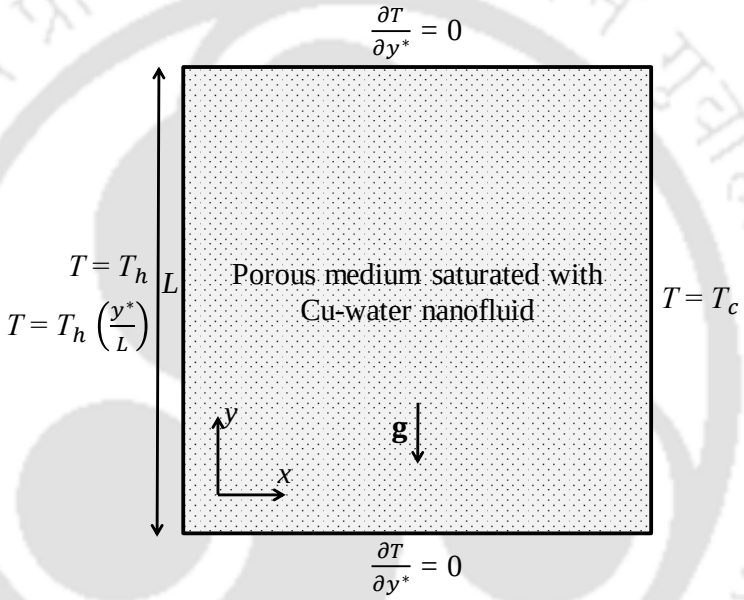

Fig. 6.1. Schematic diagram of the flow configuration with boundary conditions.

For the convenience of numerical calculation and analysis, the variables are expressed in the non-dimensional form as follows:

$$x = \frac{x^*}{L}; \qquad y = \frac{y^*}{L}; \qquad u = \frac{u^* L}{\alpha_f}; \qquad v = \frac{v^* L}{\alpha_f}; \qquad \theta = \frac{T - T_c}{T_h - T_c} \tag{6.14}$$

The boundary conditions in non-dimensional form are given as follows:

$$\begin{aligned} &u = 0, \quad v = 0, \quad \frac{\partial \theta}{\partial y} = 0 && \text{at } y = 0 \text{ and } 1 \\ &u = 0, \quad v = 0, \quad \theta = 1 \text{ or } (y) && \text{at } x = 0 \\ &u = 0, \quad v = 0, \quad \theta = 0 && \text{at } x = 1 \end{aligned} \tag{6.15}$$

6.4 Results and discussion

The numerical results obtained for the present problem of natural convection in the porous cavity are studied in two parts. The first part is already included in Chapter 4 where the effects of four different thermal boundary conditions on fluid flow and thermal behaviour during natural convection in a closed square porous cavity filled with pure water are discussed for different values of *Ra* and *Da*. It is obtained from the investigation that the bottom to top linear heating is found to be more energy-efficient than uniform heating at low Darcy-Rayleigh number, Ra_m = 10 and 10^2 for $Ra = 10^3$ and 10^4 and at lower $Da = 10^{-5}$ and 10^{-6} for $Ra = 10^5$. Whereas, the uniform heating condition is more suitable for higher $Ra_m = 10^3$ and 10^4 at $Ra = 10^4$ and 10^5 and even for lower Ra_m = 10 and 10^2 at higher $Ra = 10^5$. The current work uses Cu-water nanofluid for those optimal boundary conditions to realise the effect of nanofluid on heat transfer enhancement while maintaining volume fraction of nanoparticles (φ) less than equal to 3%. The numbers of plots are presented to show the effect of *Da*, *Ra* and φ on the average *Nu* along the left hot wall ($\overline{Nu}_{lh}$) and for the whole domain ($\overline{Nu}$) of the cavity, average total entropy generation due to heat transfer irreversibility ($\overline{S_\theta}$) and fluid friction irreversibility ($\overline{S_\psi}$), average Bejan number ($\overline{Be}$), thermal mixing (θ_{cup}) and degrees of temperature uniformity ($RMSD_{\theta_{cup}}$).

Since the current work is the extension of the previous work concerning natural convection in the square porous cavity as included in Chapter 4 under section 4.3, the same grid-independence test prevails. Therefore, the grid size of 151×151 for $Ra = 10^3$, 201×201 for $Ra = 10^4$ and 301×301 for $Ra = 10^5$ are found to be suitable for the present computations. The current code can be reduced to a two-phase SRT-LB model for nanofluid for $Da = 10^7$ and generalised SRT-LBM model for porous structure for $\varphi = 0$. Therefore, the validation of the current code can be ensured by making a comparison of present results with the different published ones dealing with porous medium and nanofluid respectively. These validation tests are already included in the preceding chapters 4 and 5 respectively under the section "Code validation". Hence, for the sake of brevity and avoid repetition, the validation tests are not included in this chapter. The present code shows a

good agreement with the published ones, which gives confidence in the numerical results obtained in this work.

6.4.1 Effect of nanofluid on fluid flow and thermal behaviour

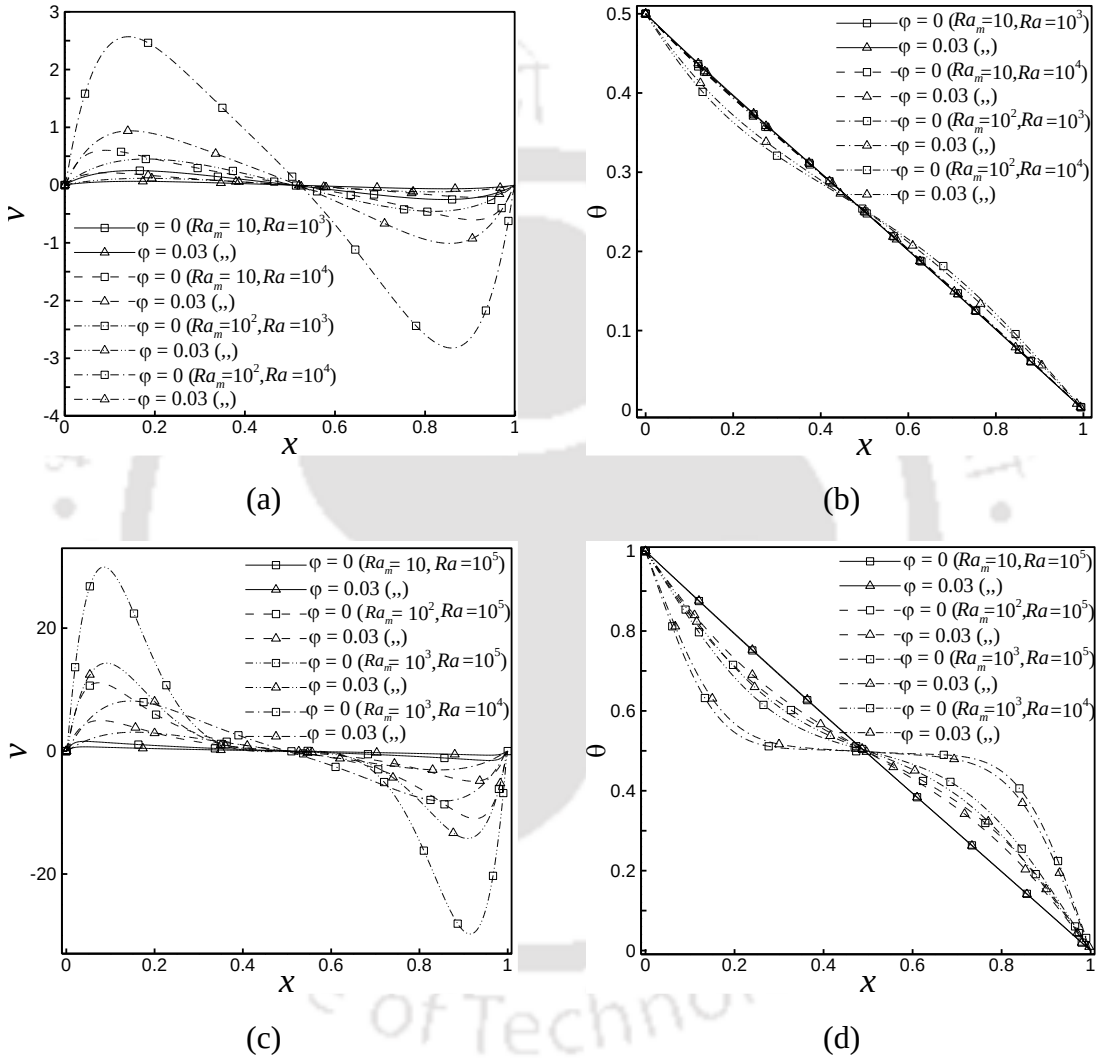

Fig. 6.2. Comparison of values of (a, c) Vertical velocity v and (b, d) Temperature θ in the horizontal midline of the cavity with φ at Ra_m = 10 and 10^2 for the bottom to top linear heating (top panel) and at Ra_m = 10, 10^2 and 10^3 for uniform heating.

Figs. 6.2(a) and (c), and (b) and (d) depict the influence of nanofluid on fluid flow and thermal behaviour in terms of the dimensionless vertical velocity v and dimensionless temperature θ distribution in the horizontal midline of the cavity for the bottom to top linear

and uniform heating at their respective optimum Darcy-Rayleigh numbers respectively. The results are obtained for Ra_m = 10 and 10^2 at Ra = 10^3 and 10^4 for bottom to top linear heating while for uniform heating they are obtained for Ra_m = 10 and 10^2 at Ra = 10^5 and Ra_m = 10^3 at Ra = 10^4 and 10^5 with φ at 0% and 3%. It is realised that for all Darcy-Rayleigh numbers, the addition of nanoparticles increases the thickness of velocity and thermal boundary layers due to augmentation in viscosity. This causes a decrease in the velocity and temperature gradients near the hot and cold vertical walls where the bulk of the fluid motion takes place. The position of maximum velocity moves away from the vertical walls with an increase in φ, which reduces the stratification of temperature in the core region. The temperature profile is found to be linear at lower Ra_m = 10 for all Ra's and at lower Ra = 10^3, which indicates that heat transfer is almost entirely dominated by conduction. However, with an increase in Ra_m to 10^3 at Ra = 10^4 and 10^5, the temperature profile deviates from linearity signifying the dominance of convection over conductive heat transfer.

6.4.2 Heat transfer rates: Nusselt number

Figs. 6.3(a) and (b) display the variation of the average Nu along the left hot wall ($\overline{Nu}_{lh}$) of the cavity with φ discretely varying from 0% to 3% for uniform and bottom to top linear heating respectively at different Darcy-Rayleigh numbers. It is observed that Nu increases with φ due to the enhancement of the thermal conductivity of the fluid. However, as discussed earlier, the increase in viscosity with φ decreases temperature gradients near the vertical walls, thus resulting in lower heat transfer rates. Therefore, there must be an optimum nanoparticle volume fraction (φ_{opt}) at which the maximum heat transfer rate occurs due to these two contradicting effects. The effect of φ on Nu is more pronounced at the lower Ra_m = 10 for all Ra's and at Ra_m = 10^2 for Ra = 10^3 and 10^4 where enhancement of Nu is observed. The reduction of Nu at Ra_m = 10^2 and 10^3 for Ra = 10^5 is attributed to the higher viscosity at the boundary layer, which overpowers the heat transfer enhancement due to thermal conductivity. The effect of φ on Nu is found to be less prominent at higher

values of Ra and Ra_m compared to lower Ra = 10^3 where the addition of nanoparticles reduces the convection heat transfer effect as they make the fluid more viscous, which eventually results in a decreasing Nusselt number after φ_{opt}. For the present study where φ is varying from 0% to 3%, the heat transfer rate is found to be maximum at φ_{opt} = 0.03 at Ra_m = 10 and 10^2 with Ra = 10^3 and 10^4 for the bottom to top linear heating and at Ra_m = 10 with Ra = 10^5 for uniform heating. The optimum volume fraction decreases with higher Ra_m = 10^3 at Ra = 10^4 and 10^5 where φ_{opt} = 0.03 which is due to the dominating retardation effect of viscosity on convective heat transfer than the aiding effect of thermal conductivity.

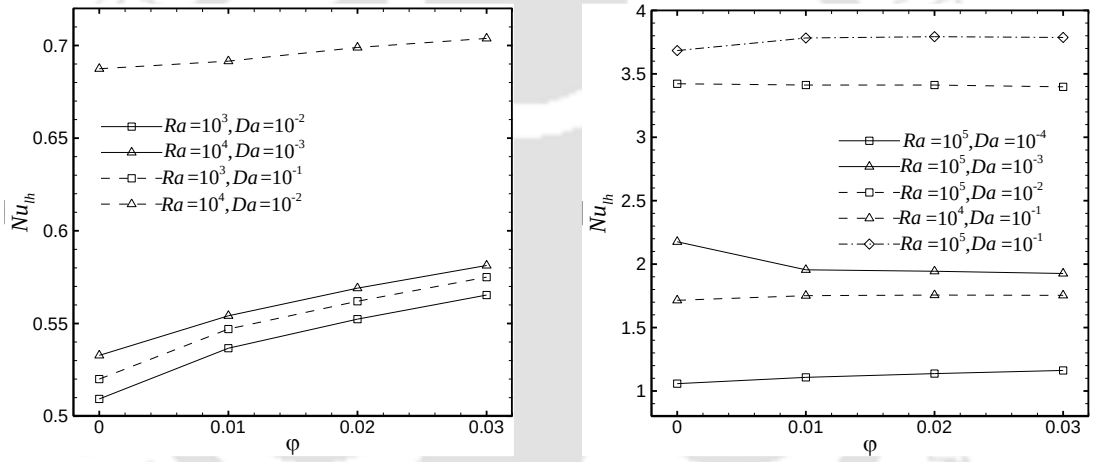

(a) (b)

Fig. 6.3. Variations of $\overline{Nu_{lh}}$ with φ for (a) bottom to top linear heating and (b) for uniform heating respectively.

6.4.3 Entropy generation and Bejan numbers

Figs. 6.4(a) and (b), (c) and (d), and (e) and (f) depict the variation of $\overline{S_\theta}$, $\overline{S_\psi}$ and $\overline{Be}$ in the whole domain of the cavity with φ for the bottom to top linear and uniform heating respectively at different Ra_m values. The variation of $\overline{S_\theta}$ with φ is comparable to the variation of the average Nu along the left hot wall, which seems obvious as both are the function of temperature gradients and S_θ is mostly concentrated on the vertical walls. It is

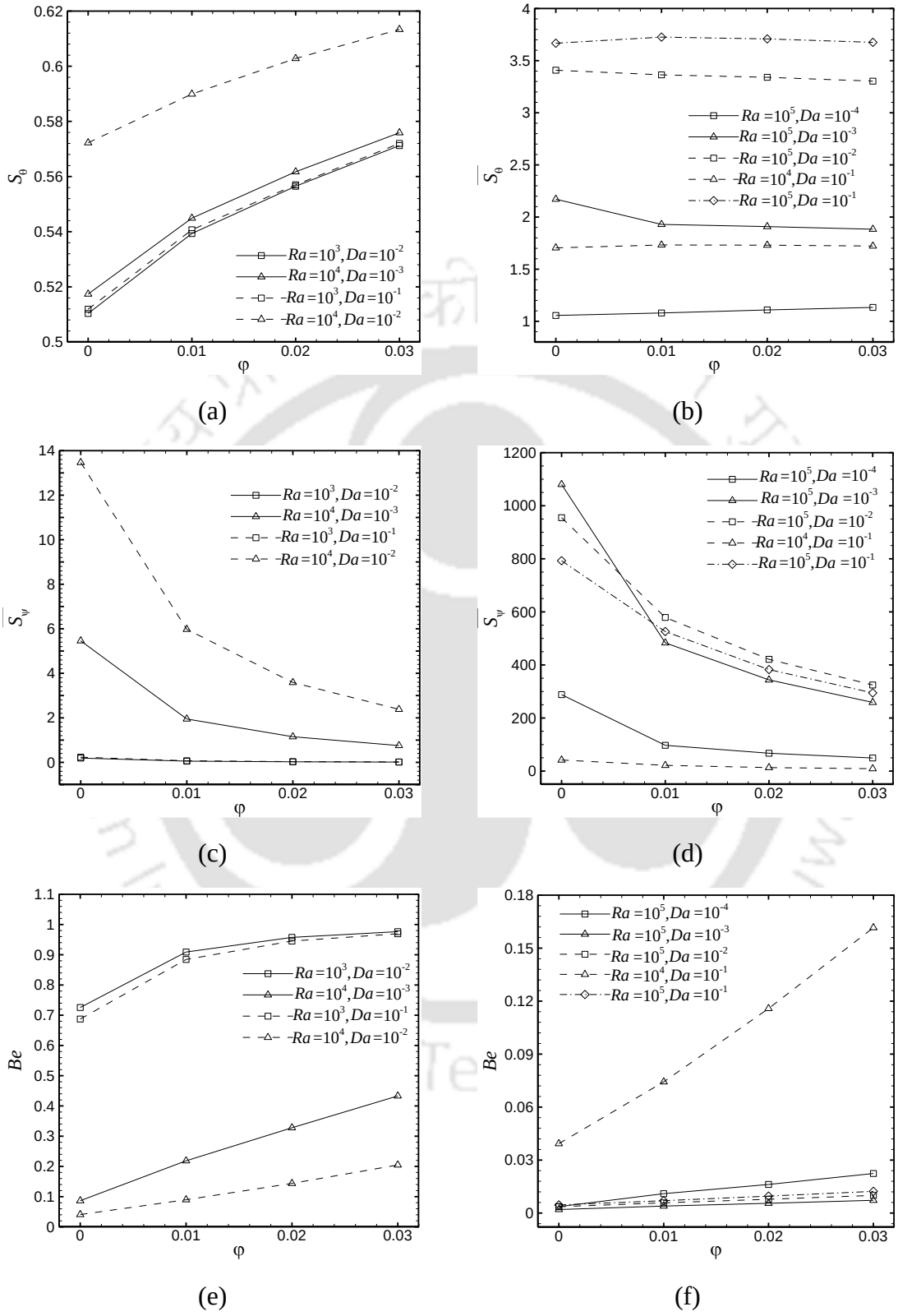

Fig. 6.4. Variations of (a, b) $\overline{S_\theta}$, (c, d) $\overline{S_\psi}$ and (e, f) $\overline{Be}$ with φ for the bottom to top linear heating (left panel) and for uniform heating (right panel) respectively.

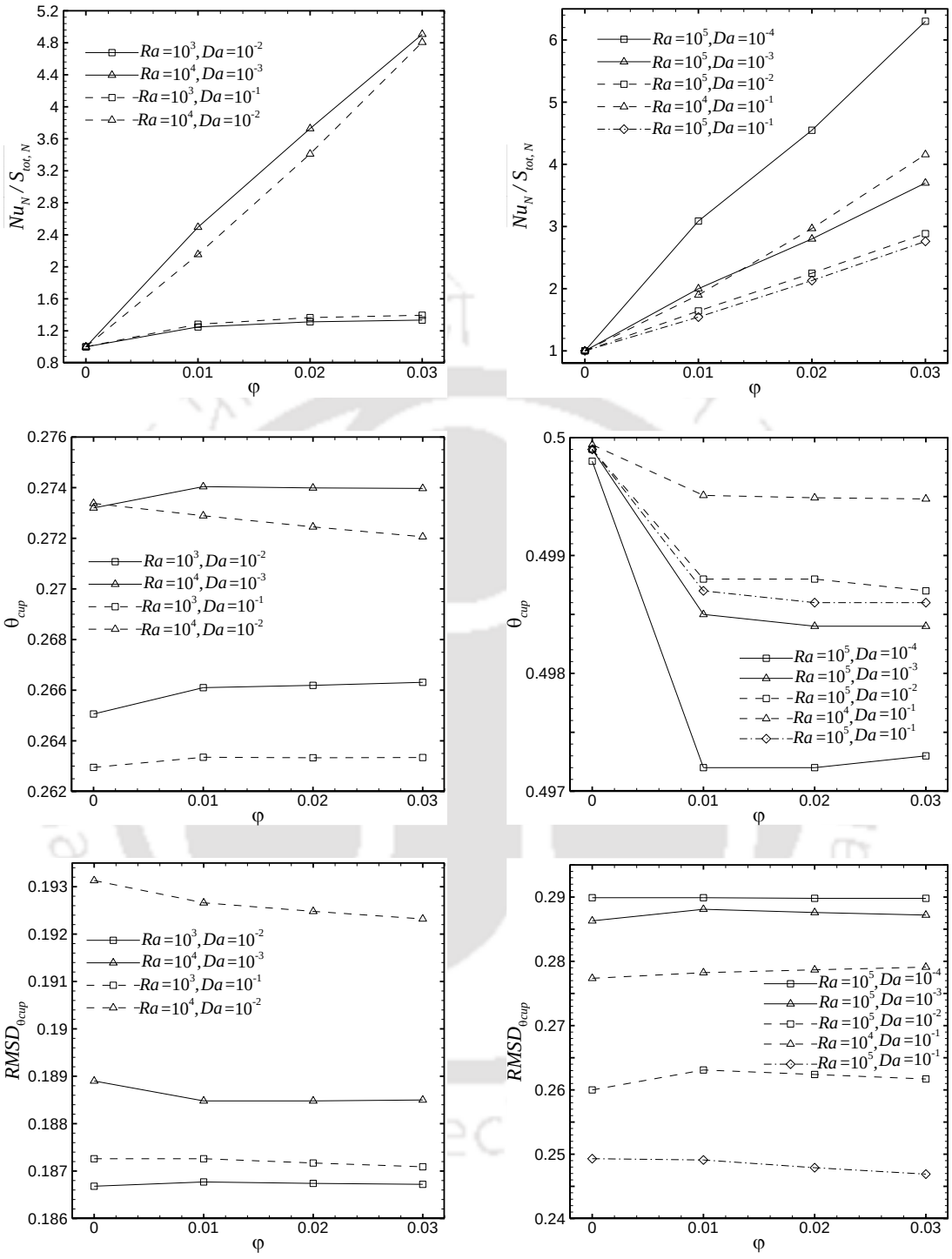

Fig. 6.5. Variations of $\overline{Nu_N}/\overline{S_{tot,N}}$ (top panel) θ_{cup} (middle panel) and $RMSD_{\theta_{cup}}$ (bottom panel) with φ for the bottom to top linear heating (left panel) and for uniform heating (right panel) respectively.

observed that $\overline{S_\psi}$ decreases with φ at all values of Ra_m which is more drastic at higher $Ra = 10^5$ due to the presence of strong buoyant force at the boundary layer which overcomes the retardation effect of increasing viscosity with the addition of nanoparticles. The average Bejan number $\overline{Be}$ increases with φ at all values of Ra_m due to increasing S_θ and decreasing S_ψ with φ. The variation of $\overline{Be}$ is more prominent for moderate $Ra = 10^4$ at all studied Ra_m values due to positive effects of thermal conductivity enhancement with φ.

6.4.4 Performance analysis

Figs. 6.5 show that the variation of $\overline{Nu_N}/\overline{S_{tot,N}}$ with φ resembles the variation of $\overline{Be}$ with φ. Therefore, it is found that $\overline{Nu_N}/\overline{S_{tot,N}}$ i.e., the system efficiency increases with φ for all Ra_m values, which denotes that the total entropy generation of the system decreases whereas heat transfer rate increases. At moderate $Ra = 10^4$, the system efficiency improves faster with an increase in φ. It is found that the nanofluid has a very marginal effect on thermal mixing and degree of temperature uniformity as the variation of θ_{cup} and $RMSD_{\theta_{cup}}$ are found to be negligible.

The results indicate that for the same Darcy-Rayleigh number, the values of calculated parameters differ with changing in Ra and Da values. The present results show that there is an optimum value of volume fraction of nanoparticles up to which the heat transfer rate can be improved for all calculated Ra_m values. Besides, nanofluid is found to be effective in reducing the total entropy generation for all values of Ra_m, which is desirable to cut heat loss for every heat transfer mechanism.

6.5 Conclusions

In the present work, a novel SRT-based two-phase LB model is developed to simulate nanofluid flow through a porous medium. It is obtained from the previous analysis for natural convection in a square porous cavity (as discussed in Chapter 4 in section 4.3) that the uniform heating at the left wall of the cavity is found to be more suitable for higher

$Ra = 10^5$, and higher $Ra_m = 10^3$ at $Ra = 10^4$. Whereas, the bottom to top linear heating can be an effective and alternative heating condition for lower $Ra = 10^3$ and 10^4 at low Darcy-Rayleigh number, $Ra_m = 10$ and 10^2. In this work, the effect of Cu-water nanofluid on fluid flow through a porous medium is investigated by considering both boundary condition at their respective optimum Ra_m values while keeping volume fraction $\varphi \leq 3\%$. It is noticed that nanofluid has successfully reduced the total entropy generation for all values of Ra_m whereas, it augments the heat transfer rate up to a certain volume fraction of nanoparticles (φ_{opt}) due to the contradicting effects of viscosity and thermal conductivity. For $\varphi > \varphi_{opt}$, the negative effect of viscosity on the heat transfer rate dominates over the positive effects of thermal conductivity. However, nanofluid has a very marginal effect on thermal mixing and degree of temperature uniformity as the variation of θ_{cup} and $RMSD_{\theta_{cup}}$ are found to be negligible. Therefore, from the point of view of both 1st and 2nd laws of thermodynamics, nanofluid is found to be an energy-efficient medium compared to the base fluid. The present 2-phase LBM code has been validated carefully with the published results, which provides greater credibility to the simulations of flow and heat transfer of nanofluid through porous structures. It is believed to be the first instance of using two-phase LBM for nanofluid in a porous medium.

Chapter 7

Investigation of an Inner Permeable Hot Square Block on Mixed Convection Flow in a Nanofluid-Filled Cavity by Two-Phase MRT-LBM

7.1 Introduction

The importance of simultaneous use of porous media and nanofluid is already discussed in the previous chapter. In that chapter, a novel SRT-based two-phase LBM model is developed to simulate natural convection flow in a nanofluid-saturated porous cavity by incorporating the Brinkman-Forchheimer-extended Darcy model. The work in this chapter deals with the development and application of MRT-based two-phase LBM model. The present work employs the previous problem of double-sided lid-driven mixed convection in a square cavity with an inner hot permeable square block (mentioned in Chapter 4 in section 4.4) by using Al_2O_3-water nanofluid as a working fluid. According to the author's knowledge, no LBM study has been reported yet to analyse the entropy generation and heat transfer rate for this kind of flow condition. Besides, a very few studies concerning two-phase techniques for nanofluid during mixed convection flow in nanofluid saturated porous enclosures are available in the literature.

7.2 Numerical methodology for nanofluid-saturated porous flow using MRT-LBM

The governing two-phase MRT-LB equation for velocity field is formulated as follows:

$$\mathbf{f}^{\sigma}(\mathbf{r}+\mathbf{e}_i\Delta t, t+\Delta t) - \mathbf{f}^{\sigma}(\mathbf{r},t) = -\mathrm{M}^{-1}\mathrm{R}^{\sigma}\{\mathbf{m}^{\sigma}(\mathbf{r},t) - \mathbf{m}^{\sigma,eq}(\mathbf{r},t)\} + \mathrm{M}^{-1}\left(\mathrm{I}-\frac{\mathrm{R}^{\sigma}}{2}\right)\mathbf{S}^{\sigma} \tag{7.1}$$

where σ refers to two components of nanofluid, $\sigma = f$ for base fluid and $\sigma = p$ for suspended nanoparticles.

The equilibrium moments $\mathbf{m}^{\sigma,eq}$ in vector form is given by,

$$\mathbf{m}^{\sigma,eq} = \left\{\rho^{\sigma}\left(1, -2+\frac{3\mathbf{u}^{\sigma 2}}{\varepsilon}, 1-\frac{3\mathbf{u}^{\sigma 2}}{\varepsilon}, u_x^{\sigma}, -u_x^{\sigma}, u_y^{\sigma}, -u_y^{\sigma}, \frac{u_x^{\sigma 2}-u_y^{\sigma 2}}{\varepsilon}, \frac{u_x^{\sigma}u_y^{\sigma}}{\varepsilon}\right)\right\}^{\mathrm{T}} \tag{7.2}$$

The total force term ($\mathbf{S}^{\sigma}$) are presented by column vector as follows:

$$\mathbf{S}^{\sigma} = \left\{\rho^{\sigma}\left(0, \frac{6\mathbf{u}^{\sigma}.\mathbf{P}^{\sigma}}{\varepsilon}, -\frac{6\mathbf{u}^{\sigma}.\mathbf{P}^{\sigma}}{\varepsilon}, P_x^{\sigma}, -P_x^{\sigma}, P_y^{\sigma}, -P_y^{\sigma}, \frac{2(u_x^{\sigma}P_x^{\sigma}-u_y^{\sigma}P_y^{\sigma})}{\varepsilon}, \frac{(u_x^{\sigma}P_y^{\sigma}+u_y^{\sigma}P_x^{\sigma})}{\varepsilon}\right)\right\}^{\mathrm{T}} \tag{7.3}$$

where

$$P_x^f = \mathbf{F} + \mathbf{N}^f;\ P_y^f = \mathbf{F} + \varepsilon\mathbf{G} + \mathbf{N}^f \tag{7.4}$$

$$P_x^p = P_y^p = \mathbf{N}^p \tag{7.5}$$

The body force **F** incorporates the momentum loss of flow through a porous medium as mentioned in Chapter 6, which is

$$\mathbf{F} = -\frac{\varepsilon\nu^f}{K}\mathbf{u}^{\mathbf{f}} - \frac{\varepsilon F_{\varepsilon}}{\sqrt{K}}|\mathbf{u}^{\mathbf{f}}|\mathbf{u}^{\mathbf{f}} \tag{7.6}$$

G is the external force term which considers the gravity by taking into account the physical properties of the base fluid as depicted earlier in Chapter 5.

$$\mathbf{G} = \rho_f\mathbf{g}\beta_f(\theta-\theta_m) \tag{7.7}$$

In moment space the diagonal relaxation matrix R^{σ} is given as:

$$\mathrm{R}^{\sigma} = \mathrm{diag}(1, r_e^{\sigma}, r_{\epsilon}^{\sigma}, 1, r_q^{\sigma}, 1, r_q^{\sigma}, r_v^{\sigma}, r_v^{\sigma}) \tag{7.8}$$

The governing two-phase MRT-LB equation for temperature field is given as:

$$g_i{}^{\sigma}(\mathbf{r} + \mathbf{e}_i\Delta t, t + \Delta t) - g_i{}^{\sigma}(\mathbf{r}, t) = -\mathbf{N}^{-1}\mathrm{C}^{\sigma}\{\mathbf{n}^{\sigma}(\mathbf{r}, t) - \mathbf{n}^{\sigma,eq}(\mathbf{r}, t)\} \tag{7.9}$$

The diagonal relaxation matrix C^{σ} for each component is given by,

$$\mathrm{C}^{\sigma} = \mathrm{diag}(1, c_{\theta}^{\sigma}, c_{\theta}^{\sigma}, c_e^{\sigma}, c_v^{\sigma}) \tag{7.10}$$

The equilibrium moments $\mathbf{n}^{\sigma,eq}$ is given by,

$$\mathbf{n}^{\sigma,eq} = \left(\theta^{\sigma}, \frac{u_x^{\sigma}.\theta^{\sigma}}{\zeta}, \frac{u_y^{\sigma}.\theta^{\sigma}}{\zeta}, a\theta^{\sigma}, 0\right)^{\mathrm{T}} \tag{7.11}$$

The coefficient ζ gives the heat capacity ratio between solid porous media and fluid, and this value is taken as 1 for simplicity in the present problem. The calculations of macroscopic variables are included in Chapter 6 under section 6.2.1.

7.3 Problem formulation

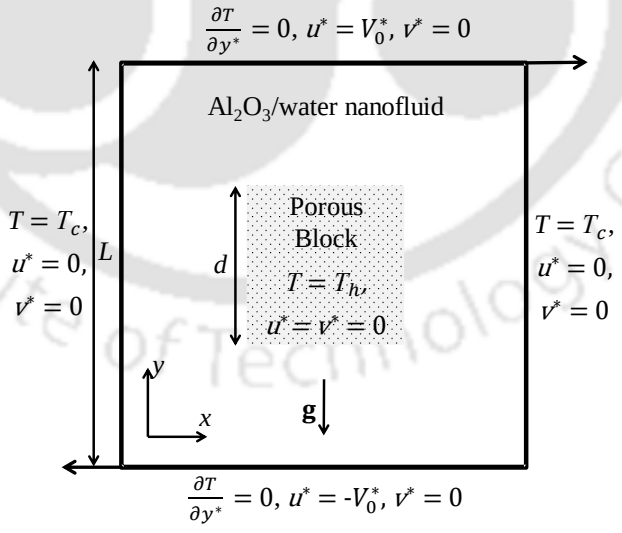

Fig. 7.1. Schematic diagram of the flow configuration with boundary conditions.

Fig. 7.1 shows the model configuration and boundary conditions for the present flow problem in a square cavity with length L including a permeable square block with varying length d at the cavity centre. In the current flow configuration, the insulated top

wall and the bottom wall of the cavity move towards the right and left respectively with a constant speed V_0^* while maintaining the vertical walls at isothermally cold and square block at isothermally hot. The cavity is filled with Al_2O_3-water nanofluid which saturates the permeable block.

For the convenience of numerical calculation and analysis, the non-dimensional forms of the variables are expressed as follows:

$$x = \frac{x^*}{L}; \qquad y = \frac{y^*}{L}; \qquad u = \frac{u^*}{V_0^*}; \qquad v = \frac{v^*}{V_0^*}; \qquad \theta = \frac{T - T_c}{T_h - T_c} \tag{7.12}$$

The boundary conditions in non-dimensional form for the square cavity is given as follows:

$$\begin{aligned} &u = 0; && v = 0; && \theta = 0 && \text{at } x = 0 \text{ and } 1 \\ &u = 0; && v = -1; && \frac{\partial \theta}{\partial y} = 0 && \text{at } y = 0 \\ &u = 0; && v = 1; && \frac{\partial \theta}{\partial y} = 0 && \text{at } y = 1 \end{aligned} \tag{7.13}$$

The boundary conditions in non-dimensional form for the inner permeable square block is:

$$u = 0; \qquad v = 0; \qquad \theta = 1 \tag{7.14}$$

7.4 Results and discussion

A detailed comprehensive study of present mixed convection problem is made for discretely varying Richardson numbers (*Ri*) from 0.1 to 10 and Darcy numbers (*Da*) from 10^{-6} to 10^{-2} at fixed Grashof number $Gr = 10^4$ while considering two blockage ratio of 0.25 and 0.5. The simulations are carried out to realise the effect of Al_2O_3-water nanofluid on heat transfer enhancement while considering the volume fraction of nanoparticles up to 3%. The numbers of plots are presented to show the effect of blockage ratio, *Da*, *Ra* and φ on the average *Nu* over the porous block surface ($\overline{Nu_h}$), average total entropy generation due to heat transfer irreversibility ($\overline{S_\theta}$) and fluid friction irreversibility ($\overline{S_\psi}$). The numerical results obtained for the current problem are discussed in detail in the following sections.

The grid size of 401×401 is found to be suitable for all computations as obtained from the grid-independence test which is included earlier in Chapter 4 under section 4.4.1. The current code can be reduced to two-phase MRT-LB model for nanofluid for large $Da = 10^7$ and to MRT-LBM model for porous structure for $\varphi = 0$. Therefore, the validation of the current code can be ensured by making a comparison of present results with the different published ones dealing with porous medium and nanofluid respectively. These validation tests are already included in the preceding chapters 4 and 5 respectively under the section "Code validation". Hence, for the sake of brevity and to avoid repetition, the validation tests are not included in this chapter. The present code shows a good agreement with the published ones which gives confidence in the numerical results obtained in this work.

7.4.1 Effect of nanofluid on fluid flow and thermal behaviour

Figs. 7.2 and 7.3 depict the effect of *Ri*, *Da* and φ on the fluid flow and thermal behaviour in terms of the distribution of non-dimensional vertical velocity v and temperature θ along the horizontal midline of the cavity respectively. The results are obtained for *Ri* = 0.1, 1.0 and 10.0 separately while maintaining φ at 0% and 3% and $Da = 10^{-2}$, 10^{-4} and 10^{-6}. Fig. 7.2 reveals that at fixed Darcy number, the flow velocity increases inside the porous block with the increase in Richardson number (as mentioned in Chapter 4 under subsection 4.4.3.2). It is observed that the flow rate diminishes and velocity approaches zero when *Da* reaches a very low value of about 10^{-6} for both blockage ratios. The addition of nanoparticles decreases the velocity for both blockage ratios as indicated by the diminishing maximum velocity. This phenomenon is attributed to the augmentation in viscosity with an increase in the volume fraction of nanoparticles φ. Fig. 7.3 indicates that there is no significant change in temperature gradient with the addition of nanoparticles at lower *Da* and *Ri* for both *BR*s as the flow is mainly dominated by conductive heat transfer. However, the slight increment of thermal boundary layer thickness is recognised at higher *Ri* = 10 and $Da = 10^{-2}$ due to enhancement of convective effect with an increase in φ.

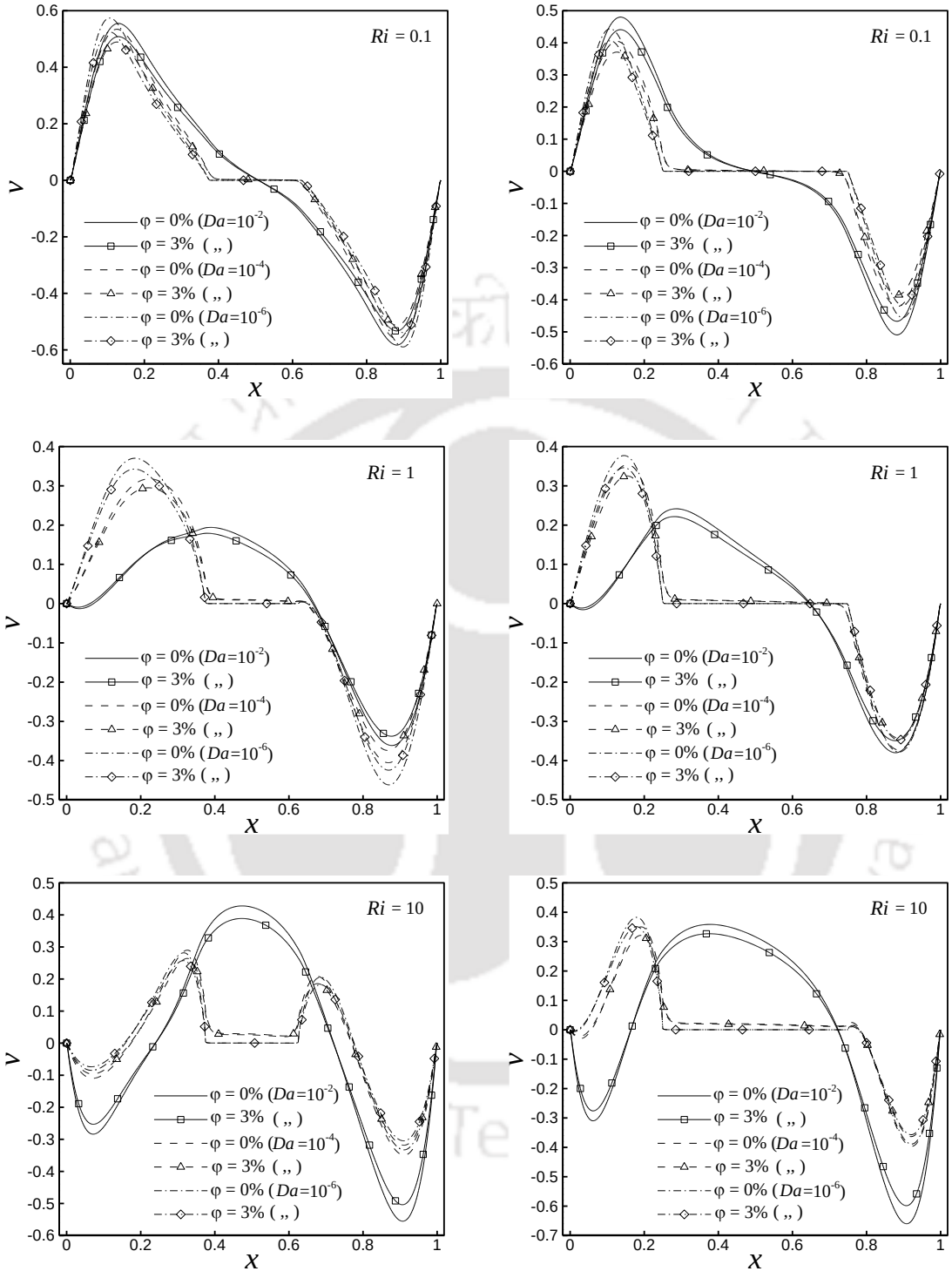

Fig. 7.2. Comparison of *v* for *Ri*'s of 0.1, 1 and 10 respectively for *BR* = 0.25 (left panel) and 0.5 (right panel).

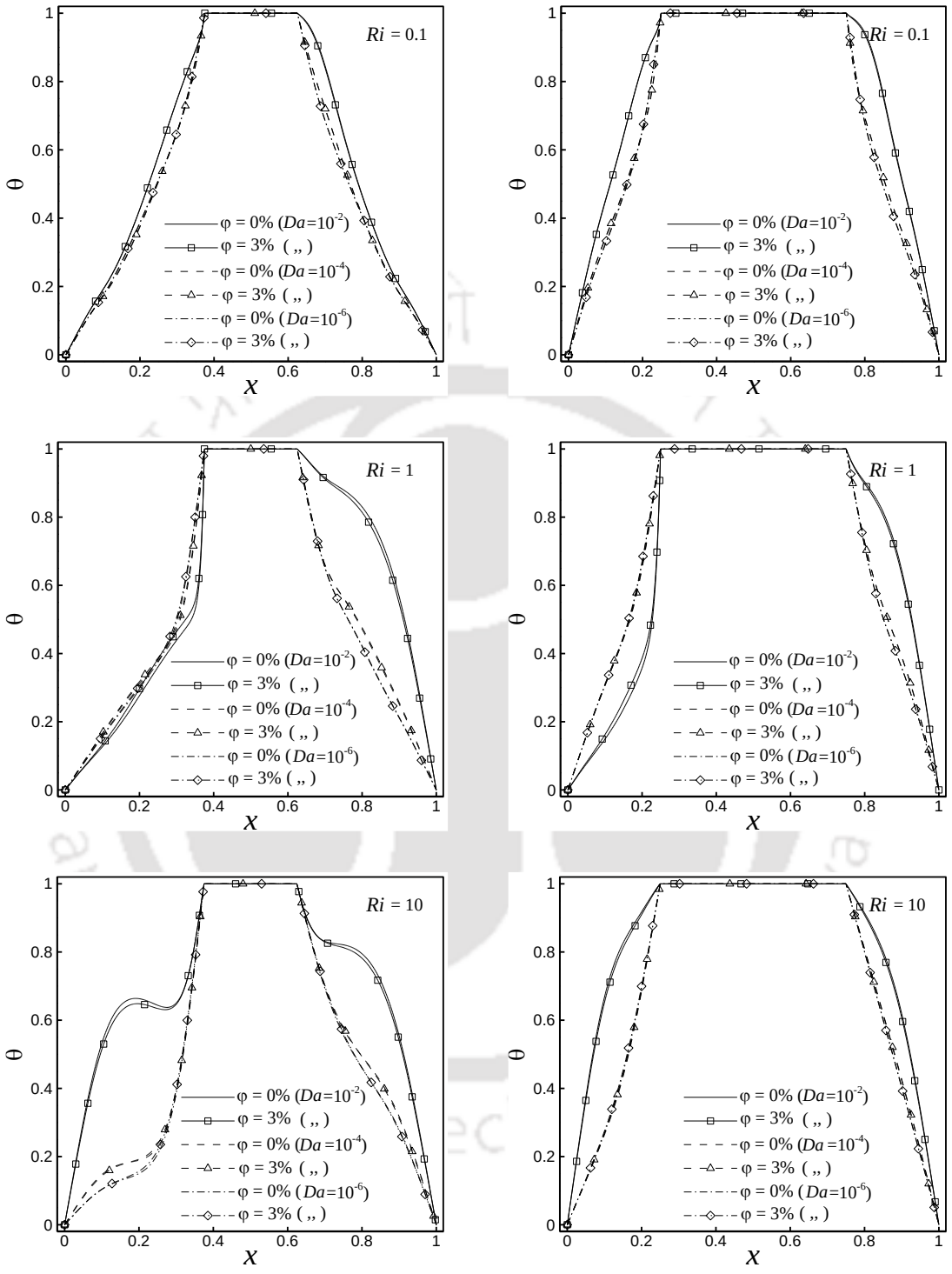

Fig. 7.3. Comparison of θ for *Ri*'s of 0.1, 1 and 10 respectively for *BR* = 0.25 (left panel) and 0.5 (right panel).

7.4.2 Heat transfer rates: Nusselt numbers

Figs. 7.4 and 7.5 respectively show the average Nusselt number over the block surface ($\overline{Nu_h}$) and normalised average Nusselt number ($\overline{Nu}_N$) with an increase in φ for three different *Ri*s and four different *Da*s at two blockage ratios. The irregular behaviour of $\overline{Nu_h}$ at *Ri* = 0.1 with a change in *Da* indicates that the effect of the square porous block is less significant on fluid flow as the flow is mostly dominated by the lid-driven induced forced convection. For all conditions, the value of $\overline{Nu_h}$ is found to be higher for *BR* = 0.5 compared to *BR* = 0.25 due to the presence of higher temperature gradients astride the block resulting from isotherm clustering. $\overline{Nu_h}$ augments with increase in *Ri* for all *Da* for *BR* = 0.25 (as mentioned earlier in Chapter 4 in section 4.4.3.3). For *BR* = 0.5, $\overline{Nu_h}$ is found to be higher at *Ri* = 1 for all *Da* in comparison to *Ri* = 0.1 except at *Da* = 10^{-4} and this enhancement of $\overline{Nu_h}$ with *Ri* is more prominent at *Da* = 10^{-2}. However, a further increase in *Ri* leads to the reduction of $\overline{Nu_h}$ with the exception of *Da* = 10^{-4}. This is attributed to the fact that at higher blockage ratio with an increase in *Ri*, the flow behave more like a channel flow than cavity flow due to restricted passage. The value of $\overline{Nu_h}$ is found to augment with φ for all conditions as the addition of nanoparticles enhances the thermal conductivity of the fluid. Fig. 7.5(a) and (b) show that the increase of normalised average Nusselt number $\overline{Nu}_N$ (ratio of average *Nu* of nanofluid to that of base fluid) with φ is found to be comparable for all *Da* at *Ri* = 0.1 as the flow is mainly controlled by forced convection due to lids movement. It is observed that the maximum $\overline{Nu}_N$ decreases with increases in *Ri* due to the augmented retardation effect of viscosity with an increase in free convection. This decrease in $\overline{Nu}_N$ is more prominent at *Da* = 10^{-2} and 10^{-3}. However, at lower *Da* = 10^{-4} and 10^{-6}, the change of $\overline{Nu}_N$ with *Ri* is insignificant as the conductive heat transfer prevails at these conditions. It is observed that at *Ri* = 0.1, the percentage enhancement of $\overline{Nu_h}$ is slightly higher for *BR* = 0.25 compared to *BR* = 0.5. Besides, the percentage augmentation of heat transfer rate gradually deteriorates with increase in φ as seen by the reducing inclination angle of $\overline{Nu}_N$ profile with φ.

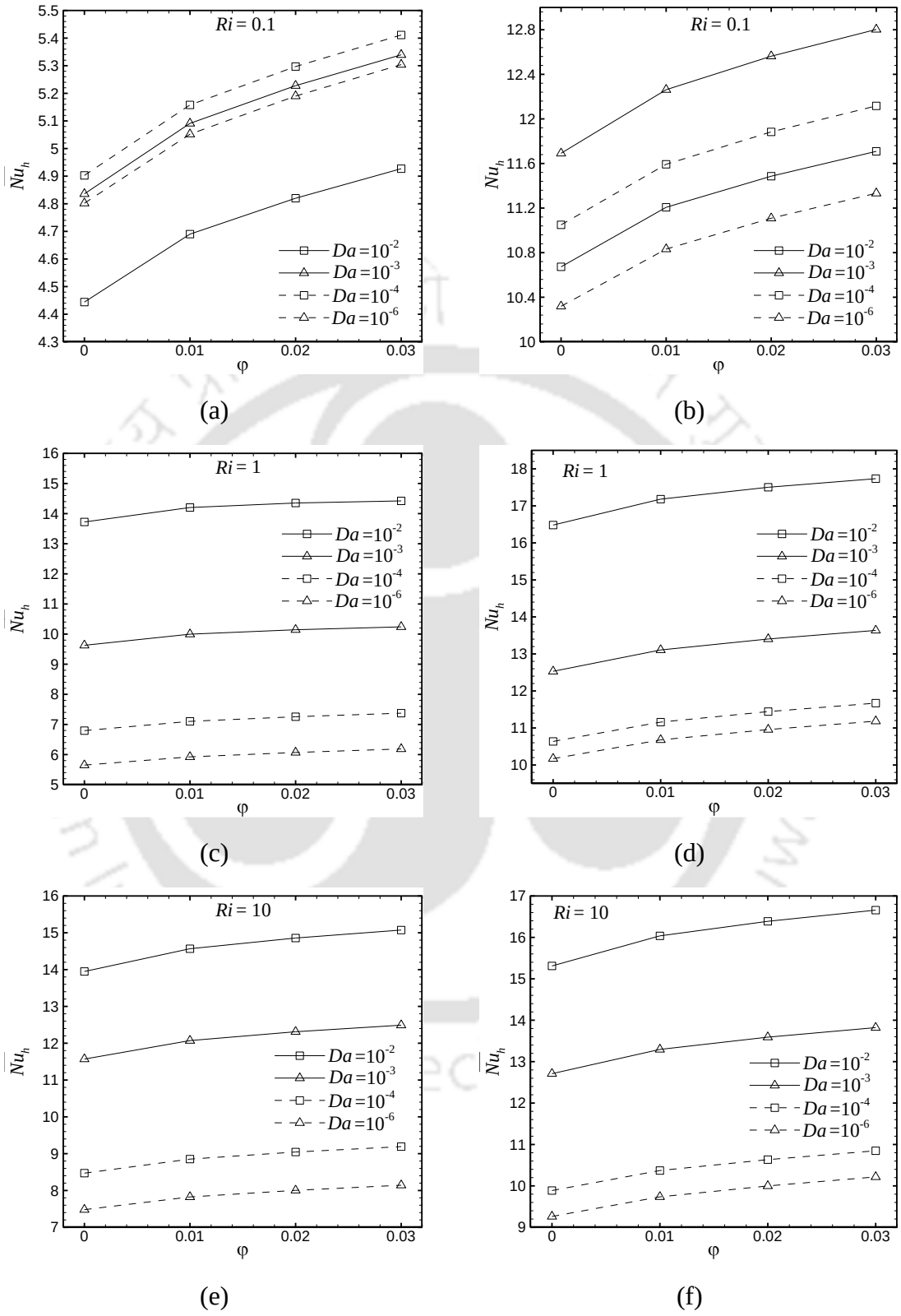

Fig. 7.4. Variations of $\overline{Nu_h}$ with φ for *Ri* = 0.1 (a and b), *Ri* = 1.0 (c and d) and *Ri* = 10.0 (e and f) at *BR* = 0.25 (left panel) and 0.5 (right panel).

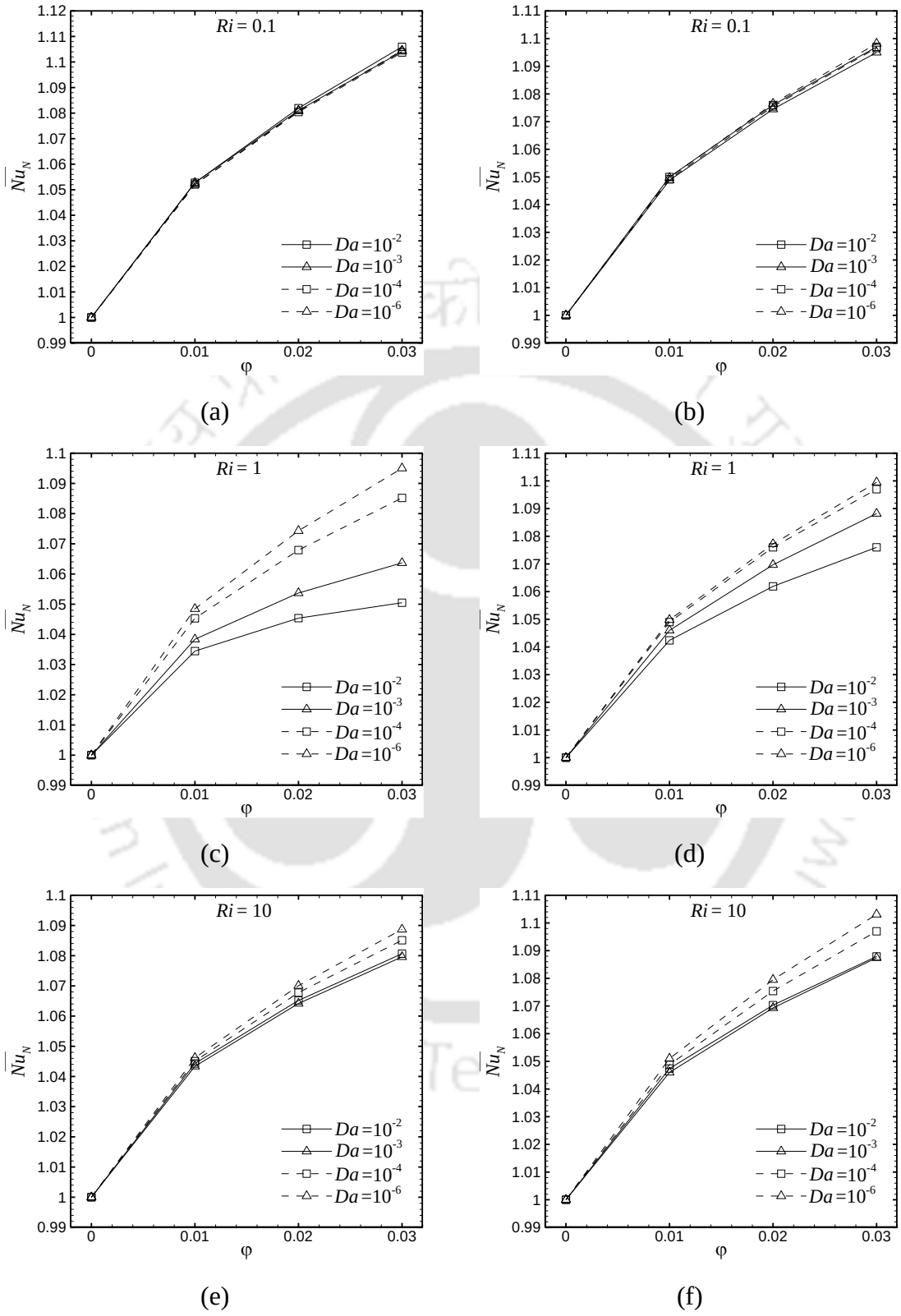

Fig. 7.5. Variations of $\overline{Nu_N}$ with φ for *Ri* = 0.1 (a and b), *Ri* = 1.0 (c and d) and *Ri* = 10.0 (e and f) at *BR* = 0.25 (left panel) and 0.5 (right panel).

7.4.3 Entropy generation and Bejan number

Fig. 7.6 reveals that the variation of average entropy generation due to heat transfer ($\overline{S_\theta}$) over the whole cavity with φ resembles the variation of $\overline{Nu_h}$ with the exception at *Ri* = 0.1 as both the quantities are functions of temperature gradients. Therefore, the same arguments can be provided for their variation with φ. However, the reduction of $\overline{S_\theta}$ with a decrease in *Da* is observed for all *Ri*s for both *BR*s which is in contrast to $\overline{Nu_h}$ at *Ri* = 0.1. This is attributed to the dominating force convection resulted from movement of horizontal walls, thus, the concentration of S_θ is found to be higher near these walls at *Ri* = 0.1. Similar to $\overline{Nu_h}$, value of $\overline{S_\theta}$ is found to be higher for *BR* = 0.5 compared to *BR* = 0.25. Fig. 7.7 depicts that the magnitudes of average total entropy generation due to viscous effect ($\overline{S_\psi}$) throughout the cavity at different values of *Ri* are found to be similar for both blockage ratios. $\overline{S_\psi}$ augments with φ for all Darcy numbers due to the enhancement of viscosity with the addition of nanoparticles. However, it is interesting to observe that the variation $\overline{S_\psi}$ with φ follows a similar pattern for all Darcy numbers. The magnitude of $\overline{S_\psi}$ increases with increase in *Da* for all *Ri*s as more fluid is allowed to flow through the highly permeable block, which results in additional and higher velocity gradients.

Fig. 7.8 shows that the entropy generation is dominated by the heat transfer irreversibility for all prescribed values of *Ri* and *Da*. This is indicated by the high average Bejan number ($\overline{Be}$) over the whole cavity due to the presence of lower entropy generation due to friction as shown in Fig. 7.7. It is observed that $\overline{Be}$ decreases with increase in φ for *Ri* = 1 and 10 as the percentage enhancement of entropy generation due to fluid friction is more prominent compared to entropy generation due to heat transfer. However, at *Ri* = 0.1, $\overline{Be}$ first increases up to φ = 0.01 (Figs. 7.8(a) and (b)) and then decreases with further increase in φ for both blockage ratios.

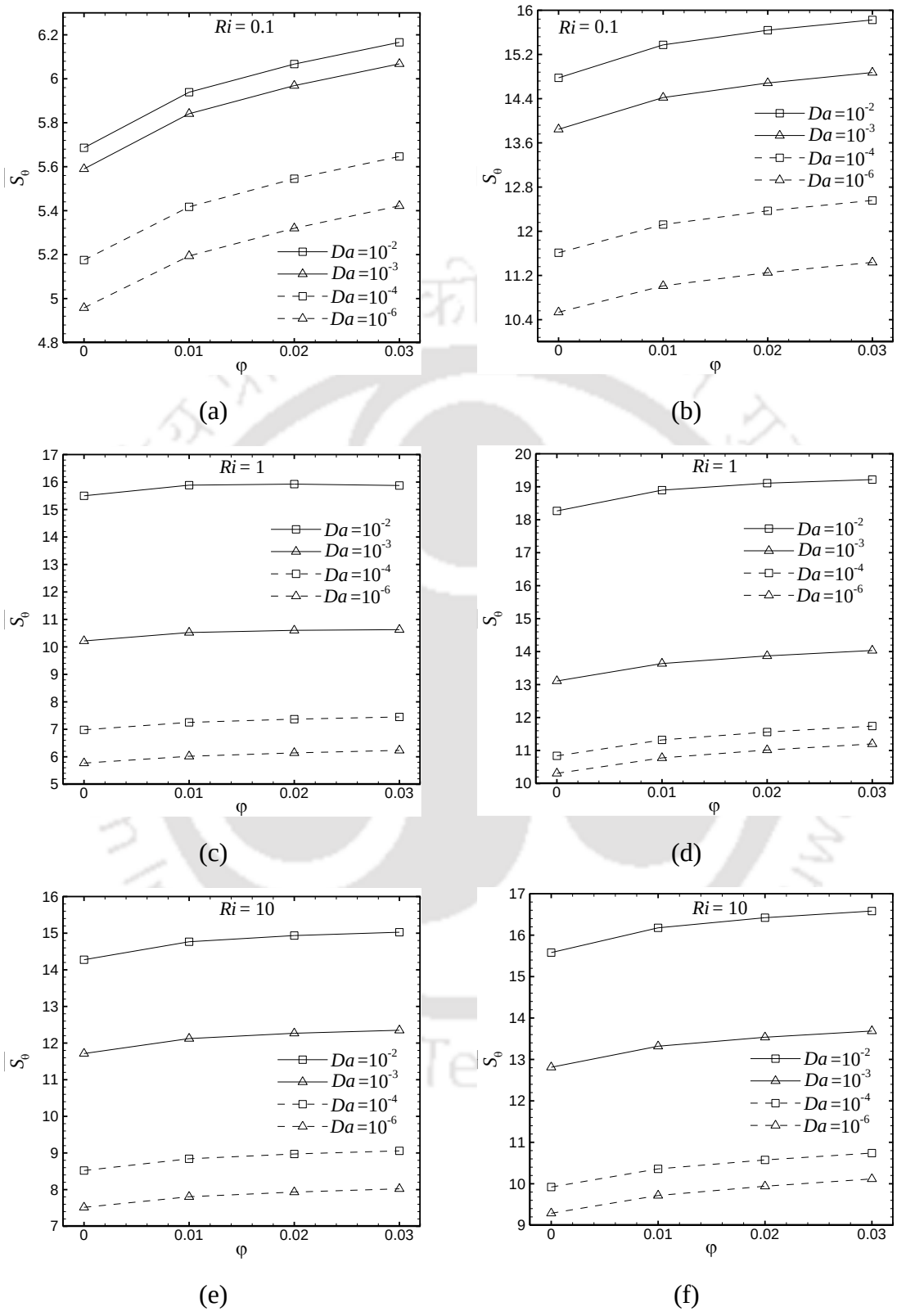

Fig. 7.6. Variations of $\overline{S_\theta}$ with φ for Ri = 0.1 (a and b), Ri = 1.0 (c and d) and Ri = 10.0 (e and f) at BR = 0.25 (left panel) and 0.5 (right panel).

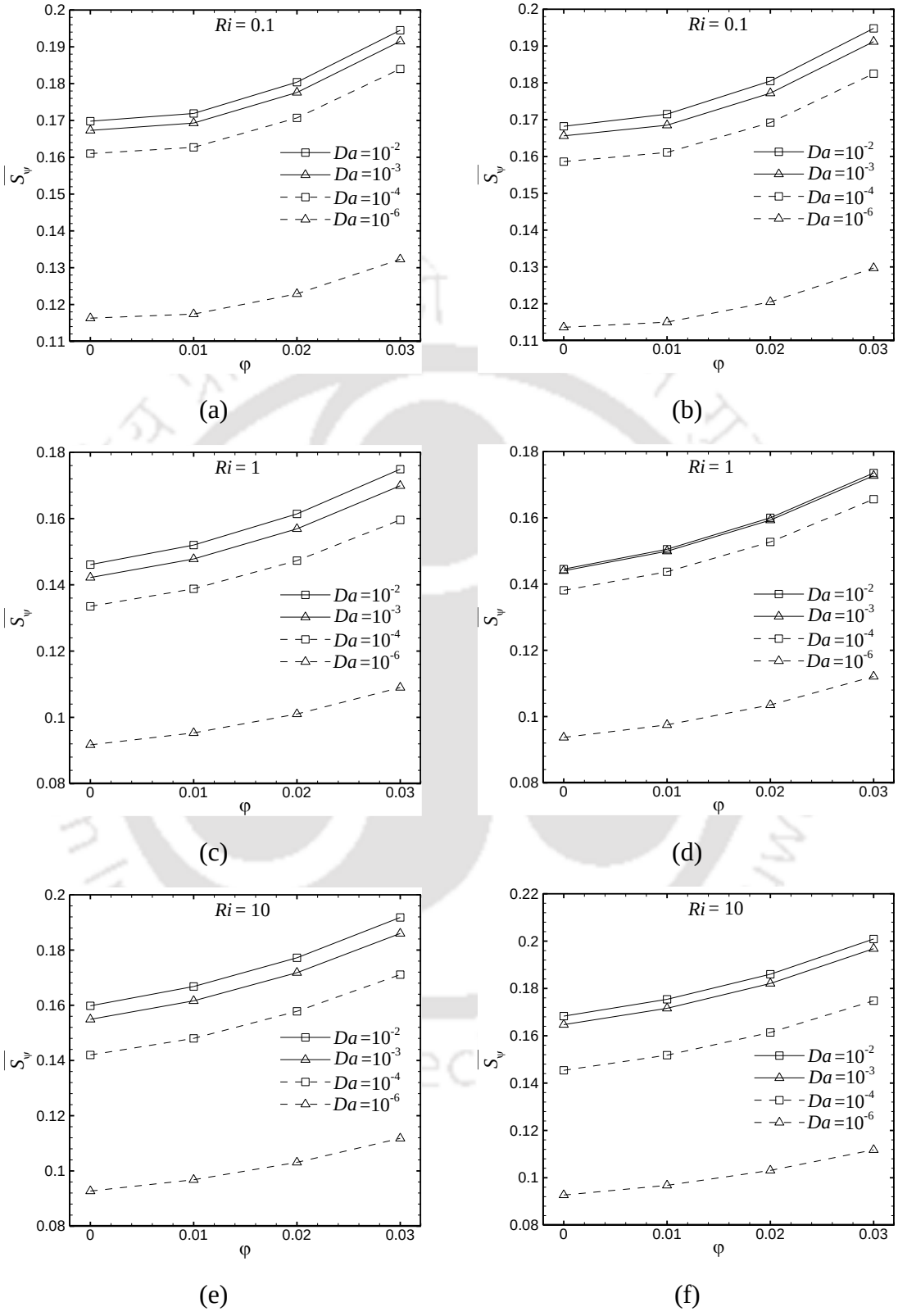

Fig. 7.7. Variations of $\overline{S_\psi}$ with φ for Ri = 0.1 (a and b), Ri = 1.0 (c and d) and Ri = 10.0 (e and f) at BR = 0.25 (left panel) and 0.5 (right panel).

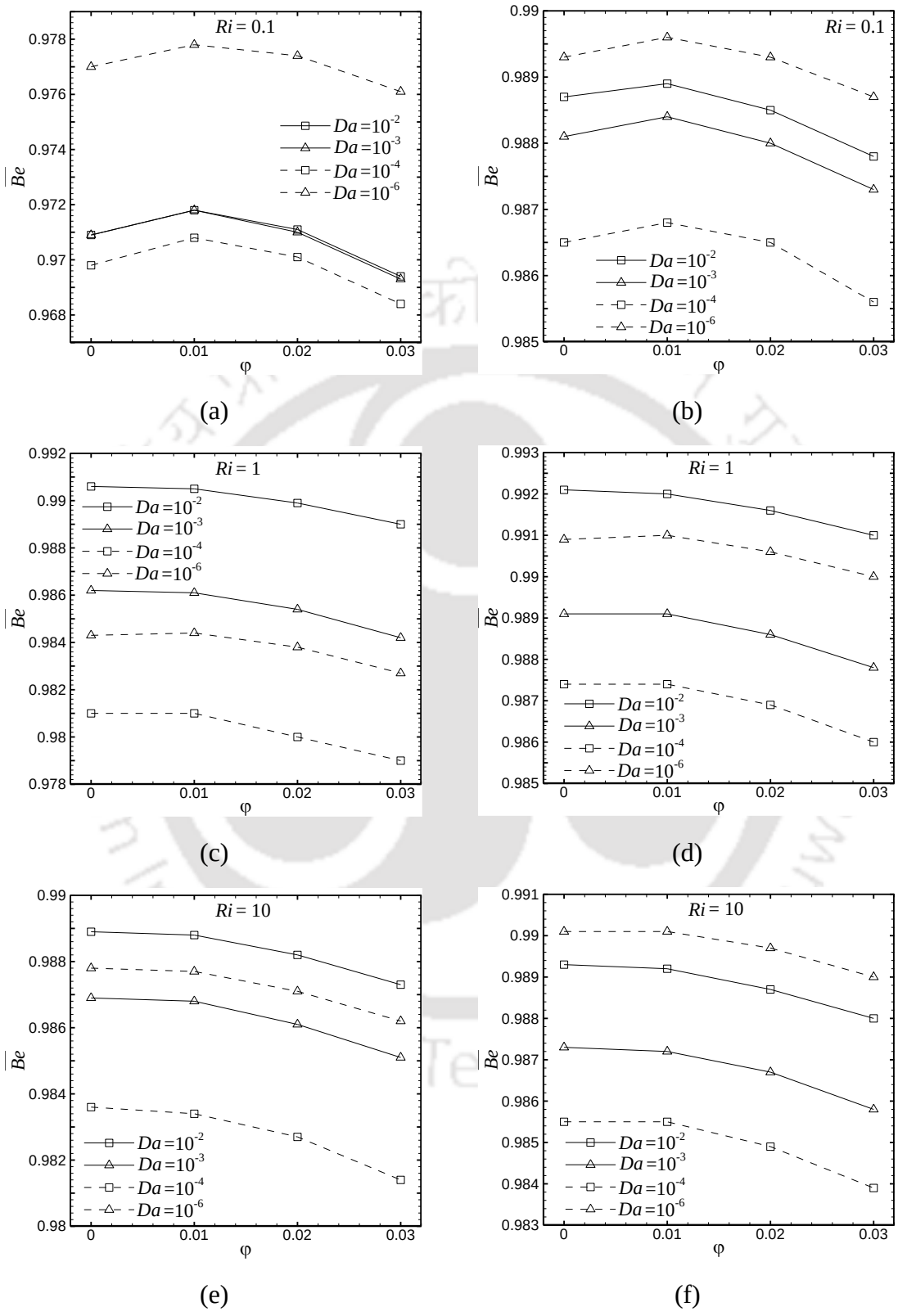

Fig. 7.8. Variations of $\overline{Be}$ with φ for Ri = 0.1 (a and b), Ri = 1.0 (c and d) and Ri = 10.0 (e and f) at BR = 0.25 (left panel) and 0.5 (right panel).

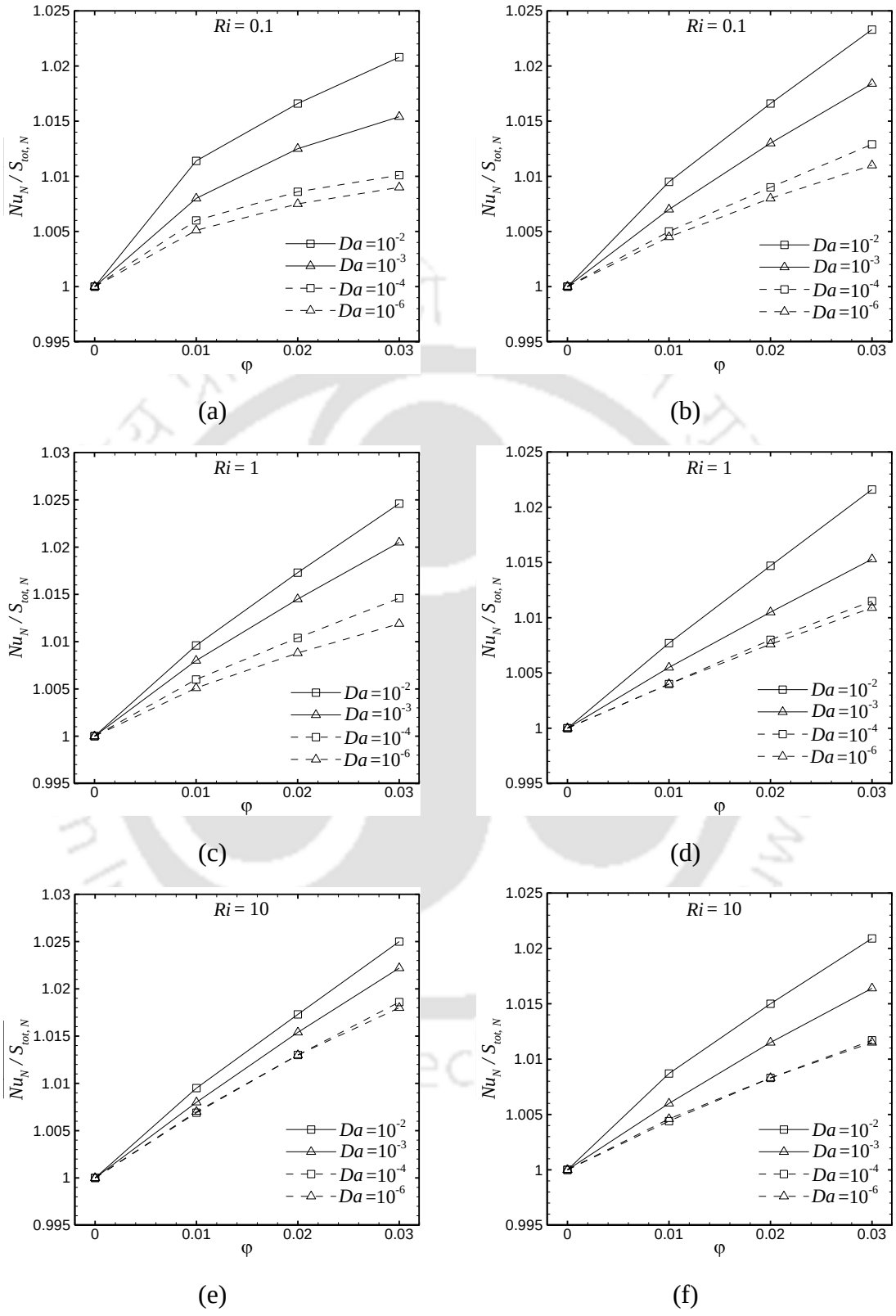

Fig. 7.9. Variations of $\overline{Nu_N}/\overline{S_{tot,N}}$ with φ for Ri = 0.1 (a and b), Ri = 1.0 (c and d) and Ri = 10.0 (e and f) at BR = 0.25 (left panel) and 0.5 (right panel).

7.4.4 Performance analysis

To consider the effect of volume fractions of nanoparticles on the overall efficiency of the system, a performance coefficient parameter is evaluated as termed by Siavashi et al. [2018]. This parameter defined as the ratio of normalised nusselt number $\overline{Nu_N}$ to normalised entropy generation $\overline{S_{tot,N}}$ signifies the heat transfer enhancement with respect to entropy generation increment. Fig. 7.9 reveals that $\overline{Nu_N}/\overline{S_{tot,N}}$ increases with increase in φ for all *Ri*s. Besides, the percentage enhancement of $\overline{Nu_N}/\overline{S_{tot,N}}$ rises with the increase in *Da*. This signifies that both nanofluid and permeable block have a prominent influence on energy efficiency. At *Ri* = 0.1, the augmentation of $\overline{Nu_N}/\overline{S_{tot,N}}$ with φ is found to be higher for *BR* = 0.5 compared to *BR* at 0.25. However, this enhancement is more at *BR* = 0.5 for higher *Ri*. It is observed for *BR* = 0.5 that both forced convection dominated flow conditions at lower *Ri* = 0.1 provide much desirable energy efficiency compared to free convection dominated condition at higher *Ri* = 10.0. This is in contrast to the case for *BR* = 0.25 where the magnitude of maximum $\overline{Nu_N}/\overline{S_{tot,N}}$ is higher at *Ri* = 10.0.

7.5 Conclusions

The present work deals with a novel MRT-based two-phase LB model to simulate nanofluid flow through a porous medium during mixed convection in the cavity while placing a hot permeable square block at the cavity centre. The effect of blockage ratios of the heated permeable block (*BR* = 0.25 and 5), Richardson numbers *Ri* (*Ri* = 0.1, 1 and 10), Darcy numbers (*Da* = 10^{-2}, 10^{-3}, 10^{-4} and 10^{-5}) and volume fractions of Al_2O_3-water nanofluid nanoparticles ($\varphi \leq 3\%$) on the flow and temperature fields are thoroughly analysed while maintaining a fixed Grashof number *Gr* = 10^4. It is noticed that nanofluid has successfully augmented the heat transfer rate due to enhanced thermal conductivity. However, the undesirable total entropy generation increases with the addition of particles. Therefore, a performance coefficient parameter is considered to evaluate the effectiveness of nanofluid based on both 1st and 2nd laws of thermodynamics. The results show that

nanofluid is found to be an energy-efficient medium compared to base fluid due to the presence of higher performance coefficient parameter. The careful validation of present 2-phase LBM code with the published results gives the confidence to carry out the simulations for nanofluid flow through porous structures.

Chapter 8

Conclusion and Scope for Future Work

8.1 Conclusion

This thesis uses a relatively new numerical technique, namely, lattice Boltzmann method to compute a variety of fluid flow and thermal problems of practical significance. Throughout the thesis, qualitative and quantitative aspects of results are systematically analysed with the help of a large number of figures and tables. All the results are produced using computer codes in FORTRAN that have been carefully developed by the author and validated through an extensive comparison exercise. This lends credibility to the results, especially to those pertaining to flow configurations that had not been studied earlier. In the course of what follows the major achievements of the thesis will be described and commented upon.

The thesis work starts with the simulations of different benchmark isothermal and thermal flow problems to validate the developed LBM code by comparing the present results with the published results obtained through conventional numerical techniques. The current work is based on two different versions of the lattice Boltzmann model, namely single-relaxation-time (SRT) and multiple-relaxation-time (MRT). The comparison of SRT and MRT results indicate that both models provide comparable solutions while dealing with laminar flow regime specified by Rayleigh number (Ra) of the order of 10^6. However, MRT-LB model is found to ensure more stability and accuracy than SRT-LB model at higher Rayleigh numbers. This is attributed to the introduction of different relaxation times which relax the respective moment of the distribution functions.

Further, to check the stability of MRT-LB model, the effect of three different Prandtl numbers (Pr = 0.025, 5.83 and 151) on convective heat transfer in a square cavity with an inner solid block is considered. The natural- and mixed-convection phenomena

based on three different boundary conditions in the cavity are investigated. As per the author's best knowledge, no investigation is made to study the effect of varying *Pr*s and blockage ratios on the heat transfer and entropy generation. The results show that the size of the block and *Pr* have a considerable influence on heat transfer rate and entropy generation for different Richardson number (*Ri*) values. The entropy generation due to heat transfer irreversibility dominates flow and temperature fields for all *Pr* irrespective of *Ri*. The drastic augmentation of average total entropy generation due to viscous effect ($\overline{S_\psi}$) with an increase in *Pr* is more pertinent to natural convection than mixed convection. Therefore, the results suggest that opting for mixed convection over natural convection could be beneficial in certain flow conditions by considering the viewpoints of both 1st and 2nd law of thermodynamics.

Next, the computations are made to analyse the entropy generation and heat transfer for two different porous flow configurations in the cavity, which are not considered yet. The first problem employs a generalised thermal lattice Boltzmann model based on SRT approach to study the effect of four different heating conditions at the left vertical wall of the cavity on fluid flow in a water-saturated porous cavity. This investigation deals with several non-dimensional parameters like *Ra* varying from 10^3-10^5, Darcy number (*Da*) from 10^{-1}-10^{-6} at $\varepsilon = 0.5$. It is understood from the results that the values of *Ra* and *Da* play a vital role in determining the optimum condition of heat transfer rate, total entropy generation, thermal mixing and temperature uniformity. The second problem utilises a generalised MRT-LB technique to investigate the effect of the hot permeable inner square block on entropy generation during mixed-convection in a water-filled cavity. The results indicate that the inclination angle of the cavity can be seen as a control parameter for fluid flow and heat transfer. The effect of the square porous block on fluid flow increases with *Ri* due to the enhancement of convective heat transfer. The entropy generation is mainly controlled by heat transfer irreversibility S_θ, whereas the effect of fluid friction irreversibility S_ψ is minimal as characterised by high average Bejan number ($\overline{Be}$) over the whole cavity. The results reveal, while considering both 1st and 2nd laws of thermodynamics, that the values of $\overline{Nu_h}/\overline{S_{tot}}$ (ratio of average Nusselt number to total

entropy generation) for inclination angles, γ = 0° and 90° are comparable to each other and higher compared to the other two inclination angles.

The main concern of this thesis is the simulation of nanofluid flow by using two-phase LBM. Here, an established single-relaxation-time based two-phase lattice Boltzmann model is first exploited and based on that a new multiple-relaxation-time two-phase model is developed for nanofluid flow. The experimental and numerical validations of current two-phase LB model show better accuracy in predicting nanofluid behaviour compared to single-phase LB model. The present investigation explores the behaviour of a new class of nanofluids known as hybrid nanofluid (Al_2O_3-Cu/water) while making a comparative analysis with regular single-particle nanofluids Al_2O_3/water and Cu/water during natural convection in a differentially heated square cavity. The results suggest that the Al_2O_3-Cu/water hybrid nanofluid can serve as an alternative fluid as it provides favourable conditions in terms of efficiency as well as stability due to its synergistic effect resulting from two different single-particle nanofluids. Further, Al_2O_3-Cu/water nanofluid with 9:1 mixture ratio (with volume fractions $\varphi \leq 3\%$) is used to investigate three separate cases of buoyancy-assisted mixed convection cavity flow based on velocity and thermal boundary conditions. To the best of author's knowledge, the two-phase model for nanofluid was not considered before for this kind of flow conditions. This study reveals that the heat transfer rate and total entropy generation of the current system are influenced by the change in boundary condition and Richardson number. The addition of nanoparticles is unable to attain desirable effectiveness in the overall improvement of this system due to the augmentation of entropy generation, despite the improvement of heat transfer rate. Brownian motion and thermophoresis effect contribute to the enhancement of the heat transfer rate by making the nanofluid less viscous while the drag force provides an attenuation effect on heat transfer. This investigation indicates the presence of two different optimal volume fractions based on the maximum heat transfer rate and performance coefficient parameter (ratio of normalised average Nusselt number ($\overline{Nu_N} = \overline{Nu}/\overline{Nu_{\varphi=0}}$) to the normalised average total entropy generation ($\overline{S_{tot,N}} = \overline{S_{tot}}/\overline{S_{tot,\varphi=0}}$)) respectively.

Next, an attempt has been made to broaden the scope of developed two-phase nanofluid code in the field of a nanofluid-saturated porous structure. While doing so, there is a need for some modifications to the existing two-phase LB model for nanofluid. This is obtained by incorporating the Brinkman–Forchheimer-extended Darcy model for porous media into the two-phase model for nanofluid by providing suitable assumptions. Two different versions of this novel two-phase LBM model are developed based on the SRT and MRT approach. First, the codes have been validated carefully with the published results, which provides greater credibility to the simulations of flow and heat transfer of nanofluid through porous structures. Both (SRT & MRT) models are then utilised to study two different flow problems. It is believed to be the first instance of using two-phase LBM for nanofluid in a porous medium. In the first problem, the SRT-based two-phase LB model is utilised to study the effect of Cu-water nanofluid during natural convection in a nanofluid-saturated square cavity. It is noticed that nanofluid has successfully reduced the total entropy generation for all values of Darcy-Rayleigh numbers whereas, it augments the heat transfer rate up to a certain volume fraction of nanoparticles due to the contradicting effects of viscosity and thermal conductivity. The second problem of nanofluid saturated porous structure deals with MRT-based two-phase LBM formulation while simulating nanofluid flow through a porous medium during mixed convection in the cavity while placing a hot permeable square cylinder at the cavity centre. It is found that both nanofluid and permeable block have a positive influence on energy efficiency. The flow configurations considered in this work to exploit the developed LBM models are not addressed before, according to the author's best knowledge.

The foregoing discussions show that a wide variety of fluid flow and heat transfer problems of varying complexities have been studied using lattice Boltzmann method. Both SRT and MRT versions of LBM are used to compute single-phase flow problems involving natural- and mixed convection with or without a porous medium. However, to study nanofluid flow, SRT-based two-phase LBM is first used to gain some experience and then a new MRT-based two-phase model is proposed and executed. Extensive literature survey reveals that no two-phase LBM model to study nanofluid-saturated porous medium exists.

To bridge this gap, a pioneering attempt has been made to develop a two-phase model based on both SRT and MRT approaches to simulate nanofluid flow in a porous medium. The success of this attempt has been substantiated through the presentation of various results and their analysis.

Thus it can be concluded that the goal of the work outlined at the beginning of the thesis has largely been met. The volume of work done and the elements of novelty therein both suggest that the work has been brought to a logical conclusion.

8.2 Scope for future work

This dissertation has been an attempt to develop and expand the field of application of LBM, particularly for nanofluid flow and porous medium. However, the potential remains to gain more insight into the two-phase nanofluid flows with or without porous media. The following are some of the recommendations that could be made for future work:

1. The present LBM code is based on the uniform grid. However, the extension of the current model to the non-uniform grids is possible by using the Taylor series expansion- and least-squares-based LBM. This extension is beneficial in implementing this model more efficiently for flows with complex geometry such as flow through a solid (or permeable) circular/elliptic cylinder while incorporating curved boundary treatment.
2. The present code can be extended further to analyse different flow problems with complex flow configurations pertinent to industrial applications.
3. The current serial code consumes high computational time to provide solutions for steady three-dimensional flow problems. Therefore, the parallelisation technique is needed to be incorporated to get computational acceleration in solving different 3D flow problems.
4. Currently, LBM studies are scarce on compressible flow. Besides most of them deal with compressible flow problems with Mach number less than or equal to one. Though difficult, there seems to be scope for extending LBM to higher Mach numbers.

5. There are examples of multigrid technique being used to accelerate LBM computations for relatively simple flows. There appears to be scope for extending multigrid to the kind of flows studied in this thesis for convergence acceleration.
6. Although the functional relationship between various dimensionless parameters are established by experiments, it is suggested that extensive numerical experiments are carried out and correlations developed.

References

Aidun, C. and Clausen, J. (2010). Lattice-Boltzmann method for complex flows. Annual Review of Fluid Mechanics, 42(1), pp. 439-472.

Alexander, F.J., Chen, S. and Sterling, J. D. (1993). Lattice Boltzmann thermohydrodynamics. Physical Review E, 47(4), pp. R2249-R2252.

Al-Hadhrami, A.K., Elliott, L. and Ingham, D.B. (2003). A new model for viscous dissipation in porous media across a range of permeability values. Transport in Porous Media, 53(1), pp. 117-122.

Al-Rashed, A.A., Kalidasan, K., Kolsi, L., Velkennedy, R., Aydi, A., Hussein, A.K. and Malekshah, E.H. (2018). Mixed convection and entropy generation in a nanofluid filled cubical open cavity with a central isothermal block. International Journal of Mechanical Sciences, 135, pp. 362-375.

Alsabery, A.I., Ismael, M.A., Chamkha, A.J. and Hashim, I. (2018). Mixed convection of Al_2O_3-water nanofluid in a double lid-driven square cavity with a solid inner insert using Buongiorno's two-phase model. International Journal of Heat and Mass Transfer, 119, pp. 939-961.

Anderson, D. Tannehill, J.C. and Pletcher R.H. (2013). Computational fluid mechanics and heat transfer. Boca Raton: CRC Press.

Ansumali, S. and Karlin I.V. (2002). Kinetic boundary conditions in the lattice Boltzmann method. Physical Review E, 66 (2), pp. 026311.

Astanina, M.S., Sheremet, M.A., Oztop, H.F. and Abu-Hamdeh, N. (2018). Mixed convection of Al_2O_3-water Nanofluid in a Lid-driven Cavity Having Two Porous Layers. International Journal of Heat and Mass Transfer, 118, pp. 527-537.

Babu, J.A.R., Kumar K.K. and Rao, S.S. (2017). State-of-art review on hybrid nanofluids. Renewable and Sustainable Energy Reviews, 77, pp. 551-565.

Bahiraei, M. (2014). A comprehensive review on different numerical approaches for simulation in nanofluids: traditional and novel techniques. Journal of Dispersion Science and Technology, 35(7), pp. 984-996.

Bairi, A., Zarco-Pernia, E. and Garcia de Maria, J.-M. (2014). A review on natural convection in enclosures for engineering applications. The particular case of the parallelogrammic diode cavity. Applied Thermal Engineering, 63(1), pp. 304-322.

Basak, T., Roy, S., Sharma, P.K. and Pop, I. (2009). Analysis of mixed convection flows within a square cavity with uniform and non-uniform heating of bottom wall. International Journal of Thermal Science, 48, pp. 891-912.

Bawazeer, S., Mohamad, A.A. and Oclon, P. (2019). Natural convection in a differentially heated enclosure filled with low Prandtl number fluids with modified lattice Boltzmann method. International Journal of Heat and Mass Transfer, 143, pp. 118562.

Baytas, A.C. (2000). Entropy generation for natural convection in an inclined porous cavity. International Journal of Heat and Mass Transfer, 43(12), pp. 2089-2099.

Bejan, A. (1984). Convective heat transfer. New York: Wiley.

Bejan, A. (1996). Entropy generation minimization: The new thermodynamics of finite-size devices and finite-time processes. Journal of Applied Physics, 79(3), pp. 1191-1218.

Benzi, R., Succi, S. and Vergassola, M. (1992). The lattice Boltzmann equation: theory and applications. Physics Reports, 222(3), pp. 145-197.

Bhatnagar, P.L., Gross, E.P. and Krook, M. (1954). A model for collision processes in gases. I. Small amplitude processes in charged and neutral one-component systems. Physical Review, 94(3), pp. 511-525.

Bhatti, M.M., Zeeshan, A., Ellahi, R. and Shit, G.C. (2018). Mathematical modeling of heat and mass transfer effects on MHD peristaltic propulsion of two-phase flow through a Darcy-Brinkman-Forchheimer porous medium. Advanced Powder Technology, 29(5), pp. 1189-1197.

Biswal, P. and Basak, T. (2017). Entropy generation vs energy efficiency for natural convection based energy flow in enclosures and various applications: A review. Renewable and Sustainable Energy Reviews, 80, pp. 1412-1457.

Buongiorno, J. (2006). Convective transport in nanofluids. ASME Journal of Heat Transfer, 128, pp. 240-250.

Cengel, Y.A. (2003). Heat Transfer a Practical Approach. New York: McGraw Hill.

Chapman, S. and Cowling, T.G. (1970). The mathematical theory of non-uniform gases. England: Cambridge University Press.

Chattopadhyay, A., Pandit, S.K., Sarma, S.S. and Pop, I. (2016). Mixed convection in a double lid-driven sinusoidally heated porous cavity. International Journal of Heat and Mass Transfer, 93, pp. 361-378.

Chen, C.L., Chang, S.C., Chen, C.K. and Chang, C.K. (2015). Lattice Boltzmann simulation for mixed convection of nanofluids in a square enclosure. Applied Mathematical Modelling, 39(8), pp. 2436-2451.

Chen, H., Chen, S. and Matthaeus, W.H. (1992). Recovery of the Navier-Stokes equations using a lattice-gas Boltzmann method. Physical Review A, 45, pp. 5339-5342.

Chen, S. and Doolen, G.D. (1998). Lattice Boltzmann method for fluid flows. Annual Review of Fluid Mechanics, 30, pp. 329-364.

Chen, S., Chen, H., Martnez, D. and Matthaeus, W. (1991). Lattice Boltzmann model for simulation of magnetohydrodynamics. Physical Review Letter, 67, pp. 3776-3779.

Cheng, T.S. (2011). Characteristics of mixed convection heat transfer in a lid-driven square cavity with various Richardson and Prandtl numbers. International Journal of Thermal Science, 50, pp. 197-205.

Choi, U.S. and Eastman, J.A. (1995). Enhancing thermal conductivity of fluids with nanoparticles. ASME fed. 231, pp. 99-103.

Corcione, M. (2011). Empirical correlating equations for predicting the effective thermal conductivity and dynamic viscosity of nanofluids. Energy Conversion and Management, 52, pp. 789-793.

d'Humi`eres, D. (1992). Generalized lattice Boltzmann equations, in rarefied gas dynamics, theory and simulations. Progress in Astronautics and Aeronautics, 159, pp. 450-458.

Das, D., Roy, M. and Basak T. (2017). Studies on natural convection within enclosures of various (non-square) shapes - A review. International Journal of Heat and Mass Transfer, 106, pp. 356-406.

Dellar, P. (2002). Lattice kinetic schemes for magnetohydrodynamics. Journal of Computational Physics, 179, pp. 95-126.

de Vahl Davis, G. (1983). Natural convection of air in a square cavity: A bench mark numerical solution. International Journal for Numerical Methods in Fluids, 3(3), pp. 249-264.

Dixit, H.N. and Babu, V. (2006). Simulations of high Rayleigh number natural convection in a square cavity using the lattice Boltzmann method. International Journal of Heat and Mass Transfer, 49, pp. 727-739.

Ergun, S. (1952). Flow through packed columns. Chemical Engineering Progress, 48, pp. 89-94.

Esfandiary, M., Mehmandoust, B., Karimipour, A. and Pakravan, H.A. (2016). Natural convection of Al_2O_3-water nanofluid in an inclined enclosure with the effects of slip velocity mechanisms: Brownian motion and thermophoresis phenomenon. International Journal of Thermal Science, 105, pp. 137-158.

Eslamian, M., Ahmed, M., El-Dosoky, M.F., Saghir, M.Z. (2015). Effect of thermophoresis on natural convection in a Rayleigh–Benard cell filled with a nanofluid. International Journal of Heat and Mass Transfer, 81, pp.142-156.

Freed, D.M. (1998). Lattice Boltzmann method for macroscopic porous media modelling. International Journal of Modern Physics C, 9, pp. 1491-1503.

Frenkel, D. and Smit, B. (2002). Understanding molecular simulation: from algorithms to applications. Computational science series, San Diego: Academic Press.

Frisch, U., Hasslacher, B. and Pomeau, Y. (1986). Lattice-gas automata for the Navier-Stokes equations. Physical Review Letter, 56, pp. 150-508.

Gangawane, K.M. (2016). Computational analysis of mixed convection heat transfer characteristics in lid driven cavity containing triangular block with constant heat flux: effect of Prandtl and Grashof numbers. International Journal of Heat and Mass Transfer, 105, pp. 34-57.

Garoosi, F., Garoosi, S. and Hooman, K. (2014). Numerical simulation of natural convection and mixed convection of the nanofluid in a square cavity using Buongiorno model. Powder Technology, 268, pp. 279-292.

Garoosi, F., Jahanshaloo, L. and Garoosi, S. (2015). Numerical simulation of mixed convection of the nanofluid in heat exchangers using a Buongiorno model. Powder Technology, 269, pp. 296-311.

Ghasemi, K. and Siavashi, M. (2017). Lattice Boltzmann numerical simulation and entropy generation analysis of natural convection of nanofluid in a porous cavity with different linear temperature distributions on side walls. Journal of Molecular Liquid, 233, pp. 415-430.

Ghia, U., Ghia, K.N., and Shin, C. T. (1982). High-Re solutions for incompressible flow using the Navier-Stokes equations and a multigrid method. Journal of Computational Physics, 48(3), pp. 387-411.

Guo, T.S. and Zhao, A. (2005). Lattice Boltzmann model for convection heat transfer in porous media. Numerical Heat Transfer, Part B: Fundamentals, 47, pp. 157-177.

Guo, Y., Bennacer, R., Shen, S., Ameziani, D.E. and Bouzidi, M. (2010). Simulation of mixed convection in slender rectangular cavity with lattice Boltzmann method. International Journal of Numerical Methods for Heat & Fluid Flow, 20, pp. 130-148.

Guo, Z. and Shu, C. (2013). Lattice Boltzmann method and its applications in engineering. Singapore: World Scientific.

Guo, Z.L., Shi, B.C. and Zheng C.G. (2002a). A coupled lattice BGK model for the Boussinesq equations, International Journal for Numerical Methods in Fluids, 39, pp. 325-342.

Guo, Z.L., Zheng, C.G. and Shi, B.C. (2002b). Non-equilibrium extrapolation method for velocity and pressure boundary conditions in the lattice Boltzmann method. Chinese Physics, 11, pp. 366-374.

Guo, Z., Zhao, T.S. (2002). Lattice Boltzmann model for incompressible flows through porous media. Physical Review E, 66, pp. 036304.

Guo, Z., Zheng, C. and Shi, B. (2002c). Discrete lattice effects on the forcing term in the lattice Boltzmann method. Physical Review E, 65.

Gupta, M., Singh, V., Kumar, R. and Said, Z. (2017). A review on thermophysical properties of nanofluids and heat transfer applications. Renewable and Sustainable Energy Reviews, 74, pp. 638-670.

Hadad, Z., Oztop, H.F., Abu-Nada. E. and Mataoui, A. (2012). A review on natural convective heat transfer of nanofluids. Renewable and Sustainable Energy Reviews, 16 (7), pp. 5363-5378.

Haldar, S.C., Mohanty, A.K. and Dubey, M.R. (2000). Laminar free convection in open-ended vertical 7-rod bundles: experiments and porous model. Nuclear Engineering and Design, 198 (3), pp. 295-305.

Hardy J., de Pazzis O., Pomeau Y. (1976). Molecular dynamics of a classical lattice gas: transport properties and time correlation functions. Physical Review A, 13, pp. 194-961.

He X. and Luo L.S. (1997). Theory of the lattice Boltzmann method: From the Boltzmann equation to the lattice Boltzmann equation. Physics Review E, 56, pp. 6811-6817.

He, X., Chen. S. and Doolen, G.D. (1998). A novel thermal model for the lattice Boltzmann method in incompressible limit. Journal of Computational Physics, 146, pp. 282-300.

He, Y., Qi, C., Hu, Y., Qin, B., Li, F. and Ding, Y. (2011). Lattice Boltzmann simulation of alumina-water nanofluid in a square cavity. Nanoscale Research Letters, 6 (1), pp. 184-191.

Higuera, F.J. and Jimenez, J. (1989). Boltzmann approach to lattice gas simulations. Europhysics Letters, 9, pp. 663-668.

Ho, C.J., Cheng, Y.T. and Wang, C.C. (1994). Natural convection between two horizontal cylinders inside a circular enclosure subjected to external convection. International Journal of Heat Fluid Flow, 15, pp. 299-306.

Ho, C.J., Huang, J.B., Tsai, P.S. and Yang, Y.M. (2011). On laminar convective cooling performance of hybrid water-based sus-pensions of Al_2O_3 nanoparticles and MEPCM particles in a circular tube. International Journal of Heat and Mass Transfer, 54, pp. 2397-2407.

Ho, C.J., Liu, W.K., Chang, Y.S. and Lin, C.C. (2010). Natural convection heat transfer of alumina–water nanofluid in vertical square enclosures: an experimental study. International Journal of Thermal Science, 49, pp. 1345-1353.

Hou, S., Zou, Q., Chen, S., Doolen G. and Cogley, A.C. (1995). Simulation of cavity flow by the lattice Boltzmann method. Journal of Computational Physics, 118, pp. 329-347.

Huang, H., Sukop, M.C. and Lu, X.Y. (2015). Multiphase lattice Boltzmann methods: theory and applications. Hoboken: Wiley-Blackwell.

Hussain, S., Mehmood, K., Sagheer, M. and Yamin, M. (2018). Numerical simulation of double diffusive mixed convective nanofluid flow and entropy generation in a square porous enclosure. International Journal of Heat and Mass Transfer, 122, pp. 1283-97.

Ijam, A. and Saidur, R. (2012). Nanofluid as a coolant for electronic devices (cooling of electronic devices). Applied Thermal Engineering, 32, pp. 76-82.

Ilis, G.G., Mobedi, M. and Sunden, B. (2008). Effect of aspect ratio on entropy generation in a rectangular cavity with differentially heated vertical walls. International Communications in Heat and Mass Transfer, 35, pp. 696-703.

Incropera, F.P. and DeWitt, D.P. (2002). Introduction to heat transfer. New York: Wiley.

Ingham, D.B. and Pop, I. (Eds.) (2005). Transport phenomena in porous media. Oxford: Pergamon.

Islam, A.W., Sharif. M.A.R. and Carlson, E.S. (2012). Mixed convection in a lid driven square cavity with an isothermally heated square blockage inside. International Journal of Heat and Mass Transfer, 55, pp. 5244-55.

Iwatsu, R., Hyun, J.M. and Kuwahara, K. (1993). Mixed convection in a driven cavity with a stable vertical temperature gradient. International Journal of Heat and Mass Transfer, 36, pp. 1601-1608.

Izadi, S., Armaghani, T., Ghasemiasl, R., Chamkha, A.J. and Molana, M.A. (2019). comprehensive review on mixed convection of nanofluids in various shapes of enclosures. Powder Technology, 343, pp. 880-907.

Jana, S., Khojin, A.S., Zhong, W.H. (2007). Enhancement of fluid thermal conductivity by the addition of single and hybrid nano-additives. Thermochimica Acta, 462, pp. 45-55.

Ji, C.Z., Shu, C. and Zhao N. (2009). Lattice Boltzmann method-based flux solver and its application to solve shock tube problem. Modern Physics Letter B, 23, pp. 313-316.

Joshi, H., Agarwal, A., Puranik, B., Shu, C. and Agrawal, A. (2010). A hybrid FVMLBM method for single and multi-fluid compressible flow problems. International Journal for Numerical Methods in Fluids, 62, pp. 403-427.

Kakaç, S. and Pramuanjaroenkij, A. (2016). Single-phase and two-phase treatments of convective heat transfer enhancement with nanofluids - a state-of-the-art review. International Journal of Thermal Science, 100, pp. 75-97.

Kaluri, R.S. and Basak, T. (2011). Entropy generation due to natural convection in discretely heated porous square cavities. Energy, 36(8), pp. 5065-5080.

Karimipour, A., Nezhad, A.H., D'Orazio. A. and Shirani, E. (2013). The effects of inclination angle and Prandtl number on the mixed convection in the inclined lid driven cavity using lattice Boltzmann method. Journal of Theoretical and Applied Mechanics, 51, pp. 447-462.

Kasaeian, A., Azarian, R.D., Mahian, O., Kolsi, L., Chamkha, A.J., Wongwises, S. and Pop, I. (2017). Nanofluid flow and heat transfer in porous media: A review of the latest developments. International Journal of Heat and Mass Transfer, 107, pp. 778-791.

Kataoka, T. and Tsutahara, M. (2004). Lattice Boltzmann method for the compressible Euler equations. Physical Review E, 69, pp. 056702.

Kaviany, S. (1995). Principles of heat transfer in porous media. New York: Springer-Verlag.

Khanafer, K. and Aithal, S.M. (2013). Laminar mixed convection flow and heat transfer characteristics in a lid driven cavity with a circular cylinder. International Journal of Heat and Mass Transfer, 66, pp. 200-209.

Khanafer, K. and Chamkha, A.J. (1999). Mixed convection flow in a lid-driven enclosure filled with a fluid-saturated porous medium. International Journal of Heat and Mass Transfer, 42, pp. 2465-2481.

Kosec, G. and Sarler, B. (2013). Solution of a low Prandtl number natural convection benchmark by a local meshless method. International Journal of Numerical Methods for Heat & Fluid Flow, 23(1), pp. 189-204.

Krishna, D.J., Thansekhar, M.R., Venkateshan, S.P., Basak, T. and Das, S.K. (2010). Natural convection in a partially heat generating rod bundle inside an enclosure. Journal of Heat Transfer, 132(10), pp. 102501.

Krüger, T., Kusumaatmaja, H., Kuzmin, A., Shardt, O., Silva, G. and Viggen, E.M. (2016). The Lattice Boltzmann Method: Principles and Practice. Switzerland: Springer.

Ku, H.C., Hirsh, R.S. and Taylor, T.D. (1987). A pseudospectral method for solution of the three-dimensional Navier–Stokes equations. Journal of Computational Physics, 70(2), pp. 439-462.

Ladd, A.J.C. (1994). Numerical simulations of particulate suspensions via a discretized Boltzmann equation. Part I. Theoretical foundation. Journal of Fluid Mechanics, 271, pp. 285-310.

Lallemand, P. and Luo, L.S. (2003). Theory of the lattice Boltzmann method: Acoustic and thermal properties in two and three dimensions. Physical Review E, 165, pp. 036706.

Lallemand, P. and Luo, L.S. (2000). Theory of the lattice Boltzmann method: Dispersion, dissipation, isotropy, Galilean invariance, and stability. Physical Review E, 61, pp. 6546-6562.

LeQuéré, P. (1991). Accurate solutions to the square thermally driven cavity at high Rayleigh number. Computer & Fluids, 20, pp. 29-41.

Li, G., Aktas, M. and Bayazitoglu, Y. (2015). A review on the discrete Boltzmann model for nanofluid heat transfer in enclosures and channels. Numerical Heat Transfer, Part B: Fundamentals, 67(6), pp. 463-488.

Li, Z., Yang, M. and Zhang, Y. (2016). Double MRT thermal lattice Boltzmann method for simulating natural convection of low Prandtl number fluids. International Journal of Numerical Methods for Heat and Fluid Flow, 26(6), pp. 1889-1909.

Liu, Q., He, Y.L., Li, Q. and Tao. W. (2014). A multiple-relaxation-time lattice Boltzmann model for convection heat transfer in porous media, International Journal of Heat and Mass Transfer, 73, pp. 761-775.

Luo, L.S. (1993). Lattice-gas automata and lattice Boltzmann equations for two-dimensional hydrodynamics. Ph.D. thesis, Georgia Institute of Technology.

Magherbi, M., Abbassi, H. and Brahim, A.B. (2003). Entropy generation at the onset of natural convection. International Journal of Heat and Mass Transfer, 46, pp. 3441-3450.

Mahapatra, P.S., De, S., Ghosh, K. and Manna, N.K. and Mukhopadhyay, A. (2013). Heat transfer enhancement and entropy generation in a square enclosure in the presence of adiabatic and isothermal blocks. Numerical Heat Transfer, Part A: Applications, 64(7), pp. 577-596.

Mahdi, R.A., Mohammed, H.A., Munisamy, K.M. and Saeid, N.H. (2015). Review of convection heat transfer and fluid flow in porous media with nanofluid. Renewable and Sustainable Energy Reviews, 41, pp. 715-734.

Mahian, O., Kianifar, A., Kleinstreuer, C., Al-Nimr, M.A., Pop, I., Sahin, A.Z., Wongwises, S. (2013). A review of entropy generation in nanofluid flow. International Journal of Heat and Mass Transfer, 65, pp. 514-532.

Mahian, O., Kolsi, L., Amani, M., Estellé, P., Ahmadi, G., Kleinstreuer, C., Marshall, J.S., Siavashi, M., Taylor, R.A., Niazmand, H., Wongwises, S., Hayat, T., Kolanjiyil, A., Kasaeian, A. and Pop, I. (2019a). Recent advances in modeling and simulation of nanofluid flows-Part I: Fundamentals and theory. Physics Reports, 790, pp. 1-48.

Mahian, O., Kolsi, L., Amani, M., Estellé, P., Ahmadi, G., Kleinstreuer, C., Marshall, J.S., Taylor, R.A., Niazmand, H., Wongwises, S., Hayat, T., Kolanjiyil, A., Kasaeian, A. and Pop, I. (2019b). Recent advances in modeling and simulation of nanofluid flows-Part II: Applications. Physics Reports, 791, pp. 1-59.

Mallinson, G.D. and de Vahl Davis, G. (1977). Three-dimensional natural convection in a box: A numerical study. Journal of Fluid Mechanics, 83, pp. 1-31.

Markatos, N.C. and Pericleous, K.A. (1984). Laminar and turbulent natural convection in an enclosed cavity. International Journal of Heat and Mass Transfer, 27, pp. 755-772.

McNamara, G. and Zanetti, G. (1998). Use of the Boltzmann equation to simulate lattice-gas automata. Physical Review Letter, 61, pp. 2332-2335.

Mehryan, S.A.M., Kashkooli, F.M., Ghalambaz, M. and Chamkha, A.J. (2017). Free convection of hybrid Al_2O_3-Cu water nanofluid in a differentially heated porous cavity, Advanced Powder Technology, 28, pp. 2295-2305.

Mei, R., Luo, L.S. and Shyy, W. (1999). An accurate curved boundary treatment in the lattice Boltzmann method. Journal of Computational Physics, 155, pp. 307-330.

Mezrhab, A., Moussaoui, M., Jami, M., Naji, H. and Bouzidi, M. (2010). Double MRT thermal lattice Boltzmann method for simulating convective flows. Physical Letters A, 374 (34), pp. 3499-3507.

Mittal, N., Manoj, V., Kumar, D.S. and Anbalagan, S. (2013). Numerical Simulation of Mixed Convection in a Porous Medium Filled with Water/Al_2O_3 Nanofluid. Heat Transfer-Asian Research, 42(1), pp. 46-59.

Moallemi, M.K. and Jang, K.S. (1992). Prandtl number effects on laminar mixed convection heat transfer in a lid-driven cavity. International Journal of Heat and Mass Transfer, 35, pp. 1881-1892.

Mohamad, A.A. (2011). Lattice Boltzmann method: Fundamentals and engineering applications with computer codes. London: Springer.

Mohamad, A.A. and Viskanta, R. (1991). Transient natural convection of low-Prandtl-number fluids in a differentially heated cavity. International Journal for Numerical Methods in Fluids, 13(1), pp. 61-81.

Mohamad, A.A. and Kuzmin, A. (2010). A critical evaluation of force term in lattice Boltzmann method, natural convection problem. International Journal of Heat and Mass Transfer, 53, pp. 990-996.

Motlagh, S.Y. and Soltanipour, H. (2017). Natural convection of Al_2O_3-water nanofluid in an inclined cavity using Buongiorno's two-phase model. International Journal of Thermal Science, 111, pp. 310-320.

Motlagh, S.Y., Taghizadeh, S. and Soltanipour, H. (2016). Natural convection heat transfer in an inclined square enclosure filled with a porous medium saturated by nanofluid using Buongiorno's mathematical model. Advanced Powder Technology, 27, pp. 2526-2540.

Nayak, R.K., Bhattacharyya, S. and Pop, I. (2016). Heat transfer and entropy generation in mixed convection of a nanolfuid within an inclined skewed cavity. International Journal of Heat and Mass Transfer, 102, pp. 596-609.

Nemati, H., Farhadi, M., Sedighi, K., Fattahi, E., and Darzi, A.A.R. (2010). Lattice Boltzmann simulation of nanofluid in lid-driven cavity. International Communications in Heat and Mass Transfer, 37(10), pp. 1528-1534.

Nguyen, M.T., Aly, A.M. and Lee, S.W. (2015). Natural convection in a non-Darcy porous cavity filled with Cu-water nanofluid using the characteristic-based split procedure in finite-element method. Numerical Heat Transfer, Part A: Applications, 67, pp. 224-247.

Nield, D.A. and Bejan, A. (1999). Convection in porous media. New York: Springer-Verlag.

Nield, D.A. and Kuznetsov, A.V. (2014). Thermal instability in a porous medium layer saturated by a nanofluid: a revised model. International Journal of Heat and Mass Transfer, 68, pp. 211-214.

Nithiarasu, P., Seetharamu, K.N. and Sundararajan, T. (1997). Natural convective heat transfer in a fluid saturated variable porosity medium. International Journal of Heat and Mass Transfer, 40 pp. 3955-3967.

Nnanna, A.G.A. (2007). Experimental model of temperature-driven nanofluid. ASME Journal of Heat Transfer, 129, pp. 697-704.

Ostrach, S. (1998). Natural convection in enclosures. Journal of Heat Transfer, 110, pp. 1175-1190.

Oztop, H.F. and Dagtekin, I. (2004). Mixed convection in two-sided lid-driven differentially heated square cavity. International Journal of Heat and Mass Transfer, 47, pp. 1761-1769.

Oztop, H.F, Al-Salem, K. (2012). A review on entropy generation in natural and mixed convection heat transfer for energy systems. Renewable and Sustainable Energy Reviews, 16(1). pp. 911-920.

Patankar, S.V. (1980). Numerical heat transfer and fluid flow. Washington: Taylor & Francis.

Peng, Y., Shu, C. and Chew, Y.T. (2003). Simplified thermal lattice Boltzmann model for incompressible thermal flows. Physical Review E, 68, pp. 026701.

Prasad, A.K. and Koseff, J.R. (1996). Combined forced and natural convection heat transfer in a deep lid-driven cavity flow. International Journal of Heat Fluid Flow, 17, pp. 460-467.

Putra, N., Roetzel, W. and Das, S.K. (2003). Natural convection of nanofluids. Heat Mass Transfer, 39, pp. 775-784.

Qi, C., Wang, G., Yang, L., Wan, Y. and Rao, Z. (2017). Two-phase lattice Boltzmann simulation of the effects of base fluid and nanoparticle size on natural convection heat transfer of nanofluid. International Journal of Heat and Mass Transfer, 105, pp. 664-672.

Qian, Y.H., d'Humieres, D. and Lallemand P. (1992). Lattice BGK models for Navier-Stokes equation. Europhysics Letters, 17, pp. 479-484.

Rajarathinam, M., Nithyadevi, N. and Chamkha, A.J. (2017). Heat transfer enhancement of mixed convection in an inclined porous cavity using Cu-water nanofluid. Advanced Powder Technology, 29, pp. 590-605.

Roache, P.J. (1997). Quantification of uncertainty in computational fluid dynamics. Annual Review of Fluid Mechanics, 29, pp. 123-160.

Roy, M., Roy, S. and Basak, T. (2015). Analysis of entropy generation on mixed convection in square enclosures for various horizontal or vertical moving wall(s). International Communications in Heat and Mass Transfer, 68, pp. 258-266.

Roy, M., Roy, S. and Basak, T. (2016). Analysis of entropy generation for mixed convection within porous square cavities: Effects of various moving walls. Numerical Heat Transfer, Part A: Applications, 70(7), pp. 738-762.

Sarkar, J., Ghosh, P. and Adil, A. (2015). A review on hybrid nanofluids: Recent research, development and applications. Renewable and Sustainable Energy Reviews, 43, pp.164-177.

Sciacovelli, A, Verda, V. and Sciubba, E. (2015). Entropy generation analysis as a design tool - a review. Renewable and Sustainable Energy Reviews, 43, pp. 1167-1181.

Seta, T., Takegoshi, E. and Okui, K. (2006). Lattice Boltzmann simulation of natural convection in porous media. Mathematics and Computers in Simulation, 72, pp. 195-200.

Shadloo, M.S. (2019). Numerical Simulation of Compressible Flows by Lattice Boltzmann Method. Numerical Heat Transfer, Part A: Applications, 75(3), pp. 167-182.

Shan, X. and Chen, H. (1994). Simulation of nonideal gases and gas-liquid phase transitions by the lattice Boltzmann equation. Physical Review E, 49, pp. 2941-2948.

Shan, X. and Chen, H., (1993). Lattice Boltzmann model for simulating flows with multiple phases and components. Physical Review E, 47, pp. 1815-1819.

Sharif, M.A.R. (2007). Laminar mixed convection in shallow inclined driven cavities with hot moving lid on top and cooled from bottom. Applied Thermal Engineering, 27, pp. 1036-1042.

Sheikholeslami, M. (2017). Lattice Boltzmann method simulation for MHD non-Darcy nanofluid free convection. Physica B: Condensed Matter, 516, pp. 55-71.

Sheikholeslami, M. (2018a). Numerical investigation for CuO-H_2O nanofluid flow in a porous channel with magnetic field using mesoscopic method. Journal of Molecular Liquids, 249, pp. 739-746.

Sheikholeslami, M. (2018b). Solidification of NEPCM under the effect of magnetic field in a porous thermal energy storage enclosure using CuO nanoparticles. Journal of Molecular Liquids, 263, pp. 303-315.

Sheikholeslami, M., Gorji-Bandpy, M., Ganji, D. and Soleimani, S. (2014). Thermal management for free convection of nanofluid using two phase model. Journal of Molecular Liquids, 194, pp. 179-187.

Sheikhzadeh, G.A., Dastmalchi, M. and Khorasanizadeh, H. (2013). Effects of nanoparticles transport mechanisms on Al_2O_3-water nanofluid natural convection in a square enclosure. International Journal of Thermal Science, 66, pp. 51-62.

Shenoy, A., Sheremet, M. and Pop, I. (2016). Convective flow and heat transfer from wavy surfaces: viscous fluids, porous media and nanofluids. New York: CRC Press.

Sheremet, M., Cimpean, D. and Pop, I. (2017). Free convection in a partially heated wavy porous cavity filled with a nanofluid under the effects of Brownian diffusion and thermophoresis. Applied Thermal Engineering, 113, pp. 413- 418.

Sheremet, M.A., and Pop, I. (2015). Free convection in a triangular cavity filled with a porous medium saturated by a nanofluid: Buongiorno's mathematical model. International Journal of Numerical Methods for Heat and Fluid Flow, 25(5). pp. 1138-1161.

Sheremet, M.A., Pop, I. and Nazar, R. (2015). Natural convection in a square cavity filled with a porous medium saturated with a nanofluid using the thermal nonequilibrium model with a Tiwari and Das nanofluid model. International Journal of Mechanical Science, 100, pp. 312-321.

Siavashi, M., Yousofvand, R. and Rezanejad, S. (2018). Nanofluid and porous fins effect on natural convection and entropy generation of flow inside a cavity. Advanced Powder Technology, 29, pp. 142-156.

Sidik, N.A.C. and Razali, S.A. (2014). Lattice Boltzmann method for convective heat transfer of nanofluids: A review. Renewable and Sustainable Energy Reviews, 38, pp. 864-875.

Sidik, N.A.C., Adamu, I.M., Jamil, M.M., Kefayati, G., Mamat, R, and Najafi, G. (2016a). Recent progress on hybrid nanofluids in heat transfer applications: a comprehensive review. International Communications in Heat and Mass Transfer, 78, pp. 68-79.

Sidik, N.A.C., Yazid, M.N.A.W.M., Samion, S., Musa, M.N. and Mamat, R. (2016b). Latest development on computational approaches for nanofluid flow modeling: Navier-Stokes based multiphase models. International Communications in Heat and Mass Transfer, 74, pp. 114-124.

Succi, S. (2001). The lattice Boltzmann equation for fluid dynamics and beyond. Oxford: Oxford University Press.

Succi, S., Foti, E. and Higuera, F. (1989). Three-dimensional flows in complex geometries with the lattice Boltzmann method. Europhysics Letter, 10, pp. 433-438.

Suresh, Ch.S.Y., Sateesh, G., Das, S.K., Venkateshan, S.P. and Rajan, M. (2005a). Heat transfer from a totally blocked fuel subassembly of a liquid metal fast breeder reactor: Part I. Experimental investigation. Nuclear Engineering and Design, 235, pp. 885-895.

Suresh, Ch.S.Y., Sundarajan, T., Venkateshan, S.P., Das, S.K. and Thansekhar, M. R. (2005b). Heat transfer from a totally blocked fuel subassembly of a liquid metal fast breeder reactor: II. Numerical simulation. Nuclear Engineering and Design, 235, pp. 897–912.

Suresh, S., Venkitaraj, K.P., Selvakumar, P. and Chandrasekar, M. (2011). Synthesis of Al_2O_3-Cu/water hybrid nanofluids using two step method and its thermos physical properties. Colloids and Surfaces A: Physicochemical and Engineering Aspects, 388, pp. 41-48.

Taghizadeh, S. and Asaditaheri, A. (2018). Heat transfer and entropy generation of laminar mixed convection in an inclined lid driven enclosure with a circular porous cylinder. International Journal of Thermal Sciences, 134, pp. 242-257.

van Leer, B. (1982). Flux-vector splitting for the Euler equations, Lecture Notes in Physics, 170, pp. 507-512.

Vanaki, Sh.M. and Ganesan, P. and Mohammed, H.A. (2016). Numerical study of convective heat transfer of nanofluids: A review. Renewable and Sustainable Energy Reviews, 54(C), pp. 1212-1239.

Varol, Y., Oztop, H.F. and Pop, I. (2009). Entropy generation due to natural convection in non-uniformly heated porous isosceles triangular enclosures at different positions, International Journal of Heat and Mass Transfer, 52(5-6), pp. 1193-1205.

Versteeg, H.K. and Malalasekera, W. (2007). An introduction to computational fluid dynamics: The finite volume method, Upper Saddle River: Pearson Education.

Vijaybabu, T.R., Anirudh, K. and Dhinakaran, S. (2017). Mixed convective heat transfer from a permeable square cylinder: A lattice Boltzmann analysis. International Journal of Heat and Mass Transfer, 115, pp. 854-870.

Vijaybabu, T.R. and Dhinakaran, S. (2019). MHD Natural convection around a permeable triangular cylinder inside a square enclosure filled with Al_2O_3-H_2O nanofluid: an LBM study. International Journal of Mechanical Sciences, 153-154, pp. 500-516.

Vishnuvardhanarao, E. and Das, M.K. (2009). Mixed convection in a buoyancy-assisted two-sided lid-driven cavity filled with a porous medium. International Journal of Numerical Methods for Heat & Fluid Flow, 19, pp. 329-351.

Waheed, M.A. (2009). Mixed convective heat transfer in rectangular enclosures driven by a continuously moving horizontal plate. International Journal of Heat and Mass Transfer, 52, pp. 5055-5063.

Wang, J., Wang, D., Lallemand, P. and Luo, L. (2013). Lattice Boltzmann simulations of thermal convective flows in two dimensions. Computers and Mathematics with Applications, 65 (2), pp. 262-286.

Wei, Y., Wang, Z, and Qian, Y. (2017). A numerical study on entropy generation in two-dimensional Rayleigh-Bénard convection at different Prandtl number. Entropy, 19(9), pp. 443.

Wolf-Gladrow, D.A. (2000). Lattice-gas cellular automata and lattice Boltzmann models: An introduction. Lecture Notes in Mathematics, 1725, Berlin: Springer.

Xuan, Y. and Yao, Z. (2005). Lattice Boltzmann model for nanofluids. Heat Mass Transfer, 41, pp. 199-205.

Yang, L.M., Shu, C. and Wu, J. (2013). A moment conservation-based non-free parameter compressible lattice Boltzmann model and its application for flux evaluation at cell interface. Computer & Fluids, 79, pp. 190-199.

Yang, L.M., Shu, C. and Wu, J. (2016). Extension of lattice Boltzmann flux solver for simulation of 3D viscous compressible flows. Computers & Mathematics with Applications, 71, pp. 2069-2081.

Yang, T., Wang, J., Yang, L.M. and Shu, C. (2019). Development of multicomponent lattice Boltzmann flux solver for simulation of compressible viscous reacting flows. Physical Review E, 100, pp. 033315.

Yapici, K. and Obut, S. (2015). Benchmark results for natural and mixed convection heat transfer in a cavity. International Journal of Numerical Methods for Heat & Fluid Flow, 25(5), pp. 998-1029.

Yu, D., Mei, R. and Luo, L.S. (2003). Viscous flow computations with the method of lattice Boltzmann equation. Progress in Aerospace Sciences, 39, pp. 329-367.

Zienkiewicz, O.C., Taylor, R.L. and Nithiarasu, P. (2014). The finite element method for fluid dynamics. Oxford: Butterworth-Heinemann.

Zou, Q. and He, X. (1997). On pressure and velocity boundary conditions for the lattice Boltzmann BGK model. Physics of Fluids, 9, pp. 1591-1597.

Appendix A

Conversion of Units

The mesh-independent quantities in a real physical system are based on SI units such as meter (m), second (s) and kilogram (kg), and they are defined as physical units (p). However, to facilitate computer simulation, there is a need for unit conversion from physical to dimensionless system as computers can only process binary numbers (i.e., dimensionless numbers) and these non-dimensional parameters are termed as lattice units (lb) in lattice Boltzmann method.

In LBM, the conversion of units is done in two sequential steps. The first step deals with the conversion of dimensional physical quantities into dimensionless quantities. The second step concerns the conversion of a dimensionless system into a discrete simulation system. All these three unit systems (the physical (p), the dimensionless (d), and the LB (lb)) are communicated through dimensionless parameters. For example, the benchmark lid-driven cavity problem can be defined fully using only one dimensionless parameter, i.e. the Reynolds number (*Re*). Therefore, to simulate the same flow problem, all three unit systems must have the same Reynolds number. The conversion of the unit from physical to dimensionless is based on the choice of a characteristic length scale and time scale. The transition from the dimensionless unit to the LB unit is made through the choice of discretisation parameters Δx and Δt, where Δx is the spacing between two adjacent lattice nodes and Δt is the time step. The procedure for conversion from physical to lattice unit is given below by considering the example of a lid-driven cavity flow problem.

The lid-driven cavity flow problem is characterised by the physical velocity of the lid (u_p), the length of the cavity (l_p) and viscosity (property) of the fluid (ν_p). These physical variables are replaced by their dimensionless counterpart as follows:

$$l_d = \frac{l_p}{L}; u_d = \frac{u_p}{V_0^*}; \nu_d = \frac{\nu_p}{V_0^* L} \tag{A. 1}$$

where L and V_0^* are taken as the reference length in metre and characteristic velocity of the fluid in metre per sec respectively. The non-dimensional parameter, Reynolds number is defined using both dimensional and non-dimensional quantities as follows:

$$Re = \frac{u_p l_p}{\nu_p} = \frac{u_d l_d}{\nu_d} \tag{A. 2}$$

Mostly in numerical simulation, L and V_0^* are considered to have the same magnitude as l_p and u_p which lead to the values of dimensionless length (l_d) and velocity (u_d) of unity. Therefore, in terms of dimensionless quantities, Re becomes equal to reciprocal of the dimensionless viscosity (ν_d).

Now, to convert these dimensionless quantities to LB quantities, the discretisation of space and time for the particular simulation has to be introduced. In LBM, the lattice spacing Δx and time step Δt are obtained by dividing the dimensionless length by the number of grid size N and the dimensionless time by the number of iteration steps N_{iter} to reach the final time (transient flow condition), i.e.,

$$\Delta x = \frac{l_d}{N} \tag{A. 3}$$

$$\Delta t = \frac{l_d}{u_d N_{iter}} \tag{A. 4}$$

For convenience, generally, these parameters Δx and Δt are set equal to one [Krüger et al., 2016]. Therefore, the dimensionless length (l_d) becomes equal to the number of grid size (N). As our problems deal with steady-state flow problems, we have to get rid of Δt, which is shown in the subsequent steps. The LB velocity and viscosity can be obtained from dimensionless quantities through a dimensionless analysis:

$$u_{lb} = \frac{\Delta t}{\Delta x} u_d \tag{A. 5}$$

$$\nu_{lb} = \frac{\Delta t}{\Delta x^2} \nu_d = \frac{u_{lb}}{\Delta x} \frac{1}{Re} = \frac{u_{lb} N}{Re} \tag{A. 6}$$

However, in LBM, the LB viscosity is defined using a relaxation time τ with a constraint that its value should be greater than 0.5 for minimizing the errors and achieving stability. The LB viscosity is determined as:

$$\nu_{lb} = {C_s}^2 \left(\tau - \frac{1}{2}\right) \tag{A. 7}$$

It is found that ν_{lb} depends on τ, u_{lb} and Δx. However, another constraint put into LBM to simulate incompressible flow problem is that LBM velocity should be less than the lattice speed of sound C_s which is equal to $\frac{1}{\sqrt{3}}$. Therefore, in LBM, the discretisation parameters such as Δx or N need to be tuned according to the problem.

Appendix B

Compressible Flow using LBM

B. 1. Introduction

In this thesis work, both SRT- and MRT- LBM have been used to study different problems pertained to viscous incompressible flow system. Generally, in LBM, the equilibrium distribution function (EDF) is derived by applying the truncated Taylor series expansion to Maxwell function which is the exponential form of particle velocity, in terms of Mach number and that inevitably limits the range of applied Mach number. Besides that, EDF should be expressed as a polynomial form of particle velocity to recover the Navier-Stokes equations using Chapman-Enskog expansion. So, attempts have been made by various researchers to change EDF in order to simulate compressible flow problems. From literature, it is found that compressible LB models encounter difficulty while performing the collision-streaming process as they become numerically unstable. Therefore, to study compressible flow, researchers have opted for schemes based on discrete velocity Boltzmann equation (DVBE) over lattice Boltzmann equation (LBE), where the discretization of space and time quantities can be treated independently. Kataoka and Tsutahara [2004] provide a simple and rigorous theoretical background in solving DVBE for compressible flows by implementing discretization techniques based on finite difference method. Considering the work towards this direction, Shadloo [2019] have recently developed a compressible FD-LBM model which couples the multiple-relaxation time LB model and two highly stable discretization schemes based on modified total variation diminishing and modified Lax-Wendroff. Although the DVBE model can simulate compressible flow with high Mach number, it loses the primary advantages of LBM such as simple implementation and algebraic operation. Besides, DVBE model may contain a significant numerical dissipation and lead to numerical instability similar to conventional numerical techniques as it contains a set of partial differential equations equal

to the number of lattice velocities, which is more than the number of conservative variables. A lattice Boltzmann flux solver (LBFS) (also termed as hybrid FVM-LBM) has been first proposed by Ji et al. [2009] to overcome defects of DVBE models. The basic idea of LBFS is to reconstruct numerical fluxes at each cell interface from local solution of 1D compressible lattice Boltzmann (LB) model for one streaming step and then to calculate the node parameters using the conventional finite volume method. LBFS is found to be very efficient and easy to implement compared with the DVBE approach. Later, the LBFS model is improved and extended to simulate different flow phenomenon by researchers like Joshi et al. [2010] and Yang et al. [2013, 2016]. Recently, Yang et al. [2019] have extended their previous model to simulate two-dimensional multicomponent compressible viscous reacting flows. However, the works concerning the LBFS model in the simulation of compressible flow is very limited, which motivates us to carry out the present work. In this preliminary work, Joshi et al.'s LBFS model [2010] is incorporated in our in-house FORTRAN code to simulate a well-established benchmark compressible flow problem.

B. 2. Numerical methodology

The LBFS (or hybrid FVM–LBM) method proposed by Joshi et al. [2010] is adopted here. As mentioned earlier, this model is based on the fundamental idea that the inter-cell face parameters are determined by the LBM and the node parameters are calculated using the conventional finite volume method.

For the convenience of numerical calculation and analysis, the variables are expressed in the non-dimensional form for one-dimensional problem as follows:

$$t = \frac{t^*}{\frac{L}{\sqrt{RT_0^*}}};\ x = \frac{x^*}{L};\ \rho = \frac{\rho^*}{\rho_0^*};\ u = \frac{u^*}{\sqrt{RT_0^*}};\ T = \frac{T^*}{T_0^*};\ P = \frac{P^*}{\rho_0^*\, RT_0^*} \tag{B.1}$$

where L, ρ_0^* and T_0^* are taken as the reference length, density and temperature respectively. The symbols with '$*$' indicate the parameters in their dimensional form and without '$*$' indicate the same in their non-dimensional form. The symbol t, x, ρ, u, T, P and R denote time, spatial coordinate, density, velocity, temperature, pressure and specific gas constant respectively.

The 1D time-dependent Euler equations in conservative form is given below,

$$U_t + F(U) = 0 \tag{B.2}$$

Here U and $F(U)$ are the vector of conserved variables and the flux vectors along the x-direction respectively, which are given as follows:

$$U = \begin{bmatrix} \rho \\ \rho u \\ E \end{bmatrix}; F(U) = \begin{bmatrix} \rho u \\ \rho u^2 + P \\ u(E+P) \end{bmatrix} \tag{B.3}$$

E is the total energy per unit volume given by,

$$E = \frac{\rho}{2}\left(u^2 + \frac{P}{\rho}b\right); b = \frac{2}{(\gamma-1)}; P = \rho RT \tag{B.4}$$

A conservative finite volume scheme is used to discretize the Equation (B.2) as follows:

$$U_j^{n+1} = U_j^n + \frac{\Delta t}{\Delta x}\left(F^n_{j-\frac{1}{2}} - F^n_{j+\frac{1}{2}}\right) \tag{B.5}$$

where U_j^n denote the conserved variable vector at the node j and at time level n. The initial condition can be given as,

$$\rho = \rho_0; u = u_0; T = T_0 \quad \text{at } t = 0 \tag{B.6}$$

To calculate fluxes at the inter-cell faces, Kataoka and Tsutahara's compressible model is used. This process gives the initial solutions of compressible Euler equations (B.2) and initial condition (B.6) in terms of particle velocity distribution function. D1Q5 lattice structure is used for solving the one-dimensional problem. The five discrete lattice velocities (e_i) in the x-direction are given as,

$$\begin{aligned} e_i &= 0 && \text{for } i = 0 \\ e_i &= v_1 cos\,(\pi i) && \text{for } i = 1, 2 \\ e_i &= v_2 cos\,(\pi i) && \text{for } i = 3, 4 \end{aligned} \tag{B.7}$$

The suffix i ($0 \le i \le 4$) refers to a distribution function with velocity e_i. To control the specific-heat ratio, new variable is introduced as follows,

$$\eta_i = \eta_0 \qquad \text{for } i = 0$$
$$\eta_i = 0 \qquad \text{for } i = 1, 2, 3, 4 \tag{B.8}$$

The parameters in LBM equations are chosen to be $v_1 = 1$, $v_2 = 3$, $\eta_0 = 2$. The local equilibrium particle velocity distribution function (f_i^{eq}) is defined as,

$$f_i^{eq} = \rho\{A_i + B_i u e_i\} \tag{B.9}$$

where,

$$A_i = \frac{T}{\eta_0^2}(b-1) \qquad \text{for } i = 0$$
$$A_i = \frac{1}{2(v_1^2 - v_2^2)}\left[-v_2^2 + \left(\frac{v_2^2}{\eta_0^2}(b-1)+1\right)T + u^2\right] \qquad \text{for } i = 1, 2 \tag{B.10}$$
$$A_i = \frac{1}{2(v_2^2 - v_1^2)}\left[-v_1^2 + \left(\frac{v_1^2}{\eta_0^2}(b-1)+1\right)T + u^2\right] \qquad \text{for } i = 3,4$$

and

$$B_i = \frac{[-v_2^2 + (b+2)T + u^2]}{2v_1^2(v_1^2 - v_2^2)} \qquad \text{for } i = 1, 2$$
$$B_i = \frac{[-v_1^2 + (b+2)T + u^2]}{2v_2^2(v_2^2 - v_1^2)} \qquad \text{for } i = 3, 4 \tag{B.11}$$

The DVBE in a non-dimensional form with BGK collision term used for solving particle velocity distribution function is given as,

$$\frac{\partial f_i}{\partial \mathrm{t}} + e_i \frac{\partial f_i}{\partial x} = \frac{1}{\varepsilon}\left(f_i^{eq}(x,t) - f_i(x,t)\right) \tag{B.12}$$

where the Knudsen number ε is expressed in terms of relaxation parameter τ as $\varepsilon = \frac{\tau\sqrt{RT_0}}{L}$. The particle velocity distribution function (f_i) is initialised by local equilibrium particle velocity distribution function (f_i^{eq}). The particle kinetic equation (PKE) (B.12) without collision term is then discretized approximating first-order forward in time and first-order

upwind in space. This discretized form of PKE is used in LBFS to carry out the LBM simulation at a new time step, given as follows:

$$(f_i)_j^{n+1} = (f_i)_j^n - \Delta t \left[\frac{(e_i+|e_i|)}{2} \left(\frac{(f_i)_j^n - (f_i)_{j-\frac{1}{2}}^n}{\frac{\Delta x}{2}} \right) - \frac{(e_i-|e_i|)}{2} \left(\frac{(f_i)_j^n - (f_i)_{j+\frac{1}{2}}^n}{\frac{\Delta x}{2}} \right) \right] \quad \text{(B.13)}$$

where Δx is the distance between two lattice nodes and inter-cell face placed between two nodes. In LBFS, the advantage of the FVM is utilized in determining the time step Δt, which is based on the Courant–Friedrichs–Lewy (CFL) criterion. But, in the DVBE scheme used by Kataoka and Tsutahara [2004], the time step is restricted by Knudsen number. The CFL criterion for LBFS is given as,

$$\Delta t \; = \; C_{cfl} \times \min\left(\frac{\Delta x}{S_j^n}\right); \quad S_j^n = \left|u_j^n\right| + a \quad \text{(B.14)}$$

C_{cfl} is the CFL number maintained at the value around 0.5. S is the wave speed, u is the macroscopic velocity component in the *x*-direction and a is the speed of sound.

The macroscopic variables, i.e., density, velocity and temperature are then calculated using the particle velocity distribution function at the new time step as:

$$\rho = \sum_{i=0}^{5} f_i \; ; \; \rho \mathrm{u} = \sum_{i=0}^{5} f_i \; \mathrm{e}_i \; ; \; \rho(bT + u^2) = \sum_{i=0}^{5} f_i \; (\mathrm{e}_i^2 + \eta_i^2) \quad \text{(B.15)}$$

The fluxes at the inter-cell faces are calculated using equation (B.3) and equation (B.5) is used to find node parameters for the next time step.

B. 3. Test problem and Results

One dimensional Sod's shock tube problem [1978] is used as the basic test problem to validate compressible flow model. The initial condition for shock tube problem is given as,

$$\begin{aligned} &\rho^* = 1.0 \text{ (kg m}^{-3}\text{)}; \; u^* = 0 \text{ (m s}^{-1}\text{)}; \; P^* = 1.0 \text{ (bar)} \quad \text{for } -10 \le X \le 0 \\ &\rho^* = 0.125 \text{ (kg m}^{-3}\text{)}; \; u^* = 0 \text{ (m s}^{-1}\text{)}; \; P^* = 0.1 \text{ (bar)} \quad \text{for } 0 \le X \le 10 \end{aligned} \quad \text{(B.16)}$$

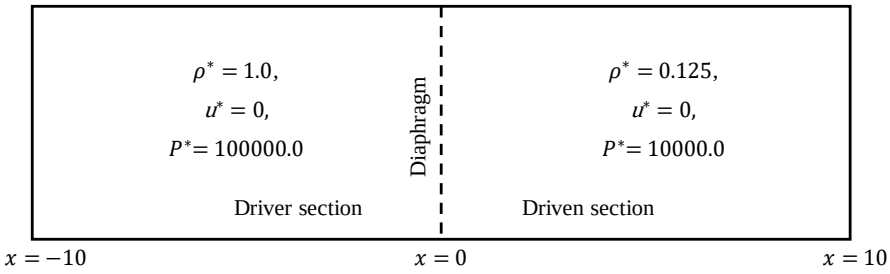

Fig. B.1 Schematic diagram of the shock tube.

The simulation is carried out for the time $t^* = 0.01$ sec with a length of shock tube $L = 20$ m while placing the diaphragm at 10 m. Fig. B.1 shows the schematic diagram of the flow configuration. A shock tube is a tube closed at both the ends having a diaphragm midway between the two ends. The tube contains air on either side of the diaphragm at two

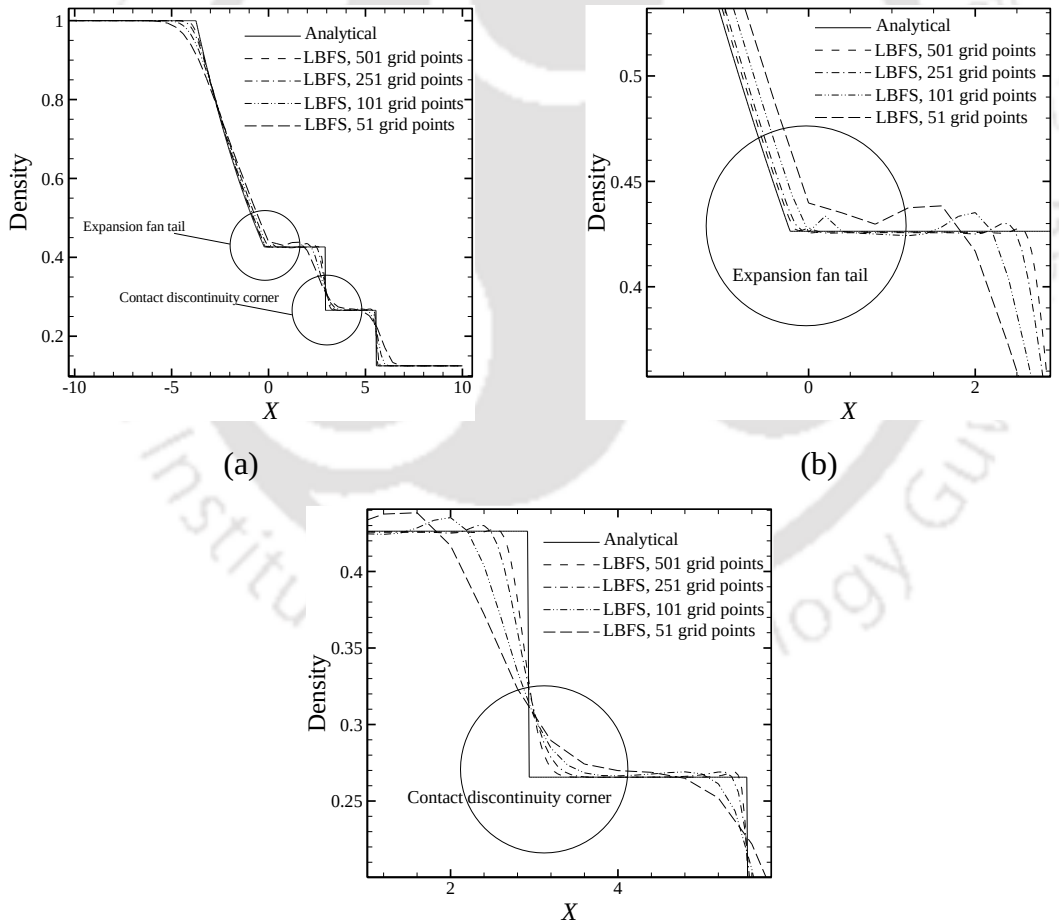

Fig. B.2 (a) Grid independence study in terms of density, (b) Enlarged view of corner for expansion fan tail and (c) Enlarged view of corner for contact discontinuity.

different states. The left chamber (Driver section) contains high pressure and high density gas, whereas the right chamber (Driven section) has relatively low pressure and density. If the axis of the tube is parallel to the *x*-axis, the locations of the two ends of the tube are given by $x^* = 0$ and 10 m and, the diaphragm is located at $x^* = 5.0$ m. Once the diaphragm breaks at the time $t^* = 0$, it results in complex flow with an expansion wave moving to the left and, a shock wave and a contact surface moving to the right. The current problem is modelled as a one-dimensional problem. The stopping time for termination of simulation is set before the waves reach the ends of the tube.

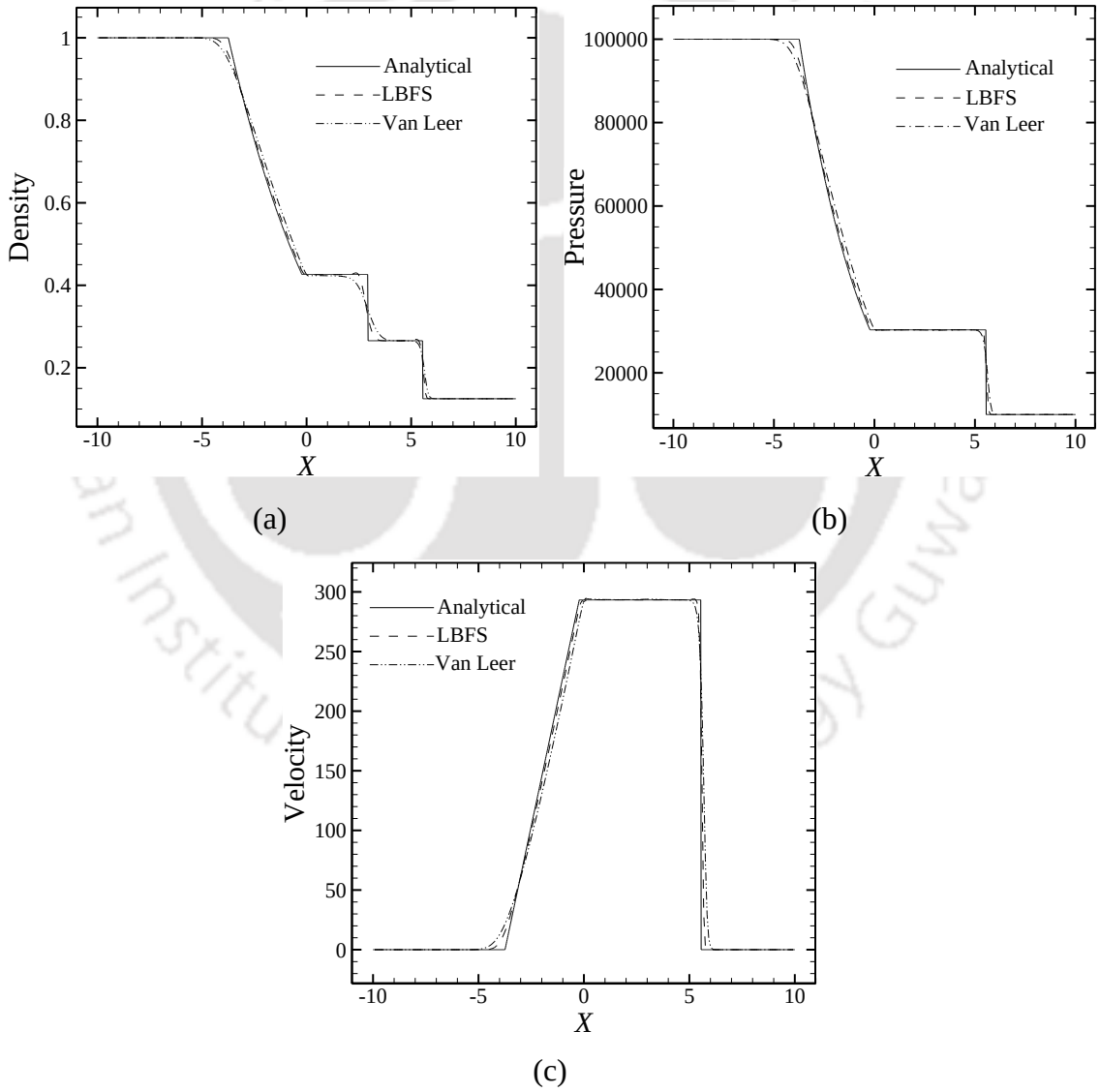

Fig. B.3 Comparison of solutions of analytical, LBFS and Van Leer scheme in terms of (a) Density, (b) Pressure and (c) Velocity profiles along the length of tube.

Figure B.2(a) shows the grid independence test in terms of density plot along the length of tube for four grid points 51, 101, 251 and 501 while comparing the results with the analytical (exact) solution for Sod's shock tube problem. Figs B.2(b) and (c) depict the magnified views of the corner for rarefaction tail and the contact discontinuity respectively. It is found that as the grid is refined from 51 points to 251 points, the size of oscillations reduces. However, noticeable change of the size of oscillations is not observed with further refinement of grid points up to 501 and therefore grid points 251 is found to be suitable for all computations while taking note of the time-wise efficiency of the numerical simulation.

Figs. B.3(a), (b) and (c) show the plots of density, pressure and velocity profiles along the length of tube respectively using LBFS scheme with the analytical solution and Van Leer's flux vector splitting scheme [10]. LBFS scheme provides a close approximation to exact solution than Van Leer's scheme for the same number grid size as observed from Figs. B.4(a) and (b) which present the zoomed view of the rarefaction tail and contact discontinuity corners of Fig. B.3(a). Fig. B.4(b) shows that very slight overshoots are observed at the contact discontinuity and shock wave for LBFS model, however, the size of these oscillations reduce with the refinement of the grid as seen from Fig. B.2(c).

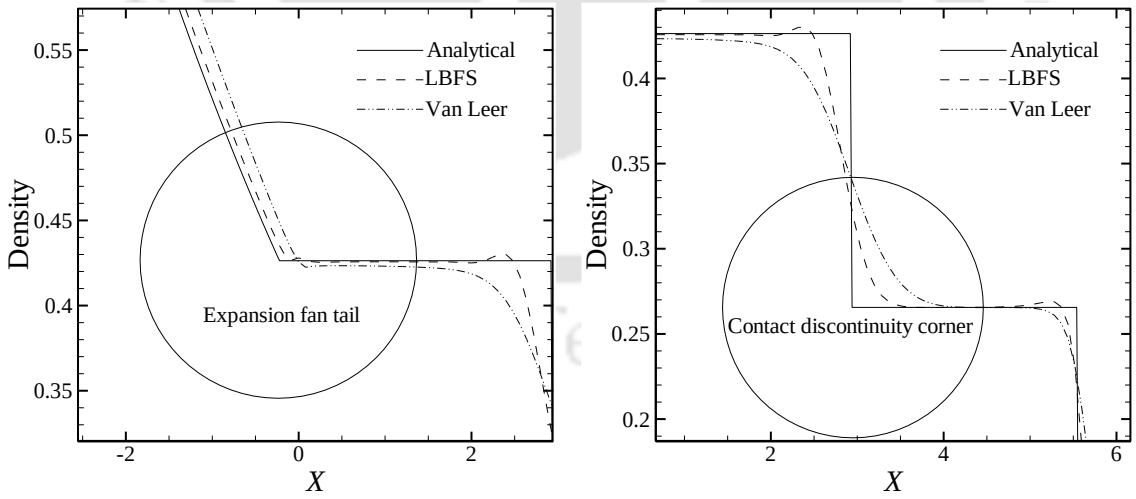

Fig. B.4 Enlarged view of Fig. B.3(a) for (a) Expansion fan tail corner and (b) Contact discontinuity corner.

B. 4. Conclusions

In this simulation, compressible flow lattice Boltzmann flux solver approach proposed by Joshi et al. [2010] is adopted. The shock tube problem is taken as test problem to validate the current method as this test case contains all the flow features involved in compressible flows such as shock, expansion and contact discontinuity. It is found from the results LBFS scheme has successfully captured all these flow features and also shown better performance than well-established van Leer's flux vector splitting scheme. However, LBFS works under a Mach number constraint of 1. The main advantage of LBFS model is that it retains the advantages of basic LBM such as simple calculation procedure and flexibility in use. There is a strong need of improvement in this model to deal with flows with Mach number greater than one. How this is done can be an interesting research problem.

List of Publications

International Journal Articles (Refereed)

1. **Kashyap, D.**, Dass, A.K., "Effect of boundary conditions on heat transfer and entropy generation during two-phase mixed convection hybrid Al_2O_3-Cu/water nanofluid flow in a cavity," **International Journal of Mechanical Sciences,** Volumes 157-158, Pages 45-59, 2019. DOI: 10.1016/j.ijmecsci.2019.04.014
2. **Kashyap, D.**, Dass, A.K., "Two-phase lattice Boltzmann simulation of natural convection in a Cu-water nanofluid-filled porous cavity: Effects of thermal boundary conditions on heat transfer and entropy generation," **Advanced Powder Technology**, Volume 29(11), Pages 2707-2724, 2018. DOI: 10.1016/j.apt.2018.07.020
3. **Kashyap, D.**, Dass, A.K., "Benchmark compressible flow simulation based on lattice Boltzmann method", **Materials Today: Proceedings**, Volume 28, Part 4, Pages 2522-2526, 2020. DOI: 10.1016/j.matpr.2020.05.007
4. **Kashyap, D.**, Dass, A.K., Oztop, H.F., Abu-Hamdeh, N., "Multiple-Relaxation-Time Lattice Boltzmann analysis of Entropy Generation in a Hot-Block-Inserted Square Cavity for different Prandtl Numbers" (Under review in International Journal of Thermal Sciences)
5. Effect of Cavity Inclination on Mixed Convection in a Double-Sided Lid-Driven Cavity with a Centrally Inserted Hot Porous Block. (Under Preparation)
6. Investigation of an inner permeable hot square cylinder on mixed convection flow in a double-sided lid-driven nanofluid filled square cavity. (Under Preparation)

Book Chapters (Refereed)

1. **Kashyap, D.**, Dass, A.K., "Analysis of Heat Transfer and Entropy Generation During Natural Convection in a Cu–Water Nanofluid-Filled Porous Cavity for Different Thermal Boundary Conditions", In: Singh S., Ramadesigan V. (eds) Advances in Energy Research, Vol. 1. Springer Proceedings in Energy. Springer, Singapore, 2020. DOI: 10.1007/978-981-15-2666-4_62
2. **Kashyap, D.**, Dass, A.K., "Simulation of Mixed Convection flow in square cavities by Lattice Boltzmann method" Fluid Mechanics and Fluid Power - Contemporary Research, Part of the series Lecture Notes in Mechanical Engineering. India: Springer; Pages 559-568, 2017. DOI: 10.1007/978-81-322-2743-4_54

International Conference Papers (Refereed)

1. **Kashyap, D.**, Dass, A.K., "Entropy Generation Analysis of Mixed Convection Flow in a Nanofluid Filled Porous Cavity Using a Two-Component Lattice Boltzmann Method." Proceedings of the ASME 2019 Gas Turbine India Conference, Volume 1: Compressors, Fans, and Pumps; Turbines; Heat Transfer;

Structures and Dynamics, V001T03A007, December 5-6, 2019, Chennai, India. DOI: 10.1115/GTINDIA2019-2544

2. **Kashyap, D.**, Dass, A.K., "Comparative study of hybrid nanofluid with regular nanofluid during natural convection in cavity using two-phase lattice Boltzmann method", 12th International Conference on Thermal Engineering: Theory and Application, February 23-26, 2019, Pandit Deendayal Petroleum University, Gandhinagar, India. Paper ID: 224. https://journals.library.ryerson.ca/index.php/ictea/article/view/1179

3. **Kashyap, D.**, Dass, A.K., "Lattice Boltzmann computation of natural convection in a square porous cavity with different thermal boundary conditions", International Conference on Computational Methods for Thermal Problems, Issue 223309, Pages 388-391, 2018. (Proceedings of THERMACOMP 2018, July 9-11 20,18, IISc Bangalore, India)

4. **Kashyap, D.**, Dass, A.K., "Simulation of Mixed Convection of Nanofluid in shallow cavity using Lattice Boltzmann method", 23rd National Heat and Mass Transfer Conference and 1st International ISHMT-ASTFE heat and mass transfer conference (IHMTC 2015), December 17-20, 2015, Indian Space Research Organisation (ISRO), Trivandrum, India. Paper No: 882

International Conference Papers (Non-refereed)

1. **Kashyap, D.**, Dass, A.K., "Study of multiple solutions in two-sided non-facing lid-driven square cavity using multiple-relaxation-time lattice Boltzmann method", 7th International Congress on Computational Mechanics and Simulation (ICCMS 2019), December 11-13, 2019, IIT Mandi, Himachal Pradesh, India. Paper ID: ICCMS19SD025053

2. **Kashyap, D.**, Dass, A.K., "Multiple relaxation time lattice Boltzmann simulation of flows over two circular cylinders in tandem arrangement", 6th International and 43rd National Conference on Fluid Mechanics and Fluid Power (FMFP 2016), December 15-17, 2016, MNNITA, Allahabad, U.P., India. Paper No: 450

3. Kalita S. S., **Kashyap, D.**, Dass, A.K., "GPU accelerated lattice Boltzmann method applied to mixed convection in a differentially heated square cavity", 6th International and 43rd National Conference on Fluid Mechanics and Fluid Power (FMFP 2016), December 15-17, 2016, MNNITA, Allahabad, U.P., India. Paper No: 532

4. **Kashyap, D.**, Dass, A.K., "Mixed Convection Flow in horizontal two-sided lid-driven differentially heated square cavity by Lattice Boltzmann method", International Symposium on Aspects of Mechanical Engineering and Technology for Industry, 2014 (AMETI 2014), December 6-8, 2014, Nerist, Arunachal Pradesh, India. Paper ID: AMETI2014-134